approach to equilibrium in high energy heavy ion collisions
Thomas Epelbaum

THÈSE DE DOCTORAT
DE L'UNIVERSITÉ PIERRE ET MARIE CURIE

Spécialité : Physique

École doctorale : « ED P2MC 389, Physique »

réalisée

à l'Institut de physique théorique, CEA Saclay

présentée par

Thomas EPELBAUM

pour obtenir le grade de :

DOCTEUR DE L'UNIVERSITÉ PIERRE ET MARIE CURIE

Sujet de la thèse :
Approche de l'équilibre dans les collisions hadroniques
à haute énergie

soutenue le 18 juin 2014

devant le jury composé de :

Dr.	François GELIS	Directeur de thèse
Pr.	Tuomas LAPPI	Examinateur
Dr.	Stéphane MUNIER	Rapporteur
Pr.	Anton REBHAN	Examinateur
Pr.	Carlos SALGADO	Rapporteur
Pr.	Jean-Bernard ZUBER	Examinateur

THÈSE DE DOCTORAT
DE L'UNIVERSITÉ PIERRE ET MARIE CURIE

Spécialité : Physique

École doctorale : « ED P2MC 389, Physique »

réalisée

à l'Institut de physique théorique, CEA Saclay

présentée par

Thomas EPELBAUM

pour obtenir le grade de :

DOCTEUR DE L'UNIVERSITÉ PIERRE ET MARIE CURIE

Sujet de la thèse :

Approche de l'équilibre dans les collisions hadroniques à haute énergie

soutenue le 18 juin 2014

devant le jury composé de :

Dr.	François GELIS	Directeur de thèse
Pr.	Tuomas LAPPI	Examinateur
Dr.	Stéphane MUNIER	Rapporteur
Pr.	Anton REBHAN	Examinateur
Pr.	Carlos SALGADO	Rapporteur
Pr.	Jean-Bernard ZUBER	Examinateur

Table des matières

Résumé

ette thèse a pour but d'étudier la théorie des premiers instants d'une collision d'ions lourds. Juste après cette collision, il a été démontré que la matière produite – appelée Plasma de Quarks et de Gluons (PQG) – est très loin de l'équilibre thermique. On voudrait donc savoir si le PQG thermalise, et quelle est l'échelle de temps caractéristique pour cela. Démontrer la thermalisation du PQG permettrait par ailleurs de justifier l'utilisation de l'hydrodynamique pour décrire l'évolution ultérieure d'une collision d'ions lourds. Après avoir rappelé quelques concepts essentiels au traitement théorique du PQG, le manuscrit expose l'étude de ces questions dans deux sortes de théories.

Dans un premier temps, on étudie une théorie scalaire. En initialisant cette dernière dans un état hors équilibre, on peut étudier l'approche de l'équilibre pour un système de volume fixe ou un système en expansion unidimensionnelle. Dans les deux cas, des preuves d'une possible thermalisation peuvent être observées : une équation d'état se forme, le tenseur des pressions devient isotrope et le nombre d'occupation tend vers une distribution d'équilibre thermique classique. Ces résultats sont obtenus à l'aide de l'approximation classique statistique (ACS), qui permet d'inclure des contributions au-delà de l'ordre dominant de la théorie des perturbations.

Dans un second temps, le "Color Glass Condensate", une théorie effective basée sur la Chromodynamique quantique adaptée à l'étude des premiers instants suivant la formation du PQG, est utilisé pour étudier de manière plus réaliste l'approche de l'équilibre thermique dans les collisions d'ions lourds. Après avoir établi quelques prérequis pour l'utilisation de l'ACS, les simulations numériques effectuées avec les équations de Yang-Mills semblent indiquer une rapide approche du PQG vers un régime hydrodynamique. Le PQG devient rapidement isotrope, tandis que son rapport viscosité sur entropie est très petit, ce qui est la caractéristique d'un fluide quasi idéal.

Mots-Clés

hromodynamique quantique
Collision d'ions lourds, Comportement Hydrodynamique
Color Glass Condensate
Approximation Classique Statistique, Simulations sur réseau

Abstract

his thesis deals with the theory of the early stages of a heavy ion collision. Just after such a collision, the matter produced – called the Quark-Gluon-Plasma (QGP) – has been shown to be far out of thermal equilibrium. One would like to know whether the QGP thermalizes, and what is the typical time scale for this. Proving that the QGP thermalizes would also justify from first principles the hydrodynamical treatment of the subsequent evolution of a heavy ion collision. After having recalled some essential theoretical concepts, the manuscript addresses these questions in two different theories

In a first part, we study a scalar field theory. Starting from an out of equilibrium initial condition, one studies the approach to equilibrium in a fixed volume or in a one-dimensional expanding system. In both cases, clear signs of thermalization are obtained: an equation of state is formed, the pressure tensor becomes isotropic and the occupation number approaches a classical thermal distribution. These results are obtained thanks to the classical statistical approximation (CSA), that includes contributions beyond the Leading Order perturbative calculation.

In a second part, the Color Glass Condensate – a quantum chromdynamics (QCD) effective theory well suited to describe the early life of the QGP – is used to treat more realistically the approach to thermalization in heavy ion collisions. After having derived some analytical prerequisites for the application of the CSA, the numerical simulations performed with the Yang-Mills equations show evidences of an early onset of hydrodynamical behavior of the QGP: the system becomes isotropic on short time scales, while the shear viscosity over entropy ratio is very small, which is characteristic of a quasi perfect fluid.

Keywords

uantum Chromodynamics
Heavy Ion Collisions, Hydrodynamical behavior
Color Glass Condensate
Classical Statistical Approximation, Lattice Simulations

Remerciements

crire ces remerciements est une tâche aussi difficile que celle de rédiger le reste du manuscrit. Car comment être sur de n'oublier personne, tant je suis redevable de nombre de collègues, d'amis (qui sont parfois les mêmes) et de proches ?

Le plus sûr est de commencer par la personne la plus évidente. Car cette thèse ne serait pas ce qu'elle est (elle ne serait même pas) sans les idées, l'aide inestimable et les discussions fréquentes que j'ai pu avoir avec mon directeur de thèse François Gelis. En plus de m'apprendre une bonne partie de ce que je sais sur la chromodynamique quantique (et sur tant d'autres sujets), François a également parfait mon niveau d'escalade, et a eu la bonté de ne pas m'abandonner (particulièrement à Table mountain) dans les randonnées que nous avons faites ensemble, où je fermais (toujours) la marche... Grâce à lui, j'ai également presque vaincu ma phobie des temps d'attente avant un train/avion, grâce à une connexion mémorable d'Eurostar... C'est au contact des autres que l'on forme et affine sa propre personnalité, et je suis heureux d'avoir pu le faire au côté de François. La dette que j'ai contractée à son égard me paraît irremboursable, mais cela ne m'empêche pas de le remercier infiniment pour tout ce qu'il a fait pour moi.

Je remercie chaleureusement mes rapporteurs de thèse Stéphane Munier et Carlos Salgado, qui ont eu la gentillesse d'accepter cette tâche. Lire ma prose n'a pas dû être de tout repos, a du leur prendre un certain temps (voire même un temps certain) et ils ont pour cela toute ma reconnaissance.

Merci également aux autres membres du jury d'avoir accepté d'y prendre part et d'avoir fait le déplacement jusqu'à Saclay en empruntant sûrement pour leur plus grand malheur le "fameux" RER B (que je ne saurai trop recommander d'éviter). Merci donc à Jean-Bernard Zuber, Tuomas Lappi et Anthon Rebhan d'avoir accepté d'être présents pour ma soutenance. Je peux aussi remercier Jean-Bernard pour son cours que j'ai eu la chance de suivre à l'ENS durant mes études, et Tuomas et Anthon pour les conseils qu'ils ont pu me prodiguer lors de nos rencontres à diverses conférences.

RER B mis à part, j'ai eu le privilège de passer les trois années de ma thèse à l'IPhT, cadre paisible mais néanmoins émulateur de nombreuses idées, grâce (entre autres) aux membres du groupe de physique des particules. Merci donc à ceux qui sont toujours présents à l'heure où j'écris ces lignes : Jean-Paul Blaizot, Fabio Dominguez, Leonard Fister, Edmond Iancu, Jose-Daniel Madrigal-Martinez, Yacine Mehtar-Tani, Jean-Yves Ollitrault, Robi Peschanski, Ekaterina Retinskaya, Gregory Soyez, Bin Wu et Li Yan. Merci également à ceux qui nous ont quittés (uniquement physiquement heureusement) mais avec qui j'ai aimé échangé : Javier Lopez-Albacete, Matthew Luzum, Cyrille Marquet et Naoto Tanji.

L'IPhT ne serait pas ce qu'il est sans le support sans failles du personnel administratif, sans aucun doute le plus efficace de France (sans contestation possible sur l'échantillon qu'il ma été donné de voir durant ma courte existence). Citons-les donc : Anne Angles, Loic Bervas, Catherine Cataldi, Emmanuelle De-Laborderie, Morgane Moulin et Laure Sauboy. Une mention spéciale pour Sylvie Zaffanella, sans qui je pense que l'IPhT n'existerait de toute façon plus. Merci également au personnel informatique qui m'a sauvé plusieurs fois de la crise de nerfs : Patrick Berthelot, Pascale Beurtey, Philippe Caresmel et Laurent Sengmanivanh.

L'IPhT ne serait pas non plus ce lieu convivial sans tous ces doctorants, que je remercie ici. Merci tout particulièrement à tous ceux qui ont dû me supporter pendant plus ou moins longtemps dans le bureau 136 (certains ont même craqué) : Jean-Phillipe Dugard, Hannah Gronqvist, Kasper Larsen (qui a tenu peu de temps), Remi Louf et Piotr Warchol. Merci également entre autres à Piotr T., Benoît et Alexandre L. qui m'ont aidé à combattre mes tendances autistiques du mieux qu'ils ont pu.

Un merci particulier va à mes collaborateurs (en plus de François bien évidemment) : Kevin Dusling, Raju Venugopalan et Bin Wu.

Grâce à la générosité de François et du groupe de physique des particules, j'ai eu la chance de voyager plus que je n'aurais jamais pu l'imaginer au cours de ma thèse, afin de me rendre à des conférences ou des workshops. Au cours de ces réunions, j'ai rencontré nombre de personnes que la place m'empêche de toutes nommer ici, mais qui m'ont néanmoins énormément apporté. Si ces personnes lisent ces lignes, elles se reconnaîtront sans aucun doute (quoique la plupart d'entre elles doivent malheureusement pour cela commencer par apprendre le français).

Certaines personnes ont eu la bonté de m'inviter pour donner des séminaires dans des contrées plus ou moins éloignés. Merci donc à Maximilian Attems, Jurgen Berges, Jorge Casalderrey-Solana, Kevin Dusling, Carsten Greiner, Guy Moore, Urko Reinosa, Carlos Salgado et Raju Venugopalan.

Je me permets de remercier tout spécialement (en plus de François, cela va toujours de soi) Jean-Paul Blaizot, Tuomas Lappi et Larry McLerran, pour leur soutien lors de mes candidatures pour un postdoctorat, que j'ai obtenu à l'université de McGill (je remercie d'ailleurs Guy Moore et les autres chercheurs de McGill de m'avoir recruté !) en partie grâce à eux.

La vie ne serait pas aussi agréable sans la présence de mes amis, qui ont autant dû supporter mon irascibilité des mauvais jours que mon engouement des bons (et le pire à endurer n'est pas forcément celui que l'on croit). Certains ont même poussé le vice jusqu'à m'écouter quand je parlais de physique ! Merci donc au témoin numéro 1, et à l'ami cher : Remy le philosophe (qui seul sait combien je lui dois) ; merci aux témoins de coeur : Antoine et sa bonhomie légendaire, Mathieu malgré son émotivité ; mais merci aussi à tous les autres amis ENSTA 2009 : Sandrine (et ses deux mains), Marie-Constance (et son fair-play), Sophie (et son nutella), Marie (quand bien même elle est nareuse), Romain C. (et son snowboard), Tal (que d'aucuns prétendent qu'il s'appellerait en vérité Nicolas ! ?), Anne (et sa discrétion), Jeremie (bonhomie bis), Alexis (et son riz aux pâtes), Florian (et son mauvais esprit), Remi (et son chat), Aude (et sa narcolepsie), Lucile (et sa soeur), Balthazar (et sa fangue qui peut parfois lourcher), Anne-Claire (et son régime alimentaire), Karine et Romain L. (malabars) Merci également aux amis de lycée : Thomas, Grégoire, Céline, Christophe, Laetitia, Sébastien et Cécile. Enfin, merci aux amis n'appartenant à aucune "tribu" mais que je n'apprécie pas moins : Jean-Phillipe ("Jean-Phillipe ! Jean-Phillipe !"), Olivier (c2-c4), Alina (spécialiste des solanacées chaleureuses à l'heure du départ), Sophie D. (et ses boucles d'oreilles), et François (et les cafards mutants).

Certains l'auront sans doute déjà deviné, mais je me permets tout de même de ne pas remercier le RER B (mention spéciale aux grèves préventives ou de solidarité), qui m'a conforté dans le fait que je préférais prendre le bus (quoique pour des raisons différentes de celles d'un chanteur français), aussi tôt soit-il...

Je m'excuse par avance de toute omission, uniquement due à la faiblesse de ma mémoire. Si quelqu'un estime qu'il a été lésé par ces remerciements, ces mots de réconfort et de gratitude sont pour lui/elle.

Il convient finalement de remercier ma famille, car si ma personnalité d'adulte est ce qu'elle est (pour le bonheur des un et le malheur de j'en suis sur la majorité des autres ; je peux donc lâchement partager la responsabilité), je le leur dois en grande partie. Merci donc à mon père, ma mère, mon frère (aha Claude, la similitude s'arrête là), Tonton (qui je pense a orienté mon choix vers la physique dès le plus jeune âge grâce à ces merveilleuses séances d'observation du ciel aux quatre coins de la France), Papi (que je te n'aime beaucoup), Mamoune et Mamie.

Je remercie Véronique d'être. Rien n'a été, ne peut être et ne sera plus beau et vital pour moi que cela.

Chapter 1

⚛ Introduction ⚛

Contents

1.1 Understanding the effectiveness of hydrodynamics in heavy ion collisions

n the past years, heavy ion collisions performed at the RHIC and the LHC have produced a huge amount of data, that theorists try to understand [1–11]. The matter produced in these collisions, called the Quark Gluon Plasma (QGP), is the first realization in a laboratory of a deconfined strongly interacting matter that existed briefly during the first instants after the Big-Bang. Understanding the QGP properties has been a very active topic in the past years.

All this theoretical work has led to a paradox. On the one hand, one of the most successful models to reproduce the RHIC and LHC data has proved to be relativistic viscous hydrodynamics, with a small value of the shear viscosity over entropy ratio [12–21]. This suggests that the QGP behaves as a nearly perfect fluid. In addition, hydrodynamical simulations require a very small starting time of the order of $0.1 - 1 \, fm/c$ in order to successfully fit the experimental data. The onset of the hydrodynamical behavior of the QGP therefore seems to be very fast. On the other hand, models based on QCD have shown that the QGP produced in a heavy ion collision is initially very far from thermal equilibrium – a state called the Glasma [22–24]. Since one of the prerequisites for hydrodynamics is that the system should be nearly thermal, it seems difficult to reconcile the out equilibrium nature of the Glasma with the early hydrodynamical behavior of the QGP.

This approach to thermal equilibrium has received a lot of attention [25–41] since the original bottom-up scenario [42], but a definitive answer has not yet been reached. One of the models used to study the transition from the Glasma to the thermalized QGP is the Color Glass Condensate (CGC) [43, 44]. This effective theory of the strong interaction takes into account gluon saturation [45, 46] and the non-linear effects that happens at high energies.

At Leading Order (LO), the CGC just amounts to solving the classical Yang-Mills equation with a classical initial condition [22, 47–50]. CGC at LO does not explain the early onset of the hydrodynamical behavior of the QGP since the anisotropy of the pressure tensor persists indefinitely [22–24]. This fact is easily understood: quantum corrections can qualitatively alter the picture due to plasma instabilities [51–54], that enhance small perturbations to the classical solution [55–57]. But taking into account these quantum corrections in a plain loop expansion leads to secular divergences. One way to cure this problem is a resummation [58] that collects

all leading unstable terms at each order of the perturbative expansion. This resummation can be implemented with the so-called classical statistical method (CSA) [59–65]. The CSA solves the classical equation of motion starting from a coherent state, that can be viewed as a Gaussian distribution of the initial classical field. The variance of this Gaussian is dictated by a one loop calculation. But this one-loop term had never been derived from first principles so far.

The objective of this thesis is therefore to apply the CSA to the CGC theory, in order to assess whether the QGP thermalizes. After having studied several simpler models in order to test this theoretical framework [66–69], we will derive the Next to Leading Order spectrum of fluctuations that enters into the initial condition of the CSA [70]. This allows us to perform the first realistic numerical simulation that goes beyond the LO CGC computations [71], and we will observe several hints for an early "hydrodynamization" of the Glasma.

1.2   How to read this thesis?

The manuscript is divided in three parts that are not independent. A chronological reading is therefore strongly advised. The first part I presents all the specific technical tools needed in order to describe at a microscopic level the collision of two heavy ions. In chapter 2, a non-technical presentation of heavy ion collision physics is done. The reader familiar with this material may skip this chapter and go directly to chapter 3, where the various tools to describe the Quark Gluon Plasma are presented, culminating with the introduction of the Color Glass Condensate. Chapters 4 cover specific technical points that allow one to go beyond the Leading Order perturbative calculation. This eventually leads to the introduction of the classical statistical approximation.

The second part II of the manuscript focuses on several scalar toy models. Studying these models, that are much simpler than QCD, is an interesting thing to do in a first time, since they can provide us a proof of concept that the framework that we have described in part I leads to the expected physical results. These scalar models will be considered in two situations: one where the volume is fixed and one where the system expands in one dimension. In the first two chapters of this part, both analytical and numerical aspects of the problem will be covered. The concluding chapter of part 2 will address some theoretical limitations of our framework.

Part III of the manuscript will finally address the main problem: the approach to equilibrium in heavy ion collisions, using the CGC model as well as numerical simulations based on the classical statistical approximation. Firstly, some key additional analytical tools are presented in the chapter 8. Secondly, the chapter 9 describes the first realistic numerical simulations performed in the CGC framework beyond Leading Order. A conclusion will end the manuscript, while more technical details are relegated in several appendices located at the end of the chapters they are referring to.

Part of this work has been published in:

- "Non-renormalizability of the classical statistical approximation" [69],
  T. *Epelbaum*, F. *Gelis*, B. *Wu*, 1402.0115 (2014).

- "Pressure isotropization in high energy heavy ion collisions" [71],
  T. *Epelbaum*, F. *Gelis*, Phys. Rev. Lett. **111**, 232301 (2013).

- "Fluctuations of the initial color fields in high energy heavy ion collisions" [70],
  T. *Epelbaum*, F. *Gelis*, Phys. Rev. **D 88**, 085015 (2013) .

- "Instability induced pressure isotropization in a longitudinally expanding system" [68],
  K. *Dusling*, T. *Epelbaum*, F. *Gelis*, R. *Venugopalan*, Phys. Rev. **D 86**, 085040 (2012).

- "Role of quantum fluctuations in a system with strong fields: spectral properties and thermalization" [67],
  T. *Epelbaum*, F. *Gelis*, Nucl. Phys. **A 872**, 210 (2011).

- "Role of quantum fluctuations in a system with strong fields: Onset of hydrodynamical flow" [66],
  K. *Dusling*, T. *Epelbaum*, F. *Gelis*, R. *Venugopalan*, Nucl. Phys. **A 850**, 69 (2010).

Part I

Theoretical background

Chapter 2

⚛ The problem of thermalization in heavy-ion collisions ⚛

Contents

2.1 The strong interaction

The aim of physics is twofold: description and prediction. One would like to be able to describe all the phenomena observed in nature, and given a certain context (launching a ball, looking at a nucleus...), being able to predict what will happen. To do so, physicists have been able to express all the interactions in nature in terms of forces. There are four forces in nature, recalled in figure 2.1.
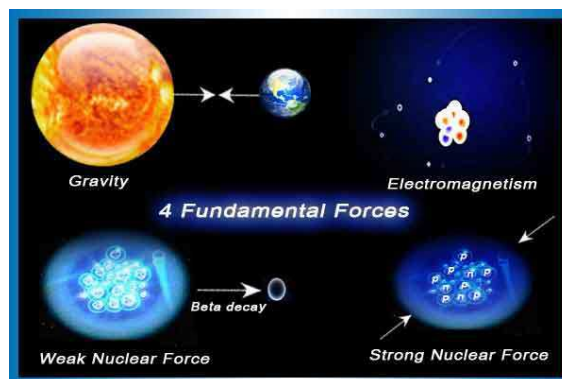

Figure 2.1: The four forces in nature.

The ones that we daily experience are gravity and electromagnetism. The ones we do not necessarily know about are the weak and the strong forces (also called the weak and strong interactions). Among its actions, the weak force is responsible for the radioactive decays.

The strong force is the one that binds the components of an atom nucleus together. Those components are the proton and the neutron, themselves formed by quarks, called valence quarks. There are six families of quarks in nature (sorted here from the lightest to the heaviest): the up quark u, the down quark d, the strange quark s, the charmed quark c, the bottom quark b and the top quark [1] t. This strong force is "strong" in the sense that it is able to counterbalance the electromagnetic repulsive force between the positive charges of the protons inside the nucleus. The strong force is the one that will keep us busy in all the following.

2.2   Looking inside a proton, first part

Our story begins with a close look of a proton at rest. This proton at rest is formed by three quarks (2 u and 1 d), as illustrated in figure 2.2.
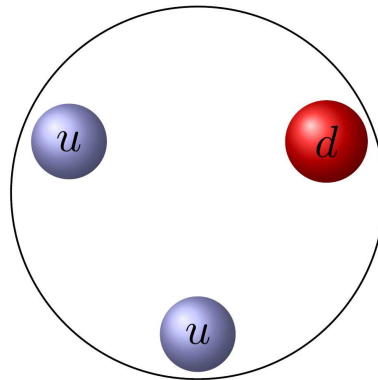
Figure 2.2: A proton at rest. It is formed by two up quarks u and one down quark d. The colors are here to differentiate the nature of the quarks, and have nothing to do with their actual color charges.

Those quarks are confined: they can't be observed traveling freely without their two fellows. This is a specificity of the strong interaction discovered by Wilson in 1974 [72] that is called the "quark confinement". This means that the attractive force between the quarks is indeed very strong at low energy. Physicists quantify this strength with a coupling constant - called α_S for the strong interaction, where the S stands for strong - which is an energy dependent quantity. Unfortunately, the theory that describes the strong force - called quantum chromodynamics, or QCD - is well understood only in its weak coupling sector, which means for α_S much smaller than 1. This allows to do a small coupling expansion of the theory and is the basis of pretty much all the perturbative techniques that are one of the main tools on the theoretical treatment of QCD. To compare it with experiment, one therefore has to make such experiments in the weak coupling sector of the strong interaction. Surprisingly, this sector is at very high energy. This could be counter intuitive: When one thinks about gravity, one expects that the further away two object are, the weaker the gravitational interaction is. The opposite happens for the strong force. A good analogy can be done with a string: when a string is pulled, it is subject to a restoring force that will tend to move closer the two endpoints of the string, and this force is stronger when the string is pulled more and more [2]. This property is called "asymptotic freedom": at infinite energy, the confinement property does not hold anymore and the quarks can indeed move freely. This surprising feature of the strong interaction was discovered in 1973-74 by Gross, Wilczek and Politzer [73–76], and is illustrated with recent experimental outputs in figure 2.3.

---

1. Predicted more than 40 years ago and discovered less than 15 years ago.
2. It is interesting to know that "string theory", a very active field in theoretical physics which consider all objects to be formed by infinitesimal strings, was first developed in order to describe QCD and more precisely this striking feature of the energy dependence of the strong force.
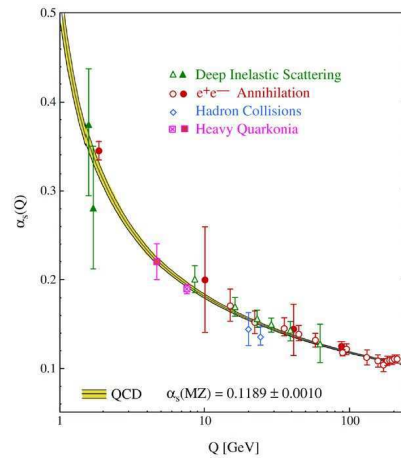
Figure 2.3: The value of the coupling constant α_S in function of the energy [77]. α_S seems to decrease as the energy increases.

2.3 Heavy Ion collisions

As we just discussed, theorists only know well the weak regime of the strong force. Since they still want to compare their predictions with experiments, people have built very large colliders (see figure 2.4 and 2.6), to reach an energy scale sufficiently high so that the strong interaction is probed in its weakly coupled sector (the typical energy scale being much greater than Λ_{QCD}, the QCD confinement scale)

Figure 2.4: The Large Hadron Collider (LHC) built between France and Switzerland.

In these colliders, proton and heavy ion beams are accelerated to reach almost the speed of light, in order to be subsequently collided.
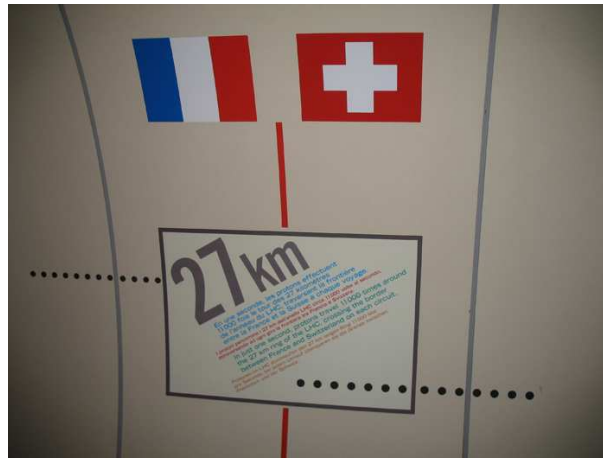
Figure 2.5: The protons and heavy ions inside the LHC are traveling at more than 99% of the speed of light, which means that they travel 11.000 times in one second the LHC ring of diameter 27km.

The experiments performed in those colliders serve two purposes. The first family of experiment was designed to search the Higgs boson, the only missing particle of the standard model. This search proved to be fruitful, as the Higgs boson was finally discovered in 2012 [78, 79] – more than forty years after its theoretical prediction [80, 81] – and led to a Nobel prize in 2013.

The second family of experiment currently performed at the RHIC [1–4] and the LHC [5–11] is looking at collisions between heavy ions, in order to understand better the QCD matter at weak coupling.
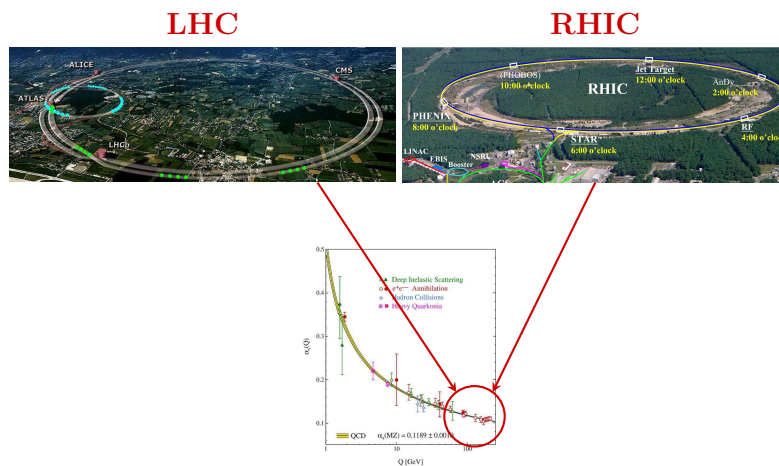
Figure 2.6:   The coupling scale (corresponding to very high energies) that the Relativistic Heavy Ion Collider (RHIC, American collider) and the LHC try to approach. So far the best that the LHC can do is to reach an energy such that α_S is of the order ~ 0.3.

This is the topic that interests us, and what will be the main subject of this thesis.

2.4   Looking at a proton, second part

We go back to our proton (the same is true for a heavy ion, but to keep things simple only protons are drawn so far) of figure 2.2, but now consider it highly accelerated, as it is truly in the RHIC and LHC rings. It turns out that in this case, the picture given in figure 2.2 is too

simplistic: it is in fact only valid when the proton is at rest. When the proton is moving at almost the speed of light, the picture is drastically changed. There are indeed other partons (a generic term regrouping the gluons and the quarks) that appear inside the proton. They are the sea quarks[3] and the gluons, which are the mediators of the strong interaction, as the photons are the mediators of the electromagnetic force. Why is it so? This is related to one of the most important principles in quantum theory called the Heisenberg uncertainty principle. What this principle essentially states is that it is not possible to know exactly at the same time the position and the speed of a particle, nor is it possible to know exactly its energy at a given time. This last uncertainty implies that on sufficiently small time scales - and in a heavy ion collisions, we are talking about a few times 10^{-24} seconds - the uncertainty on the energy triggers incredibly high fluctuations of its intensity at any point of space so that sometimes, the vacuum can acquire sufficiently high energy so that a pair of particles is created. This is called vacuum fluctuations, and is one of the explanation for such a rich content of a proton at high energy. Figure 2.7 illustrates the part of momentum which is carried by the different constituents of the protons in function of the momentum scale.
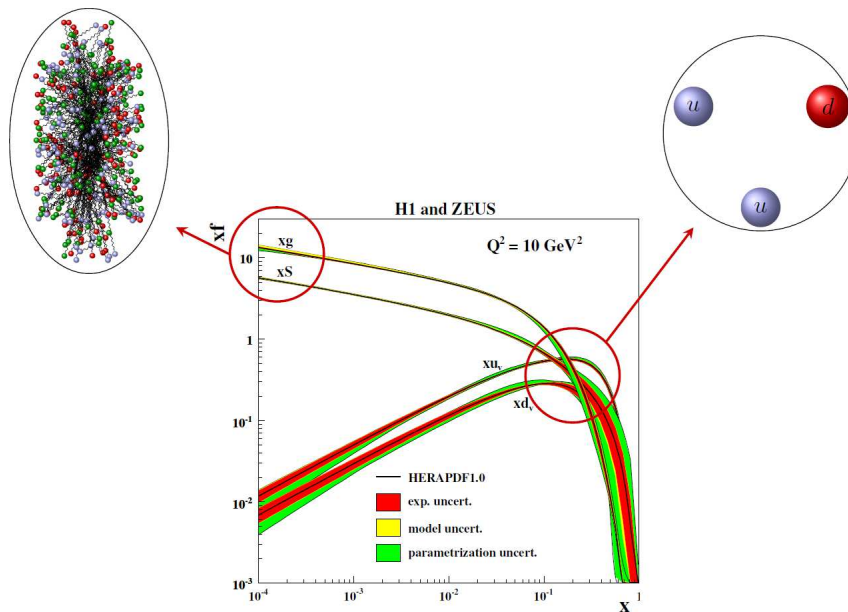
Figure 2.7: Fraction of the total momentum of the proton carried by the gluons xg, the sea quarks xS, the valence quarks u xu_v and v xd_v (adapted from HERA data [82]).

Physicists quantify the momentum of a parton with a quantity called[4] x and which is inversely proportional to E. At very high energy, we therefore speak about small x physics. At low energy (large x), one expects that only the valence quarks carry the proton momentum if we are to trust what we saw in figure 2.2. This is what is indeed observed: one can read on figure 2.7 that at large x, approximately 2/3 of the momentum of the proton is carried by u quarks and 1/3 for the d quark[5]. At very high energy, most of the momentum is carried by the gluons and gluon dynamics is therefore (mostly) the one of interest at very small x. This is the physics that we will want to describe in the present manuscript, and we will come back in more technical details on figure 2.7 later on. Let us end this part by showing in figure 2.8 what a highly energetic proton may look like.

---

3. in opposition to the valence quarks, the sea quarks are quarks that are not the fundamental constituent of the proton and only appear at high energy.

4. The use of this variable x was introduced in Deep Inelastic Scattering studies (see [83–86]).

5. Obviously because they are twice as many u quarks as d quarks inside the proton.
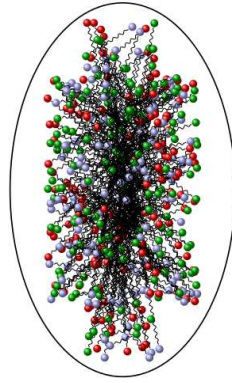
Figure 2.8: A proton at high energy. The balls are representing quarks and the lines gluons.

2.5   The quark-gluon-plasma: experimental evidences

When two heavy ions that look at figure 2.8 collide at very high energy, one can anticipate that the matter produced out of their collision is extremely complicated to describe. Indeed, gluons from one nucleus can interact with those from the other. The matter formed by this collision is called the Quark-Gluon-Plasma (QGP).
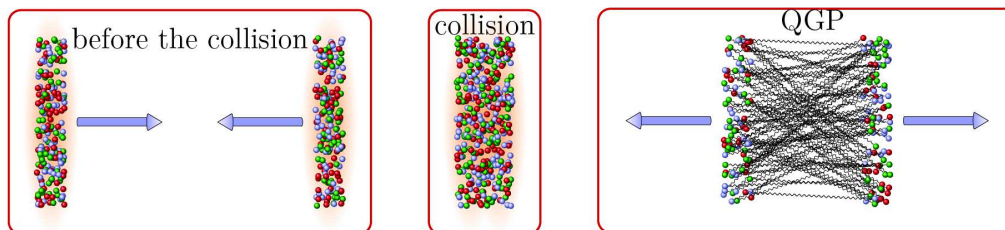
Figure 2.9: The formation of the quark-gluon-plasma (or QGP) in a heavy ion collision.

What are the evidences for this new form of matter? The best one is the observation in the experimental detectors of very energetic fluxes, corresponding to very located in space particles. The latter are called "jets". The reasoning is the following: let's assume for the time being that the QGP exists. In a heavy ion collision, as already mentioned, products are observed in the detectors of the RHIC and the LHC. But out of these products, some of them are much more energetic than others. Those are the result of the collisions of the most energetic objects in the nuclei – the collisions that imply the valence quarks for instance. When such collisions happen in the center of the QGP, one will usually observe two "back-to-back" jets, which means two very energetic beams of produced particles that cross both half of the QGP and then go hit the detector in opposite directions. Because those jets travel in opposite direction, they are correlated: the probability of finding the second jet at 180 degrees of the first one is very high. Now, consider again a very energetic collision, but happening this time at the edge of the QGP. In this situation one of the jet will only have to cross a tiny region of the QGP before escaping and hitting the detector, while the other has to cross most of the QGP. During this crossing, the jet will interact with the QGP and loose most of its energy [6]. So if the QGP exists, one should sometimes observe in heavy ion collisions two correlated back-to-back jets, but with one being much more energetic than the other. Our expectation is illustrated in figure 2.10.

---

6. By successive gluon emission. Studying this energy loss (also called jet quenching [87]) is a lively field in particle physics [88–96].
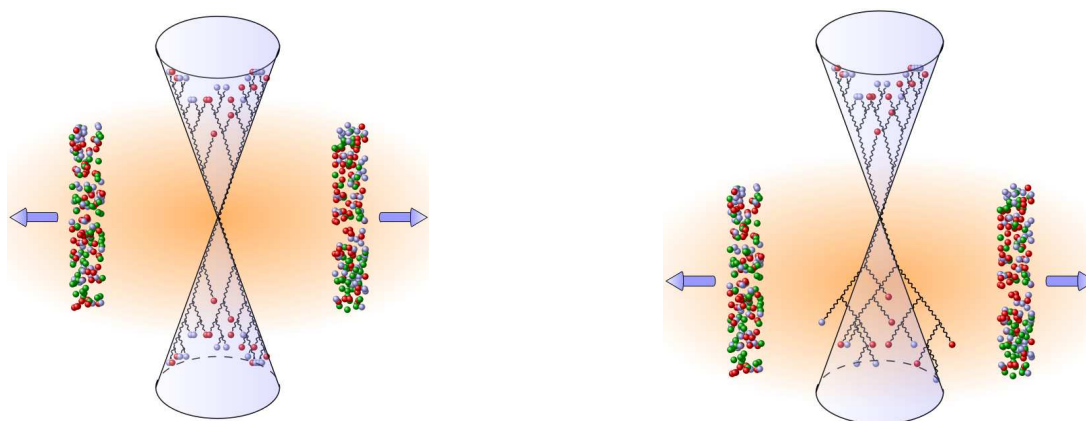
Figure 2.10: Evidence for the existence of the QGP. On the left, a central energetic collision that produces two back-to-back jets that will hit the detector with almost the same energy. On the right, a non-central collision that will produce two back-to-back jets, one (on top) being much more energetic and collimated than the other (on bottom).

These tests have been performed and what has been obtained by the CMS group (one of the experimental team working at the LHC) is shown in figure 2.11. This neat confirmation of a theoretical prediction is a strong argument in favor of the existence of the QGP.
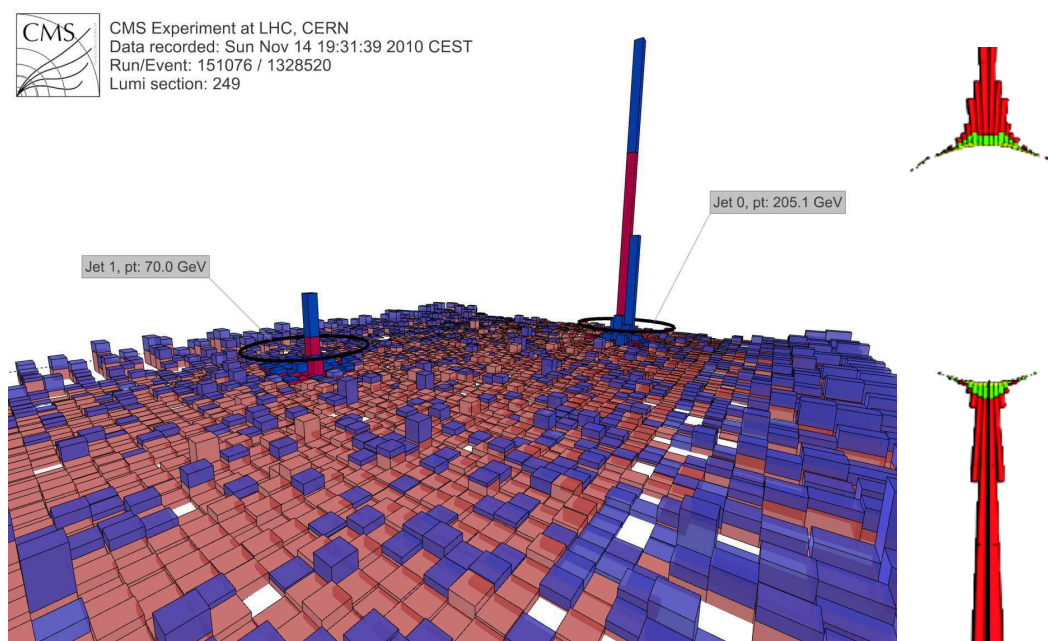
Figure 2.11: Evidence for the existence of the QGP. Left part: two back-to-back jets with very asymmetric energies hit the CMS detector (the two peaks). The most energetic jet has more than twice the energy of the other. Right part: The subleading jet (on top) is less collimated.

2.6 Has the QGP ever existed in the history of the universe?

Since the heavy ion collisions are so energetic, they are sometimes referred to as the "little-bangs". The different phases of the little-bang are illustrated in figure 2.12.
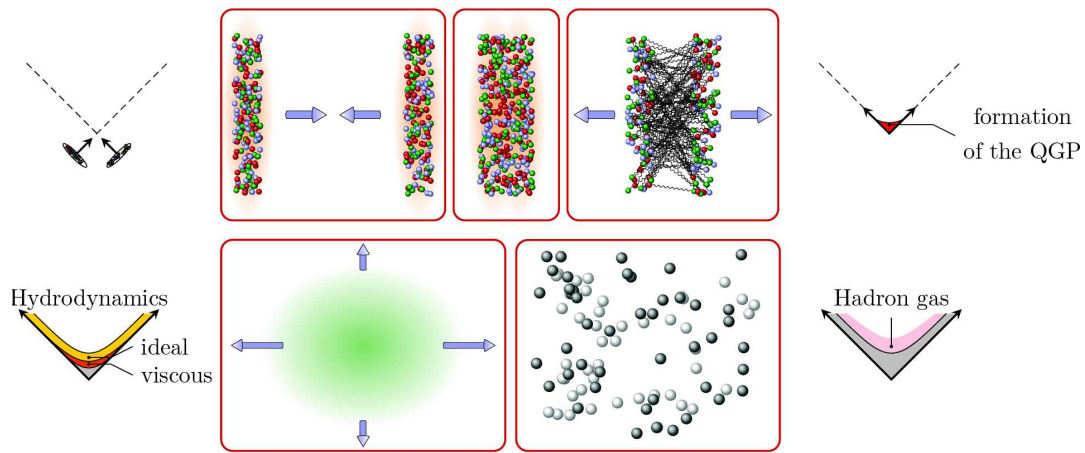
Figure 2.12: The little bang. phase 1 to 5 (from left to right, top to bottom): two very energetic heavy ion approach each other at almost the speed of light. They collide and form a new state of matter called QGP. As we will see later on, this QGP is out of equilibrium (and is in this case sometimes referred to as the glasma) at the initial time after the collision. Nevertheless, this glasma is assumed to equilibrate very fast, and the products of the collision can be described as an ideal or viscous fluid (as we will see later on, this puts some strong constraints on the system: the latter should not be too far from equilibrium). This fluid then form particles (a process named "hadronization") that reach the detectors.

This analogy in name between the little-bang and its older (and bigger) brother the big-bang is due to the fact that the early stages of a heavy ion collisions can probe the first instants of the life of our own universe. This is why some theoretical physicists study the little-bangs in order to learn more about the big-bang, from which a cartoon picture is given in figure 2.13.
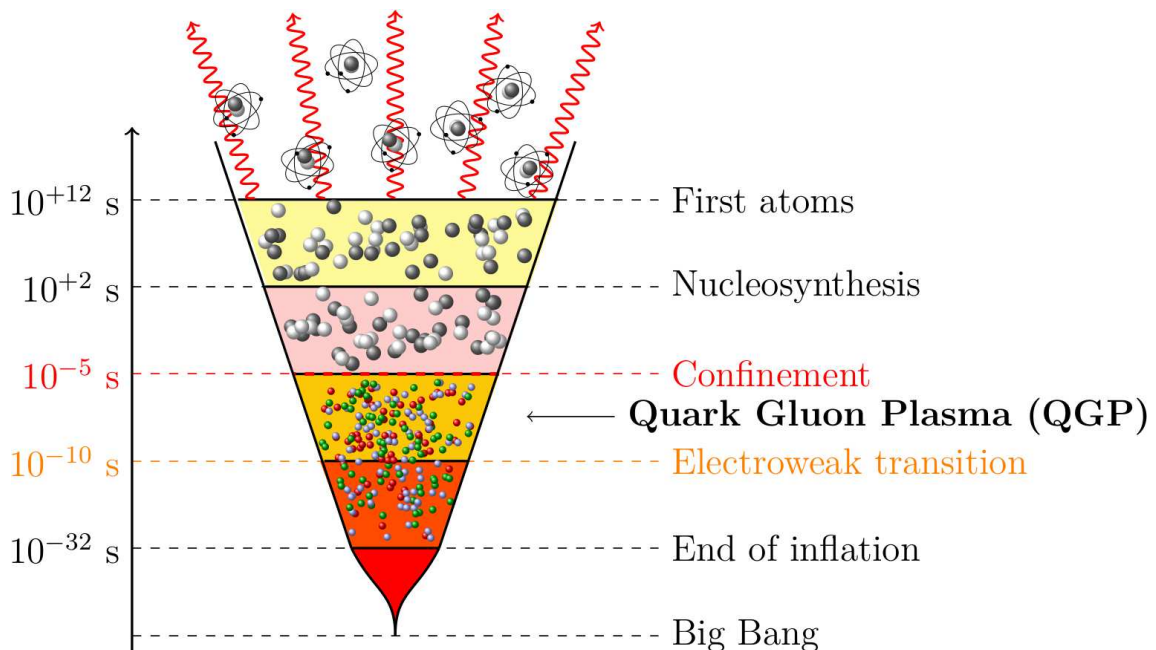
Figure 2.13: Schematic view of the big-bang.

In particular, an hypothetic phase during the creation of the universe called the inflation has attracted a lot of attention recently. Inflation is an expansion of the structure of the universe itself at a speed way faster that the speed of light during a very short time. The inflation

scenario has been introduced in the 80's [97], when people discovered a relic of the formation of the universe called the Cosmic Microwave Background (or CMB). This radiation has the specificity to have a black body temperature of 2.8 Kelvin (with only 10^{-5} variations) every-where in the universe [7], even in regions that are not causally related today [8]. The inflation, and especially the thermalization that occurred at the end of it, is able to explain this paradox. This thermalization shares a lot with the one that happens in the little-bangs.

2.7 Quark-gluon-plasma: the puzzle

Theoretical models trying to describe this quark-gluon-plasma have been intensively de-veloped in the past twenty years. The conclusion of all these models is that the QGP should experienced an initial phase where it is very far from being at thermal equilibrium. If such an equilibrium was reached, it would imply some strong constraints for the QGP at both the macroscopic and microscopic level. At the macroscopic level, there should be a one to one relation between the energy density and the pressure of the system: a relation called equation of state (EOS). At the microscopic level, the distribution of the particle given their energy should be dictated by a specific function. This specific function, called the occupation num-ber (or distribution function) should follow a Bose-Einstein statistics for bosonic particles like gluons [9].

Meanwhile, other less fundamental theories such as macroscopic models have been used in order to try to reproduce the outcome of the collisions. The one that is best able to do so is relativistic hydrodynamics. This theory relies on the Navier-Stokes equations, that describe the motion of a relativistic fluid. It can be either ideal or viscous. It is a macroscopic theory as it describes the system with a very limited amount of parameters: the energy density of the fluid, its pressure and velocity. It turns out that relativistic hydrodynamics has been so successful in describing the outcome of the experiments that this is a puzzle for the heavy-ion community.

The issue is the following: in order for relativistic hydrodynamics to work, it requires some postulates, and one of the most important is a very rapid thermal equilibration [10] of the QGP. But as already mentioned, more fundamental theoretical models that adopt a microscopic description of the QGP fail to predict such a short thermalization time.

A lot of work has been done in order to try to understand why a short transition from an out-of-thermal equilibrium QGP (also called Glasma) to a thermalized QGP is possible. The holy grail of the field is therefore the understanding of the assumed to be fast transition illustrated in figure 2.14.

---

7. This temperature is time dependent: it was much warmer when the CMB was effectively produced when the universe was about 300.000 years old. But its striking feature is that it is not space dependent.
8. Nothing –nor forces neither information – could have traveled from one region to another because their mutual distance is bigger that the lifetime of the universe multiplied by the speed of light. And one of the postulates of special relativity is that nothing can travel faster than the speed of light.
9. For quarks, it would be the Fermi-Dirac statistics.
10. As we will discuss at length in the subsequent part of this manuscript, full thermalization (EOS, Bose-Einstein distribution) is not really required in order for hydrodynamics to work.
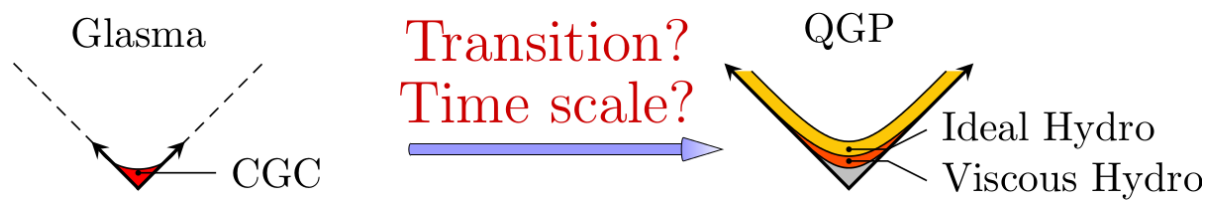
Figure 2.14: One of the current puzzles on the theoretical side of heavy ion collisions. The acronym CGC, standing for "Color Glass Condensate" indicates that the latter is one of the promising theoretical models that could describe the transition. This is the one that we will be using in this manuscript. The CGC will be introduced in the section 3.6.

One of the best models to study the microscopic properties of the pre-QGP state is called the Color Glass Condensate. It is a QCD effective theory: it deals with the usual tools of QCD but do some approximations that can be performed because of the specific kinematics of a heavy ion collision. The description of this model will be done in the next chapter.

Chapter 3

⚛ Theoretical tools to deal with the Quark-Gluon-Plasma ⚛

Contents

his chapter aims at introducing the main theoretical tools that can describe the Quark-Gluon-Plasma, and explain why we will be using the Color Glass Condensate theory throughout this thesis. It will be complemented by the more technical considerations in the chapter 4.

3.1 Kinetic Theory

One of the tools to study the Quark-Gluon-Plasma is kinetic theory. Kinetic theory assumes that the QGP is formed by particles and it describes how these particles interact with each other. Different kind of interactions – elastic, inelastic – could be involved. They are all described by a collision term. The collision term forms the right hand side of the Boltzmann equation, that aims at computing the time dependence of the occupation number in an out of equilibrium system (as the QGP is, see section 3.8). The Boltzmann equation takes the form

$$\frac{\partial f}{\partial t} = C[f] \, , \tag{3.1}$$

where f is the occupation number of the QGP constituents (as we will see in section 3.5.1, these are mostly gluons) and $C[f]$ the collision term. Kinetic theory has been very successful in studying the late time behaviour of the QGP, and numerous works have been performed in that direction [33, 41, 98].

But the key problem in using the kinetic theory in order to describe the QGP time evolution lies in its very first postulate. Indeed, as we will see in section 3.5.1, the QGP is the siege of very large fields after the collision, rendering in principle impossible a particle picture of the QGP at these instants. We will therefore not consider kinetic theory in the present manuscript[1].

3.2   Hydrodynamics

As it name suggests, hydrodynamics is the theory that governs the motion of a fluid. This theory is macroscopic: it does not seek to describe fully a system at the microscopic level (like QCD would), but rather study a few macroscopic quantities: the energy density ϵ, the pressure p, and the velocity of the fluid u^μ, where from now on Greek letters stand for Lorentz indices that go from 0 (time dimension) to 3 (1, 2 and 3 being the spatial indices). This means 5 independent variables, since $u_\mu u^\mu = 1$. In order to determine these unknown quantities, one therefore needs five equations. If the fluid is ideal (meaning that it is not viscous), the laws that govern the fluid movements have been derived more than 250 years ago (in 1755 to be precise) by Leonhard Euler. There are the Euler equations. We will not repeat them here as we are more interested in the non-ideal case. Indeed, as we will see, the QGP is viscous[2].

3.2.1   Relativistic viscous hydrodynamics

If the fluid if viscous[3], then the equations that govern the fluid motion are the Navier-Stokes equations. They are a consequence of Energy momentum conservation $\partial_\mu T^{\mu\nu}$. The first one reads

$$(\epsilon + p)Du^\alpha - \nabla^\alpha p + \Delta^\alpha{}_\nu \partial_\mu \Pi^{\mu\nu} = 0 \,, \tag{3.2}$$

where the different operators that appear in (3.2) are defined by

$$D = u_\mu \partial^\mu \,, \qquad \nabla^\alpha = \Delta^{\mu\alpha}\partial_\mu = \Delta^\alpha{}_\mu \partial^\mu \,, \qquad \Delta^{\mu\nu} = g^{\mu\nu} - u^\mu u^\nu \,. \tag{3.3}$$

$\Pi^{\mu\nu}$ is the viscous tensor

$$\Pi^{\mu\nu} = \underbrace{\eta \nabla^{<\mu}u^{\nu>}}_{\pi^{\mu\nu}} + \Delta^{\mu\nu} \underbrace{\zeta \nabla_\alpha u^\alpha}_{\Pi} \,, \tag{3.4}$$

where η is the shear viscosity of the fluid and ζ the bulk one. We denote

$$\nabla^{<\mu}u^{\nu>} = 2\nabla^{(\mu}u^{\nu)} - \frac{2}{3}\Delta^{\mu\nu}\nabla_\alpha u^\alpha \,, \qquad \nabla^{(\mu}u^{\nu)} = \frac{1}{2}(\nabla^\mu u^\nu + \nabla^\nu u^\mu) \,. \tag{3.5}$$

$\Pi^{\mu\nu}$ characterizes the deviation of the fluid from an ideal one. For the energy-momentum tensor of the theory it means that

$$T^{\mu\nu}_{\text{visc}} = T^{\mu\nu}_{\text{ideal}} + \Pi^{\mu\nu} \,, \tag{3.6}$$

---

1. Here it is worth mentioning that the hard momentum sector of the QGP could in principle be described by particles, as we will argue in section 3.5.1 that the fields are only large in magnitude up to a momentum scale called the saturation scale Q_S. Some recent studies [25, 32, 99, 100] have therefore coupled the Yang-Mill equations to describe the soft sector of the QGP with a Vlasov equation (Boltzmann equation with vanishing collision term) to treat the hard sector [101] and got promising results. A lot remains to be done in this direction, since very drastic assumptions were performed on both side until so far (Vlasov instead of Boltzmann equation, unrealistic initial condition for the soft sector...).

2. To be more precise the shear viscosity η is very large for the QGP [102–105], but the dimensionless shear viscosity over entropy ratio $\frac{\eta}{s}$ is very small [106].

3. Reviews on viscous hydrodynamics can be found in [107–109].

where

$$T^{\mu\nu}_{\text{ideal}} = (\epsilon + p)u^\mu u^\nu - pg^{\mu\nu} = \begin{pmatrix} \epsilon & 0 & 0 & 0 \\ 0 & p & 0 & 0 \\ 0 & 0 & p & 0 \\ 0 & 0 & 0 & p \end{pmatrix}, \tag{3.7}$$

is the energy-momentum tensor of an ideal fluid at rest in the comoving frame ($u^\mu = (1,0,0,0)$): diagonal and traceless (i.e. $p = \frac{\epsilon}{3}$. This will be used in the chapters 6 and 9). (3.2) only stands for 3 equations, as it gives 0 when contracted with u_α. From the energy momentum conservation one can also deduce the conservation law [4]

$$D\epsilon + (\epsilon + p)\partial_\mu u^\mu - \Pi^{\mu\nu}\nabla_{(\mu}u_{\nu)} = 0, \tag{3.8}$$

To close the system, we need one additional equation, as (3.2-3.8) stand for 4 equations while we have five unknowns. This last equation is the so-called equation of state [5], that relates the energy and the pressure of the system

$$\epsilon = f(p). \tag{3.9}$$

This equation cannot be derived inside hydrodynamics: it is a postulate. In addition, both (3.4) and (3.8) have been derived by doing a gradient expansion, and it turns out that this expansion is not valid if the system is too anisotropic. If the pressures in the various spatial directions are not equal, they should not be too different [6]. Finally, to perform a hydrodynamical simulation, i.e. to solve numerically [7] the Navier-Stokes equations, one needs an initial condition. This means knowing at an initial time the energy density, as well as the pressures and the fluid four-velocity. One also needs to know the values of the viscous tensor parameters [8]: the shear viscosity η and the bulk viscosity ζ that appear in the viscous tensor 3.4. The latter is often taken equal to 0, as it is not present in conformally invariant systems, which the QGP is often assumed to be. With all this in mind, let us shortly illustrate one of the hydrodynamics greatest success: the reproduction of the large elliptic flow observed in heavy-ion collisions.

3.2.2   Hydrodynamical simulations can reproduce the RHIC and LHC data

Since the start of RHIC, hydrodynamical simulations have managed to reproduce very successfully the outcome of heavy-ion collisions. Many works have been performed in this framework (see for instance [12, 14–21]), and we will only discuss here one of these studies [13], that will serve our purpose later on: the large elliptic flow observed in heavy-ion collisions. The measurement of the elliptic flow v_2 is explained in [112] [9], and one can also understand there why the measured v_2 is larger than one may naively expect. The numerical results obtained by Luzum and Romatschke in [13] are reproduced in the figure 3.1

---

4. That will prove useful to derive Bjorken's law in the appendix 3.A.

5. Note that this equation is satisfied by construction for an ideal fluid at rest in the comoving frame.

6. As we will see later on in section 3.8, this is the case in the Color Glass Condensate Effective Theory at its Leading Order.

7. Actually, the equations that are solved numerically are not exactly the Navier-Stokes equations (3.4) and (3.8) presented here,because they violate causality. To restore causality in the Navier-Stokes equations, one has to include new terms. This is the essence of the Israel-Stewart theory [110], the framework in which the equations that are truly solved numerically can be derived. For a good reference on this see [108]. Latest improvements of this framework can be found in [111].

8. In Israel-Stewart theory there are additional parameters.

9. The main idea is to measure correlations between particles in the final state. More on the elliptic flow can be found in [112–114].
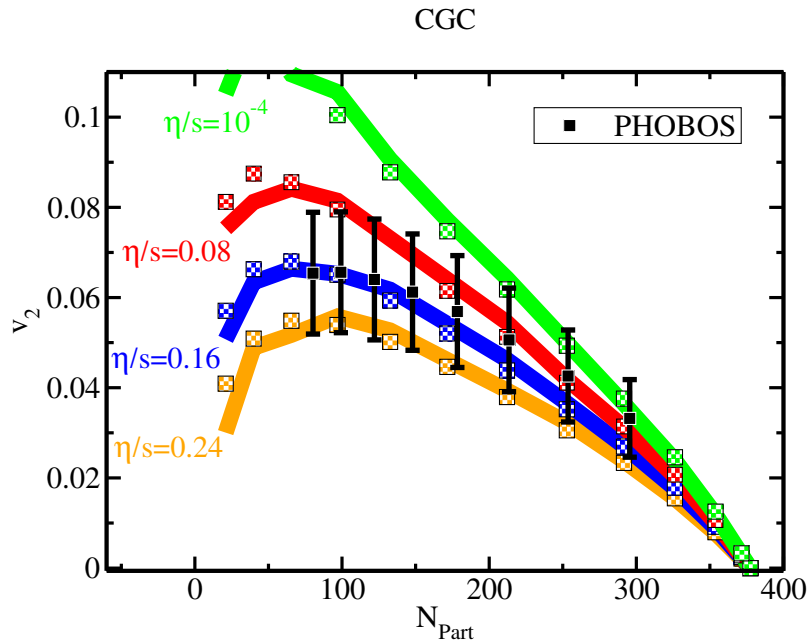
Figure 3.1: The elliptic flow obtained by viscous hydrodynamical simulations, using CGC-like initial conditions (to be defined in the section 3.8), represented here as a function of the number of participants in the collision.

Several important conclusions can be drawn from this figure. The first one is that relativistic viscous hydrodynamics simulations (color lines, corresponding to different values of the shear viscosity over entropy ratio $\frac{\eta}{s}$) can successfully reproduce the experimental data (black points). In addition, they work for a very small value of $\frac{\eta}{s}$, very close to its conjectured lower bound $\frac{1}{4\pi} \sim 0.08$ computed using AdS/CFT techniques (see [115]). The second important fact for the simulations to reproduce the experimental data is that the hydrodynamical simulations must be started very early after the collision. If we call the time at which hydrodynamical simulations are initialized τ_0, we therefore need $Q_s \tau_0 \lesssim 5 - 10$ (here Q_s is the saturation momentum that will be defined later). The system must therefore hydrodynamize very fast, while it does not behave at all like hydrodynamics just after the collision, as we will argue in the section 3.8. The success of the work shown in the figure 3.1, among with numerous other achievements of viscous hydrodynamics therefore suggests that the conditions on $\frac{\eta}{s}$ and τ_0 that we have just presented are fulfilled. But can this be justified from first principles?

3.2.3   Are hydrodynamics postulates satisfied in the QGP?

To summarize, in order for hydrodynamics to work, several assumptions must be satisfied

Hydrodynamics Prerequisites (1)

0) The pressure and the energy are related by an equation of state (EOS).
I) At the initialization time τ_0, we should know the macroscopic variables: ϵ, p, u^μ.
II) At all times, we should know the viscosity parameters η and ζ (if the latter is not taken to be 0). $\frac{\eta}{s}$ should be small, very close to its conjectured lower bound $\frac{1}{4\pi}$.
III) The initialization time should be small. In realistic simulations reproducing the LHC data, $\tau_0 \lesssim 0.5 - 1 fm/c$.
IV) At the initialization time τ_0 (and during the whole evolution of the system), the anisotropy of the pressure tensor should be small.

As we will see in the section 3.8, postulate 0 is satisfied by construction in gauge theories. It is nevertheless not fulfilled at all times in scalar theories, and we will need to prove it

there. This will be one of the goals of the chapters 5 and 6. Postulates $I - IV$ should be derived from a more fundamental microscopic theory: QCD in the high energy limit (that is reached at the RHIC and the LHC). To be more precise, we will see in the section 3.8 that the pressure tensor is very anisotropic just after the collision. IV could therefore be rephrased as: "Between the collision and the initialization time τ_0, the pressure tensor should have become nearly isotropic". In addition, during the whole evolution of the system the anisotropy in the pressure tensor should remain small.

Hydrodynamics Prerequisites (2)

> IV') The pressure tensor should isotropize very fast after the collision .

As we saw in the section 3.2.2, hydrodynamics has been very successful in reproducing the RHIC and LHC data. Therefore the fact that its postulates are satisfied very shortly after the collision seems natural. But as we will see in the next sections, none of those prerequisites are easy to derive from a QCD point of view. The aim of this thesis is to address this central yet unanswered question.

Are the postulates of hydrodynamics I)-IV') satisfied during the early stages of a heavy-ion collision?

It turns out that this is a very difficult question to answer. Using weakly-coupled QCD techniques at Leading Order, one would be tempted to conclude that those postulate are not fulfilled at all. In this microscopic theory, the pressure anisotropy remains huge during several fm/c, voiding the validity of IV' [22–24]. In addition, $\frac{\eta}{s}$ is predicted to be much larger than $\frac{1}{4\pi}$ in this framework [103], which invalidates the postulate II. Does this mean that weakly coupled techniques cannot describe the QGP? This is the point of view adopted by several works using AdS/CFT techniques (see [116]), that assume that the QGP is in fact strongly coupled. We will present their findings in the next section. Another possibility could be that hydrodynamics postulates are indeed not fulfilled? Could other theories, relaxing some of the postulates $I - IV'$, still be able to reproduce successfully heavy-ion data? This is the starting point of anisotropic hydrodynamics, which has been recently developed [117–119] and that shows promising results. Finally, it might also be that Leading Order perturbation theory does not give the correct qualitative results, and that the Next to Leading Order corrections bring new physical effects on the system, that have qualitative consequences on isotropization and the value of $\frac{\eta}{s}$? This is the point of view that we will adopt in this thesis, for reasons that will be explained throughout this manuscript.

3.3 Strongly coupled techniques: fast "hydrodynamisation"
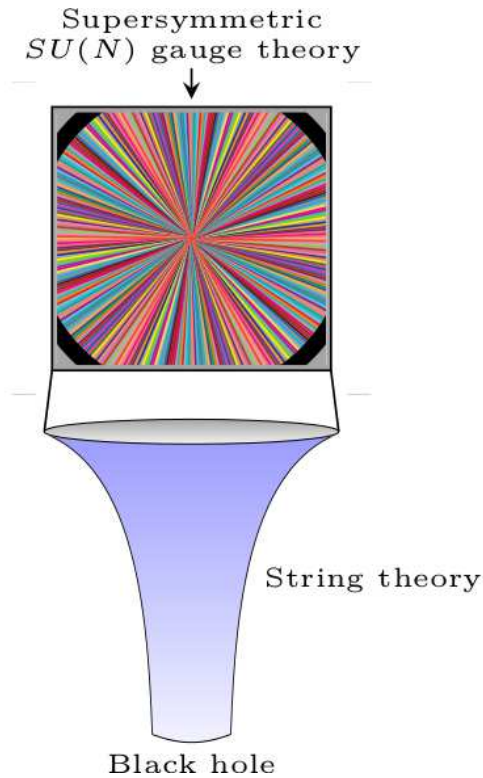
Figure 3.2: A schematic view of the AdS/CFT setup.

The strongly coupled techniques that are used in order to describe the early life of the out of equilibrium QGP rely on the AdS/CFT conjecture [116], illustrated in figure 3.2. This conjecture establishes a link between supersymmetric gauge theories (which QCD is not) and string theories in a five dimensional Anti de-Sitter curved space time. In the limit where the gauge coupling becomes infinite, the string theory reduces to general relativity, and one therefore just needs to solve Einstein's equations to calculate the quantities of interest in the theory. This is what has been done in [29], where Einstein's equations have been solved for various initial conditions. The results are reproduced in the figure 3.3
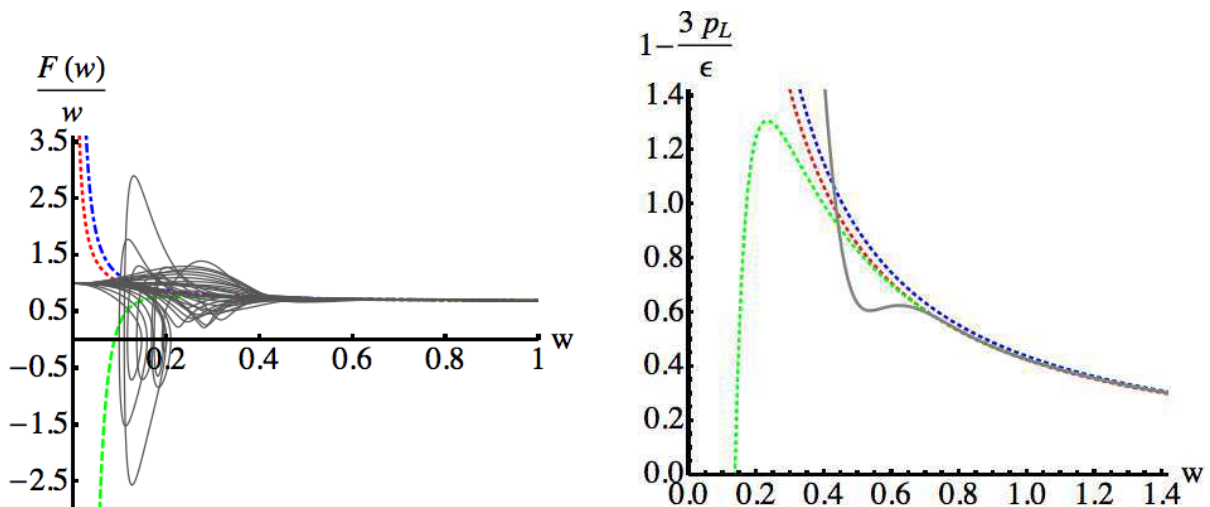
Figure 3.3: Left: comparison between first order (green), second order (blue) and third order (red) hydrodynamical simulations with the resolution of Einstein's equation with various initial conditions (gray). Right: momentum anisotropy.

We see that the out-of-equilibrium AdS/CFT calculations very rapidly coincide with the viscous hydrodynamical simulations. This is illustrated in the left plot (where w plays the role of the time τ), where the agreement between the two theories is compatible with the $\tau_0 \sim 1 fm/c$ mentioned in the previous sections. The surprise comes from the right plot, where we see that this agreement already happens when the system is rather far from being isotropic. Does this means that the range of applicability of hydrodynamics is broader than we may expect given the postulates $I - IV'$? More realistic initial conditions (colliding shock waves in the AdS space in order to mimic the heavy-ions) are currently investigated in order to answer in a more definitive way this question at strong coupling [34].

Another important result found within the AdS/CFT framework is the fact that hydrody-namics – as perturbation theories – is based on an asymptotic expansion [120]. The radius of convergence of the gradient expansion is in fact 0. This comparison between hydrodynamics and AdS/CFT techniques has been very fruitful. The AdS/CFT framework is an interesting playground to understand what is happening in heavy-ion collisions, but should not be con-sidered as more than a toy model. Indeed, the assumption that the QGP is infinitely strongly coupled seems extreme, as one can see on figure 2.3. At the scale $Q_s \approx 1 - 2 GeV$, the strong coupling constant α_s is of the order of 0.3. In addition, QCD is pretty different from a super-symmetric gauge theory. This is what motivates our choice to stay within a weakly coupled description of the QGP in the remaining parts of this manuscript.

3.4 Quantum Chromodynamics

Quantum Chromodynamics is the theory that governs the strong interaction. It shares many similarities with quantum electrodynamics (QED) and even more with the electroweak interaction (EW). But unlike QED, it is a non-abelian interaction: its symmetry group is $SU(3)$ [10]. Unlike electroweak theory, its boson mediator – the gluon – is massless [11]. The QCD Lagrangean reads

$$\mathcal{L} = -\frac{1}{4} F^a_{\mu\nu} F^{\mu\nu a} + \sum_f \psi^a_f (i\slashed{D} - m_f) \bar{\psi}^a_f \ . \tag{3.10}$$

Here the latin letters a, b stand for the color indices [12], while f denotes the quark flavor. For reasons that will be explained in the section 3.5.1, we will only consider the gluonic sector of QCD in the remaining parts of this manuscript. As it is well known, the gauge symmetry prevents one to directly derive the propagator without first fixing a gauge. We will use the axial gauge throughout this thesis, which involves the addition of the following term to the Lagrangean

$$\Delta\mathcal{L} = \frac{1}{2\xi} (n^\mu A^a_\mu)^2 \ ; \tag{3.11}$$

where one sets $\xi = 0$ at the end. Among its advantages, this gauge choice prevents the appearance of the unphysical ghost particles. The calculations of chapter 8 will also be sim-plified thanks to this gauge choice. To summarize, the QCD Lagrangean that we consider is

---

10. While for QED it is the abelian group $U(1)$ and for the EW interaction it is $SU(2)$. To reduce the computation time, the numerical simulations performed in chapter 9 are done using $SU(2)$ and not $SU(3)$ gauge group. This is not a drastic approximation, as it has been shown previously that this does not affect too much the numerical results [121].

11. The $W^\pm$ and the Z are massive because of the spontaneous EW symmetry breaking.

12. That plays the same role as the electrical charge in QED, and is called the color charge.

the following one

$$\mathcal{L} = \underbrace{-\frac{1}{4}(\partial_\mu A_\nu^a - \partial_\nu A_\mu^a)^2 + \frac{1}{2\xi}(n^\mu A_\mu^a)(n^\nu A_\nu^a)}_{\text{free Yang-Mills theory}}$$

$$\underbrace{- g f^{abc}(\partial_\mu A_\nu^a) A^{\mu b} A^{\nu c}}_{\text{3-vertex}} + \underbrace{\frac{g^2}{4} f^{eab} f^{ecd} A_\mu^a A_\nu^b A^{\mu c} A^{\nu d}}_{\text{4-vertex}} . \tag{3.12}$$

The FEYNMAN rules associated with this Lagrangean are

- the gluon propagator :

$$\begin{aligned}
\overset{a}{\underset{\mu}{\mathrm{\sim\!\!\sim\!\!\sim\!\!\sim}}}\ \overset{b}{\underset{\nu}{}} \ =\ & -i\delta^{ab} \left(\frac{g^{\mu\nu}}{k^2 + ik^0\epsilon} - \frac{k^\mu k^\nu}{(n.k + i\epsilon)^2} \left(\xi - \frac{n^2}{k^2 + ik^0\epsilon} \right) \right. \\
& \left. - \frac{k^\mu n^\nu + k^\nu n^\mu}{(k^2 + ik^0\epsilon)(n.k + i\epsilon)} \right) . \tag{3.13}
\end{aligned}$$

- the 3 gluon vertex :

$$= g f^{abc} \left[g^{\alpha\beta}(k_1 - k_2)^\gamma + g^{\beta\gamma}(k_2 - k_3)^\alpha + g^{\gamma\alpha}(k_3 - k_1)^\beta \right] . \tag{3.14}$$

- the 4 gluon vertex :

$$= -ig^2 \begin{bmatrix} f^{abe} f^{cde} \left(g^{\alpha\gamma} g^{\beta\delta} - g^{\alpha\delta} g^{\beta\gamma} \right) \\ + f^{ace} f^{bde} \left(g^{\alpha\beta} g^{\gamma\delta} - g^{\alpha\delta} g^{\gamma\beta} \right) \\ + f^{ade} f^{bce} \left(g^{\alpha\beta} g^{\delta\gamma} - g^{\alpha\gamma} g^{\beta\delta} \right) \end{bmatrix} . \tag{3.15}$$

This gives a perturbative framework where analytical calculations can be performed. Unfortunately, usual Feynman diagrammatic techniques will prove impractical in the context of heavy ion collisions. Why is it so is related to the saturation phenomenon.

3.5 Specificities of heavy-ion collisions

3.5.1 Gluon saturation

Consider a proton at rest. It is only made of its three valence quarks, as illustrated in the figure (3.4)
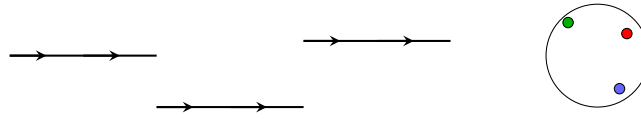
Figure 3.4: A proton at rest.

Now, increase the energy of this proton. The quarks emit gluons by bremsstrahlung. At higher energies, more and more gluons (that could later decay into sea quarks) can be emitted, as can be seen in the figure (3.5)
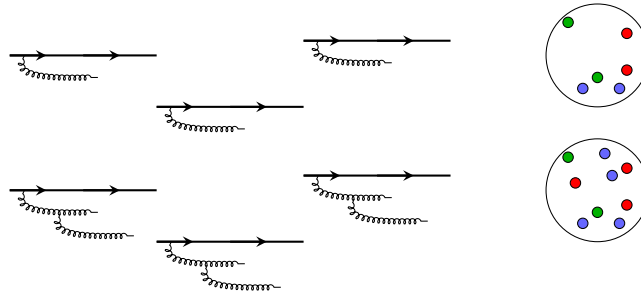
Figure 3.5: More and more gluons are emitted at higher energies. The color dots on the right part of the figures are either gluons or quarks.

But this process cannot go on forever. Indeed, when the room inside the proton is not sufficient to accommodate new gluons, they will start to recombine, as illustrated in the figure (3.6)
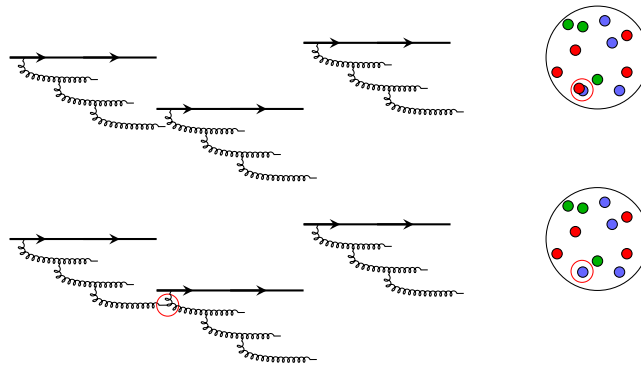
Figure 3.6: The gluon recombination phenomenon.

At high energy, a saturation phenomenon occurs [46]: there will be as many emissions as recombinations. This is characterized by a specific momentum: the saturation scale Q_s. Following Gribov, Levin and Ryskin [45], one can roughly estimate it as follows: denoting the gluon distribution $xG(x, Q^2)$, the number of gluons per unit are is

$$\rho \sim \frac{xG(x, Q^2)}{\pi R_A^2} \, , \tag{3.16}$$

where R_A is the radius of the nucleus involved [13]. The recombination cross-section of two gluons into one gluons scales as [45]

$$\sigma_{gg \to g} \sim \frac{\alpha_s}{Q^2} \, , \tag{3.17}$$

_____

13. $A = 1$ for a proton, $A = 197$ for gold and $A = 208$ for Lead (isotopes used at RHIC and LHC).

Saturation is reached when $\rho\sigma_{gg\rightarrow g} \sim 1$, which means

$$Q_s^2 \sim \frac{\alpha_s xG(x,Q^2)}{\pi R_A^2} \tag{3.18}$$

Phenomenologically, this parametric estimate scales as

$$Q_s^2 \sim \frac{A^{\frac{1}{2}}}{x^{0.3}} \ . \tag{3.19}$$

This is illustrated [14] in the figure (3.7)
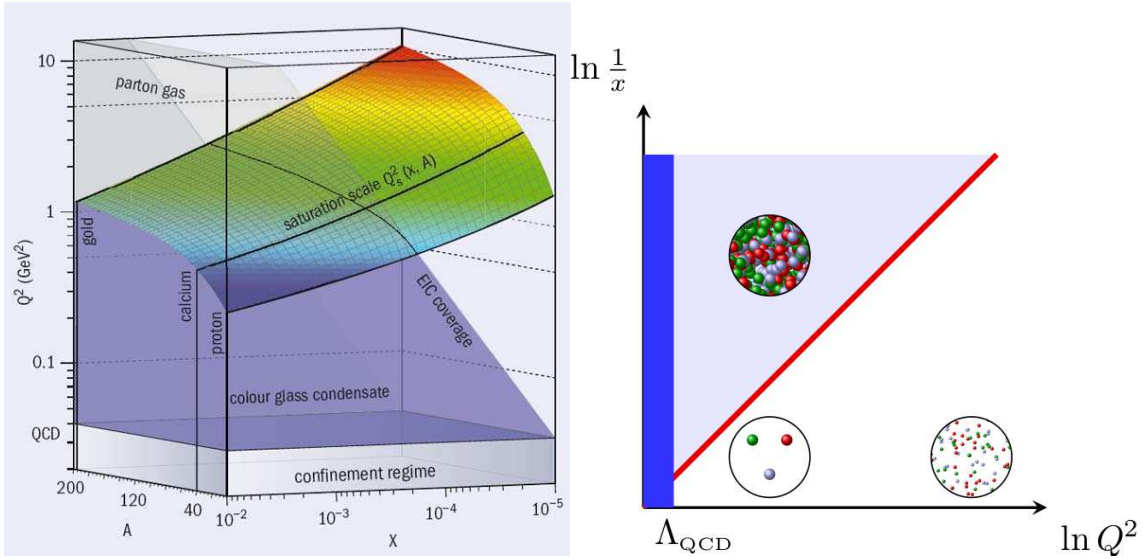
Figure 3.7: Left side: the limit between the domain of gluon saturation and the dilute partonic matter. Right side: a slice of the left panel at fixed A, with the schematic picture of what the nucleus looks like.

The other very important conclusion that can be drawn from the parametric estimate of equation (3.18) is that in the saturated regime, the gluon occupation number is

$$f(x,Q^2) \sim \frac{xG(x,Q^2)}{\pi R_A^2 Q_s^2} \sim \frac{1}{\alpha_s} \ . \tag{3.20}$$

In other words, the **gluon occupation is very large** at weak coupling. Because of the Pauli exclusion principle, the occupation number of the quarks in contrast cannot be bigger than 1. It therefore made sense to neglect them in (3.10). This high gluon occupancy – meaning that even if the QGP is weakly coupled it is strongly interacting – is one of the key physical features behind the the Color Glass Condensate effective theory.

3.5.2   Time dilation for highly boosted nuclei

To understand what are the phenomenological consequences of the time dilation phenomenon, consider again a proton at rest. We would like to probe this proton during a finite amount of time (the time length of the probe being for instance the duration of a collision). This probe would see the three valence quarks, as illustrated in the figure (3.8)

---

14. Here one should not be deceived by the reversed Q-x axis between the two plots, meaning that the saturation regime is at the bottom on the left figure and at the top in the right one.
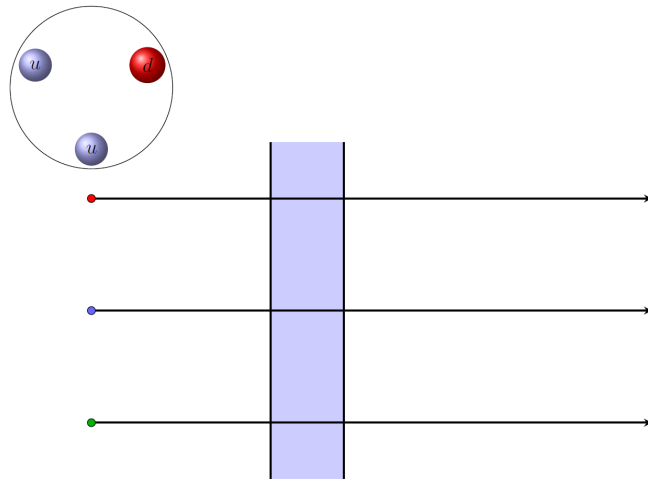
Figure 3.8: A proton at rest probed during a finite amount of time (represented by the blue band. Only the three valence quarks are visible.

Now, if we increase energy, the valence quarks radiate gluons by bremsstrahlung and the probe sees a much denser configuration of gluons and quarks, illustrated in the figure (3.9)
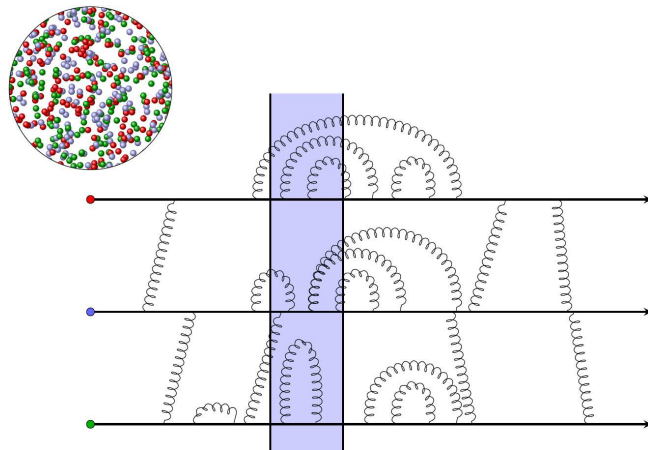
Figure 3.9: A proton at high energy, radiating gluons. Some of the gluons appear as free gluons with respect to the probe length.

At modest energies, most of the gluons probed are either emitted or reabsorbed during the interaction with the probe. These gluons therefore do not appear as free particles. Only a few of them do appear as free gluons. Consider now a proton at much higher energies. Firstly, due to Lorentz space contraction, the proton looks like a pancake localized in the plane transverse to the collision axis. Secondly, due to Lorentz time dilation, the time between the emission and absorption of a gluon is considerably increased. The schematic picture would therefore be the one of the figure (3.10)
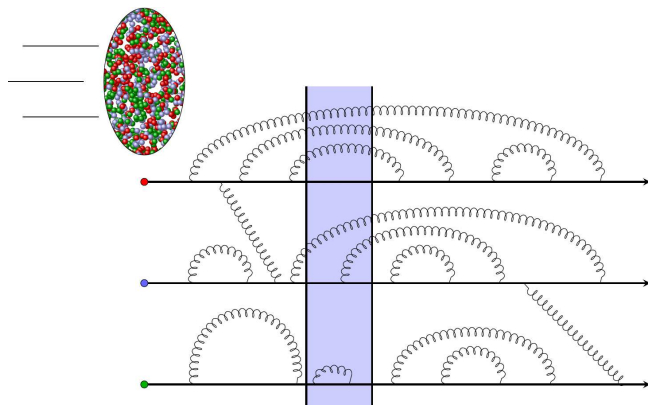
Figure 3.10: A proton at very high energy.

More and more gluons appear as free gluons. These are the gluons that move the fastest (hence those who suffer the most from the Lorentz time dilation). The dynamics of these gluons appears to be frozen. This is the other key ingredient of the Color Glass Condensate (CGC).

3.6   The Color Glass Condensate (CGC) effective theory

In the McLerran-Venugopalan model [43, 44] that gave birth to the modern version of the CGC, a momentum separation scale [15] $\Lambda^{\pm}$ is introduced between slow and fast gluons. Slow gluons are treated as usual gauge fields $\mathcal{A}_\mu^a$, while fast gluons are described as static color sources J_μ^a. They are considered to be moving at the speed of light. In light cone coordinates (z being taken to be the direction of the collision axis throughout this manuscript) $x^{\pm} = \frac{x^+ \pm x^-}{\sqrt{2}}$, the two color currents J_n^μ modeling the fast partons of the two projectiles (the $n = 1, 2$ index either standing for projectile one or two) are located on the light-cone axes. Schematically, the CCC picture looks like the figure (3.11)
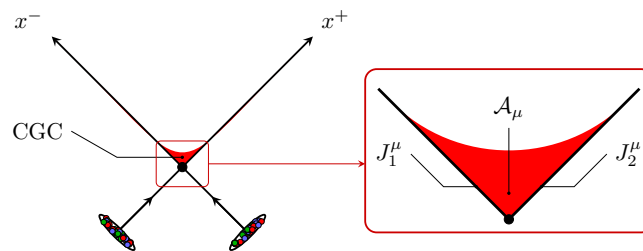
Figure 3.11: CGC picture. The slow gluons are described by the gauge field A_μ while the fast ones are described by the sources J_n^μ.

More precisely, these sources have the following form

$$J_1^{\mu a} = \delta^{\mu-}\delta(x^+)\rho_1^a(\boldsymbol{x}_\perp) , \qquad\qquad J_2^{\mu a} = \delta^{\mu+}\delta(x^-)\rho_2^a(\boldsymbol{x}_\perp) , \qquad (3.21)$$

where the $\delta(x^{\pm})$ is due to the time dilation. Both currents are conserved [16] $\mathcal{D}_\mu^{ab} J_n^{\mu b} = 0$. Finally, we need to specify the ρ_n. This will be the topic of the next section. For the moment, it suffices to give their parametric scaling. For dimensionality reasons (because J has dimension mass^3), we have $\rho_n \sim Q_s^2$. In the gluon saturation regime, it turns out that

$$\rho_n \sim \frac{Q_s^2}{g} \qquad (3.22)$$

where g is related to the strong coupling constant through $\alpha_s = \frac{g^2}{4\pi}$. The Lagrangean of the CGC [122–124] is

$$\mathcal{L} = -\frac{1}{4}F_{\mu\nu}^a F^{\mu\nu a} + A_\mu^a \left(J_1^{\mu a} + J_2^{\mu a} \right) . \qquad (3.23)$$

Now we are armed to understand why naive perturbation theory fails to compute observables in this framework. Indeed, since $J \sim \frac{1}{g}$ adding more sources to a tree diagram does not change the power counting in terms of g. To illustrate this, look at the three diagrams that all contribute at leading order in g to the observable $\langle A^\mu \rangle$ (each green blob corresponding to a source J)

$$(3.24)$$

Despite having a different number of three and four gluon vertices, these three diagrams are of the same order. The following graph has also the same order in g
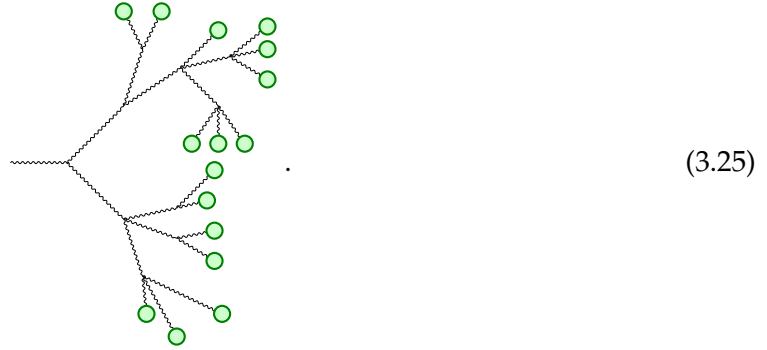
$$ (3.25) $$

As one can see, there are five 4-gluon and five 3-gluon vertices for 16 sources, which gives an overall power of $g^{10}g^5g^{-16} = \frac{1}{g}$ as before. The conclusion is that **all tree diagrams contribute to the leading order (LO) of any observable**. Therefore, one cannot rely on usual diagrammatic techniques to compute this infinite sum of contributions. We will see in the chapter 4 the other tools at our disposal to do calculations in the CGC framework (the bottom line being that the LO can be computed by solving the classical equation of motions with retarded initial conditions).

3.7 JIMWLK equation

In the previous section, we saw that an arbitrary momentum scale $\Lambda^{\pm}$ was introduced for each nucleus in order to separate the slow gluons from the fast ones. As a consequence, we can expect that physical observables computed with the Lagrangean (3.23) will depend on $\Lambda^{\pm}$. This is an issue because a physical observable should not depend on these unphysical parameters. The way to circumvent the problem is the following. Firstly, we have not been very specific on how to choose the color sources ρ_n. The best way to describe them is through a distribution function $W[\rho_n]$, meaning that we have only a probabilistic knowledge of the fast gluons. The key idea behind the JIMWLK renormalization group equation [125–131] is then to make W depends on the momentum cutoff in such a way that it precisely cancels the $\Lambda^{\pm}$ dependence of the physical observable. To be able to do so, one has to prove that the $\Lambda^{\pm}$ dependence can be factorized [58], i.e. that the unphysical dependence coming from the two nuclei do not mix. The JIMWLK equation then reads

$$ \Lambda^{\pm}\frac{\partial W_{\Lambda^{\pm}}[\rho_n]}{\partial \Lambda^{\pm}} = -\mathcal{H}W_{\Lambda^{\pm}}[\rho_n] \,, \tag{3.26} $$

where $\mathcal{H}$ is the JIMWLK Hamiltonean.

3.8 LO CGC results: Impossible matching with hydrodynamics

To calculate physical observables after the collision we need to know what are the gauge fields at that time. It turns out that one can compute them analytically [22, 47–50] in the proper time/rapidity coordinate system

$$ \tau = \sqrt{t^2 - z^2} \,, \qquad\qquad \eta = \frac{1}{2}\ln\frac{t + z}{t - z} \,. \tag{3.27} $$

There are two ways to do so: a matching of the singular terms in the Yang-Mills equation above and below the light cone axes [22, 47–49], and a second method [50] which we will present in the chapter 8, as it will prove very useful there in order to go beyond LO. In the

temporal axial gauge $\mathcal{A}^\tau = 0$ called the Fock-Scwhinger gauge, the solution at a small proper time $Q_s \tau \ll 1$ reads

$$
\begin{aligned}
\mathcal{E}^\eta(\tau, \boldsymbol{x}_\perp, \eta) &\sim F(\boldsymbol{x}_\perp) , & \mathcal{E}^i(\tau, \boldsymbol{x}_\perp, \eta) &\sim \tau^2 \\
\mathcal{A}_\eta(\tau, \boldsymbol{x}_\perp, \eta) &\sim \tau^2 , & \mathcal{A}_i(\tau, \boldsymbol{x}_\perp, \eta) &\sim G(\boldsymbol{x}_\perp) ,
\end{aligned} \tag{3.28}
$$

where $\mathcal{E}^\mu = -\tau g^{\mu\nu} \partial_\tau \mathcal{A}_\nu$ are the electric fields. The precise form of the functions F and G will be given in the chapter 8. Here one can notice that the fields are rapidity independent. How these field evolve after $Q_s \tau \ll 1$ is not known analytically, and one has to rely on numerical simulations in order to compute them. In order to answer to points $I - IV'$, recall that we need to know if the transverse and longitudinal pressures converge towards the same value. From the canonical definition of the energy-momentum tensor in gauge theories

$$
T^{\mu\nu} = \frac{1}{4} g^{\mu\nu} \mathcal{F}^a_{\rho\sigma} \mathcal{F}^{\rho\sigma a} - \mathcal{F}^{\mu a}_\rho \mathcal{F}^{\rho\nu a} , \tag{3.29}
$$

and the magnetic fields

$$
\mathcal{B}^\mu = \frac{1}{2} \epsilon^{\mu\nu\rho} \mathcal{F}_{\nu\rho} , \tag{3.30}
$$

we find that

$$
\begin{aligned}
\epsilon = T^{\tau\tau} &= \frac{1}{2} \left(\mathcal{E}^{ia}\mathcal{E}^{ia} + \mathcal{E}^{\eta a}\mathcal{E}^{\eta a} + \mathcal{B}^{ia}\mathcal{B}^{ia} + \mathcal{B}^{\eta a}\mathcal{B}^{\eta a} \right) \\
P_T = \frac{T^{xx} + T^{yy}}{2} &= \frac{1}{2} \left(\mathcal{E}^{\eta a}\mathcal{E}^{\eta a} + \mathcal{B}^{\eta a}\mathcal{B}^{\eta a} \right) \\
P_L = T^{\eta\eta} &= \frac{1}{2} \left(\mathcal{E}^{ia}\mathcal{E}^{ia} - \mathcal{E}^{\eta a}\mathcal{E}^{\eta a} + \mathcal{B}^{ia}\mathcal{B}^{ia} - \mathcal{B}^{\eta a}\mathcal{B}^{\eta a} \right) .
\end{aligned} \tag{3.31}
$$

From (3.28), we get

$$
\mathcal{B}^{ia}(\tau, \boldsymbol{x}_\perp, \eta) \sim \tau^2 \qquad\qquad \mathcal{B}^{\eta a}(\tau, \boldsymbol{x}_\perp, \eta) \sim H(\boldsymbol{x}_\perp) . \tag{3.32}
$$

At $\tau = 0^+$, only the longitudinal electric and magnetic fields are not zero. This implies that the energy density is equal to the transverse pressure, and is the opposite of the longitudinal one.

$$
\epsilon \approx P_T \approx -P_L . \tag{3.33}
$$

By solving numerically the classical Yang-Mills equations, one can obtain P_T and P_L at later times $\tau > 0$, as illustrated in the figure 3.12
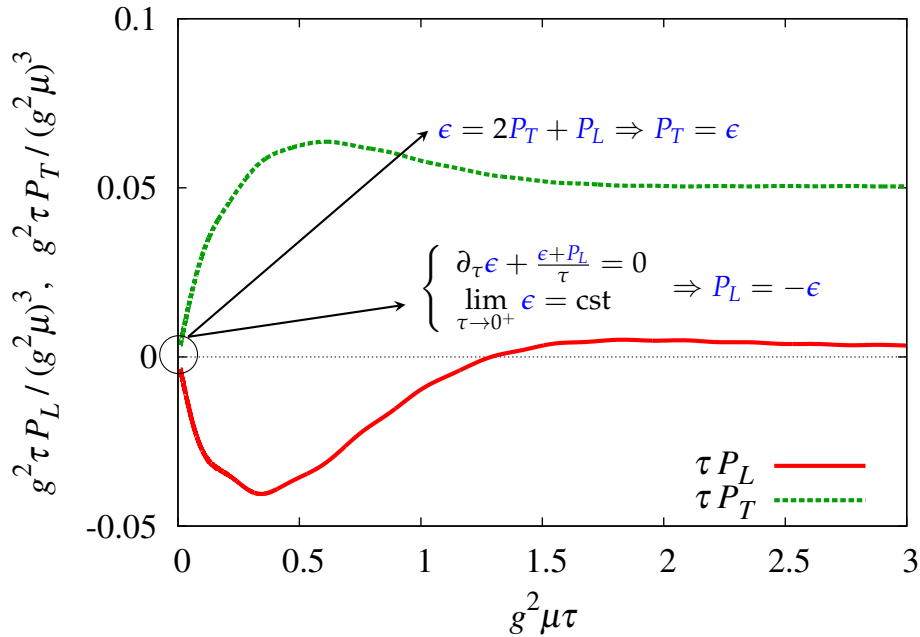
Figure 3.12: τP_T and τP_L as a function of the proper time. μ is related to the saturation scale Q_s through $Q_s = \mu g^2$.

As one can see, the transverse and longitudinal pressures start at opposite values, to later evolve into a stage where $P_L \approx 0$. This is in contradiction with postulate *IV'*, so here one has two choices: either abandon the weak-coupling description of the QGP, or try to understand whether there are large corrections beyond LO in the CGC. We will adopt the second point of view throughout this manuscript. It is also worth mentioning that the initial anisotropy is not specific to the CGC. It is in fact a consequence of energy-momentum conservation, that implies

$$\partial_\tau \epsilon + \frac{\epsilon + P_L}{\tau} = 0 \ . \tag{3.34}$$

For the energy-density to remain finite as the proper time goes to 0^+, one must have, as written in the figure 3.12,

$$\lim_{\tau \to 0} P_L = -\epsilon \ . \tag{3.35}$$

In addition, one can check on (3.31) that $T^{\mu\nu}$ is traceless in the Yang-Mills theory, which gives

$$\epsilon = 2P_T + P_L \ . \tag{3.36}$$

As a consequence

$$\lim_{\tau \to 0} P_T = \epsilon \ . \tag{3.37}$$

So the fact that at $\tau = 0$ the pressure tensor is anisotropic is not a peculiarity of the CGC. But the fact that this anisotropy remains large indefinitely (as will be shown to be in the chapter 9) is a limitation of the Leading Order CGC calculation, which is missing some important physical mechanisms.

3.9 NLO CGC results: Weibel instabilities and secular divergences

Since the LO CGC is not compatible with the assumptions of hydrodynamics, one can try to extend this QCD effective description by computing higher order corrections. As we

will show in the section 4.2, the Next to Leading Order (NLO) can be computed by starting with plane waves in the remote past and by propagating them on top of the classical fields (3.28) with the linearized equation of motion. How can this have a sizable effect, since the quantum corrections are α_s corrections to the fields of (3.28)? This has to do with instabilities. Indeed, it turns out that the Yang-Mills equations are subject to Weibel [17] instabilities [51–54] in anisotropic systems. These instabilities happen for modes that are rapidity dependent. So if one initializes the Yang-Mills numerical simulations with rapidity dependent fluctuations, the following happens [55–57]
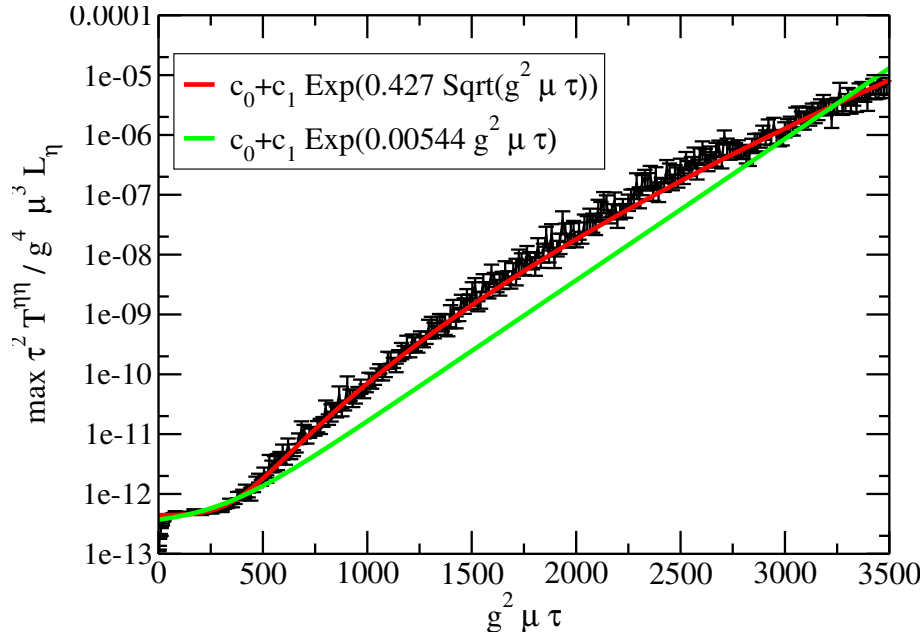
Figure 3.13:   The longitudinal pressure as a function of proper-time for a system initialized with rapidity dependent fluctuations.

As one can see in this figure, initially tiny fluctuations grow exponentially as $e^{\#\sqrt{Q_s\tau}}$. Starting from a NLO magnitude which is α_s smaller than the LO, it takes a time

$$Q_s\tau_{\mathrm{NLO}} \sim \ln^2\frac{1}{\alpha_s} \, , \qquad (3.38)$$

for the NLO corrections to reach the magnitude of the classical background field. Therefore, it is important to include these NLO corrections into the CGC framework. Unfortunately, this is not the end of the story. Indeed, we will see in the section 5.3.3 that the NLO term alone grows forever, leading to unphysical divergences in the pressure at late times. To cure this problem of secular divergences, a resummation is necessary, that we will present in the section 4.2. This leads to the classical-statistical method, that will be used throughout this thesis (see the chapters 5, 6 and 9 for numerical results, the chapter 7 for its theoretical limitations and the chapter 8 for its initial condition in the Yang-Mills case), to be introduced in the section 4.3.

---

17. First derived in QED [132]. For a qualitative analytic analysis of Weibel instabilities, see [133–136].

3.10 Summary

• The Quark-Gluon Plasma can be very succesfully described by nearly ideal hydrodynamics.
• Deriving the hydrodynamical prerequisites from QCD has proved to be very difficult so far.
• One of the best QCD effective theory to describe the QGP is the CGC. It takes into account the specific kinematics (gluon saturation, time dilation) of a heavy ion collisions.
• The CGC at its LO cannot account for the early onset of a hydrodynamical behavior of the QGP. Going beyond LO CGC in a satisfactory manner in order to account for this possible early hydrodynamization is the aim of this manuscript.

Appendix

3.A Bjorken's law for an ideal fluid

In the proper time/rapidity coordinate system, the four velocity of a fluid at rest in the comoving frame reads

$$u^\mu = (u^\tau, u^x, u^y, u^\eta) = (1, 0, 0, 0) \,. \tag{3.39}$$

In the Minkowskian coordinates, this trivially gives

$$u^{\tilde\mu} = (u^t, u^x, u^y, u^z) = \frac{1}{\tau}(t, 0, 0, -z) \,, \tag{3.40}$$

from which one can deduce

$$\nabla_\alpha u^\alpha = \frac{1}{\tau} \,. \tag{3.41}$$

Therefore, the conservation law (3.8) for an ideal fluid

$$D\epsilon + (\epsilon + p)\partial_\mu u^\mu = 0 \tag{3.42}$$

becomes

$$\partial_\tau \epsilon + \frac{\epsilon + p}{\tau} = 0 \,. \tag{3.43}$$

This is the famous Bjorken's law [137].

Chapter 4

⚛ Beyond standard perturbation theory

⚛

Contents

his chapter aims at describing techniques that go beyond the standard perturbation theory approach. The first section will introduce a formalism that is more suited to study real time evolution processes. The second section introduces one important tool that will be later used numerically: a resummation technique that allows one to account for a subset of quantum correction at any order of the perturbative expansion of an inclusive observable. Finally, the third section re-express in a different way the final result of the second section, by introducing the so-called Classical Statistical Approximation (CSA).

4.1   Schwinger-Keldysh formalism

In this section, we present an alternative formalism to the usual Feynman perturbation theory. The reason is that while the latter allows to compute transition amplitudes such as $\langle p' q'_{\text{out}} | p q_{\text{in}} \rangle$ (amplitude for two particles of momenta p, q in the initial state to become two other particles of momenta p', q' in the final state), it is not ideal when it comes to evaluate $\langle \text{in} | | \text{in} \rangle$ quantities such as $\langle \text{in} | a^\dagger_{\text{out}}(p) \, a_{\text{out}}(p) | \text{in} \rangle$, that counts the number of particles of momentum p in the final state. After having recalled some general principles of perturbation theory in the first part of this section, we will introduce the Schwinger-Keldysh [138, 139] formalism to deal with correlators of the form $\langle \text{in} | \phi(x_1) \cdots \phi(x_n) \phi(y_1) \cdots \phi(y_p) | \text{in} \rangle$. The

SCHWINGER-KELDYSH formalism is the adapted framework to describe out of equilibrium systems and time evolving processes as the ones we will encounter in the chapters 5-6-9. To keep things simple, we will do this for a Lagrangean of the form

$$\mathcal{L}[\phi] = \underbrace{\frac{1}{2}\left(\partial_\mu \phi\right)\left(\partial^\mu \phi\right)}_{\mathcal{L}_{\text{vac}}} \underbrace{-\frac{g^2}{4!}\phi^4}_{\mathcal{L}_{\text{int}}} , \tag{4.1}$$

that is, a Lagrangean that describes a massless scalar field theory with a quartic coupling.

4.1.1 Feynman Formalism: Notations, properties

Here we will recall some standard technique of perturbation theory in the Feynman formalism. To do so, we will consider operators of the form $\langle \boldsymbol{p}_{1\text{out}} \cdots \boldsymbol{p}_{n\text{out}} | 0_{\text{in}} \rangle$, where 0_{in} is the initial vacuum state. We start with some notations. We will denote (omitting the hat on the operators to lighten a bit the notations)

$$\phi_{\text{in}} = \lim_{x_0 \to -\infty} \phi , \qquad\qquad \phi_{\text{out}} = \lim_{x_0 \to +\infty} \phi . \tag{4.2}$$

In HEISENBERG representation, one has the following definition for ϕ

$$\phi(x) = U(-\infty, x_0)\phi_{\text{in}}(x)U(x_0, -\infty) , \tag{4.3}$$

where U is the usual evolution operator , defined by the following first order differential equation

$$\frac{\partial}{\partial x_0} U(x_0, -\infty) = i\left[\int \mathrm{d}^3 x\, \mathcal{L}_{\text{int}}\left[\phi_{\text{in}}(x_0, \vec{x})\right]\right] U(x_0, -\infty) . \tag{4.4}$$

The initial condition is trivially found by imposing that there are no interactions at $x^0 = -\infty$

$$\lim_{x_0 \to -\infty} U(x_0, -\infty) = \mathbb{I} . \tag{4.5}$$

by solving (4.4), U can therefore be written as

$$U(x_0, -\infty) = T e^{i\int_{-\infty}^{x_0} \mathrm{d}z_0 \int \mathrm{d}^3 z\, \mathcal{L}_{\text{int}}[\phi_{\text{in}}(z_0, z)]} , \tag{4.6}$$

where T is the time ordering operator

$$T(A(y_0)B(z_0)) = \theta(y_0 - z_0)A(y_0)B(z_0) + \theta(z_0 - y_0)B(z_0)A(y_0) . \tag{4.7}$$

Some properties of the evolution operator include

$$U(x_0, y_0)U(y_0, z_0) = U(x_0, z_0) \qquad U(x_0, y_0) = U^{-1}(y_0, x_0) = U^\dagger(y_0, x_0) . \tag{4.8}$$

Now, recalling the usual expressions for ϕ_{in} and ϕ_{out} in term of creation and annihilation operator

$$\phi_{\text{in}} = \int \frac{\mathrm{d}^3 k}{2|\boldsymbol{k}|(2\pi)^3}\left(a_{\text{in}}(\boldsymbol{k})e^{-ikx} + a_{\text{in}}^\dagger(\boldsymbol{k})e^{ikx}\right) ,$$

$$\phi_{\text{out}} = \int \frac{\mathrm{d}^3 k}{2|\boldsymbol{k}|(2\pi)^3}\left(a_{\text{out}}(\boldsymbol{k})e^{-ikx} + a_{\text{out}}^\dagger(\boldsymbol{k})e^{ikx}\right) . \tag{4.9}$$

and noticing that because of (4.3)

$$\phi_{\text{out}}(x) = U(-\infty, +\infty)\phi_{\text{in}}(x)U(+\infty, -\infty) , \tag{4.10}$$

we must have

$$a^\dagger_{\text{out}}(x) = U(-\infty, +\infty)a^\dagger_{\text{in}}(x)U(+\infty, -\infty) , \quad a_{\text{out}}(x) = U(-\infty, +\infty)a_{\text{in}}(x)U(+\infty, -\infty) , \tag{4.11}$$

and since

$$a_{\text{in}}(\boldsymbol{k}) |0_{\text{in}}\rangle = 0 , \quad a_{\text{out}}(\boldsymbol{k}) |0_{\text{out}}\rangle = 0 , \quad |\boldsymbol{k}_{\text{in}}\rangle = a^\dagger_{\text{in}}(\boldsymbol{k}) |0_{\text{in}}\rangle , \quad |\boldsymbol{k}_{\text{out}}\rangle = a^\dagger_{\text{out}}(\boldsymbol{k}) |0_{\text{out}}\rangle , \tag{4.12}$$

one has

$$U(+\infty, -\infty)a_{\text{out}}(x)U(-\infty, +\infty) |0_{\text{in}}\rangle = 0 , \tag{4.13}$$

and

$$|0_{\text{out}}\rangle = U(-\infty, +\infty) |0_{\text{in}}\rangle , \qquad\qquad |0_{\text{in}}\rangle = U(+\infty, -\infty) |0_{\text{out}}\rangle , \tag{4.14}$$

so

$$|\boldsymbol{p}_1..\boldsymbol{p}_n \text{ out}\rangle = U(-\infty, +\infty) |\boldsymbol{p}_1..\boldsymbol{p}_n \text{ in}\rangle , \qquad \langle 0_{\text{in}}| = \langle 0_{\text{out}}| U(-\infty, +\infty) . \tag{4.15}$$

Finally, a very useful property concerning the creation and annihilation operator can be obtained by inverting (4.9)

$$a(\boldsymbol{p}) = i \int \mathrm{d}^3\boldsymbol{x} \, e^{ipx} \overset{\leftrightarrow}{\partial_0} \phi(x) , \qquad\qquad a^\dagger(\boldsymbol{p}) = -i \int \mathrm{d}^3\boldsymbol{x} \, e^{-ipx} \overset{\leftrightarrow}{\partial_0} \phi(x) , \tag{4.16}$$

Armed with all those definitions and properties, we can present what is the one particle production in the final state.

$$\langle \boldsymbol{p}_{\text{out}}|0_{\text{in}}\rangle = i \int \mathrm{d}^4x \, e^{ipx} \Box_x \langle 0_{\text{out}}|\phi(x)|0_{\text{in}}\rangle . \tag{4.17}$$

This result is easily extendable to the multi-particle production case, up to one subtlety, which is the time ordering. The result is the LEHMANN–SYMANZIK–ZIMMERMANN formula [140]

$$\left\langle \boldsymbol{p}_n \cdots \boldsymbol{p}_{1,\text{out}}|0_{\text{in}}\right\rangle = i^n \int \mathrm{d}^4x_1 \cdots \mathrm{d}^4x_n \, e^{i(p_1 x_1 + \cdots + p_n x_n)} \Box_{x_n} \cdots \Box_{x_1} \langle 0_{\text{out}}|T\phi(x_n) \cdots \phi(x_1)|0_{\text{in}}\rangle . \tag{4.18}$$

It is now time to use (4.12-4.15) to express

$$I = \langle 0_{\text{out}}|T\phi(x_1) \cdots \phi(x_n)|0_{\text{in}}\rangle , \tag{4.19}$$

in term of free operators. To do so, we will make the following choice on the dummy variables $x_1 \cdots x_n$

$$-\infty \xrightarrow{\quad\underset{x_n}{|} \cdots \underset{x_1}{|}\quad} +\infty \tag{4.20}$$

so that

$$\begin{aligned} I = \langle 0_{\text{out}}| &U(-\infty, x_1^0)\phi_{\text{in}}(x_1)U(x_1^0, -\infty)U(-\infty, x_2^0)\phi_{\text{in}}(x_1)U(x_2^0, -\infty) \\ &U(-\infty, x_n^0)\phi_{\text{in}}(x_n)U(x_n^0, -\infty) |0_{\text{in}}\rangle . \end{aligned} \tag{4.21}$$

Using (4.8), we get

$$\begin{aligned} I &= \langle 0_{\text{out}}| U(-\infty, +\infty)U(+\infty, x_1^0)\phi_{\text{in}}(x_1)U(x_0^1, x_2^0)\phi_{\text{in}}(x_1) \cdots U(x_n^0, -\infty |0_{\text{in}}\rangle \\ &= \left\langle 0_{\text{in}}|U(+\infty, x_1^0)\phi_{\text{in}}(x_1)U(x_0^1, x_2^0)\phi_{\text{in}}(x_1) \cdots \phi_{\text{in}}(x_n)U(x_n^0, -\infty)|0_{\text{in}}\right\rangle , \end{aligned} \tag{4.22}$$

Reintroducing the time ordering operator T, we obtain

$$\langle 0_{\text{out}}|T\phi(x_1)..\phi(x_n)|0_{\text{in}}\rangle = \left\langle 0_{\text{in}}|T\phi_{\text{in}}(x_1)..\phi_{\text{in}}(x_n)e^{i\int \mathcal{L}_{int}(\phi_{\text{in}}(z))d^4z}|0_{\text{in}}\right\rangle . \tag{4.23}$$

One can then introduce the following generating functional

$$\mathcal{Z}[\eta] = \left\langle 0_{\text{in}}|Te^{i\int_{-\infty}^{+\infty}[\mathcal{L}_{\text{int}}(\phi_{\text{in}}(z))+\eta(z)\phi_{\text{in}}(z)]d^4z}|0_{\text{in}}\right\rangle . \tag{4.24}$$

This is the central tool of perturbation theory since from it we can easily derive

$$\left\langle 0_{\text{in}}|T\phi_{\text{in}}(x_1)..\phi_{\text{in}}(x_n)e^{i\int \mathcal{L}_{\text{int}}(\phi_{\text{in}}(z))d^4z}|0_{\text{in}}\right\rangle = \frac{\delta\mathcal{Z}[\eta]}{i\delta\eta(x_1)..i\eta(x_n)}\Big|_{\eta=0} . \tag{4.25}$$

Thanks to the property

$$F(\frac{d}{idx})e^{iax} = F(a)e^{iax} , \tag{4.26}$$

obtained by Taylor expanding F, Z can be rewritten as

$$\mathcal{Z}[\eta] = e^{i\int_{-\infty}^{+\infty}\mathcal{L}_{int}\left(\frac{\delta}{i\delta\eta(z)}\right)d^4z}\left\langle 0_{\text{in}}|Te^{i\int_{-\infty}^{+\infty}\eta(z)\phi_{\text{in}}(z)d^4z}|0_{\text{in}}\right\rangle . \tag{4.27}$$

Finally, a standard result in perturbation theory tells us that

$$\mathcal{Z}_0[\eta] = \left\langle 0_{\text{in}}|Te^{i\int_{-\infty}^{+\infty}\eta(z)\phi_{\text{in}}(z)d^4z}|0_{\text{in}}\right\rangle , \tag{4.28}$$

can be rewritten as

$$\mathcal{Z}_0[\eta] = e^{-\frac{1}{2}\int d^4x\,d^4y\,\eta(x)G_F(x,y)\eta(y)} \tag{4.29}$$

with (see [140] for a standard derivation of the Feynman propagator)

$$G_F(x,y) = \langle 0_{\text{in}}|T\phi_{\text{in}}(x)\phi_{\text{in}}(y)|0_{\text{in}}\rangle = i\int \frac{d^4p}{(2\pi)^4}\frac{e^{ip(x-y)}}{p^2+i\epsilon} , \tag{4.30}$$

G_F being the FEYNMAN propagator. Z can therefore be written as

$$\boxed{\mathcal{Z}[\eta] = e^{i\int_{-\infty}^{+\infty}\mathcal{L}_{int}\left(\frac{\delta}{i\delta\eta(z)}\right)d^4z}e^{-\frac{1}{2}\int d^4x\,d^4y\,\eta(x)G_F(x,y)\eta(y)}} \tag{4.31}$$

This generating functional is the central tool of FEYNMAN formalism and is the perfect tool to compute the multi-particle production in the final state. Unfortunately, some of the simplifications that we used for its derivation cannot be used anymore when it comes to the computation of the number of particles with momentum p in the final state. This is the reason why we introduce SCHWINGER-KELDYSH formalism in the next section.

4.1.2   The problem of in-in correlators: Schwinger-Keldysh formalism

We now introduce the SCHWINGER-KELDYSH formalism in order to compute

$$\left\langle 0_{\text{in}}\Big|a_p^\dagger a_p\Big|0_{\text{in}}\right\rangle , \tag{4.32}$$

which is just the number of particle in the final state with the momentum p. As we will see, the FEYNMAN formalism presented in the previous section is not well suited for computing such a quantity. To see this, let us try to apply the same tricks that the ones already used in section 4.1.1. We start from

$$a_p = i\int d^4x\,e^{ipx}\,\square\phi(x) , \qquad\qquad a_p^\dagger = -i\int d^4x\,e^{-ipx}\,\square\phi(x) , \tag{4.33}$$

which gives very similarly [1] to (4.18)

$$\left\langle 0_{in} \middle| a_{\boldsymbol{p}}^{\dagger} a_{\boldsymbol{p}} \middle| 0_{in} \right\rangle = \int d^4 y \, d^4 x \, e^{-ipx+ipy} \, \Box_x \Box_y \left\langle 0_{in} | \phi(x) \phi(y) | 0_{in} \right\rangle . \tag{4.34}$$

We write

$$\phi(x) = U(-\infty, x_0) \phi_{in}(x) U(x_0, -\infty) \tag{4.35}$$

$$\phi(x)\phi(y) = U(-\infty, x_0) \phi_{in}(x) U(x_0, y_0) \phi_{in}(y) U(y_0, -\infty) . \tag{4.36}$$

But now things start to be different. There are two reasons for that: the first one is that we have an $\langle 0_{in}|$ state instead of an $\langle 0_{out}|$ one, and the second reason is the lack of the T product in the previous expression. The first one implies that we can't reorganize the U evolution operators as we did before. The trick in the SCHWINGER-KELDYSH formalism will therefore be different, and consists in artificially duplicating the time contour in the following way

$$\text{(4.37)}$$

where the separation between the $+$ and $-$ has been exaggerated for readability. This is the main specificity of the SCHWINGER-KELDYSH formalism. By analogy with the FEYNMAN formalism, we call P the path ordering along the blue contour $\mathcal{C}$. P is equal to T if both x^0 and y^0 belong to the $+$ branch, opposite to T if they belong to the $-$ branch and proportional to a θ function if the two times don't belong to the same branch. Thus, calling $\phi^{(\pm)}$ the field on the $\pm$ branch, we get

$$\left\langle 0_{in} \middle| a_{\boldsymbol{p}}^{\dagger} a_{\boldsymbol{p}} \middle| 0_{in} \right\rangle = \int d^4 y \, d^4 x \, e^{-ipx+ipy} \, \Box_x \Box_y \left\langle 0_{in} \middle| P \phi_{in}^{(-)}(x) \phi_{in}^{(+)}(y) e^{i \int_{\mathcal{C} \times \mathbb{R}^3} \mathcal{L}_{int}(\phi_{in}(z)) d^4 z} \middle| 0_{in} \right\rangle , \tag{4.38}$$

with

$$e^{i \int_{\mathcal{C} \times \mathbb{R}^3} \mathcal{L}_{int}(\phi_{in}(z)) d^4 z} = e^{i \int_{\mathbb{R} \times \mathbb{R}^3} \mathcal{L}_{int}(\phi_{in}^{(+)}(z)) d^4 z} e^{-i \int_{\mathbb{R} \times \mathbb{R}^3} \mathcal{L}_{int}(\phi_{in}^{(-)}(z)) d^4 z}. \tag{4.39}$$

The generating functional of this formalism is

$$\overline{\mathcal{Z}}[\eta^+, \eta^-] = \left\langle 0_{in} \middle| P e^{i \int_{\mathcal{C} \times \mathbb{R}^3} (\mathcal{L}_{int}(\phi_{in}(z)) + \eta(z) \phi_{in}(z)) d^4 z} \middle| 0_{in} \right\rangle , \tag{4.40}$$

and therefore

$$\left\langle 0_{in} \middle| P \phi_{in}^{\epsilon_1}(x_1) .. \phi_{in}^{\epsilon_n}(x_n) e^{i \int_{\mathcal{C} \times \mathbb{R}^3} \mathcal{L}_{int}(\phi_{in}(z)) d^4 z} \middle| 0_{in} \right\rangle = \frac{\delta \overline{\mathcal{Z}}[\eta^+, \eta^-]}{i \delta \eta^{\epsilon_1}(x_1) .. i \eta^{\epsilon_n}(x_n)} \bigg|_{\eta^{\pm}=0}. \tag{4.41}$$

as in the FEYNMAN formalism, $\overline{\mathcal{Z}}$ can be rewritten as

$$\overline{\mathcal{Z}}[\eta^+, \eta^-] = e^{i \int_{\mathcal{C} \times \mathbb{R}^3} \mathcal{L}_{int}\left(\frac{\delta}{i \delta \eta(z)}\right) d^4 z} e^{-\frac{1}{2} \int_{\mathcal{C} \times \mathbb{R}^3} d^4 x \, d^4 y \, \eta(x) \overline{G}(x,y) \eta(y)} , \tag{4.42}$$

with

$$\overline{G}(x,y) = \langle 0_{in} | P \phi_{in}(x) \phi_{in}(y) | 0_{in} \rangle , \tag{4.43}$$

with $\overline{G}(x,y)$ such that

- if $x, y \in +$, then $P = T$ and

$$\overline{G}(p) = G_{++}(p) = \frac{i}{p^2 + i\epsilon} . \tag{4.44}$$

---

1. But the devil (and the SCHWINGER-KELDYSH formalism) is in the details.

- if $x, y \in -$, then $P = \overline{T}$ and

$$\overline{G}(p) = G_{--}(p) = \frac{-i}{p^2 - i\epsilon} \, . \tag{4.45}$$

- if $x \in -, y \in +$, then

$$\overline{G}(p) = G_{-+}(p) = 2\pi\theta(p_0)\delta(p^2) \, . \tag{4.46}$$

- if $x \in +, y \in -$, then

$$\overline{G}(p) = G_{+-}(p) = 2\pi\theta(-p_0)\delta(p^2) \, . \tag{4.47}$$

$G_{\pm\pm}$ are the SCHWINGER-KELDYSH propagators. It is trivial to check

$$G_{++} + G_{--} = G_{+-} + G_{-+} \, , \tag{4.48}$$

obtained thanks to the following property of the delta function [2]

$$\pi\delta(x) = \frac{i}{x + i\epsilon} - i\mathbb{P}\left(\frac{1}{x}\right) \, . \tag{4.49}$$

it will be useful for the future developments to define a new propagator

$$
\begin{aligned}
G_{++} - G_{+-} &= \theta(x_0 - y_0) \langle 0_{\text{in}} | \phi_{\text{in}}(x)\phi_{\text{in}}(y) | 0_{\text{in}} \rangle + (\theta(y_0 - x_0) - 1) \langle 0_{\text{in}} | \phi_{\text{in}}(y)\phi_{\text{in}}(x) | 0_{\text{in}} \rangle \\
&= \theta(x_0 - y_0) \langle 0_{\text{in}} | [\phi_{\text{in}}(x)\phi_{\text{in}}(y)] | 0_{\text{in}} \rangle = G_R(x, y) \, ,
\end{aligned}
\tag{4.50}
$$

which is the retarded propagator. By looking at the definition of the $G_{\pm\pm}$ and using again (4.49), it is easy to find that

$$G_R(p) = \frac{i}{p^2 + ip^0\epsilon} \, . \tag{4.51}$$

The SCHWINGER-KELDYSH formalism allows for an important simplification. Indeed, since for a physical source we have $\eta^{(+)} = \eta^{(-)} = \eta$, one can show that in SCHWINGER-KELDYSH formalism, vacuum diagrams do not participate to the amplitude $\langle 0_{\text{in}} | \phi_{\text{in}}(x)\phi_{\text{in}}(y) | 0_{\text{in}} \rangle$. FEYNMAN rules in the SCHWINGER-KELDYSH formalism are the following: to each propagator we associate

$$x \underset{\epsilon = \pm \quad \epsilon' = \pm}{\rule{4cm}{0.4pt}} y \;\Rightarrow G_{\epsilon\epsilon'}(x, y), \tag{4.52}$$

to each source (indicated by a blue dot ○)

$$x \underset{\epsilon = \pm}{\rule{3cm}{0.4pt}} y \;\Rightarrow i\epsilon \int \mathrm{d}^4x \, \eta(x) \tag{4.53}$$

and to each vertex

$$\epsilon' = \pm \quad \Rightarrow -i\lambda\epsilon \tag{4.54}$$

---

2. $\mathbb{P}(x)$ indicates the principal value of x.

Let us notice here the main difference between the two propagators G_F and G_R of the two formalisms presented so far: their poles are not located in the same place in the complex plane[3]. Indeed, since

$$G_F(p) = \frac{i}{p^2 + i\epsilon} \qquad\qquad G_R(p) = \frac{i}{p^2 + ip_0\epsilon} \, , \qquad (4.55)$$

we have in the complex plane

$$(4.56)$$
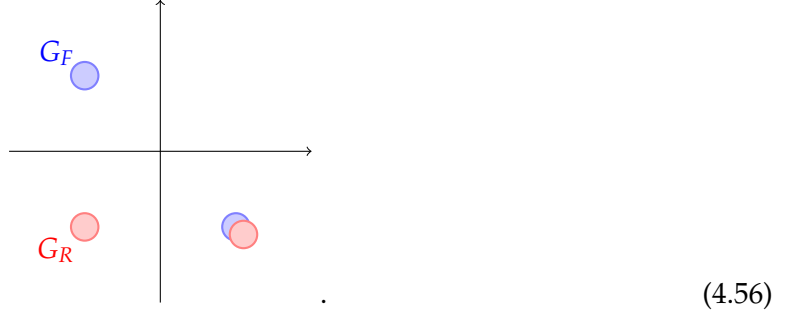
The other main difference between FEYNMAN and SCHWINGER-KELDYSH has already been indicated: the latter does not contain vacuum-vacuum diagrams. But besides these differences, there is a functional identity that strongly relates the two formalisms. With what we already saw, it is indeed possible to rewrite the SCHWINGER-KELDYSH generating functional thanks to the one of the FEYNMAN formalism

$$\overline{\mathcal{Z}}[\eta^{(+)}, \eta^{(-)}] = e^{\int d^4x \, d^4y \, G_{+-}(x,y)\Box_x\Box_y \frac{\delta^2}{\delta\eta^{(-)}(x)\delta\eta^{(+)}(y)}} \, \mathcal{Z}[\eta^{(+)}]\mathcal{Z}^*[\eta^{(-)}] \, . \qquad (4.57)$$

If this property holds for Z_0 (without $\mathcal{L}_{\mathrm{int}}$), then it is simple to see that it is also true for the Z. The demonstration being tedious, it is derived in the appendix 4.A. To conclude this section, we present an alternate basis of the SCHWINGER-KELDYSH formalism which is closer to what is done in numerical simulations: the retarded-advanced basis. This will serve our interests in the chapter 7.

4.1.3 The retarded-advanced formalism

It turns out that the $\pm$ basis presented so far is not the most convenient one to use for numerical computation. Indeed, one can try to take advantage of (4.48) to find a basis where one of the four propagators cancel. Among these bases, the most famous one is the retarded-advanced basis, obtained by a simple rotation of the $\pm$ basis. Denoting the propagators in this new basis $G_{\alpha\beta}$ with $\alpha, \beta \in 1, 2$, we have

$$G_{\alpha\beta} = \sum_{\epsilon,\epsilon'=\pm} \Omega_{\alpha\epsilon} G_{\epsilon\epsilon'} \Omega^\dagger_{\epsilon'\beta} \, , \qquad (4.58)$$

with the rotation matrix defined as

$$\Omega = \begin{pmatrix} 1 & -1 \\ \frac{1}{2} & \frac{1}{2} \end{pmatrix} \, . \qquad (4.59)$$

Performing the trivial calculation gives

$$\mathbb{G} = \begin{pmatrix} G_{11} & G_{12} \\ G_{21} & G_{22} \end{pmatrix} = \begin{pmatrix} 0 & G_{++} - G_{-+} \\ G_{++} - G_{+-} & \frac{1}{2}\left(G_{-+} + G_{+-}\right) \end{pmatrix} \, . \qquad (4.60)$$

For reasons that will appear clear in a moment, we will denote

$$G_A = G_{12} \, , \qquad\qquad G_R = G_{21} \, , \qquad\qquad G_S = G_{22} \, . \qquad (4.61)$$

---

3. This will have crucial consequences in chapter 7.

Indeed, in momentum space, one can deduce from (4.44-4.47) that

$$G_A(p) = \frac{i}{p^2 - ip^0\epsilon} \, , \qquad G_R(p) = \frac{i}{p^2 + ip^0\epsilon} \, , \qquad G_S(p) = \pi\delta(p^2) \, . \qquad (4.62)$$

and the first two equations give in coordinate space after having performed the integral over p^0 in the complex plane

$$G_R(x,y) = -\theta(x^0 - y^0) \int \frac{\mathrm{d}^3\boldsymbol{p}}{2|\boldsymbol{p}|(2\pi)^3} e^{i\boldsymbol{p}(x-y)} \left(e^{i|\boldsymbol{p}|(x^0 - y^0)} - e^{-i|\boldsymbol{p}|(x^0 - y^0)} \right) \qquad (4.63)$$

$$G_A(x,y) = -\theta(y^0 - x^0) \int \frac{\mathrm{d}^3\boldsymbol{p}}{2|\boldsymbol{p}|(2\pi)^3} e^{i\boldsymbol{p}(x-y)} \left(e^{i|\boldsymbol{p}|(x^0 - y^0)} - e^{-i|\boldsymbol{p}|(x^0 - y^0)} \right) \, . \qquad (4.64)$$

We now clearly see why one of the two propagator is called retarded while the other is named advanced: the θ function causes G_R to be 0 if $y^0 > x^0$ while the opposite is true for G_A. The inverse relations will also prove helpful

$$\begin{pmatrix} G_{++} & G_{+-} \\ G_{-+} & G_{--} \end{pmatrix} = \begin{pmatrix} \frac{1}{2}(G_{12} + G_{21}) + G_{22} & \frac{1}{2}(G_{12} - G_{21}) + G_{22} \\ -\frac{1}{2}(G_{12} - G_{21}) + G_{22} & -\frac{1}{2}(G_{12} + G_{21}) + G_{22} \end{pmatrix} \, . \qquad (4.65)$$

4.2   Resummation formula

In this section, we will present the resummation technique [141, 142] that allows one to go beyond the Leading Order CGC results presented in section 3.8. Let us mention from the start that this formula only works for inclusive observables, meaning observables that do not require the complete knowledge of the final state. As a warm-up, and since it will prove useful in the scalar field theory chapters 5-6-7, we will start by computing at Leading Order (LO) and Next to Leading Order (NLO) the expectation value of the fields $\phi^{\pm}$ in the SCHWINGER-KELDYSH formalism. We will then explain what characterizes the resummation technique, its main ingredient being a formal relation that exists between the LO and the NLO. The adaptation of the content of this section to the gauge case can be found in [58].

4.2.1   Leading Order: the classical level

At Leading Order, as explained in section 3.7 for the gauge case, only tree diagrams are involved in the calculation of inclusive observables. In order to fix the ideas, let us consider again our scalar field Lagrangean with a quartic coupling and an additional coupling to a source term η

$$\mathcal{L} = \frac{1}{2}\left(\partial_\mu\phi\right)\left(\partial^\mu\phi\right) - \frac{g^2}{4!}\phi^4 + \eta\phi \, . \qquad (4.66)$$

As already mentioned, in order to mimic a heavy ion collision the source has to be very intense, inversely proportional to the coupling constant $\eta \sim \frac{1}{g}$. This gives the same scaling for the field $\phi \sim \frac{1}{g}$ at the classical level. If we want to compute the connected contribution to the expectation values $\left\langle \phi^{(\pm)} \right\rangle$ at Leading Order, that we shall denote $\varphi^{(\pm)}$, we have to compute at leading order the first derivative of the connected generating functional of the SCHWINGER-KELDYSH formalism $\mathcal{W}[\eta^{(+)}, \eta^{(-)}]$, where

$$\overline{\mathcal{Z}}[\eta^{(+)}, \eta^{(-)}] = e^{\mathcal{W}[\eta^{(+)}, \eta^{(-)}]} \, . \qquad (4.67)$$

This means

$$\varphi^{(\pm)}(x) = \left.\frac{\delta\mathcal{W}[\eta^{(+)}, \eta^{(-)}]}{i\delta\eta^{(\pm)}(x)}\right|_{\eta^{(\pm)}=\eta} = \left.\frac{1}{\overline{\mathcal{Z}}[\eta^{(+)}, \eta^{(-)}]} \frac{\delta\mathcal{Z}[\eta^{(+)}, \eta^{(-)}]}{i\delta\eta^{(\pm)}(x)}\right|_{\eta^{(\pm)}=\eta} \, . \qquad (4.68)$$

In terms of graphs, it corresponds as announced to all the tree diagrams. To be more precise we can write the following (exact) diagrammatic expression

$$\varphi^{(+)} = \quad (4.69)$$

$$\varphi^{(-)} = \quad (4.70)$$

where the green and red blobs respectively denote $\varphi^{(+)}$ and $\varphi^{(-)}$, and the blue blob the strong physical source $\eta = \eta^{(+)} = \eta^{(-)}$. At the leading order, all the propagators are bare ones and we can therefore write the following equations

$$\varphi^{(\epsilon)}(x) = \sum_{\epsilon'=\pm 1} i \int d^4 y \, G_{\epsilon\epsilon'}(x,y) \, \eta(y) - i \sum_{\epsilon'=\pm 1} \frac{g^2}{6} \int d^4 y \, G_{\epsilon\epsilon'}(x,y) \left(\varphi^{(\epsilon')}(y) \right)^3 . \quad (4.71)$$

If one takes the d'Alembertian of this expression, since (one can check those properties by Fourier transforming (4.44-4.47))

$$\Box G_{++}(x,y) = \Box G_{--}(x,y) = -i\delta(x-y) \qquad \Box G_{+-}(x,y) = \Box G_{-+}(x,y) = 0 , \quad (4.72)$$

this implies that

$$\Box \varphi^{(\epsilon)}(x) = \eta(x) - \frac{g^2}{6} \left(\varphi^{(\epsilon)}(x) \right)^3 , \quad (4.73)$$

and so

$$\Box \varphi^{(\epsilon)}(x) + V'(\varphi^{(\epsilon)}(x)) = \eta(x) . \quad (4.74)$$

We therefore just showed that the fields $\varphi^{(\epsilon)}$ obey the classical equation of motion. We now need to find the corresponding boundary conditions. Taking a field which obeys to

$$\Box \varphi^{(+)}(y) + V'(\varphi^{(+)}(y)) = \eta(y) , \quad (4.75)$$

multiplying on the left by $G_{++}(x,y)$ and integrating on y

$$\int d^4 y \, G_{++}(x,y) \Box_y \varphi^{(+)}(y) + \int d^4 y \, G_{++}(x,y) V'(\varphi^{(+)}(y)) = \int d^4 y \, G_{++}(x,y) \eta(y) , \quad (4.76)$$

in addition

$$G_{++}(x,y) \overset{\leftarrow}{\Box}_y = -i\delta(x-y)$$
$$\int d^4 y \, G_{++}(x,y) \overset{\leftarrow}{\Box}_y \varphi^{(+)}(y) = -i\varphi^{(+)}(x) . \quad (4.77)$$

We subtract these two equations to get

$$\int d^4 y \, G_{++}(x,y) \overset{\leftrightarrow}{\Box}_y \varphi^{(+)}(y) + \int d^4 y \, G_{++}(x,y) V'(\varphi^{(+)}(y)) - \int d^4 y \, G_{++}(x,y) \eta(y) = i\varphi^{(+)}(x) , \quad (4.78)$$

where

$$A \overset{\leftrightarrow}{\Box} B = A \overset{\rightarrow}{\Box} B - A \overset{\leftarrow}{\Box} B . \quad (4.79)$$

By analogy for $\varphi^{(-)}(y)$, combining it with $G_{+-}(x,y)$

$$i \int d^4y \, G_{+-}(x,y) \overset{\leftrightarrow}{\Box}_y \varphi^{(-)}(y) + i \int d^4y \, G_{+-}(x,y)V'(\phi^{(-)}(y)) - i \int d^4y \, G_{+-}(x,y)\eta(y) = 0 \, . \tag{4.80}$$

Using (4.71), we get the following relations

$$\int d^4y \, G_{++}(x,y) \overset{\leftrightarrow}{\Box}_y \varphi^{(+)}(y) - \int d^4y \, G_{+-}(x,y) \overset{\leftrightarrow}{\Box}_y \varphi^{(-)}(y) = 0$$

$$\int d^4y \, G_{-+}(x,y) \overset{\leftrightarrow}{\Box}_y \varphi^{(+)}(y) - \int d^4y \, G_{--}(x,y) \overset{\leftrightarrow}{\Box}_y \varphi^{(-)}(y) = 0 \, . \tag{4.81}$$

Thanks to the identity

$$A \overset{\leftrightarrow}{\Box} B = \partial_\mu (A \overset{\leftrightarrow}{\partial^\mu} B) \, , \tag{4.82}$$

we obtain

$$\int d^4y \, G_{++}(x,y) \overset{\leftrightarrow}{\Box}_y \varphi^{(+)}(y) = \int d^4y \, \partial^0 (G_{++}(x,y) \overset{\leftrightarrow}{\partial_0} \varphi^{(+)}(y)) + \partial^i (G_{++}(x,y) \overset{\leftrightarrow}{\partial_i} \varphi^{(+)}(y))$$

$$= \int d^3y \left[G_{++}(x,y) \overset{\leftrightarrow}{\partial_0} \varphi^{(+)}(y) \right]^{y_0=+\infty}_{y_0=-\infty} \, , \tag{4.83}$$

where we have assumed that the fields vanish at the spatial boundaries. Doing the same for the other terms, we get

$$0 = \int d^3y \left[G_{++}(x,y) \overset{\leftrightarrow}{\partial_0} \varphi^{(+)}(y) - G_{+-}(x,y) \overset{\leftrightarrow}{\partial_0} \varphi^{(-)}(y) \right]^{y_0=+\infty}_{y_0=-\infty}$$

$$0 = \int d^3y \left[G_{-+}(x,y) \overset{\leftrightarrow}{\partial_0} \varphi^{(+)}(y) - G_{--}(x,y) \overset{\leftrightarrow}{\partial_0} \varphi^{(-)}(y) \right]^{y_0=+\infty}_{y_0=-\infty} \, . \tag{4.84}$$

Writing $\phi^{(\pm)}$ in terms of its Fourier components

$$\varphi^{(\pm)}(y) = \int \frac{d^3p}{2|p|(2\pi)^3} \left(f^{(\pm)}_{-,y_0}(p)e^{-ipy} + f^{(\pm)}_{+,y_0}(p)e^{ipy} \right) \, , \tag{4.85}$$

together with the formula

$$\int d^3y \, e^{i\epsilon p(x-y)} \overset{\leftrightarrow}{\partial_0} e^{i\epsilon'kx} = ie^{i\epsilon px}(\epsilon p_0 + \epsilon' k_0) \int d^3y \, e^{iy(\epsilon'k-\epsilon p)} = 2i|p|\delta_{\epsilon\epsilon'}e^{i\epsilon'kx}(2\pi)^3\delta(|p|-|k|) \, , \tag{4.86}$$

we obtain

$$f^{(\pm)}_{\pm,-\infty}(p) = 0 \qquad\qquad f^{(\pm)}_{\mp,+\infty}(p) = f^{(\mp)}_{\mp,+\infty}(p) \, . \tag{4.87}$$

which means that at $y_0 = +\infty$,

$$\varphi^{(+)} = \varphi^{(-)} \qquad\qquad \dot\varphi^{(+)} = \dot\varphi^{(-)} \, . \tag{4.88}$$

Since $\varphi^{(+)}$ and $\varphi^{(-)}$ satisfy the same EOM and are equal at $y^0 = +\infty$, they are equals everywhere. In addition $f^{(\pm)}_{\pm,-\infty}(p) = 0$ at $y_0 = -\infty$ leads to

$$\varphi^{(+)} = \varphi^{(-)} = \varphi = 0 \qquad\qquad \dot\varphi^{(+)} = \dot\varphi^{(-)} = \dot\varphi = 0. \tag{4.89}$$

We have therefore been able to show that φ obeys to the classical EOM, and we rigorously justified the retarded boundary conditions (meaning that the field φ and its derivative vanish at $-\infty$).

4.2.2 NLO corrections

In this section, we will focus on the computation of the expectation value of the two point function $\left\langle \phi^{(+)} \phi^{(-)}(y) \right\rangle$. This is equal to

$$
\begin{aligned}
\left\langle \phi^{(+)} \phi^{(-)}(y) \right\rangle &= \frac{1}{\overline{\mathcal{Z}}[\eta^{(+)}, \eta^{(-)}]} \frac{\delta^2 \overline{\mathcal{Z}}[\eta^{(+)}, \eta^{(-)}]}{\delta \eta^{(+)}(x) \delta \eta^{(-)}(y)} \Bigg|_{\eta^{(\pm)}=\eta} \\
&= \frac{\delta^2 W[\eta^{(+)}, \eta^{(-)}]}{\delta \eta^{(+)}(x) \delta \eta^{(-)}(y)} \Bigg|_{\eta^{(\pm)}=\eta} + \frac{\delta W[\eta^{(+)}, \eta^{(-)}]}{\delta \eta^{(+)}(x)} \Bigg|_{\eta^{(+)}=\eta} \frac{\delta W[\eta^{(+)}, \eta^{(-)}]}{\delta \eta^{(-)}(y)} \Bigg|_{\eta^{(-)}=\eta}.
\end{aligned}
\tag{4.90}
$$

The last term is just the product of $\left\langle \phi^{(+)} \right\rangle \left\langle \phi^{(-)} \right\rangle$. The first term is the connected two point function $\mathbb{G}_{+-}$, that we now denote $\mathbb{G}$ instead of G not to confound with the free propagator. The computation at LO of $\left\langle \phi^{(+)} \phi^{(-)}(y) \right\rangle$ is straightforward. Given what we did in the previous section, and realizing that $\mathbb{G} \sim 1 + \mathcal{O}(g^2)$, we get

$$
\left\langle \phi^{(+)}(x) \phi^{(-)}(y) \right\rangle_{\text{LO}} = \left\langle \varphi^{(+)}(x) \right\rangle \left\langle \varphi^{(-)}(y) \right\rangle \sim \frac{1}{g^2}.
\tag{4.91}
$$

Calling $\left\langle \varphi^{(\pm)} \right\rangle_{\text{NLO}} = \psi^{(\pm)}$ and $\mathbb{G}^{\text{LO}} = \mathcal{G}$, we therefore need to compute at NLO

$$
\left\langle \phi^{(+)}(x) \phi^{(-)}(y) \right\rangle_{\text{NLO}} = \varphi^{(+)}(x) \psi^{(-)}(y) + \psi^{(+)}(x) \varphi^{(-)}(y) + \mathcal{G}_{+-}(x, y).
\tag{4.92}
$$

Before starting the computation of the different terms in this equation, let's make two formal analysis that will prove to be very useful.

4.2.2.1 Green's formula

In this section, the Green's formula that will appear in many places in this manuscript makes its first appearance. Let's consider the classical field φ that obeys the Klein-Gordon equation, and a propagator G (which could be FEYNMAN, retarded or other depending on the formalism considered) that obeys the usual propagator equation

$$
\Box_y \varphi(y) + V'(\varphi(y)) = 0 \qquad\qquad \Box_x G(x, y) = \Box_y G(x, y) = -i\delta(x - y).
\tag{4.93}
$$

Then, by multiplying the first equation by $G(x, y)$, subtracting to it the second multiplied by $\varphi(y)$ and integrating on a space Ω which admits has one of its boundary a space like surface Σ, the other boundaries being located at infinity, we obtain

$$
\varphi(x) = -i \int_{\Omega} \mathrm{d}^4 y \, G(x, y) \overset{\leftrightarrow}{\Box}_y \varphi(y) - i \int_{\Omega} \mathrm{d}^4 y \, G(x, y) V'(\varphi(y)).
\tag{4.94}
$$

Using again the identity (4.82), and recalling the fact that the integral of a divergence is 0 we get

$$
\varphi(x) = -i \int_{\Sigma} \mathrm{d}^3 \Sigma_y \, G(x, y) \left(n . \overset{\leftrightarrow}{\partial}_y \varphi(y) \right) - i \int_{\Omega} \mathrm{d}^4 y \, G(x, y) V'(\varphi(y))
\tag{4.95}
$$

where n^μ is a unitary vector normal to Σ and $\mathrm{d}\Sigma_y$ the measure on Σ. This is the announced Green's formula. By expanding in powers of the coupling constant g (which plays a role through the second term that contains $V'(\varphi)$), it allows to express $\varphi(x)$ at any space-time point in the domain Ω as a function of the value of φ on the surface Σ. As we will see later, this surface will play the role of the initial time of the numerical computation ($x^0 = 0$ in Minkowskian coordinate system and $Q_s \tau_0 \ll 1$ in the proper-time rapidity coordinate system).

4.2.2.2 Small perturbations as a differential operator action on Σ

In this section, we will use the fact that given a first order differential operator $\widehat{L}$ acting on φ, we have

$$\widehat{L}f(\varphi) = f'(\varphi)\widehat{L}\varphi \, . \tag{4.96}$$

Starting from (4.95) and taking $a = \widehat{L}\varphi$ we can then deduce

$$a(x) = -i\int_\Omega d^4y\, G(x,y)V''(\varphi(y))a(y) - i\int_\Sigma d\Sigma_y\, d^3\Sigma_y\, G(x,y)(n.\overset{\leftrightarrow}{\partial_y})a(y), \tag{4.97}$$

We thus have that a satisfies the following EOM and boundary conditions

$$\left[\Box_x + V''(\varphi(x))\right]a(x) = 0 \qquad\qquad a, (n.\partial)a \text{ known on } \Sigma \, , \tag{4.98}$$

provided that $\widehat{L}$ is defined as

$$\widehat{L} = \int_\Sigma d\Sigma_z \left[a(z)\frac{\delta}{\delta\varphi(z)} + (n.\partial_z)a(z)\frac{\delta}{\delta(n.\partial_z)\varphi(z)} \right] \, . \tag{4.99}$$

As a last remark, let us notice that taking an a as we did is equivalent to study a small perturbation a on top of a background field φ. Calling $\phi = \varphi + a$, $a \ll \varphi$ and φ, ϕ satisfying the classical EOM, we have

$$0 = \Box\phi + V'(\phi) = \Box\varphi + \Box a + V'(\varphi) + aV''(\varphi) + \mathcal{O}(a^2) = \Box a + aV''(\varphi) + \mathcal{O}(a^2) \, , \tag{4.100}$$

which as announced is equivalent to the linear EOM (4.98).

4.2.2.3 Propagator at LO

We start our NLO computation with the study of $\frac{\delta^2 W}{\delta\eta^{(+)}(x)\delta\eta^{(-)}(y)}$. To calculate it, one has to consider the following tree diagrams (where the last diagram is just one example taken in the infinite set of contributing diagrams)

$$\mathcal{G}_{+-}(x,y) = x\overset{+}{=\!=\!=\!=\!=}\overset{-}{y} \; = \; x^+ \underset{\text{(tree diagram)}}{\underline{\hspace{4cm}}} \,^-y \tag{4.101}$$

Diagrammatically, we can also write the following (exact) equations

$$\mathcal{G}_{+-}(x,y) = x\overset{+}{=\!=\!=\!=\!=}\overset{-}{y} \; = \; x^+\underset{z}{\underline{\hspace{2cm}}}\,^-y \; - \; x^+\underset{z}{\underline{\hspace{2cm}}}\,^-y \tag{4.102}$$

$$= \; x\overset{+}{=\!=\!=}\underset{z}{\underline{\hspace{2cm}}}\,^-y \; - \; x\overset{+}{=\!=\!=}\underset{z}{\underline{\hspace{2cm}}}\,^-y \, . \tag{4.103}$$

Considering the first expression

$$\mathcal{G}_{+-}(x,y) = \int d^4z\,(-iV''(\varphi(z)))\,(G_{++}(x,z)\mathcal{G}_{+-}(z,y) - G_{+-}(x,z)\mathcal{G}_{--}(z,y)) \, , \tag{4.104}$$

and taking the d'Alembertian with respect to x, we obtain

$$\Box_x\mathcal{G}_{+-}(x,y) = -V''(\varphi(x))\mathcal{G}_{+-}(x,y) \, . \tag{4.105}$$

By analogy, for the second expression

$$\Box_y \mathcal{G}_{+-}(x,y) = - V''(\varphi(y))\mathcal{G}_{+-}(x,y) \,. \tag{4.106}$$

Let's recall here that when $x_0, y_0 \mapsto -\infty$, we have

$$\mathcal{G}_{+-}(x,y) = G_{+-}(x,y) \,. \tag{4.107}$$

Knowing in addition that in the free case, we can write (v stands for vacuum)

$$G_{+-}(x,y) = \int \frac{d^3 k}{2|k|(2\pi)^3} a^v_{+k}(x) a^v_{-k}(y), \tag{4.108}$$

with

$$\Box a^v_{\pm k}(x) = 0 \,, \qquad \lim_{x_0 \mapsto -\infty} a^v_{\pm k}(x) = e^{\pm ikx} \,, \qquad \lim_{x_0 \mapsto -\infty} \dot{a}^v_{\pm k}(x) = \pm i|k| e^{\pm ikx} \,, \tag{4.109}$$

then it is easy to extend this form to the interacting case

$$\mathcal{G}_{+-}(x,y) = \int \frac{d^3 k}{2|k|(2\pi)^3} a_{+k}(x) a_{-k}(y) \,, \tag{4.110}$$

with

$$\left[(\Box + V''(\varphi(x))) \right] a_{\pm k}(x) = 0 \,, \quad \lim_{x_0 \mapsto -\infty} a^v_{\pm k}(x) = e^{\pm ikx} \,, \quad \lim_{x_0 \mapsto -\infty} \dot{a}^v_{\pm k}(x) = \pm i|k| e^{\pm ikx} \,. \tag{4.111}$$

Now, given what we saw in section 4.2.2.2, this implies that if we call

$$a_{\pm k}(u)\widehat{T}(u) = a_{\pm k}(u)\frac{\delta}{\delta\varphi(u)} + (n.\partial_z)a_{\pm k}(u)\frac{\delta}{\delta(n.\partial_u)\varphi(u)} \,, \tag{4.112}$$

then at lowest order, because

$$a_{\pm k}(x) = \widehat{L}_{\pm k}\varphi(x) = \int_\Sigma d\Sigma_u \left[a_{\pm k}(u)\widehat{T}(u) \right] \varphi(x) \,, \tag{4.113}$$

we have

$$\mathcal{G}_{+-}(x,y) = - \int \frac{d^3 k}{2|k|(2\pi)^3} \int_{bm\Sigma} d\Sigma \, d\Sigma \, \left(\left[a_{+k}(u)\widehat{T}(u) \right] \varphi(x) \right) \left(\left[a_{-k}(v)\widehat{T}(v) \right] \varphi(y) \right) \,, \tag{4.114}$$

and the same holds for $\mathcal{G}_{-+}$.

4.2.2.4 Expectation value of the field at NLO

We now want to calculate $\psi^{(\pm)}$. For this, one has to consider the following diagrammatic (exact) equations

$$\psi^{(+)}(x) = \quad x \stackrel{+}{=\!=\!=} \stackrel{\epsilon}{\bigcirc} z \qquad\qquad \psi^{(-)}(x) = \quad x \stackrel{-}{=\!=\!=} \stackrel{\epsilon}{\bigcirc} z \tag{4.115}$$

Not forgetting the $\frac{1}{2}$ symmetric factor, we have

$$\psi^{(+)}(x) = \sum_{\epsilon=\pm} \epsilon \int d^4 z \, \mathcal{G}_{+\epsilon}(x,z) \left[-\frac{i}{2}V'''(\varphi(z)) \right] \mathcal{G}_{\epsilon\epsilon}(z,z), \tag{4.116}$$

and a similar formula holds for $\psi^{(-)}(x)$, with

$$\mathcal{G}_{++}(x,y) = \theta(x_0 - y_0)\mathcal{G}_{-+}(x,y) + \theta(y_0 - x_0)\mathcal{G}_{+-}(x,y)$$
$$\mathcal{G}_{--}(x,y) = \theta(x_0 - y_0)\mathcal{G}_{+-}(x,y) + \theta(y_0 - x_0)\mathcal{G}_{-+}(x,y) \,, \qquad (4.117)$$

We can notice that

$$\mathcal{G}_{++}(z,z) = \mathcal{G}_{--}(z,z) = \mathcal{G}_{-+}(z,z) = \mathcal{G}_{+-}(z,z) = \int \frac{\mathrm{d}^3 k}{2|k|(2\pi)^3} a_{+k}(z)a_{-k}(z) \,, \qquad (4.118)$$

and therefore

$$\psi(x) = \psi^{(+)}(x) = \psi^{(-)}(x) = \int \mathrm{d}^4 z \left[-\frac{i}{2}V'''(\varphi(z)) \right] \mathcal{G}_R(x,z)\mathcal{G}_{++}(z,z) \qquad (4.119)$$

$$= \int \mathrm{d}^4 z \int \frac{\mathrm{d}^3 k}{2|k|(2\pi)^3} \left[-\frac{i}{2}V'''(\varphi(z)) \right] \mathcal{G}_R(x,z)a_{+k}(z)a_{-k}(z) \,. \qquad (4.120)$$

Knowing that

$$\left[\Box_x + V''(\varphi(x)) \right] \mathcal{G}_R(x,y) = -i\delta(x-y) \,, \qquad (4.121)$$

we have

$$\left[\Box_x + V''(\varphi(x)) \right] \psi = -\frac{V'''(\varphi(x))}{2} \int \frac{\mathrm{d}^3 k}{2|k|(2\pi)^3} a_{+k}(x)a_{-k}(x) = \sigma(x)$$
$$\lim_{x_0 \mapsto -\infty} \psi, \dot{\psi} = 0 \,, \qquad (4.122)$$

Where the boundary conditions follow from the presence of a retarded propagator. We will try to find a new Green's formula to help us. Since

$$\mathcal{G}_R(x,y) \left(\overleftarrow{\Box}_y + V''(\varphi)(y) \right) \psi(y) = -i\delta(x-y)\psi(y)$$
$$\mathcal{G}_R(x,y) \left(\overrightarrow{\Box}_y + V''(\varphi)(y) \right) \psi(y) = \mathcal{G}_R(x,y)\sigma(y) \,. \qquad (4.123)$$

We can deduce

$$\psi(x) = \underbrace{i \int_\Omega \mathrm{d}^4 y \, \mathcal{G}_R(x,y)\sigma(y)}_{\psi_1(x)} \underbrace{-i \int_\Sigma \mathrm{d}\Sigma_u \, \mathcal{G}_R(x,y)(n.\overleftrightarrow{\partial_u})\psi(y)}_{\psi_2(x)} \,. \qquad (4.124)$$

Concerning ψ_2, since x does not belong to Σ, we have

$$\left[\Box + V''(\varphi(x)) \right] \psi_2(x) = 0 \qquad\qquad \lim_{x \in \Sigma} \psi_2(x) = \psi(x) \,, \qquad (4.125)$$

and we can use the results of section 4.2.2.2, from which we obtain

$$\psi_2(x) = i \int_\Sigma \mathrm{d}\Sigma_u \left(\psi(u)\widehat{T}(u) \right) \varphi(x) \,. \qquad (4.126)$$

Concerning ψ_1

$$\left[\Box + V''(\varphi(x)) \right] \psi_1(x) = \sigma(x) \qquad\qquad \lim_{x \in \Sigma} \psi_1(x) = 0 \,. \qquad (4.127)$$

It will be useful to write another Green's formula for ψ_1, but now with the free propagator $G_R(x,y)$. Since

$$\Box_y G_R(x,y) = -i\delta(x-y) \,, \qquad (4.128)$$

we have that

$$\psi_1(x) = -i \int_\Omega d^4y\, G_R(x,y)\left(V''(\varphi(y))\psi_1(y) - \sigma(y)\right) - i \int_\Sigma d\Sigma_u\, G_R(x,y)(n.\overset{\leftrightarrow}{\partial_u})\psi_1(y)\,,$$

(4.129)

and the second term is 0, since ψ_1 is the part of ψ that does not belong to Σ. Considering the operator $\widehat{D} = \int_\Sigma d\Sigma_v \left[a_{-k}(v)\widehat{T}(v)\right]$ acting on a_{+k}, we thus have (still using the results of section 4.2.2.2)

$$\widehat{D}a_{+k}(x) = -i \int_\Omega d^4y\, G_R(x,y)\widehat{D}\left[V''(\varphi(y))a_{+k}(y)\right] - i \int_\Sigma d\Sigma_u\, G_R(x,u)(n.\overset{\leftrightarrow}{\partial_u})\widehat{D}a_{+k}(u)$$

$$= -i \int_\Omega d^4y\, G_R(x,y)\left[V'''(\varphi(y))\left[\widehat{D}\varphi(y)\right]a_{+k}(y) + V''(\varphi(y))\widehat{D}a_{+k}(y)\right]\,. \quad (4.130)$$

On the first line, the action of $\widehat{D}$ on $a_{+k}(y)$ with $y \in \Sigma$ gives 0 because this boundary term does not depend on the value of the classical field φ. Finally, calling

$$\xi(x) = -\frac{1}{2}\int \frac{d^3k}{2|k|(2\pi)^3}\iint d\Sigma_u\, d\Sigma_v\left[\left(a_{+k}(u)\widehat{T}(u)\right)\left(a_{-k}(v)\widehat{T}(v)\right)\varphi(x)\right]\,,$$

(4.131)

we will prove that $\xi(x) = \psi_1(x)$. First

$$\xi(x) = \frac{i}{2}\int \frac{d^3k}{2|k|(2\pi)^3}\int_\Sigma d\Sigma_v\left(a_{-k}(v)\widehat{T}(v)\right)a_{+k}(x) = \frac{i}{2}\int \frac{d^3k}{2|k|(2\pi)^3}\widehat{D}a_{+k}(x)\,, \quad (4.132)$$

and given (4.130) we can write

$$\xi(x) = \frac{1}{2}\int \frac{d^3k}{2|k|(2\pi)^3}\int_\Omega d^4y\, G_R(x,y)\left[V'''(\varphi(y))\left[\widehat{D}\varphi(y)\right]a_{+k}(y) + V''(\varphi(y))\widehat{D}a_{+k}(y)\right]$$

$$= \frac{-i}{2}\int \frac{d^3k}{2|k|(2\pi)^3}\int_\Omega d^4y\, G_R(x,y)V'''(\varphi(y))a_{-k}(y)a_{+k}(y) - i\int_\Omega d^4y\, G_R(x,y)V''(\varphi(y))\xi(y)$$

$$= -i\int_\Omega d^4y\, G_R(x,y)\left(V''(\varphi(y))\xi(y) - \sigma(y)\right)\,, \quad (4.133)$$

which is the same equation than for ψ_1. In addition, because $\xi(y) = 0$ if $y \in \Sigma$. We can therefore deduce $\xi = \psi_1$. We thus have

$$\psi(x) = \int_\Sigma d\Sigma_u\left[i\left(\psi(u)\widehat{T}(u)\right) - \frac{1}{2}\int \frac{d^3k}{2|k|(2\pi)^3}\int d\Sigma_v\left[\left(a_{+k}(u)\widehat{T}(u)\right)\left(a_{-k}(v)\widehat{T}(v)\right)\right]\right]\varphi(x)\,.$$

(4.134)

4.2.2.5 Full Next To Leading Order for the two point function

Let us notice here that result of section 4.2.2.3

$$\mathcal{G}_{+-}(x,y) = \left.\frac{\delta^2 W\left[\eta^{(+)},\eta^{(-)}\right]}{\delta\eta^{(+)}(x)\delta\eta^{(-)}(y)}\right|^{LO}_{\eta^\pm=0}$$

$$= -\int \frac{d^3k}{2|k|(2\pi)^3}\iint_\Sigma d\Sigma_u\, d\Sigma_v\left[\left[a_{+k}(u)\widehat{T}(u)\right]\varphi(x)\right]\left[\left[a_{-k}(v)\widehat{T}(v)\right]\varphi(y)\right]\,,$$

(4.135)

can be rewritten as

$$\mathcal{G}_{+-}(x,y) = -\frac{1}{2}\int \frac{d^3k}{2|k|(2\pi)^3}\iint_\Sigma d\Sigma_u\, d\Sigma_v\left(\left[\left[a_{+k}(u)\widehat{T}(u)\right]\varphi(x)\right]\left[\left[a_{-k}(v)\widehat{T}(v)\right]\varphi(y)\right]\right.$$

$$\left. + \left[\left[a_{-k}(u)\widehat{T}(u)\right]\varphi(x)\right]\left[\left[a_{+k}(v)\widehat{T}(v)\right]\varphi(y)\right]\right)\,.$$

(4.136)

Starting back from (4.92), we write for the part the does not involve $\mathcal{G}$

$$\left(\left\langle \phi^{(+)}(x) \right\rangle \left\langle \phi^{(-)}(y) \right\rangle \right)_{\text{NLO}} = \frac{\delta W[\eta^{(+)}, \eta^{(-)}]}{\delta \eta^{(+)}(x)} \bigg|_{\eta^{(+)}=0} \frac{\delta W[\eta^{(+)}, \eta^{(-)}]}{\delta \eta^{(-)}(y)} \bigg|_{\eta^{(-)}=0}$$

$$= \psi_1(x)\varphi(y) + \varphi(x)\psi_1(y) + \psi_2(x)\varphi(y) + \varphi(x)\psi_2(y) . \quad (4.137)$$

Since

$$A = \psi_2(x)\varphi(y) + \varphi(x)\psi_2(y) = i \int_\Sigma d\Sigma_u \left[\left(\psi(u)\widehat{T}(u) \right) \right] \varphi(x)\varphi(y) , \quad (4.138)$$

and

$$B = \psi_1(x)\varphi(y) + \varphi(x)\psi_1(y) + \mathcal{G}_{+-}(x,y)$$

$$= -\frac{1}{2} \int \frac{d^3 k}{2|k|(2\pi)^3} \iint d\Sigma_u \, d\Sigma_v \left(\left[a_{+k}(u)\widehat{T}(u) \right] \left[a_{-k}(v)\widehat{T}(v) \right] \right) \varphi(x)\varphi(y) . \quad (4.139)$$

we can rewrite the full NLO as

$$\left\langle \phi^{(+)}(x)\phi^{(-)}(y) \right\rangle_{\text{NLO}} = \left[i \int_\Sigma d\Sigma_u \left(\psi(u)\widehat{T}(u) \right) - \frac{1}{2} \int \frac{d^3 k}{2|k|(2\pi)^3} \right.$$

$$\left. \iint d\Sigma_u \, d\Sigma_v \left[a_{+k}(u)\widehat{T}(u) \right] \left[a_{-k}(v)\widehat{T}(v) \right] \right] \varphi(x)\varphi(y) . \quad (4.140)$$

4.2.3   Resummation

Let us summarize what we have seen so far. At LO

$$\left\langle \phi^{(+)}(x)\phi^{(-)}(y) \right\rangle_{\text{LO}} = \varphi(x)\varphi(y) , \quad (4.141)$$

where

$$\left[\Box + V'(\varphi(x)) \right] \varphi(x) = 0 , \qquad \lim_{x_0 \mapsto -\infty} \varphi, \dot{\varphi} = 0 . \quad (4.142)$$

At NLO, calling

$$\widehat{O} = \left[i \int_\Sigma d\Sigma_u \left(\psi(u)\widehat{T}(u) \right) - \frac{1}{2} \int \frac{d^3 k}{2|k|(2\pi)^3} \iint d\Sigma_u \, d\Sigma_v \left[a_{+k}(u)\widehat{T}(u) \right] \left[a_{-k}(v)\widehat{T}(v) \right] \right] , \quad (4.143)$$

we have

$$\left\langle \phi^{(+)}(x)\phi^{(-)}(y) \right\rangle_{\text{NLO}} = \widehat{O}\varphi(x)\varphi(y) = \widehat{O} \left\langle \phi^{(+)}(x)\phi^{(-)}(y) \right\rangle_{\text{LO}} . \quad (4.144)$$

Considering the quantity

$$\left\langle \phi^{(+)}(x)\phi^{(-)}(y) \right\rangle_{\text{resum}} = \sum_{n=0}^\infty \frac{\widehat{O}^n}{n!} \left\langle \phi^{(+)}(x)\phi^{(-)}(y) \right\rangle_{\text{LO}} = e^{\widehat{O}} \left\langle \phi^{(+)}(x)\phi^{(-)}(y) \right\rangle_{\text{LO}} , \quad (4.145)$$

we trivially see by Taylor expanding the exponential that it fully contains the LO and the NLO of $\left\langle \varphi^{(+)}(x)\varphi^{(-)}(y) \right\rangle$, but also a subset of every higher order corrections. The analogous formulas for $T^{\mu\nu}$ and f_k, respectively the energy-momentum tensor and the occupation number of the scalar theory, to be defined later in chapter 5, will be the formulas of crucial importance. Splitting $\widehat{O}$ into a linear and quadratic part in $\widehat{T}$

$$\widehat{O}_1 = i \int_\Sigma d\Sigma_u \left(\psi(u)\widehat{T}(u) \right)$$

$$\widehat{O}_2 = -\frac{1}{2} \int \frac{d^3 k}{2|k|(2\pi)^3} \iint d\Sigma_u \, d\Sigma_v \left[a_{+k}(u)\widehat{T}(u) \right] \left[a_{-k}(v)\widehat{T}(v) \right] , \quad (4.146)$$

we will re-express (4.145) in a less formal way. First, since

$$e^{a\partial_x} f(x) = f(x+a) \, ,\tag{4.147}$$

we have

$$e^{\hat{O}_1} \left\langle \phi^{(+)}(x) \right\rangle_{LO} = \varphi(x) + \psi(x) \, .\tag{4.148}$$

Secondly, by performing the equivalent of a Fourier transform of $e^{\hat{O}_2}$ that we can formally see as a Gaussian $e^{-\frac{\alpha x^2}{2}}$ in the variable $x = \hat{T}$, with $\alpha = \int \frac{d^3 k}{2|\boldsymbol{k}|(2\pi)^3} a_{+k} a_{-k} = \mathcal{G}_{+-}$, we can re-express [4]

$$\widetilde{e^{-\frac{kx^2}{2}}}(b) = \int dx e^{ibx} e^{-\frac{b^2}{2k}} \, ,\tag{4.149}$$

and therefore, in our case this gives

$$\widetilde{e^{\hat{O}_2}} = \int [\mathcal{D} a] \, e^{i \int_\Sigma d\Sigma_u \, a(u) \hat{T}(u)} e^{-\frac{1}{2} \int\int d\Sigma_u \, d\Sigma_v a(u) \mathcal{G}_{+-}^{-1}(u,v) a(v)} \, ,\tag{4.150}$$

and calling [5] $F[\varphi_{\text{in}}] = \left\langle \phi^{(+)}(x)\phi^{(-)}(y) \right\rangle_{LO}$ one can finally write the central result of this section

$$\boxed{e^{\hat{O}} F[\varphi_{\text{in}}] = \int [\mathcal{D} a] \, e^{-\frac{1}{2} \int\int d\Sigma_u \, d\Sigma_v a(u) \mathcal{G}_{+-}^{-1}(u,v) a(v)} F[\varphi + a + \psi]}\tag{4.151}$$

This result allows us to evaluate in a relatively simple way The $\left\langle \phi^{(+)}(x)\phi^{(-)}(y) \right\rangle_{\text{resum}}$. This formula is equivalent to the classical-statistical approximation.

4.3 The Classical-statistical approximation: a path integral approach

The final formula of the previous section is useful when it comes to numerical computations, but it is difficult so see diagrammatically what it contains. We already know that it corresponds to a resummation for inclusive observables that fully includes the LO, the NLO and a subset of higher order corrections. But to what kind of truncation does it correspond to? To answer this question, let us consider the SCHWINGER-KELDYSH Lagrangean of a scalar field with a strong physical source ($\eta^{(+)} = \eta^{(-)} = \eta$)

$$\begin{aligned}
\mathcal{L}[\phi^{(+)}, \phi^{(-)}] &= \mathcal{L}[\phi^{(+)}] - \mathcal{L}[\phi^{(-)}] \\
&= \left[\frac{1}{2} \left(\partial_\mu \phi^{(+)} \right) \left(\partial^\mu \phi^{(+)} \right) - \frac{m^2}{2} \left(\phi^{(+)} \right)^2 - \frac{g^2}{4!} \left(\phi^{(+)} \right)^4 + \eta \phi^{(+)} \right] \\
&\quad - \left[\frac{1}{2} \left(\partial_\mu \phi^{(-)} \right) \left(\partial^\mu \phi^{(-)} \right) - \frac{m^2}{2} \left(\phi^{(-)} \right)^2 - \frac{g^2}{4!} \left(\phi^{(-)} \right)^4 + \eta \phi^{(-)} \right] \, .
\end{aligned}\tag{4.152}$$

The expectation value of some local observable $\mathcal{O}(\phi(x))$ can be expressed as a path integral in the SCHWINGER-KELDYSH formalism

$$\begin{aligned}
\langle \mathcal{O}(\phi(x)) \rangle = &\int \left[D\phi_i^{(+)}(x) \right] \left[D\phi_i^{(-)}(x) \right] \rho \left[\phi_i^{(+)}(x), \phi_i^{(-)}(x) \right] \\
&\times \int_{\phi^{(\pm)}(x_i^0,\boldsymbol{x})=\phi_i^{(\pm)}(\boldsymbol{x})} \left[D\phi^{(+)}(x) \right] \left[D\phi^{(-)}(x) \right] e^{i \int_{x_i^0}^{x^0} \mathcal{L}[\phi^{(+)},\phi^{(-)}]} \mathcal{O}(\phi^{(+)}(x)) \, .
\end{aligned}\tag{4.153}$$

---

4. The Fourier transform of a Gaussian $f(x) = e^{-\frac{\alpha x^2}{2}}$ being a Gaussian $\tilde{f}(p) = e^{-\frac{p^2}{2\alpha}}$.
5. The in standing for the fact that F only depends on the initial value of φ on the surface Σ.

Here several clarifications are in order. Firstly, $\rho\left[\phi_i^{(+)}(x), \phi_i^{(-)}(x)\right]$ is the initial density operator, that characterizes the system at the initial time x_0^i. Secondly, the upper time boundary for the integration on the Lagrangean is x^0 and not $+\infty$ because of causality: a measurement done at the time x^0 cannot depend on the future. To go further, we can introduce new fields that are respectively the half sum and the difference of the $\pm$ fields

$$\varphi(x) = \frac{\phi^{(+)}(x) + \phi^{(-)}(x)}{2}, \qquad\qquad \sigma(x) = \phi^{(+)}(x) - \phi^{(-)}(x). \qquad (4.154)$$

The fields correspond to different paths in the amplitude and in the complex conjugate [6]. Since at the classical level the system follows a deterministic trajectory (the one that minimizes the action), it means that at the classical level $\phi^{(+)}(x) = \phi^{(-)}(x) = \varphi(x)$. We had already seen this in the section 4.2.1. This means that in the classical limit $\sigma = 0$. With that in mind, we rewrite the Lagrangean (4.152) in terms of the φ and σ fields

$$\mathcal{L}[\varphi, \sigma] = (\partial_\mu \varphi)(\partial^\mu \sigma) - m^2 \varphi\sigma - \frac{g^2}{3!}\varphi^3\sigma - \frac{g^2}{4!}\varphi\sigma^3 + \eta\sigma. \qquad (4.155)$$

Here all the terms are linear in σ except the term $\frac{g^2}{4!}\varphi\sigma^3$. **The classical-statistical approximation consists in discarding the $\frac{g^2}{4!}\varphi\sigma^3$ vertex [59–64].** Let us define

$$\mathcal{L}_{\text{CSA}}[\varphi, \sigma] = (\partial_\mu \varphi)(\partial^\mu \sigma) - m^2 \varphi\sigma - \frac{g^2}{3!}\varphi^3\sigma + \eta\sigma. \qquad (4.156)$$

To see the consequences of this approximation, it is simpler to deal with a Hamiltonian formulation of the problem. To do so, we introduce the conjugate momenta $\pi^{(\pm)}$ of the fields, so that

$$\mathcal{L}[\phi^{(+)}, \pi^{(+)}] = \frac{1}{2}\pi^{(+)}\dot\phi^{(+)} - \frac{1}{2}\left(\nabla\phi^{(+)}\right)\left(\nabla\phi^{(+)}\right) - \frac{m^2}{2}\left(\phi^{(+)}\right)^2 - \frac{g^2}{4!}\left(\phi^{(+)}\right)^4 + \eta\phi^{(+)}$$

$$\mathcal{H}[\phi^{(+)}, \pi^{(+)}] = \phi^{(+)}\pi^{(+)} - \mathcal{L}[\phi^{(+)}, \pi^{(+)}]$$

$$= \frac{1}{2}\pi^{(+)}\dot\phi^{(+)} + \frac{1}{2}\left(\nabla\phi^{(+)}\right)\left(\nabla\phi^{(+)}\right) + \frac{m^2}{2}\left(\phi^{(+)}\right)^2 + \frac{g^2}{4!}\left(\phi^{(+)}\right)^4 - \eta\phi^{(+)}$$

$$(4.157)$$

and in addition

$$\mathcal{L}[\phi^{(\pm)}, \pi^{(\pm)}] = \mathcal{L}[\phi^{(+)}, \pi^{(+)}] - \mathcal{L}[\phi^{(-)}, \pi^{(-)}]$$

$$\mathcal{H}[\phi^{(\pm)}, \pi^{(\pm)}] = \pi^{(+)}\dot\phi^{(+)} - \pi^{(-)}\dot\phi^{(-)} - \mathcal{L}[\phi^{(\pm)}, \pi^{(\pm)}]. \qquad (4.158)$$

In the φ, σ basis, we define

$$\pi_\varphi = \frac{\pi^{(+)} + \pi^{(-)}}{2}, \qquad\qquad \pi_\sigma = \pi^{(+)} - \pi^{(-)}. \qquad (4.159)$$

This leads to

$$\mathcal{L}_{\text{CSA}}[\varphi, \pi_\varphi, \sigma, \pi_\sigma] = \pi_\sigma\dot\varphi + \pi_\varphi\dot\sigma - \pi_\sigma\pi_\varphi - (\nabla\varphi)(\nabla\sigma) - m^2\varphi\sigma - \frac{g^2}{3!}\varphi^3\sigma + \eta\sigma. \qquad (4.160)$$

First rewriting (4.153) as

$$\langle\mathcal{O}(\phi(x))\rangle = \int\left[D\phi_i^{(+)}(x)\right]\left[D\phi_i^{(-)}(x)\right]\rho\left[\phi_i^{(+)}(x), \phi_i^{(-)}(x)\right]\int_{\phi^{(\pm)}(x_i^0, x) = \phi_i^{(\pm)}(x)}\left[D\phi^{(+)}(x)\right]\left[D\phi^{(-)}(x)\right]$$

$$\times\left[D\pi^{(+)}(x)\right]\left[D\pi^{(-)}(x)\right]e^{i\int_{x_i^0}^{x^0}\mathcal{L}_{\text{CSA}}[\phi^{(\pm)}, \pi^{(\pm)}]}\mathcal{O}(\phi^{(+)}(x)), \qquad (4.161)$$

---

6. Here it is instructive to recall the equivalence between the SCHWINGER-KELDYSH generating functional and the product of two FEYNMAN ones.

we obtain

$$\langle \mathcal{O}(\phi(x)) \rangle = \int [D\varphi_i(x)]\,[D\sigma_i(x)]\,\rho\left[\varphi_i(x) + \frac{\sigma_i(x)}{2}, \varphi_i(x) - \frac{\sigma_i(x)}{2}\right] \int_{\substack{\varphi(x_i^0,x)=\varphi_i(x)\\ \sigma(x_i^0,x)=\sigma_i(x)}} [D\varphi(x)]\,[D\sigma(x)]$$

$$\times\, [D\pi_\varphi(x)]\,[D\pi_\sigma(x)]\, e^{i\int_{x_i^0}^{x^0}\sigma\left(\pi_\sigma\dot\varphi + \pi_\varphi\dot\sigma - \pi_\sigma\pi_\varphi - (\nabla\varphi)(\nabla\sigma) - m^2\varphi\sigma - \frac{g^2}{3!}\varphi^3\sigma + \eta\sigma\right)}\,\mathcal{O}(\varphi(x))\,. \tag{4.162}$$

To go further, we need to re-express the terms

$$\int_{x_i^0}^{x^0} d^4x\,\left[\pi_\varphi(x)\dot\sigma(x) - (\nabla\varphi(x))(\nabla\sigma(x))\right]\,. \tag{4.163}$$

For the first one, an integration by part gives

$$\int_{x_i^0}^{x^0} d^4x\,\pi_\varphi(x)\dot\sigma(x) = -\int_{x_i^0}^{x^0} d^4x\,\dot\pi_\varphi(x)\sigma(x) + \int d^3x\,\pi_{\varphi,i}(x)\sigma_i(x)\,. \tag{4.164}$$

For the second term, one uses the fact that

$$-(\nabla\varphi(x))(\nabla\sigma(x)) = -\nabla\left[\sigma(x)\nabla\varphi(x)\right] + \sigma(x)\Delta\varphi(x)\,. \tag{4.165}$$

The first term being a total derivative, it vanishes after the spatial $\int d^3x$ integration. We are left with

$$\langle \mathcal{O}(\phi(x)) \rangle = \int [D\varphi_i(x)]\,[D\sigma_i(x)]\,\rho\left[\varphi_i(x) + \frac{\sigma_i(x)}{2}, \varphi_i(x) - \frac{\sigma_i(x)}{2}\right] e^{i\int d^3x\,\sigma_i(x)\pi_{\varphi,i}(x)} \int_{\substack{\varphi(x_i^0,x)=\varphi_i(x)\\ \sigma(x_i^0,x)=\sigma_i(x)}} [D\varphi(x)]$$

$$\times\, [D\sigma(x)]\,[D\pi_\varphi(x)]\,[D\pi_\sigma(x)]\, e^{i\int_{x_i^0}^{x^0}\sigma\left(-\dot\pi_\varphi + \Delta\varphi - m^2\varphi - \frac{g^2}{3!}\varphi^3 - \eta\right)}\, e^{i\int_{x_i^0}^{x^0}\pi_\sigma(\dot\varphi - \pi_\varphi)}\,\mathcal{O}(\varphi(x))\,. \tag{4.166}$$

Now one can easily do the functional integrations on σ (this would not have been true if we had kept the $\varphi\sigma^3$ vertex) and on π_σ

$$\int [D\pi_\sigma(x)]\, e^{i\int_{x_i^0}^{x^0}\pi_\sigma(\dot\varphi - \pi_\varphi)} = \delta\left(\dot\varphi - \pi_\varphi\right)$$

$$\int [D\sigma(x)]\, e^{i\int_{x_i^0}^{x^0}\sigma\left(-\Box\varphi + m^2\varphi + \frac{g^2}{3!}\varphi^3 + \eta\right)} = \delta\left(\dot\pi_\varphi - \Delta\varphi + m^2\varphi + \frac{g^2}{3!}\varphi^3 - \eta\right)\,. \tag{4.167}$$

One can also recognize the Wigner distribution [143, 144] of the ρ density operator

$$W\left[\varphi_i, \pi_{\varphi,i}\right] = \int [D\sigma_i(x)]\,\rho\left[\varphi_i(x) + \frac{\sigma_i(x)}{2}, \varphi_i(x) - \frac{\sigma_i(x)}{2}\right] e^{i\int d^3x\,\sigma_i(x)\pi_{\varphi,i}(x)}\,, \tag{4.168}$$

so that (4.152) can finally be rewritten as

$$\langle \mathcal{O}(\phi(x)) \rangle_{\mathrm{CSA}} = \int [D\varphi_i(x)]\,[D\pi_{\varphi,i}(x)]\, W\left[\varphi_i, \pi_{\varphi,i}\right] \times$$

$$\int_{\substack{\varphi(x_i^0,x)=\varphi_i(x)\\ \pi_{\varphi,i}(x_i^0,x)=\pi_{\varphi,i}(x)}} [D\varphi(x)]\,[D\pi_\varphi(x)]\,\delta\left(\dot\varphi - \pi_\varphi\right)\delta\left(\dot\pi_\varphi - \Delta\varphi + m^2\varphi + \frac{g^2}{3!}\varphi^3 - \eta\right)\mathcal{O}(\varphi(x))\,. \tag{4.169}$$

The meaning of this formula is the following: starting from an initial state characterized by the Wigner distribution $W\left[\varphi_i, \pi_{\varphi,i}\right]$, the system evolves with the classical equation of motion

until the time at which the physical observable $\mathcal{O}$ is evaluated. Schematically, one therefore has

$$\boxed{\langle \mathcal{O}(\phi(x)) \rangle_{\text{CSA}} = \text{quantum initial condition} \times \text{classical evolution}}$$

(4.170)

This is the equivalent to the formula (4.151) except that in (4.151) the variance of the initial Gaussian distribution was known in terms of the spectrum of fluctuations a_k of (4.111). Here, this would correspond to a Gaussian Wigner distribution [145]. This has the precise meaning in quantum mechanics that the initial state is a coherent state. A coherent state is an eigenvector of the creation operator of the free Hamiltonian, but it can also be viewed as a quantum state centered around a classical value with the minimal variance allowed by Heisenberg's uncertainty principle. A coherent state is however not an eigenvector of the interacting Hamiltonian, and letting the system evolve with the classical non linear equation of motion will lead this initial state to decohere (see the sections 5.3.5.3-5.3.5.4). We have just explained the last physical building block that will prove useful when it comes to understand the outcome of the CSA simulations performed in the chapters 5, 6 and 9. The following figures illustrate what the CSA is, can do and what it cannot do.
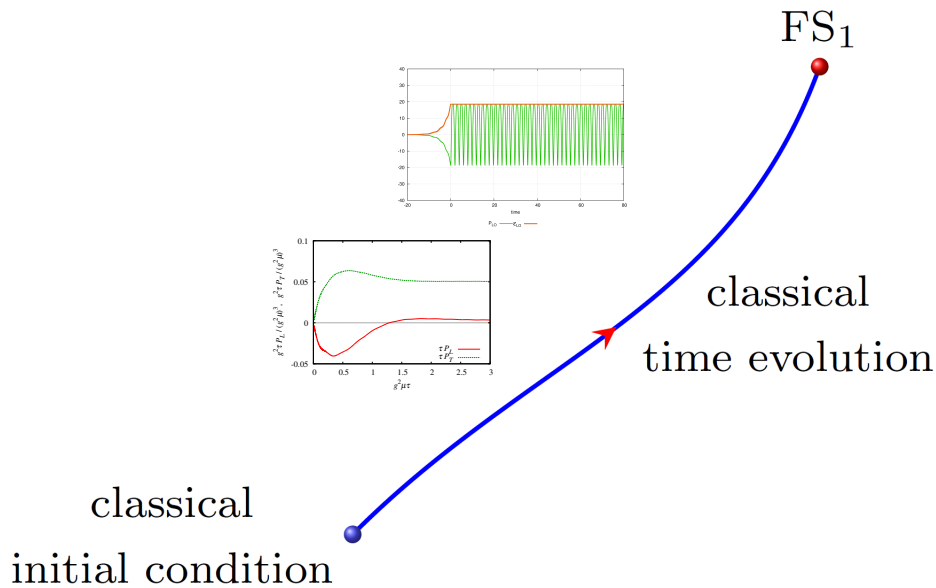

Figure 4.1: Classical world: the initial Wigner distribution is a δ function, and the system evolves with the classical equation of motion. For inclusive observables this gives the LO result, but nothing more. As shown in the sections 3.8 and 5.3.2, important physical mechanisms (instabilities, decoherence) are missing.
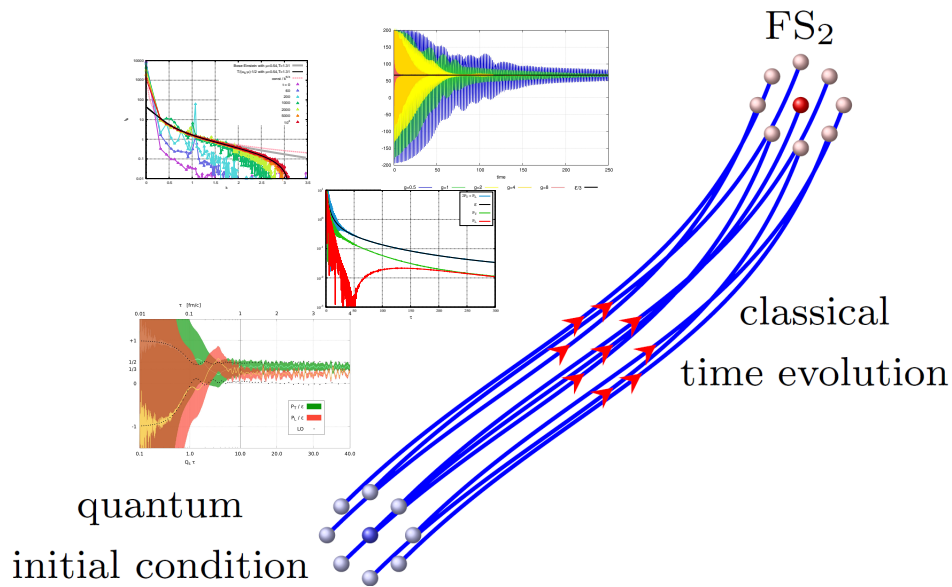
Figure 4.2: Classical-statistical approximation. Here the initial condition has quantum fluctuations. It corresponds to a Gaussian Wigner distribution with a variance of order $\hbar$. The system still evolves classically. For inclusive observables this gives the LO and NLO results, as well as a subset of higher order corrections. This approximation captures the relevant physics at intermediate time scales, but does not lead to the full thermal equilibrium.
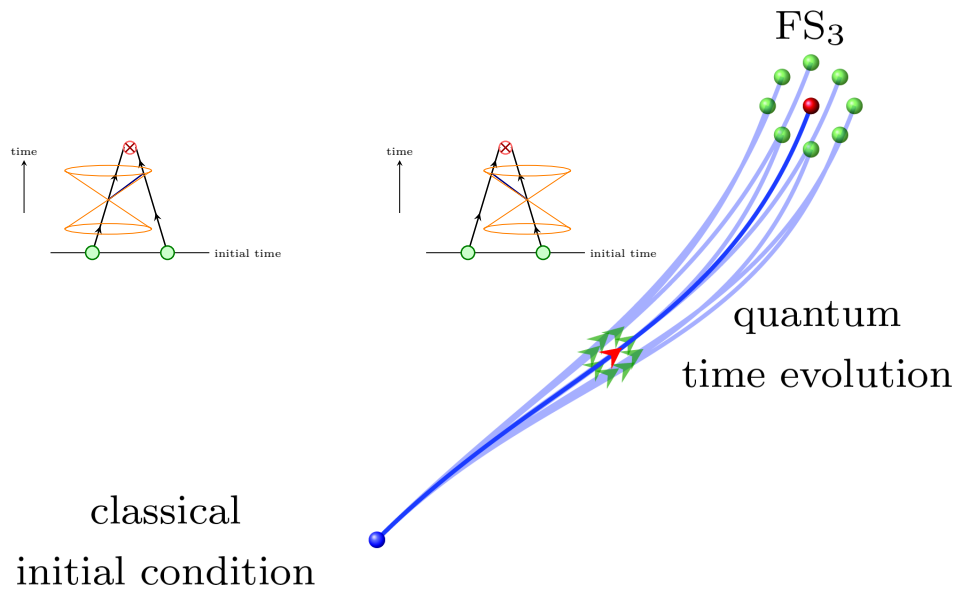

Figure 4.3: The quantum evolution is only accessible with other resummation techniques (e.g. the 2PI resummation technique [146]). These quantum corrections arise only at NNLO.

To conclude, let us recall that the CSA requires that $\varphi \gg \sigma$. This has the following consequence on the occupation number [65]

$$f_k \gg 1 \, . \tag{4.171}$$

4.3.1   Summary

• The FEYNMAN formalism is designed to compute $\langle \text{out}||\text{in}\rangle$ correlators

• The essence of perturbation theory in the FEYNMAN formalism is the generating functional $\mathcal{Z}$, that depends on the FEYNMAN propagator G_F.

• To compute $\langle \text{in}||\text{in}\rangle$ expectation values, one needs to introduce a new formalism: the SCHWINGER-KELDYSH formalism, that involves the generating functional $\overline{\mathcal{Z}}$ and the propagators $G_{\pm\pm}$.

• $\overline{\mathcal{Z}}$ can be formally related to $\mathcal{Z}$, stressing the connection between the FEYNMAN and the SCHWINGER-KELDYSH formalisms.

• Several bases can encode the SCHWINGER-KELDYSH formalism. The retarded-advanced basis uses the relation between the propagators in the original $\pm$ basis in order to eliminate one of the four components of the propagator matrix. This is the one that will be considered at length later in this manuscript.

• In the SCHWINGER-KELDYSH formalism, the fields at LO obeys the classical EOM with retarded boundary conditions: $\lim\limits_{x^0 \to -\infty} \varphi, \dot{\varphi} = 0$

• Thanks to a Green's formula, one can formally relate a field at any space-time point to its value on an initial space-like surface.

• The NLO of any inclusive quantity can be related to its LO value, via a differential operator that acts on the value of the fields on some initial space-like surface.

• Exponentiating this operator and letting it act on the LO value gives a resummed quantity that contains the LO, the NLO and a subset of higher order corrections.

• Re-expressing in a less formal way this resummed quantity leads to the classical-statistical method.

• The CSA consists in solving the classical equation of motion with as initial condition a quantum state centered around the classical value. Its variance is the minimal one allowed by Heisenberg's uncertainty principle.

Appendix

4.A   Relation between Schwinger-Keldysh and Feynman generating functionals

In this section we derive a relation between the generating functionals of the FEYNMAN and SCHWINGER-KELDYSH formalism by proving the following formula

$$\overline{\mathcal{Z}}[\eta^{(+)},\eta^{(-)}] = e^{\int d^4x d^4y\, G_{+-}(x,y)\Box_x\Box_y \frac{\delta^2}{\delta\eta^{(-)}(x)\delta\eta^{(+)}(y)}} \mathcal{Z}[\eta^{(+)}]\mathcal{Z}^*[\eta^{(-)}] \tag{4.172}$$

with

$$\mathcal{Z}[\eta] = e^{i\int \mathcal{L}_{int}\left(\frac{\delta}{i\delta\eta(z)}\right)d^4z} \mathcal{Z}_0[\eta]\,, \qquad \overline{\mathcal{Z}}[\eta^{(+)},\eta^{(-)}] = e^{i\int_{\mathcal{C}\times\mathbb{R}^3} \mathcal{L}_{int}\left(\frac{\delta}{i\delta\eta(z)}\right)d^4z} \overline{\mathcal{Z}}_0[\eta^{(+)},\eta^{(-)}] \tag{4.173}$$

and

$$\mathcal{Z}_0[\eta] = e^{-\frac{1}{2}\int d^4x\, d^4y\, \eta(x)G_F(x,y)\eta(y)}\,, \qquad \overline{\mathcal{Z}}_0[\eta^{(+)},\eta^{(-)}] = e^{-\frac{1}{2}\int_{\mathcal{C}\times\mathbb{R}^3} d^4x\, d^4y\, \eta(x)\bar{G}(x,y)\eta(y)}\,. \tag{4.174}$$

Given these definitions, it is easy to see that if the result holds for $\overline{\mathcal{Z}}_0[\eta^{(+)},\eta^{(-)}]$, it will also hold for $\mathcal{Z}[\eta^{(+)},\eta^{(-)}]$. Expanding the argument of the exponential in $\overline{\mathcal{Z}}_0[\eta^{(+)},\eta^{(-)}]$, we get

$$\overline{\mathcal{Z}}_0[\eta^{(+)},\eta^{(-)}] = e^{-\frac{1}{2}\int d^4x\, d^4y\, \left(\eta^{(+)}(x)G_{++}(x,y)\eta^{(+)}(y)+\eta^{(-)}(x)G_{--}(x,y)\eta^{(-)}(y)-2\eta^{(+)}(x)G_{+-}(x,y)\eta^{(-)}(y)\right)}\,, \tag{4.175}$$

and noticing that $G_F = G_{++}$, we see that we formally need to prove an identity that looks like

$$e^{-\frac{1}{2}(Ax^2 + By^2 - 2C'xy)} = e^{C\partial_x\partial_y}e^{-\frac{1}{2}(Ax^2 + By^2)} , \tag{4.176}$$

where by analogy with (4.172) x, y play respectively the role of $\eta^{(+)}, \eta^{(-)}$, A, B those of G_{++}, G_{--} and C, C' are free parameters proportional to G_{+-}, that we will try to adjust in function of A and B. Using the following identities obtained by Taylor expansions

$$e^{a\partial_y}f(y) = f(y+a) , \qquad\qquad f(\partial_x)e^{ikx} = f(ik)e^{ikx} , \tag{4.177}$$

we get

$$I = e^{C\partial_x\partial_y}e^{-\frac{1}{2}(Ax^2 + By^2)} = e^{-\frac{1}{2}B(y+C\partial_x)^2}e^{-\frac{1}{2}Ax^2} . \tag{4.178}$$

performing a Fourier transform of $e^{-\frac{1}{2}Ax^2}$

$$\int dx\, e^{-ikx - \frac{1}{2}Ax^2} = e^{-\frac{k^2}{2}A^{-1}}\int dx\, e^{-\frac{A}{2}(x+ikA^{-1})^2} = \sqrt{2\pi A^{-1}}e^{-\frac{1}{2A}k^2} , \tag{4.179}$$

so

$$I = e^{-\frac{1}{2}B(y+C\partial_x)^2}\int \frac{dk}{2\pi}\sqrt{2\pi A^{-1}}e^{-\frac{k^2}{2}A^{-1}}e^{ikx} = \sqrt{2\pi A^{-1}}\int \frac{dk}{2\pi}e^{-\frac{k^2}{2}A^{-1}}e^{-\frac{1}{2}B(y+iCk)^2}e^{ikx}$$

$$= \sqrt{2\pi A^{-1}}\int \frac{dk}{2\pi}e^{-\frac{A^{-1}}{2}(k^2 + ABy^2 + 2iABCyk - ABC^2k^2 - 2iAxk)} . \tag{4.180}$$

We now try to complete the square for k^2

$$I = \sqrt{2\pi A^{-1}}e^{-\frac{1}{2}By^2}\int \frac{dk}{2\pi}e^{-\frac{A^{-1}(1-ABC^2)}{2}\left(k+iA(1-ABC^2)^{-1}(BCy-x)\right)}e^{-\frac{A(1-ABC^2)^{-1}}{2}(BCy-x)^2}$$

$$= \sqrt{(1-ABC^2)^{-1}}e^{-\frac{1}{2}By^2}e^{-\frac{A(1-ABC^2)^{-1}}{2}(BCy-x)^2} = \sqrt{(1-ABC^2)^{-1}}e^{-\frac{(1-ABC^2)^{-1}}{2}(Ax^2 + By^2 - 2ABCxy)} . \tag{4.181}$$

Calling $C' = ABC$, we can rewrite the previous expression as follows [7]

$$I = e^{-\frac{1}{2}(Ax^2 + By^2 - 2C'xy)} . \tag{4.182}$$

Taking $C' = G_{+-}$ and $C = p^4G_{+-} = A^{-1}B^{-1}G_{+-}$ therefore gives the desired result.

---

7. Noticing that $A^{-1}B^{-1}C'^2 = 0$ since $C' \propto G_{+-}$ which is a function of $\delta(p^2)$ while $A^{-1} = ip^2$.

Part II

Study of a scalar field theory

Chapter 5

☢ Scalar field theory in a fixed volume ☢

Contents

5.1 Setup of the problem, specificities of the scalar model

e start our toy model studies with a scalar field theory with a quartic potential. In addition, in order to mimic the CGC model, we will add a strong source to the theory. Its Lagrangean therefore reads

$$\mathcal{L} = \frac{1}{2} \left(\partial_\mu \phi \right) \left(\partial^\mu \phi \right) - \frac{g^2}{4!} \phi^4 + J\phi \, , \tag{5.1}$$

where as stated in section 3.6 the source is intense, which means inversely proportional to the coupling which is assumed to be weak

$$J(x) \sim \theta(-x^0) \frac{Q^3}{g} \, . \tag{5.2}$$

To pursue the analogy with the CGC (where we recall that the sources are located on the light cone, meaning that they are 0 for positive proper-times), we took a heavyside function in J, meaning that it is non-zero only for negative times. Its effective role is to drive the value of the classical background field φ (see the section 4.2.1) to its initial value at $x^0 = 0$. In the numerical simulations the prefactor in J will be taken such that it asymptotically vanishes at $x^0 = -\infty$. The scale Q mimics the saturation scale Q_s of the CGC and is the only dimensionful parameter of the model. Our task within this model will be to study the macroscopic and microscopic evidences of a possible thermal equilibration of the system. It is an interesting question even if this theory is pretty far from the CGC, because as we will see along the way the scalar model shares some features with QCD. After a brief presentation on the physics of instabilities in the section 5.2, followed by a quick description of the numerical implementation, we will study in the section 5.3 and the subsequent ones the energy-momentum tensor, and see that an equation of state (EOS) forms. We then look at the microscopic properties of the theory in the section 5.4, where the spectral function and the occupation number are studied. All this will allow us to conclude that the system indeed seems to thermalize.

5.2 The physics of instabilities

Imagine a swing that oscillates at a fixed frequency. Now what would happens if each time that the swing is at its highest altitude (its speed being therefore 0), someone pushes it a little higher? There would be an amplification of the oscillations, leading to an instability in the swing oscillations (of course for a swing this is limited by the fact that at some point the swing will do a full 2π rotation). The analogy between this swing instability and the one that concerns us is the following: in the scalar field theory with the quartic coupling presented in (5.1), the oscillations of the ϕ amplitude inside the potential well $\frac{g^2}{4!}\phi^4$ are limited by the initial condition. If one starts with $(\phi, \dot{\phi}) = (\varphi_0, 0)$, then the amplitude of ϕ can never go higher than φ_0. But there are instabilities that affect the linearized Klein Gordon equation, that could induce an exponential growth of small perturbations to the classical solution. This is the topic of this section.

5.2.1 Parametric resonance band

The equation of motion (EOM) of the scalar theory is obtained from the Euler-Lagrange equation

$$\partial_\mu \frac{\delta \mathcal{L}}{\delta(\partial_\mu \phi)} = \frac{\delta \mathcal{L}}{\delta \phi} \, , \tag{5.3}$$

which gives the Klein-Gordon (KG) EOM

$$\Box \phi + \frac{g^2}{3!} \phi^3 = J \, . \tag{5.4}$$

Assuming that we are interested in what happens at positive times, we look at small perturbations around a solution φ. Writing $\phi = \varphi + a$ with both ϕ and φ satisfying the KG EOM (5.4), we find for the small fluctuation a, keeping only the linear terms in the latter (a being a small correction to φ, the terms that are in $O(a^2)$ can be neglected in a first approximation)

$$\left(\Box + \frac{g^2}{2} \varphi^2 \right) a = 0 \, . \tag{5.5}$$

To pursue the analytical study further, we will assume in this section that the classical background field depends only on time. Therefore (5.4) reads at positive times for the classical background field

$$\ddot{\varphi}(x^0) + \frac{g^2}{3!} \varphi^3(x^0) = 0 \, , \tag{5.6}$$

and one can perform a Fourier transform of the small fluctuations, leading to

$$\ddot{a}_k(x^0) + \left(k^2 + \frac{g^2}{2} \varphi^2(x^0) \right) a_k(x^0) = 0 \; . \tag{5.7}$$

To find whether there are instabilities in the scalar theory, we ask the following question: **are there some solution to (5.7) that exponentially grow as time increases?** The technical steps are relegated to the appendix 5.A. The result is that for

$$\frac{m_0}{2^{\frac{1}{2}}} < k < \frac{m_0}{3^{\frac{1}{4}}} \; , \tag{5.8}$$

where $m_0^2 = \frac{g^2 \varphi_0^2}{2}$, one finds exponentially growing modes a_k. There are therefore instabilities in the scalar $\phi^{\frac{4}{4}}$ theory.

5.2.2 Saturation of the instabilities

Given the form of the source J that drives the field φ, one has for the latter the same parametric estimate as in the gauge case (see section 3.6-3.8), namely

$$\varphi \sim \frac{Q}{g} \; . \tag{5.9}$$

From the previous section, we know that some modes a_k with k in the resonance band increase exponentially with time. After a finite time x^{sat}, they will therefore also reach

$$a_k(x^{\text{sat}}) \sim \frac{Q}{g} \; . \tag{5.10}$$

What happens after this time? One can see that (5.7) is no longer a good approximation of the a behaviour, since the terms neglected

$$\varphi a_k^2(x^{\text{sat}}), \; a_k^3(x^{\text{sat}}) \sim \varphi^2 a_k(x^{\text{sat}}) \tag{5.11}$$

are of the same order as the linear term we kept in (5.7). This means that after x^{sat} one should not use (5.7) as the EOM for the fluctuation. We will see that this will have some important effects later on when we discuss the behaviour of the energy-momentum tensor at different orders.

5.3 Macroscopic observables: the formation of an EOS

5.3.1 The energy-momentum tensor: definition, parametric estimates

The canonical energy-momentum tensor is defined as

$$T^{\mu\nu} = \Pi^\mu \partial^\nu \phi - g^{\mu\nu} \mathcal{L} \; , \tag{5.12}$$

where the conjugate momentum Π is

$$\Pi^\mu = \frac{\delta \mathcal{L}}{\delta(\partial_\mu \phi)} = \partial^\mu \phi \; . \tag{5.13}$$

This gives at positive times

$$T^{\mu\nu} = \partial^\mu \phi \partial^\nu \phi - \frac{g^{\mu\nu}}{2} (\partial_\rho \phi)(\partial^\rho \phi) + g^{\mu\nu} \frac{g^2}{4!} \phi^4 \; . \tag{5.14}$$

Since ϕ obeys the KG EOM (5.4), it is trivial to check that the energy-momentum is conserved

$$\partial_\mu T^{\mu\nu} = 0 \; . \tag{5.15}$$

Given what we saw in section 3.8 and chapter 4, we know that we can perform a perturbative expansion of $T^{\mu\nu}$ in term of the coupling constant. This expansion reads

$$T^{\mu\nu} = T^{\mu\nu}_{\text{LO}} + T^{\mu\nu}_{\text{NLO}} + ... = \frac{Q^4}{g^2} \left[c^{\mu\nu}_0 + g^2 c^{\mu\nu}_1 + g^4 c^{\mu\nu}_2 + ... \right] . \tag{5.16}$$

In the next section we will be interested in computing numerically $T^{\mu\nu}_{\text{LO}}$, $T^{\mu\nu}_{\text{NLO}}$ and the $T^{\mu\nu}_{\text{resum}}$ that can be deduced from formula (4.151).

5.3.2   The energy momentum tensor at Leading Order (LO)

Given what was explained in section 3.6, the coefficients $c^{\mu\nu}$ should be infinite series in the combination gJ, and since $J \sim g^{-1}$ all the terms in the series contribute to the same order in g. What this means is that as already stated in section 3.6, Leading Order quantities receive contributions from all the tree diagrams, while Next to Leading Order receives contributions from all the $1-$loop diagrams, and so on... Given the work performed in chapter 4.2, we know that the sum of all the tree diagrams can be re-expressed as the solution of the classical equation of motion with retarded initial conditions

$$\Box\varphi + \frac{g^2}{6}\varphi^3 = J \qquad\qquad \lim_{t\to-\infty} \varphi, \dot{\varphi} = 0 , \tag{5.17}$$

and $T^{\mu\nu}$ at leading order therefore reads (at positive times)

$$T^{\mu\nu}_{\text{LO}} = c^{\mu\nu}_0 \frac{Q^4}{g^2} = \partial^\mu\varphi\partial^\nu\varphi - \frac{g^{\mu\nu}}{2}\left(\partial_\rho\varphi\right)\left(\partial^\rho\varphi\right) + g^{\mu\nu}\frac{g^2}{4!}\varphi^4 . \tag{5.18}$$

The $\frac{Q^4}{g^2}$ behaviour of $T^{\mu\nu}$ at leading order can now easily be understood from (5.18) since $\varphi \sim \frac{Q}{g}$. To keep things simple here, we take J spatially homogeneous. Therefore so is φ, and $T^{\mu\nu}_{\text{LO}}$ has the following form

$$T^{\mu\nu}_{\text{LO}}(x) = \begin{pmatrix} \epsilon_{\text{LO}} & 0 & 0 & 0 \\ 0 & p_{\text{LO}} & 0 & 0 \\ 0 & 0 & p_{\text{LO}} & 0 \\ 0 & 0 & 0 & p_{\text{LO}} \end{pmatrix} , \tag{5.19}$$

with the leading order energy density and pressure given by

$$\epsilon_{\text{LO}} = \frac{1}{2}\dot{\varphi}^2 + \frac{g^2}{4!}\varphi^4 , \qquad\qquad p_{\text{LO}} = \frac{1}{2}\dot{\varphi}^2 - \frac{g^2}{4!}\varphi^4 . \tag{5.20}$$

Given these equations, on can easily check that the energy is conserved at positive times (where the source J is turned off) thanks to the classical KG EOM. But this is not so the case for the pressure of the system : it indeed indefinitely oscillates between ϵ and $-\epsilon$ as one can see on the figure 5.1
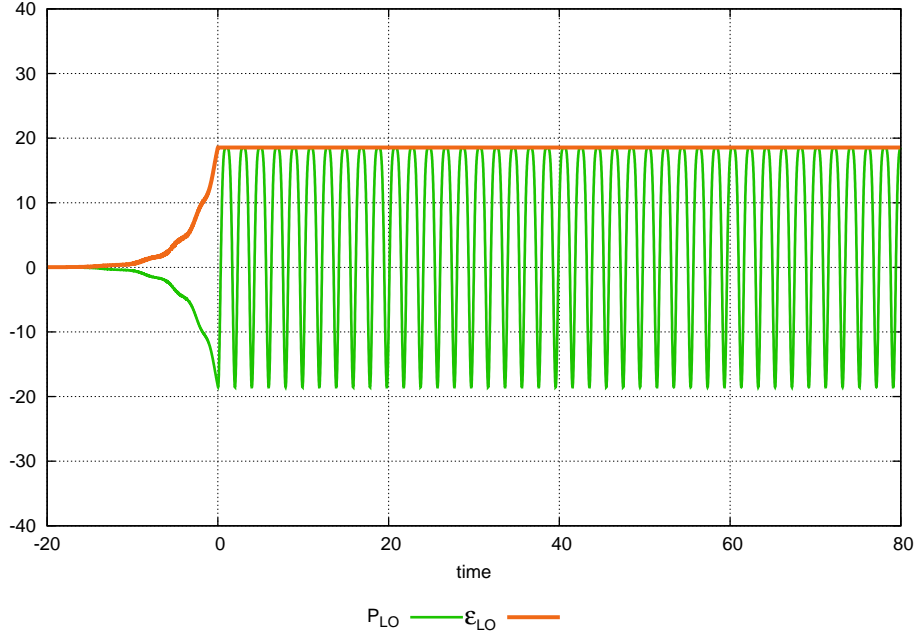
Figure 5.1: The various components of the energy-momentum tensor at Leading Order $T_{\text{LO}}^{\mu\nu}$. Here the external source has be taken to be spatially uniform: $J = \theta(-x^0)\frac{Q^3}{g}e^{bQx^0}$ (with $g = 1, b = 0.1$ and $Q = 2.5$) so that it vanishes adiabatically in the remote past.

This was to be expected. Indeed since

$$\dot{p}_{\text{LO}} = -\frac{g^2}{3}\varphi^3\dot{\varphi} \,, \tag{5.21}$$

one can see that $\dot{p}_{\text{LO}} = 0$ either if $\varphi = 0$ and in this case

$$p_{\text{LO}} = \epsilon_{\text{LO}} = \frac{1}{2}\dot{\varphi}^2 \,, \tag{5.22}$$

or if $\dot{\varphi} = 0$ and in this case

$$p_{\text{LO}} = -\epsilon_{\text{LO}} = -\frac{g^2}{4!}\varphi^4 \,. \tag{5.23}$$

There is therefore no equation of state at Leading Order.

5.3.3 Energy momentum tensor at Next to Leading Order

As we saw in section 3.8 in the QCD case, we should have anticipated that because of the presence of instabilities in the theory, the NLO contribution [1] has a sizable effect on the system after a finite time, and should therefore be taken into account. Recalling the result of section 4.2.2.5, the NLO is given by

$$T_{\text{NLO}}^{\mu\nu} = \widehat{O} \, T_{\text{LO}}^{\mu\nu} \,, \tag{5.24}$$

and replacing $\widehat{O}$ with equation (4.143), we find (calling $k = |\boldsymbol{k}|$)

$$T_{\text{NLO}}^{\mu\nu} = (\partial^\mu a)(\partial^\nu \varphi) + (\partial^\mu \varphi)(\partial^\nu a) - g^{\mu\nu}\left((\partial_\rho \varphi)(\partial^\rho a) - \frac{g^2}{6}a\phi^3\right)$$
$$+ \int \frac{\mathrm{d}^3\boldsymbol{k}}{(2\pi)^3 2k}\left[(\partial^\mu a_{+\boldsymbol{k}})(\partial^\nu a_{-\boldsymbol{k}}) - \frac{1}{2}g^{\mu\nu}\left((\partial^\rho a_{+\boldsymbol{k}})(\partial_\rho a_{-\boldsymbol{k}}) - \frac{g^2}{2}\varphi^2 a_{+\boldsymbol{k}}a_{-\boldsymbol{k}}\right)\right] \,, \tag{5.25}$$

---

1. And in fact every higher contribution. This is why we will come to use $T_{\text{resum}}^{\mu\nu}$.

with

$$\Box\varphi + \frac{g^2}{6}\varphi^3 = J \qquad\qquad \lim_{t\to-\infty}\varphi, \dot\varphi = 0$$

$$\left(\Box + \frac{g^2}{2}\varphi^2\right)a_{\pm k} = 0 \qquad\qquad \lim_{t\to-\infty}a_{\pm k} = e^{\pm ikx}$$

$$\left(\Box + \frac{g^2}{2}\varphi^2\right)a = -\frac{g^2}{2}\varphi\int\frac{\mathrm{d}^3k}{(2\pi)^3 2|\boldsymbol{k}|}a_{-\boldsymbol{k}}a_{+\boldsymbol{k}} \qquad\qquad \lim_{t\to-\infty}a = 0\,. \qquad (5.26)$$

Using the three EOM for a, a_k and φ, it is trivial to check that[2] the energy-momentum tensor is conserved at NLO

$$\partial_\mu T^{\mu\nu}_{\mathrm{NLO}} = 0\,, \qquad\qquad (5.27)$$

as it should be. Since J is spatially homogeneous, a, φ only depend on x^0

$$\ddot a + \frac{g^2}{2}\varphi^2 a = -\frac{g^2}{2}\varphi\int\frac{\mathrm{d}^3k}{(2\pi)^3 2k}a_{-\boldsymbol{k}}a_{+\boldsymbol{k}}\,, \qquad\qquad \ddot\varphi + \frac{g^2}{2}\varphi^3 = J\,, \qquad (5.28)$$

while the EOM for the small fluctuations a_k simplifies into the one that we already encountered (5.7)

$$\ddot a_k + \left(k^2 + \frac{g^2}{2}\varphi^2(x^0)\right)a_{\pm k} = 0\,. \qquad\qquad (5.29)$$

The energy density and the pressure[3] at NLO read

$$\epsilon_{\mathrm{NLO}} = \dot\varphi\dot a + \frac{g^2}{6}a\varphi^3 + \frac{1}{2}\int\frac{\mathrm{d}^3k}{(2\pi)^3 2k}\left[\dot a_{+\boldsymbol{k}}\dot a_{-\boldsymbol{k}} + \left(k^2 + \frac{g^2}{2}\varphi^2\right)a_{+\boldsymbol{k}}a_{-\boldsymbol{k}}\right]$$

$$p_{\mathrm{NLO}} = \dot\varphi\dot a - \frac{g^2}{6}a\varphi^3 + \frac{1}{2}\int\frac{\mathrm{d}^3k}{(2\pi)^3 2k}\left[\dot a_{+\boldsymbol{k}}\dot a_{-\boldsymbol{k}} - \left(k^2 - 2k_x^2 + \frac{g^2}{2}\varphi^2\right)a_{+\boldsymbol{k}}a_{-\boldsymbol{k}}\right]\,. \qquad (5.30)$$

Using (5.28) and (5.29), it is a trivial matter to check that the energy density is conserved for positive times $\dot\epsilon_{\mathrm{NLO}} = 0$. Note that this expression of the pressure is not rotationally invariant, but the three pressures are equal. Solving numerically (5.28) and (5.29) with the initial conditions depicted in (5.26) gives what is represented on the figure (5.2).

---

2. Since this property is satisfied for the full energy-momentum tensor, it should obviously be satisfied at each order of the perturbative expansion in g^2.

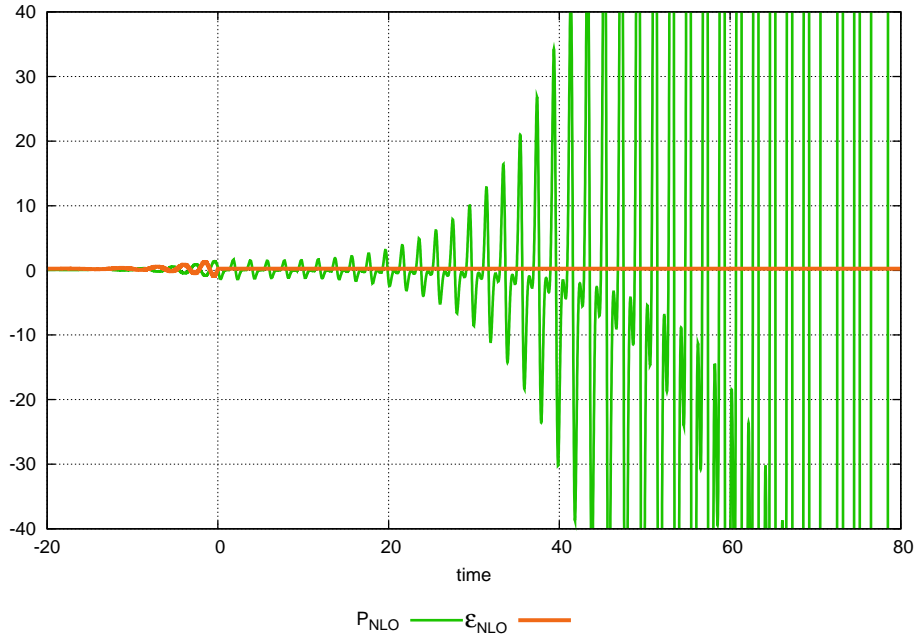3. The pressures are still equal since the system is isotropic.

Figure 5.2: Components of $T^{\mu\nu}_{\mathrm{NLO}}$ for a spatially uniform external source.

Here we see that ϵ_{NLO} is indeed conserved. In addition, one can observe that $\epsilon_{\mathrm{NLO}} = 0.014\epsilon_{\mathrm{LO}}$. A perturbative expansion for ϵ seems therefore justified [4]. This is not the case for the pressure. After a finite time where the NLO contribution is indeed very small in comparison to the LO one, we see that p_{NLO} starts to increase exponentially, voiding the validity of the pertubative expansion of p after a finite time. In some sense, the situation is even worse when one takes into account the NLO corrections in our framework. This is the secular divergence phenomenon, already described for QCD in section 3.8.

5.3.4 The instabilities at work

As we have explained in section 5.2, a resonance band in the theory causes some modes a_k to grow exponentially with time. The consequence of this is that integrals such as

$$I(x^0) = \int \frac{\mathrm{d}^3 \boldsymbol{k}}{(2\pi)^3 2k} \dot{a}_{+\boldsymbol{k}} \dot{a}_{-\boldsymbol{k}} \, , \tag{5.31}$$

that appears in (5.28) are divergent when the time x^0 goes to infinity. This causes the exponential growth observed in the pressure – but not in the energy, since it is protected by conservation laws. One can check this by plotting $I(x^0)$, as was done in the figure 5.3.

---

4. At least at this order. The perturbative expansion for ϵ could be an asymptotic series.
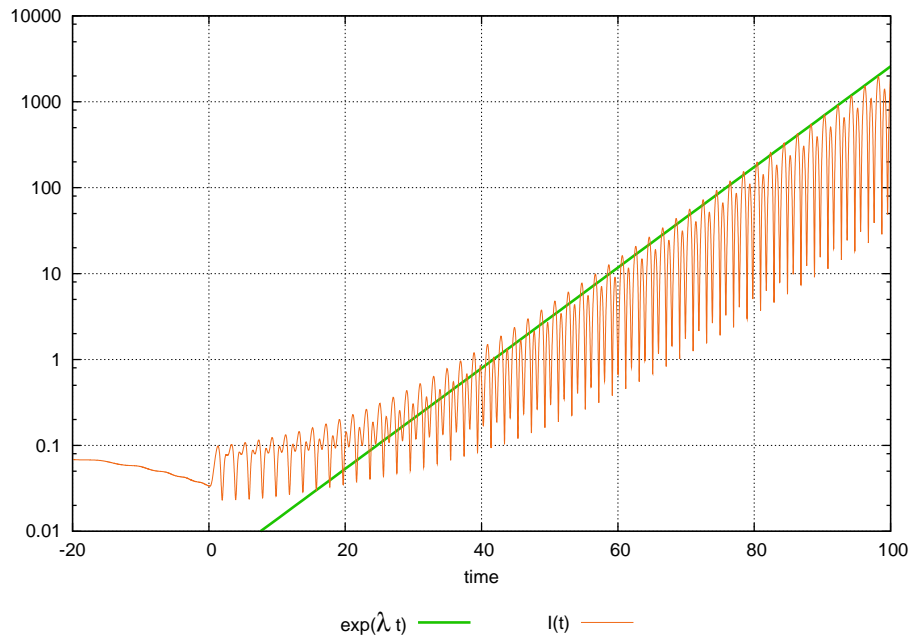
Figure 5.3:   Numerical evaluation of the integral defined in eq. (5.31). The line denotes an exponential fit to the envelope.

Here the envelope of the oscillations grows exponentially with time, with a growth rate $\lambda = 2\mu_{\max}$, where $\mu_{\max}$ is the maximum Lyapunov exponent in the resonance band (see the appendix 5.A for more details on the resonance band and the Lyapunov exponent). Interestingly, if one used an upper cutoff on the previous integral (5.31) to exclude the resonance band, one would only observe a linear growth of $I(x^0)$, presumably caused by the remaining modes that grow linearly with time (the mode $k = 0$ for instance). The remaining question is: is the exponential growth of p_{NLO} physical? And if not, how to cure it? It turns out that we have already answered to both parts of this question. Firstly, this exponential growth that happens when $x^0 \to \infty$ is not physical: this is due to the fact that we are still solving the linear EOM (5.28) for a_k even after it becomes large, despite the parametric estimate (5.11). Secondly, a possible way to cure this issue could be to compute the resummed $T^{\mu\nu}$ given by formula (4.151)

$$T^{\mu\nu}_{\mathrm{resum}} = e^{\widehat{O}} T^{\mu\nu}_{\mathrm{LO}} \, , \tag{5.32}$$

which can be calculated with the Classical-Statistical Approximation (CSA), depicted in the section 4.3. In this method, the full non-linear – but classical – EOM are solved, so that the exponential growth observed in 5.2 should therefore saturate at some point.

5.3.5   The spatially uniform case

5.3.5.1   The model, analytical considerations

Before dealing with the full $3 + 1$D theory, it is interesting to focus on a much simpler yet illuminating example: the spatially uniform theory. This will allow us to understand the effect of the fluctuating term on the energy-momentum tensor. Recalling that (5.32) is equivalent to [5]

$$\int [\mathcal{D}\, a] \, e^{-\frac{1}{2} \int \mathrm{d}^3 \boldsymbol{u} \, \mathrm{d}^3 \boldsymbol{v} \, a(0,\boldsymbol{u}) \mathcal{G}^{-1}_{+-}(u,v) a(0,\boldsymbol{v})} \, T^{\mu\nu}_{\mathrm{LO}}[\varphi + a] \, , \tag{5.33}$$

_____

5. The shift term ψ has been absorbed in φ (section 4.2.3).

where the initial surface is at $x^0 = 0$. The functional integral reduces to an ordinary integral if the fluctuations are spatially homogeneous. One can therefore generate $T^{\mu\nu}_{\text{resum}}$ as [6]

$$\int \mathrm{d}a \, \mathrm{d}\dot{a} \, e^{-\left(\frac{a^2}{2\sigma_1} + \frac{\dot{a}^2}{2\sigma_2}\right)} T^{\mu\nu}_{\text{LO}}[\varphi + a, \dot{\varphi} + \dot{a}] \,. \tag{5.34}$$

Here $\sigma_{1,2}$ are two real parameters that control the size of the fluctuations around the background field. If we take $\sigma_{1,2} \to 0$, we recover the result of the figure 5.1. But before doing so, let us notice that thanks to this simplistic model, the equation of motion reduces to an ordinary differential equation and can be solved analytically. Indeed, starting from an initial condition $(\varphi_0, 0)$ one can integrate (5.28) at positive times

$$\ddot{\varphi} + \frac{g^2}{6}\varphi^3 = 0 \,, \tag{5.35}$$

and this gives

$$\frac{\dot{\varphi}}{\varphi_0} = \frac{m_0}{\sqrt{6}}\sqrt{1 - \frac{\varphi^4}{\varphi_0^4}} \,, \tag{5.36}$$

Therefore

$$x^0 - \text{cst} = \frac{\sqrt{6}}{m_0}\int_0^{\varphi(x^0)} \frac{\mathrm{d}\xi}{\sqrt{1 - \frac{\xi^4}{\varphi_0^4}}} \,, \tag{5.37}$$

which is an elliptic integral, therefore

$$\varphi(x^0) = \varphi_0 \, \text{cn}_{\frac{1}{2}}\left(\frac{m_0}{\sqrt{12}} + \text{cst}\right) \,, \tag{5.38}$$

where $\text{cn}_{\frac{1}{2}}$ is the Jacobi elliptic function of the first kind with the elliptic modulus $k = \frac{1}{2}$ [147]. It is important to note here that this function is periodic, with a period

$$T = K\left(\frac{1}{2}\right)\frac{\sqrt{48}}{m_0} \,, \tag{5.39}$$

where $K\left(\frac{1}{2}\right) \approx 1.85$ is the compete elliptic function of the first kind. The prefactor is not of any particular interest, but the fact that $T \propto \varphi_0$, meaning that **the period depends on the amplitude of the background field** will play a crucial role in the physical interpretation of our numerical results.

5.3.5.2 Numerical study

In this simple model, the energy density and the pressure read

$$\epsilon_{\text{resum}} = \left\langle \frac{1}{2}\dot{\varphi}^2 + \frac{g^2}{4!}\varphi^4 \right\rangle_{a,\dot{a}} \,, \qquad p_{\text{resum}} = \left\langle \frac{1}{2}\dot{\varphi}^2 - \frac{g^2}{4!}\varphi^4 \right\rangle_{a,\dot{a}} \,, \tag{5.40}$$

where the bracket denotes the average over all the possible values $a, \dot{a}$ in the initial condition of equation (5.34), and where φ satisfies the classical spatially homogeneous EOM (5.28). If we take the limit $\sigma_{1,2} \to 0$, then as announced we recover the same pattern as the Leading Order result of the full theory (see figure 5.1).

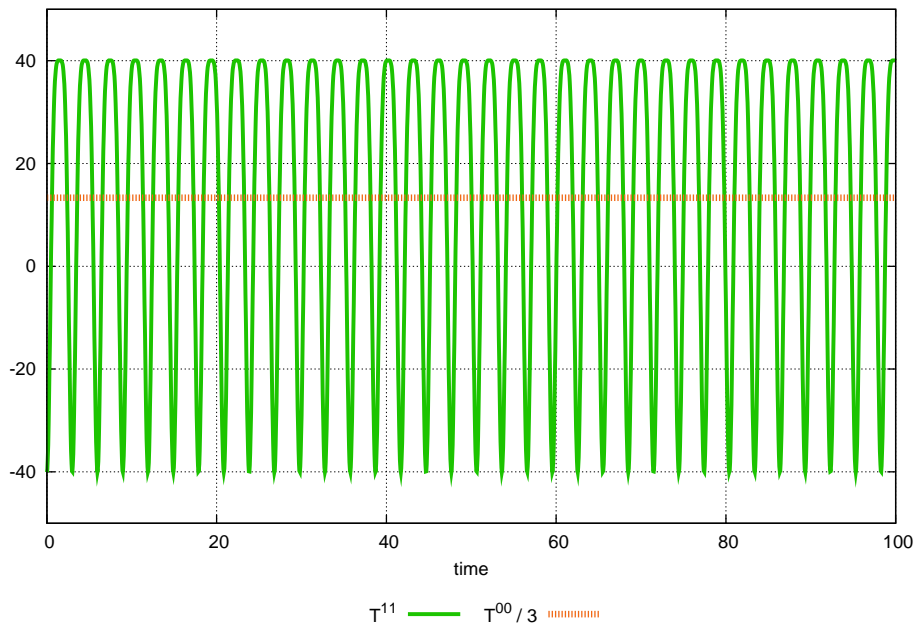6. Not forgetting that one also needs the value of $\dot{\varphi}$ on the initial surface.

Figure 5.4: The various components of $T^{\mu\nu}_{\mathrm{LO}}$ for the simplistic spatially homogeneous model. No quantum fluctuations are included ($\sigma_{1,2} \to 0$).

Notice here that we have plotted $\frac{\epsilon_{\mathrm{resum}}}{3}$ in figure 5.4 instead of $\epsilon_{\mathrm{resum}}$ for reasons that will be clear shortly. Indeed, performing now the same simulation but with non-zero $\sigma_{1,2}$ we find a qualitatively completely different result, depicted in figure 5.5
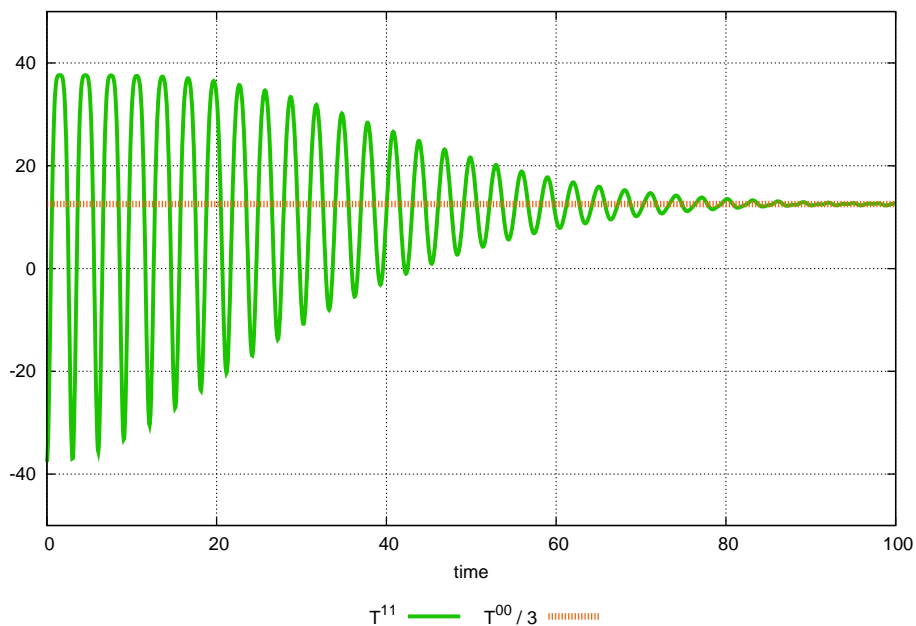

Figure 5.5: The various components of $T^{\mu\nu}_{\mathrm{resum}}$ obtained with to formula (5.34).

Here, the pressure oscillations are damped and one finds that there is a one-to-one relation between p_{resum} and $\epsilon_{\mathrm{resum}}$ after a time $x^0 \geq 80$

$$p_{\mathrm{resum}} = \frac{\epsilon_{\mathrm{resum}}}{3} . \qquad (5.41)$$

This is the first macroscopic hint of an equilibration taking place into the system, as this relation confirms the **formation of an equation of state**, precisely the one expected for a scale

invariant $3 + 1$D theory. How to interpret this result? What made the pressure oscillations decrease?

5.3.5.3 The physics of decoherence: intuitive explanation

Given (5.39), we know that the period of the oscillations of φ depends on their amplitude φ_0. This is illustrated in the next figure 5.6.
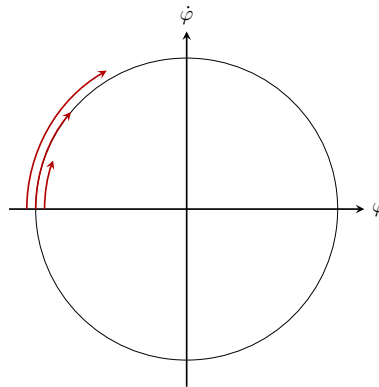

Figure 5.6: Different initial conditions oscillate with a different period.

So, what would happen to a system initialized as the superposition of several $(\varphi_0, 0)$ configurations, as the one shown in 5.7?
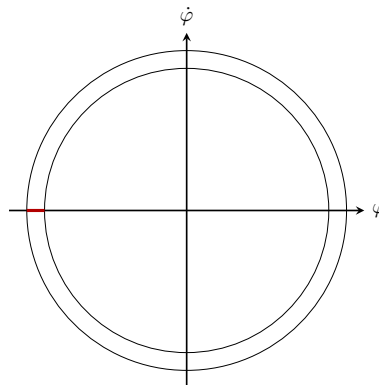

Figure 5.7: A system formed by the superposition of several $(\varphi_0, 0)$ configurations (red band).

Because of the spread in the periods, the initial condition will start to expand in the constant energy shell between $\varphi_0^{\min}$ and $\varphi_0^{\max}$. This can be seen in 5.8.
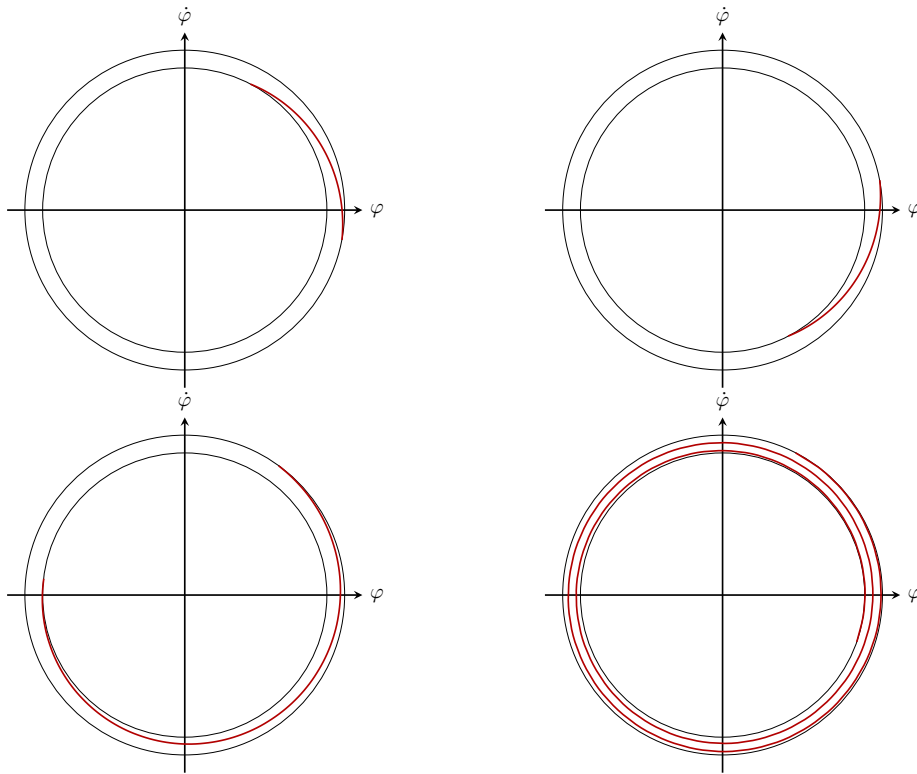
Figure 5.8: The constant energy shells between $\varphi_0^{\min}$ and $\varphi_0^{\max}$ are populated at different rhythms because of the φ_0 dependent period.

After a finite time, the shell between $\varphi_0^{\min}$ and $\varphi_0^{\max}$ will be completely occupied. This is the phenomenon of phase **decoherence**, illustrated in figure 5.9.
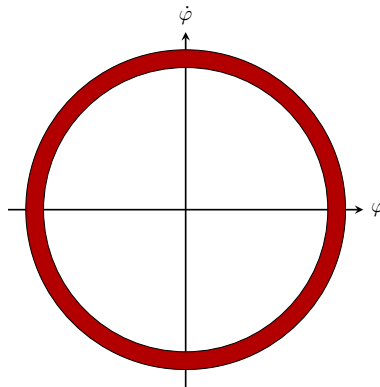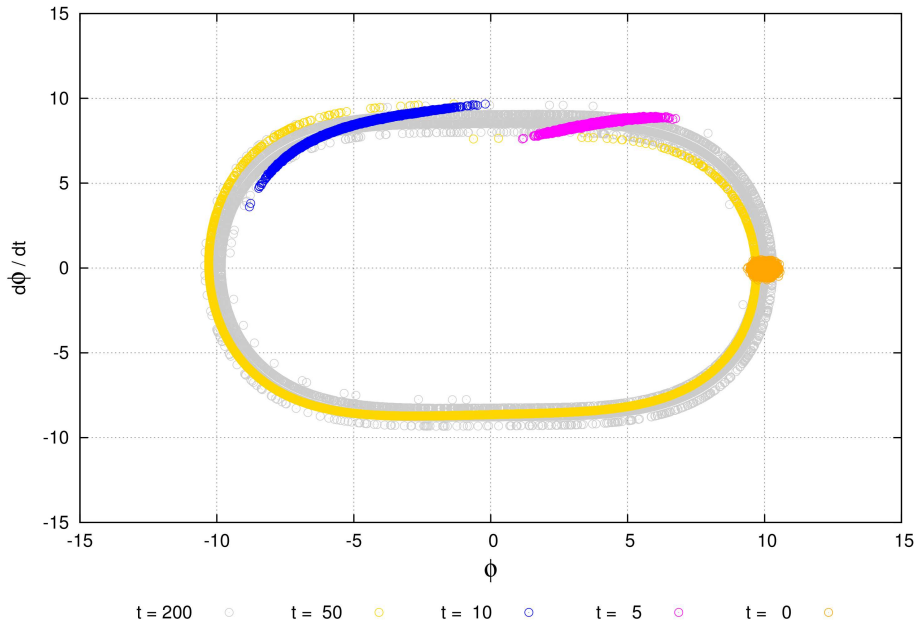

Figure 5.9: Decoherence phenomenon: the inner shell between $\varphi_0^{\min}$ and $\varphi_0^{\max}$ is completely occupied.

It turns out that the initial state from which we start in the full theory (see equation (5.34)) is a coherent state. In simple physical terms it is a quantum state that has the minimal width in phase-space $(\varphi, \dot{\varphi})$ allowed by Heisenberg uncertainty principle. But this state is not an eigenstate of the interacting theory, hence the decoherence phenomenon that is observed in the figure 5.5.

5.3.5.4 Numerical confirmation

One can plot as a function of time the phase-space density $\rho_t(\varphi, \dot{\varphi})$ of the points $(\varphi, \dot{\varphi})$ as the system evolves. The result is shown on the figure 5.10.

Figure 5.10: $\rho_t(\varphi, \dot{\varphi})$ at different times.

At the initial time, a Gaussian profile centered around $(\varphi_0, 0)$ was taken as initial condition, as the orange blob indicates. Then, as time increases, the decoherence phenomenon described in the previous section takes place. After a time ~ 200 the system has completely decohered, the only reminiscence of the initial condition being through the narrow dispersion of the radial coordinate. One can understand this from the Liouville equation

$$\frac{\partial \rho_t}{\partial t} + \{\rho_t, H\} = 0 \,, \tag{5.42}$$

where $\{.,.\} =$ is the Poisson bracket

$$\{A, B\} = \frac{\partial A}{\partial \dot{\varphi}} \frac{\partial B}{\partial \varphi} - \frac{\partial B}{\partial \dot{\varphi}} \frac{\partial A}{\partial \varphi} \,, \tag{5.43}$$

and H is the Hamiltonian $H = \frac{1}{2}\dot{\varphi}^2 + \frac{g^2}{4!}\varphi^4$. Looking at the Liouville equation, we see that a stationary solution can only depend on $(\varphi, \dot{\varphi})$ through H – therefore making the Poisson bracket vanish. The asymptotic behaviour of ρ_t is therefore a uniform distribution on a constant energy shell. In micro-canonical equilibrium language, this means that all the micro-states that have the same energy are equally likely. Finally, we can estimate the decoherence time thanks to formula (5.39). Complete decoherence can be said to happen when the angular spread of the points on the previous figure reaches 2π. For one field configuration, the angular variable is (up to a phase that depends on the initial condition) $\theta = \omega x^0$, where given (5.39)

$$\omega = \frac{2\pi}{T} = 0.346 g \varphi_0 \,. \tag{5.44}$$

If we now take two field configurations, their angular variable difference $\Delta\theta$ is $\Delta\theta = x^0 \Delta\omega$, where $\Delta\omega$ is the difference between their angular velocities. Thus

$$\Delta\theta \approx 0.346 \, g x^0 \, \Delta\varphi_0 \,, \tag{5.45}$$

where $\Delta\varphi_0$ is the difference between the maximal amplitude of the two configurations. This reaches 2π for

$$x^0_{\text{decoh}} \approx \frac{18.2}{g \Delta\varphi_0} \,, \tag{5.46}$$

Interestingly, this time is inversely proportional to the coupling constant g: the stronger the interaction is, the faster decoherence will happen. x^0_{decoh} is also inversely proportional to the difference of the field amplitudes: a narrow initial Gaussian distribution will decohere slower than a broader one.

5.3.5.5   Why do an equation of state form?

If we look at the trace of the energy momentum tensor, which is nothing but $\epsilon - 3p$ in the spatially homogeneous case, we get

$$T^{\mu}{}_{\mu} = -\left(\partial_{\mu}\varphi\right)\left(\partial^{\mu}\varphi\right) + \frac{g^2}{6}\varphi^4 \ . \tag{5.47}$$

Using the fact that $\partial_{\mu}\left(\varphi\partial^{\mu}\varphi\right) = \varphi\Box\varphi + \left(\partial_{\mu}\varphi\right)\left(\partial^{\mu}\varphi\right)$, we get

$$T^{\mu}{}_{\mu} = \varphi\left(\Box\varphi + \frac{g^2}{6}\varphi^3\right) - \partial_{\mu}\left(\varphi\partial^{\mu}\varphi\right) \ . \tag{5.48}$$

The fact that the first term – using the EOM – of the right hand side is zero comes from the fact that the scalar field theory with a quartic coupling is a scale invariant theory in 4 dimensions

$$\frac{g^2}{6}\varphi^3 = V'(\varphi) = 4\frac{V(\varphi)}{\varphi} \ . \tag{5.49}$$

Therefore, we have

$$T^{\mu}{}_{\mu} = -\frac{\mathrm{d}\left(\varphi\dot{\varphi}\right)}{\mathrm{d}x^0} \ , \tag{5.50}$$

which is a total derivative. This means that, even for a single field configuration, this quantity vanishes when it is averaged over one period

$$\overline{T^{\mu}{}_{\mu}} = \int_{x^0}^{x^0+T} \mathrm{d}t\, T^{\mu}{}_{\mu}\left[\varphi(t), \dot{\varphi}(t)\right] = -\int_{x^0}^{x^0+T} \mathrm{d}t\, \frac{\mathrm{d}\left(\varphi\dot{\varphi}\right)}{\mathrm{d}t} = 0 \ . \tag{5.51}$$

This will prove useful for the computation of the resummed $T^{\mu}{}_{\mu}$, which is related to the phase-space density $\rho_t(\varphi, \dot{\varphi})$ by the following ensemble average

$$\left\langle T^{\mu}{}_{\mu}\right\rangle_{a,\dot{a}} = \int \mathrm{d}\varphi\,\mathrm{d}\dot{\varphi}\,\rho_t(\varphi, \dot{\varphi})\, T^{\mu}{}_{\mu}(\varphi, \dot{\varphi}) \ , \tag{5.52}$$

where the time dependence of the left hand side comes completely from ρ_t. To go further, we perform the change of variables $(\varphi, \dot{\varphi}) \to (E, \theta)$ where the latter are the energy and the angle of one field configuration

$$\left\langle T^{\mu}{}_{\mu}\right\rangle_{a,\dot{a}} = \int \mathrm{d}E\mathrm{d}\theta\,\tilde{\rho}_t(E, \theta)\, T^{\mu}{}_{\mu}(E, \theta) \ , \tag{5.53}$$

here $\tilde{\rho}_t$ is the phase-space density in the (E, θ) coordinate system. Since we have shown in the previous section that $\tilde{\rho}_t(E, \theta) \longrightarrow \tilde{\rho}_t(E)$ at late times, we have

$$\left\langle T^{\mu}{}_{\mu}\right\rangle_{a,\dot{a}} \overset{x^0 \to \infty}{\approx} \int \mathrm{d}E\,\tilde{\rho}_t(E) \int \mathrm{d}\theta\, T^{\mu}{}_{\mu}(E, \theta) \ . \tag{5.54}$$

The last integral in the right hand side is related to the trace of $T^{\mu}{}_{\mu}$ for a single field configuration averaged over one period, already computed in equation (5.51)

$$\int \mathrm{d}\theta\, T^{\mu}{}_{\mu}(E, \theta) = \frac{2\pi}{T}\int_{t}^{x^0+T} \mathrm{d}t\, T^{\mu}{}_{\mu}(\varphi(t), \dot{\varphi}(t)) = 0 \ . \tag{5.55}$$

We have therefore proved

$$\epsilon - 3p = \left\langle T^{\mu}{}_{\mu}\right\rangle_{a,\dot{a}} \overset{x^0 \to \infty}{\approx} 0 \ , \tag{5.56}$$

in agreement with the late time behaviour of figure (5.5). Given how we obtained this equality, the time at which (5.56) is satisfied should be the same as the one found in (5.46), e.g. the time at which $\tilde{\rho}_t$ becomes independent θ.

5.3.6 The full 3+1D case

5.3.6.1 Resummed energy-momentum tensor

To compute the resummed energy-momentum tensor in the full theory, one needs to solve at positive time the classical equation of motion for the field ϕ

$$\Box\phi + \frac{g^2}{6!}\phi^3 = 0 . \tag{5.57}$$

ϕ is formed at the initial time $t = 0$ by the superposition of the classical background field φ and the spectrum of fluctuations a_k weighted by random Gaussian numbers c_k

$$\phi(0, \boldsymbol{x}) = \varphi_0 + \int \frac{\mathrm{d}^3\boldsymbol{k}}{(2\pi)^3\sqrt{2\omega_k}} \mathrm{Re}\left[c_{\boldsymbol{k}}\, a_{\boldsymbol{k}}(0, \boldsymbol{x})\right] ,$$

$$\dot{\phi}(0, \boldsymbol{x}) = \int \frac{\mathrm{d}^3\boldsymbol{k}}{(2\pi)^3\sqrt{2\omega_k}} \mathrm{Re}\left[c_{\boldsymbol{k}}\, \dot{a}_{\boldsymbol{k}}(0, \boldsymbol{x})\right] , \tag{5.58}$$

where $\omega_k = \sqrt{k^2 + m_0^2}$ and

$$\langle c_k c_l^* \rangle = (2\pi)^3 \delta^3(\boldsymbol{k} - \boldsymbol{l}) , \qquad\qquad \langle c_k c_l \rangle = \langle c_k^* c_l^* \rangle = 0 . \tag{5.59}$$

To find a_k, we need to solve the linear equation of motion (5.29) from $x^0 = -\infty$ starting with plane waves initial conditions, jointly with the classical EOM for φ (5.28). To summarize, at negative times we solve

$$\Box\varphi + \frac{g^2}{6}\varphi^3 = J , \qquad\qquad \left(\Box + \frac{g^2}{2}\varphi^2\right) a_k(x) = 0 . \tag{5.60}$$

5.3.6.2 Numerical implementation

The numerical implementation is performed in the following way
— Time is kept as a continuous variable, meaning that the time step can be taken as small as necessary in order to reach the desired numerical accuracy. The latter can be tested thanks to the energy conservation. In practice we use a fourth order low storage Runge-Kutta algorithm, described in [148].
— all the spatial dimensions are discretized on L^3 lattice, and the discrete spatial indices i, j, k range from 0 to $L - 1$. We take periodic boundary conditions.

Given those choices, one easily extend all the continuum equations (5.57-5.60) to the discrete case. the discrete momenta read

$$k_{k_x, k_y, k_z} = \frac{1}{a}\sqrt{2\left(3 - \cos\left[\frac{2\pi k_x}{L}\right] - \cos\left[\frac{2\pi k_y}{L}\right] - \cos\left[\frac{2\pi k_z}{L}\right]\right)} , \tag{5.61}$$

where a is the lattice step. The biggest momentum included in our numerical simulation is therefore

$$\Lambda = \frac{\sqrt{12}}{a} . \tag{5.62}$$

5.3.6.3 Numerical results

In the following, the numerical computations are performed on a 12^3 lattice. The resummed energy-momentum tensor is computed thanks to the functional integration of equation (5.33), that we approximate by a Monte-Carlo average over 1000 configurations. The numerical outcome for $g = 0.5$ is represented in figure the 5.11.
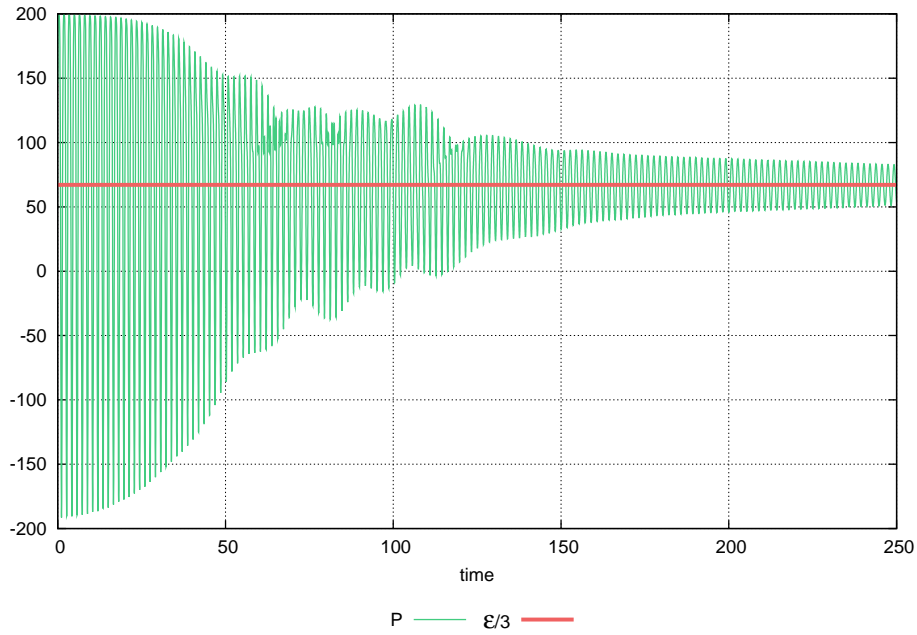
Figure 5.11: Time evolution of the resummed energy-momentum tensor given by (5.33) and computed thanks to the average over the fluctuating initial conditions (5.58). The resonance band is completely included in the simulation. The coupling constant is $g = 0.5$.

Here the lattice cutoff Λ in (5.62) has been chosen such that the resonance band is completely included in the simulation (i.e. $\Lambda > 3^{-\frac{1}{4}} m_0$). All the previous quantities are represented in lattice units, meaning that x^0 really reads $a^{-1} x^0$ while ϵ and p should read $a^4 \epsilon$ and $a^4 p$. Finally, let us mention that a second average over the lattice volume is performed for $T^{\mu\nu}_{\text{resum}}$. So what is really plotted is

$$\left\langle \left\langle T^{\mu\nu}_{\text{resum}} \right\rangle_{a,\mathring{a}} \right\rangle_{\text{lattice volume}} \tag{5.63}$$

Here, as in the figure 5.5 we observe the dampening of the oscillations of the pressure and its relaxation towards the expected value in order for an equation of state to form: $p = \frac{\epsilon}{3}$. Qualitatively, this relaxations happens through two distinct stages: the first one ($x^0 \leq 50$ for the $g = 0.5$ result of the previous plot) experiences a quick dampening of the pressure oscillations, while for the second stage ($x^0 \geq 50$) this relaxation is slower. figure 5.11 is the central result of this section, and the first hint of a possible equilibration of the system. We will conclude this macroscopic study by looking at how the previous result depends on the resonant modes and the coupling constant, while this section will be followed by a first look at what happens locally in the theory, by studying the local energy density profile.

5.3.6.4   How do the resonant modes affect the figure 5.11?

Given the study that we have performed in the section 5.2 and in the appendix 5.A on the stability of the modes a_k, one could ask what happens if we exclude the resonance band from our simulation. Would we loose the result of the figure 5.11? It turns out that this is not the case, as illustrated in the figure 5.12
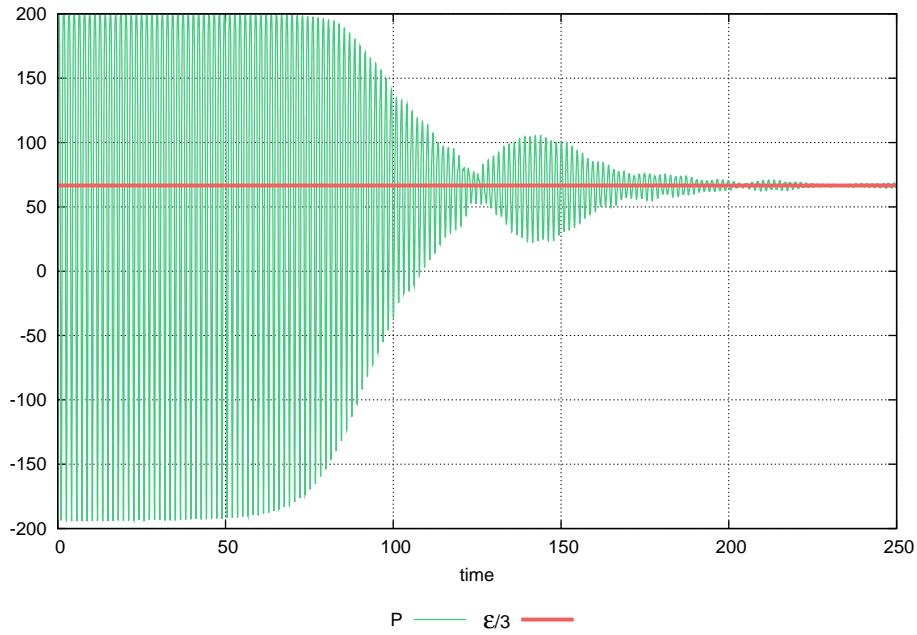
Figure 5.12: Time evolution of the resummed energy-momentum tensor. The resonance band is completely excluded in this simulation. The coupling constant is $g = 0.5$.

Here what we see is that while the relaxation process takes longer to start, is still happens and the final result at late times is unchanged: one still observes the formation of an equation of state. The two stages for this relaxation to take place are now the two followings: on a first part ($x^0 \leq 75$ for the $g = 0.5$ result of the previous plot) the pressure oscillates as in figure (5.1), while during the second stage the decrease of the oscillation is way faster than for 5.11. The conclusion of this short study is that while the final result of the macroscopic study of $T^{\mu\nu}$ does not depend on the resonant band, the intermediate stages are strongly affected by it.

5.3.6.5 How does the strength of the interactions affect figure 5.11?

What happens if we now change the value of the coupling constant g? Is there some transition between a regime where an EOS do form and a regime where it doesn't for some critical g? Is there some scaling between the EOS formation time x^0_{EOS} and g? We have performed several numerical simulations for g ranging from 0.5 to 8 (of course the last value should not be taken too seriously, as it corresponds to a $\frac{g^2}{4!} > 1$ where perturbative techniques may not be valid. This is presumably the reason why the last point of figure 5.14 is so off the fit), and the outcome is shown in the figure 5.13.
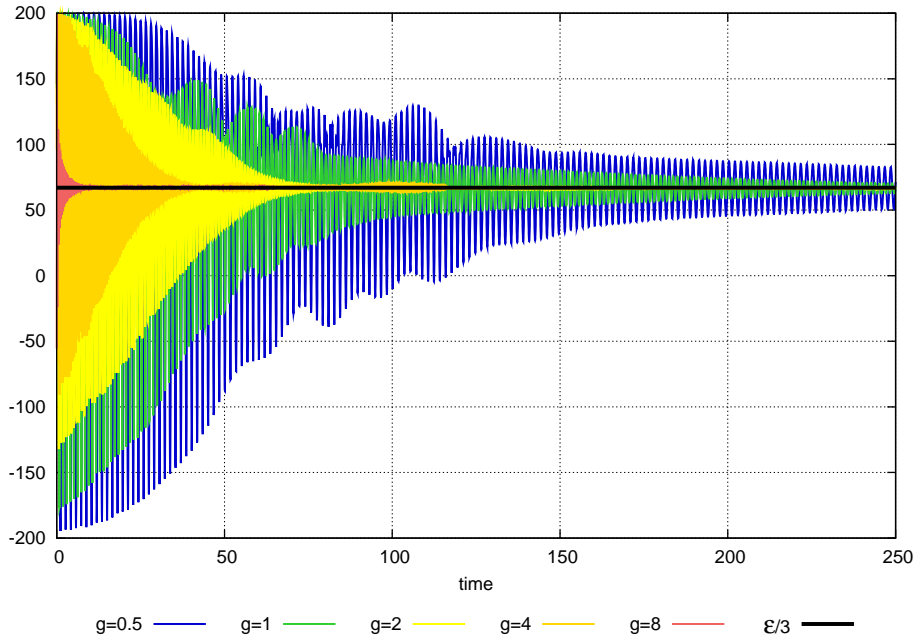
Figure 5.13: Time evolution of the resummed energy-momentum tensor for various values of the coupling constant: $g = 0.5, 1, 2, 4, 8$. The resonance band is completely included in the simulations.

Here we performed all the computations for the same energy density. This can be done since $\epsilon \propto Q^4/g^2$ with Q being the only dimensionful parameter of our theory. The latter can therefore be adjusted (through the choice of J) in order to have the same ϵ for all the values of g studied, which is the only way to make a meaningful comparison. What figure 5.13 teaches us is therefore that the stronger the interaction is, the faster the pressure relaxes towards its equilibrium value. To confirm this fact in a more quantitative way, we defined x^0_{EOS} in the different simulations as the time at which the pressure amplitude has been divided by four

$$p_{\text{resum}}\left(x^0_{\text{EOS}}\right) = \frac{p_{\text{resum}}(0)}{4} \ . \tag{5.64}$$

The different x^0_{EOS} obtained for the different values of g that we considered are represented in figure 5.14
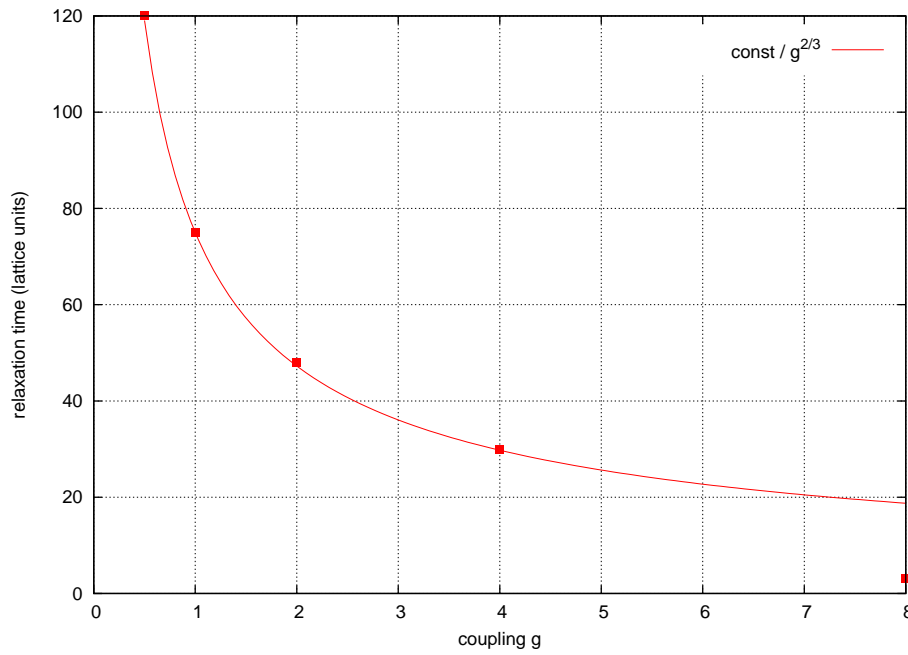
Figure 5.14: x^0_{EOS} defined through equation (5.64) as a function of the coupling g. The line represents the power law fit of equation (5.65)

As we can see, a power law fit seems to work pretty well for all the coupling that we used except the strongest one, possibly for the reasons explained before. The fit reads

$$x^0_{\mathrm{EOS}} = \frac{\mathrm{const}}{g^{\frac{2}{3}} \epsilon^{\frac{1}{4}}} \, , \tag{5.65}$$

in contrast with the result of equation (5.46) obtained in the previous simplistic spatially homogeneous model.

5.3.6.6 Local energy-density fluctuations

So far we have only looked at average quantities over the lattice volume. But we know that the equilibration of the system requires much more stringent conditions at the microscopic level. Since we are no longer in the spatially uniform case of the section 5.3.5, we cannot look at the phase-space density anymore, since it is now an infinite dimensional object. We could however look at the local energy-density fluctuations and seek there the first hints of local equilibration. Indeed, even if the energy is globally conserved, there are local energy fluctuations that could teach us how a subvolume exchanges energy with the rest of the system that acts as a heat bath. In particular, if the system is in local equilibrium, then the energy fluctuations should be those of a canonical ensemble with a density operator $\rho = e^{-\beta H}$ (where $\beta = \frac{1}{T}$). We have therefore studied the smallest subsystem achievable on a lattice: a single lattice site. The first thing that we looked at is the energy-density distribution at several times, shown on figure 5.15.
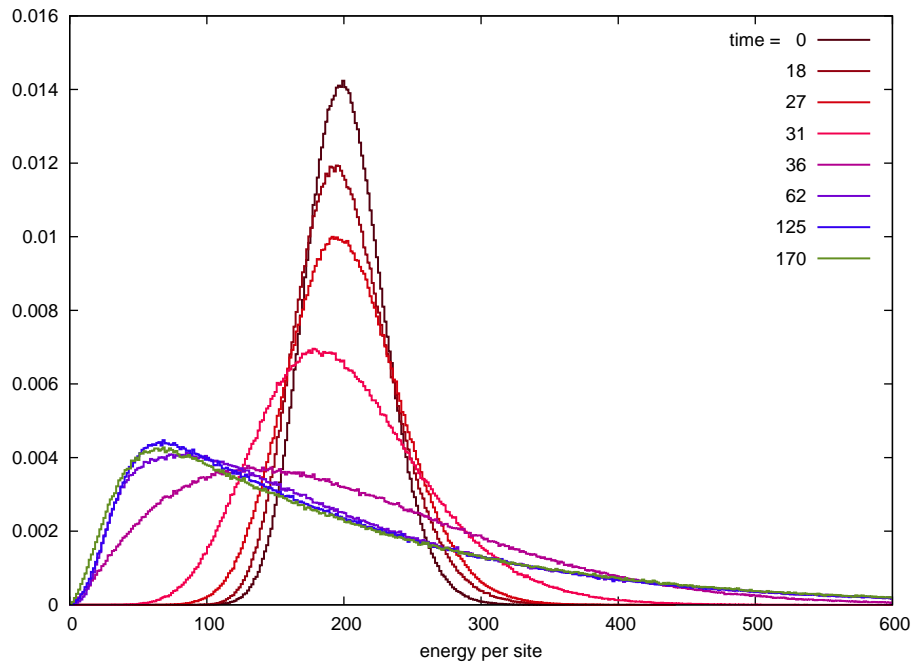
Figure 5.15: Distribution of ϵ at one lattice site, at different x^0 in the evolution. Here we have used $g = 0.5$.

These histograms are the probability distributions for the value of the energy-density on one lattice site. We see that the probability distribution at $x^0 = 0$ is completely dictated by the fluctuating spectrum (5.58) and (5.59). More precisely, the distribution of ϵ is a Gaussian centered on the mean energy density ($\frac{g^2}{4!}\varphi_0^4$ given our initial condition) with a width determined by (5.58) and (5.59). During the first stages of this evolution (three following times), the distribution of ϵ remains Gaussian-like, but its width tends to increase. Around $t \approx 36$ in lattice units, a drastic change occurs: the peak shifts towards smaller energies, its amplitude decreases and the tail of the distribution extends towards higher energies. After this change, the evolution is much slower, and a stationary distribution seems to be obtained at the latest times considered. This is in agreement with the decoherence of the pressure already discussed. Another study that can be performed on the energy-density is to look at its moments, defined as

$$C_n = \frac{\langle \epsilon^n \rangle}{\langle \epsilon \rangle^n} \ . \tag{5.66}$$

These moments are increasingly (with n) sensitive to changes in the shape of the distribution, as shown in the figure 5.16
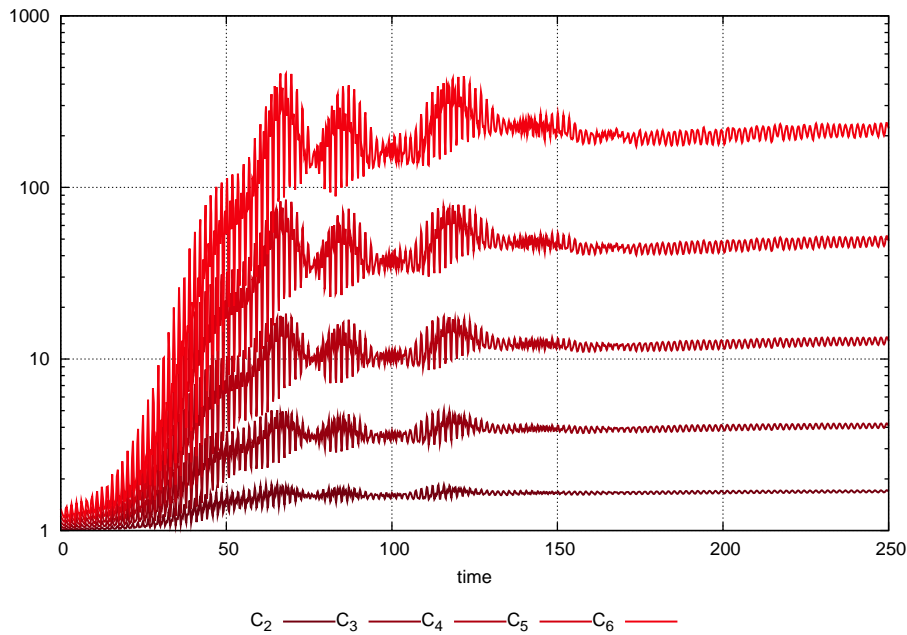
Figure 5.16: C_n defined as (5.66) as a function of time on one lattice site, for n ranging from 2 to 6. Here we have used $g = 0.5$.

At early stages, all the moments are comparable, in agreement with the narrow Gaussian shape for the local energy-density distribution observed in figure 5.15. Around $x^0 \approx 30$ a rapid change occurs and the moments start to become different, their amplitude being higher for higher n. After $x^0 \approx 70$, no subsequent change is observed and the moments seem to reach a plateau. This ends our study of the energy-momentum tensor of the fixed volume scalar field theory, and we will now consider other microscopic properties, like the spectral function and the occupation number.

5.4 Microscopic properties of fixed volume scalar field theory

We now consider some microscopic quantities that will tell us more about a possible equilibration of the scalar theory. We will study two quantities: the spectral function of the system and its the occupation number. The shape of the spectral function will teach us whether quasi-particles exist in the system, while the occupation number is an indication of a possible thermal equilibration (for which we expect a Bose-Einstein distribution, since scalar fields are spin 0 bosons). This section will be divided in three parts. Firstly, we will derive the analytical formulas necessary to numerically compute the spectral function ρ and the occupation number f_k. Secondly, we will compute these quantities and analyze the outcome of our simulations. We will in a third part make some side-remarks and compute other quantities like the entropy.

5.4.1 Analytical derivation of the spectral function and the occupation number

5.4.1.1 Spectral function

The spectral function is related to the retarded propagator in the following way

$$\rho(\omega, \boldsymbol{k}, y^0) = 2\text{Im} \int_0^{+\infty} \mathrm{d}x^0 \int \mathrm{d}^3\boldsymbol{x}\, e^{i\omega x^0} e^{-i\boldsymbol{k}.\boldsymbol{x}} \mathcal{G}_R(x^0 + y^0, \boldsymbol{x}, y^0, 0)\,, \tag{5.67}$$

where $\mathcal{G}_R$ is the dressed retarded propagator, related to the $\mathcal{G}^{\pm\pm}$ that we described in great detail in the section 4.2

$$\mathcal{G}_R = \mathcal{G}_{++} - \mathcal{G}_{+-}\,. \tag{5.68}$$

Diagrammatically at leading order, it also looks like equation (4.101)

$$\mathcal{G}_R^{\text{LO}}(x,y) = \; x \rule[0.5ex]{3em}{0.4pt} \; y \quad = \quad x \cdots y \; . \tag{5.69}$$

This should also be improved by the same resummation as the one used for $T^{\mu\nu}$. However, $T_{\text{NLO}}^{\mu\nu}$ was of order 1, whereas $\mathcal{G}_R^{\text{LO}}$ is of order 1, and $\mathcal{G}_R^{\text{NLO}}$ is of order g^2. The computation of $\mathcal{G}_R^{\text{NLO}}$ is therefore in a sense very similar to the computation[7] we would perform for $\left\langle \phi^{(+)}(x)\phi^{(-)}(y)\right\rangle_{\text{NNLO}}$. There are three kind of topologies that contribute to $\mathcal{G}_R^{\text{NLO}}$

$$\mathcal{G}_R^{\text{NLO}} = \; x \cdots y \; + \; x \cdots y \; + \; x \cdots y$$

$$= \mathcal{G}_1^{\text{NLO}} + \mathcal{G}_2^{\text{NLO}} + \mathcal{G}_3^{\text{NLO}} \; . \tag{5.70}$$

Given the section 4.2, it is easy to relate those diagrams to the operator $\widehat{O}$. Firstly, one can see that the operator that gave ψ is exactly the one which gives $\mathcal{G}_1^{\text{NLO}}$ if it acts on one of the φ of the previous figure. Therefore

$$\mathcal{G}_1^{\text{NLO}}(x,y) = \int_\Sigma \mathrm{d}\boldsymbol{\Sigma}_u \left[i\left(\psi(u)\widehat{T}(u)\right) \right.$$
$$\left. -\frac{1}{2}\int \frac{\mathrm{d}^3\boldsymbol{k}}{2|\boldsymbol{k}|(2\pi)^3} \int \mathrm{d}\boldsymbol{\Sigma}_v \left[\left(a_{+\boldsymbol{k}}(u)\widehat{T}(u)\right)\left(a_{-\boldsymbol{k}}(v)\widehat{T}(v)\right)\right] \right]_{\text{same } \varphi} \mathcal{G}_R^{\text{LO}}(x,y) \; . \tag{5.71}$$

Here same φ means that the operators $\widehat{T}(u)\widehat{T}(v)$ should act on the same φ, i.e.

$$\left[\widehat{T}(u)\widehat{T}(v)\right]_{\text{same } \varphi} \varphi(x_1)\cdots\varphi(x_n) = \sum_{i=1}^n \varphi(x_1)\cdots\varphi(x_{i-1})\left[\widehat{T}(u)\widehat{T}(v)\varphi(x_i)\right]\varphi(x_{i+1})\cdots\varphi(x_n) \; . \tag{5.72}$$

Secondly, we have

$$\mathcal{G}_2^{\text{NLO}} = \left[-\frac{1}{2}\int_\Sigma \mathrm{d}\boldsymbol{\Sigma}_u \int \frac{\mathrm{d}^3\boldsymbol{k}}{2|\boldsymbol{k}|(2\pi)^3}\int \mathrm{d}\boldsymbol{\Sigma}_v \left[\left(a_{+\boldsymbol{k}}(u)\widehat{T}(u)\right)\left(a_{-\boldsymbol{k}}(v)\widehat{T}(v)\right)\right]\right]_{\text{same } V''(\varphi)} \mathcal{G}_R^{\text{LO}} \tag{5.73}$$

Here same $V''(\varphi)$ means that the operators $\widehat{T}(u)\widehat{T}(v)$ act on one $V''(\varphi)$, one T on each φ. Diagrammatically this operator removes the two φ's of the same insertion, and puts $\mathcal{G}_{+-}$ instead (see equation (4.101)). Finally, Things are a bit more complicated for the last diagram. First, we rewrite it as

$$\mathcal{G}_3^{\text{NLO}}(x,y) = \int \mathrm{d}^4w\,\mathrm{d}^4z\, \mathcal{G}_R^{\text{LO}}(x,w)\,\Sigma_R^{1-\text{loop}}(w,z)\,\mathcal{G}_R^{\text{LO}}(z,y) \; . \tag{5.74}$$

---

7. This makes sense since $\left\langle \phi^{(+)}(x)\phi^{(-)}(y)\right\rangle$ at lowest order is the sum of two disconnected diagrams and gives $\varphi(x)\varphi(y)\sim\frac{1}{g^2}$, while this cannot be the case for

$$\mathcal{G}_R \sim \left\langle \left[\phi^{(+)}(x),\phi^{(-)}(y)\right]\right\rangle \; ,$$

which gives $[\varphi,\varphi]=0$ at order $\frac{1}{g^2}$. All the orders are therefore shifted between $\mathcal{G}_R$ and $\left\langle \phi^{(+)}(x)\phi^{(-)}(y)\right\rangle$.

In the language of the $1 - 2$ basis, we know (see chapter 7) that since φ is attached to 2 and $\mathcal{G}_R = \mathcal{G}_{21}$, $\Sigma_R^{1-\text{loop}}$ receives only one contribution [8]

$$\Sigma_R^{1-\text{loop}}(w,z) = \frac{1}{2} V'''(\varphi(w)) V'''(\varphi(z)) \mathcal{G}_R^{\text{LO}}(w,z) \left(\mathcal{G}_{-+}(w,z) + \mathcal{G}_{+-}(w,z) \right) . \tag{5.75}$$

Using the result of equation (4.114) for $\mathcal{G}_{+-}$, this gives

$$\mathcal{G}_3^{\text{NLO}} = \left[-\frac{1}{2} \int_\Sigma d\Sigma_u \int \frac{d^3 k}{2|\mathbf{k}|(2\pi)^3} \int d\Sigma_v \left[\left(a_{+\mathbf{k}}(u) \widehat{T}(u) \right) \left(a_{-\mathbf{k}}(v) \widehat{T}(v) \right) \right] \right]_{\text{distinct } \varphi's} \mathcal{G}_R^{\text{LO}} . \tag{5.76}$$

Here distinct $\varphi's$ means that the two $T's$ in the operator of the previous formula must act on $\varphi's$ that live on different space-time points. Putting everything together, (5.71), (5.73) and (5.76) gives the expected result

$$\mathcal{G}_R^{\text{NLO}}(x,y) = \int_\Sigma d\Sigma_u \left[i \left(\psi(u) \widehat{T}(u) \right) \right.$$
$$\left. -\frac{1}{2} \int \frac{d^3 k}{2|\mathbf{k}|(2\pi)^3} \int d\Sigma_v \left[\left(a_{+\mathbf{k}}(u) \widehat{T}(u) \right) \left(a_{-\mathbf{k}}(v) \widehat{T}(v) \right) \right] \right] \mathcal{G}_R^{\text{LO}}(x,y) , \tag{5.77}$$

which is nothing but

$$\mathcal{G}_R^{\text{NLO}}(x,y) = \widehat{O} \, \mathcal{G}_R^{\text{LO}}(x,y) . \tag{5.78}$$

We will therefore define $\mathcal{G}_R^{\text{resum}}(x,y)$ as

$$\mathcal{G}_R^{\text{resum}}(x,y) = e^{\widehat{O}} \, \mathcal{G}_R^{\text{LO}}(x,y) , \tag{5.79}$$

which can also be re-expressed (as shown in the case of $T^{\mu\nu}$) as

$$\mathcal{G}_R^{\text{resum}} = \int [\mathcal{D}\,a] \, e^{-\frac{1}{2} \int\int d^3 u \, d^3 v \, a(0,u) \mathcal{G}_{+-}^{-1}(u,v) a(0,v)} \mathcal{G}_R^{\text{LO}} [\varphi + a, \dot{\varphi} + \dot{a}] . \tag{5.80}$$

Numerically, it is more involved to compute it as it depends on two space-time points. But even if the system that we consider is (at least initially) out of equilibrium, meaning that time translation invariance of $\mathcal{G}_R^{\text{LO}}$ is broken, it is not the case for translation invariance in space. We can therefore limit ourselves to the computation of $\mathcal{G}_R^{\text{LO}}(x^0, \mathbf{x}, y^0, 0)$. And there is a simple way to obtain this quantity. Firstly, recall that (see the section 4.2.2.1)

$$\left[\Box_y + V''(\varphi(y)) \right] \mathcal{G}_R^{\text{LO}}(x,y) = -i\delta(x-y) \tag{5.81}$$

Secondly, considering a small fluctuation a propagating on top of φ

$$\left[\Box_y + V''(\varphi(y)) \right] a(y) = 0 , \tag{5.82}$$

we easily get the following Green's formula, following the same steps as in the section 4.2.2.1

$$a(x) = -i \int_{y^0} d^3 y \left[\mathcal{G}_R^{\text{LO}}(x,y) \partial_y^0 a(y) - a(y) \partial_y^0 \mathcal{G}_R^{\text{LO}}(x,y) \right] . \tag{5.83}$$

Therefore, if we initialize a by defining

$$a(y^0, \mathbf{y}) = 0 , \qquad\qquad \partial_y^0 a(y^0, \mathbf{y}) = i\delta(\mathbf{y}) , \tag{5.84}$$

we get

$$a(x) = \mathcal{G}_R^{\text{LO}}(x^0, \mathbf{x}, y, \mathbf{0}) , \tag{5.85}$$

Numerically we will therefore use this trick and compute $a(x)$ with the linearized EOM (5.82) initialized at y^0 with (5.84) in order to have access to $\mathcal{G}_R^{\text{LO}}(x^0, \mathbf{x}, y, \mathbf{0})$, from which we get $\mathcal{G}_R^{\text{resum}}(x^0, \mathbf{x}, y, \mathbf{0})$ thanks to the resummation technique (5.80).

---

8. From the closed loop $G_{22}(w,z) G_{21}(w,z)$, where $G_{22} = \frac{1}{2} \left(\mathcal{G}_{-+} + \mathcal{G}_{+-} \right)$ has been replaced in (5.75).

5.4.1.2   Occupation number

The occupation number f_k "counts" the number of particle with a given momentum k. It is therefore related to the creation and annihilation operators that we have introduced in the section 4.1. We can write for f_k

$$2\omega_k V(1 + 2f_k) = \left\langle a_k^\dagger a_k + a_k a_k^\dagger \right\rangle ,\tag{5.86}$$

where[9] $\omega_k = \sqrt{k^2 + m^2}$, V is the volume and $\langle\rangle$ stands for the average over field initial conditions. Using equation 4.16, we can rewrite the right hand side as

$$\left\langle a_k^\dagger a_k + a_k a_k^\dagger \right\rangle = \int d^3x d^3y \left[e^{ik(x-y)} \overset{\leftrightarrow}{\partial_x^0} \overset{\leftrightarrow}{\partial_y^0} \left\langle \phi^+(x)\phi^-(y) + \phi^-(x)\phi^+(y) \right\rangle \right]_{x^0 = y^0} ,\tag{5.87}$$

where the $x^0 = y^0$ equality is only taken after the derivatives have acted on the fields. The field dependent term of the right hand side is nothing but

$$\left\langle \phi^+(x)\phi^-(y) + \phi^-(x)\phi^+(y) \right\rangle = \mathcal{G}_{+-}(x,y) + \mathcal{G}_{-+}(x,y) = 2\mathcal{G}_{22}(x,y) ,\tag{5.88}$$

where we recall that G_{22} is the symmetric propagator. It can be treated exactly in the same way as $\left\langle \phi^{(+)}(x)\phi^{(-)}(y) \right\rangle$ was in section 4.2 to get the same resummation formula. Knowing that

$$\mathcal{G}_{22}^{\text{LO}}(x,y) = \varphi(x)\varphi(y) ,\tag{5.89}$$

One gets the result

$$f_k^{\text{resum}}(x^0) = \frac{1}{2\omega_k V} \left\langle \left| \int d^3x \, e^{ikx} \overset{\leftrightarrow}{\partial_x^0} \phi(x) \right| \right\rangle - \frac{1}{2} = \frac{1}{2\omega_k V} \left\langle |\dot\phi_k(x^0)|^2 + \omega_k^2 |\phi_k(x^0)|^2 \right\rangle - \frac{1}{2} ,\tag{5.90}$$

where ϕ_k is the 3D Fourier transform of ϕ

$$\phi_k = \int d^3x \, e^{ikx} \phi(x) ,\tag{5.91}$$

and as usual ϕ is the solution of the classical EOM for the initial condition depicted in formula 5.58. Evaluating numerically f_k is therefore an easier task than evaluating ρ.

5.4.2   Numerical results

5.4.2.1   Formation of quasi-particles

A trivial assertion is that if the retarded propagator is very close from the one of a free massive theory, then since

$$G_R(p^2) = \frac{i}{p^2 - m^2 + ip^0\epsilon} ,\tag{5.92}$$

using the equality (where pv stands for principal value)

$$\frac{i}{x + i\epsilon} = \text{pv}\left(\frac{1}{x}\right) + \pi\delta(x) ,\tag{5.93}$$

we would have

$$\mathcal{G}_R(p^2) \approx \pi\epsilon(p^0)\delta((p^0)^2 - |p|^2 - m^2) + i\text{pv}\left(\frac{1}{(p^0)^2 - |p|^2 - m^2} \right) ,\tag{5.94}$$

---

9. We will see later on that even if we start with a massless scalar field theory, a thermal mass develops during the time evolution of the system.

and plugging this into (5.67) would give

$$\rho(\omega, \boldsymbol{k}, y^0) \sim \delta\left(\omega^2 - |\boldsymbol{k}|^2 - m^2\right) . \tag{5.95}$$

Numerically, we cannot reproduce this δ function even if it was present: indeed, we cannot do the $\int_0^{+\infty} \mathrm{d}x^0$ integration, as it would imply to follow the evolution of the system during an infinite time. What we really compute is therefore

$$\rho(\omega, \boldsymbol{k}, y^0) = 2\mathrm{Im} \int_0^{+\infty} \mathrm{d}x^0 \int \mathrm{d}^3 \boldsymbol{x}\, e^{i\omega x^0} e^{-\frac{(x^0)^2}{\sigma^2}} e^{-i\boldsymbol{k}.\boldsymbol{x}} \mathcal{G}_R(x^0 + y^0, \boldsymbol{x}, y^0, 0) , \tag{5.96}$$

where σ is chosen in such a way that we only have to follow the evolution of the system during a finite – numerically manageable – amount of time, as the integrand goes to 0 for $x^0 \gg \sigma$. The price to pay for this simplification is that the width that will appear in the (ω, k) plane for the spectral function will be unphysical, related to the value of σ. In the figure 5.17, we have represented $\rho(\omega, k, y^0 = 0)$ for a coupling constant $g = 1$.
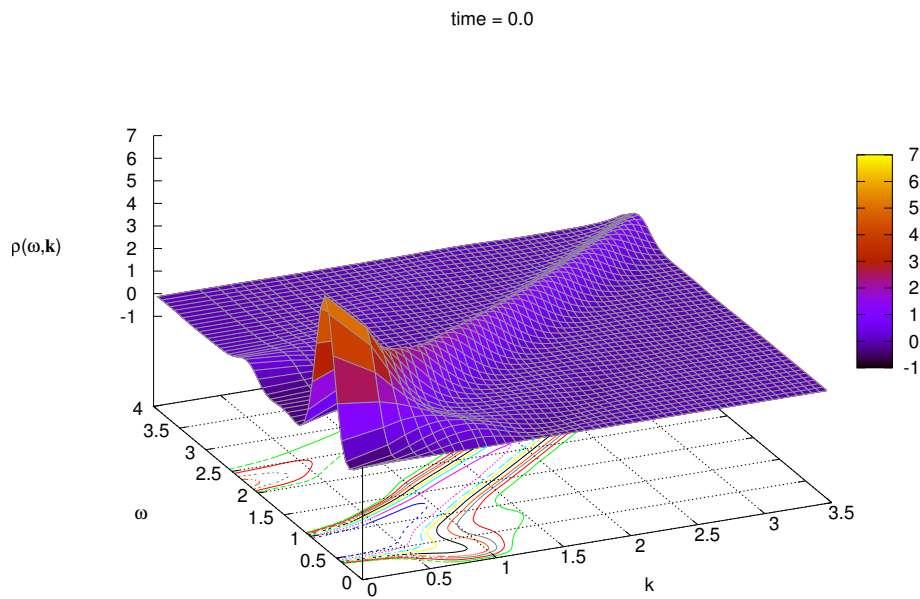
Figure 5.17: Spectral function $\rho(\omega, \boldsymbol{k}; y^0 = 0)$ at the initial time. The computation is performed on a 20^3 lattice, and the coupling constant is $g = 1$.

We observe a branch (ω, k) along a curve $\omega^2 = k^2 + m^2$. But this is not the only structure that emerges. There are also higher mass excitations with a smaller magnitude for ρ. This picture is qualitatively modified during the time evolution of the system, as one can see on the following two plots
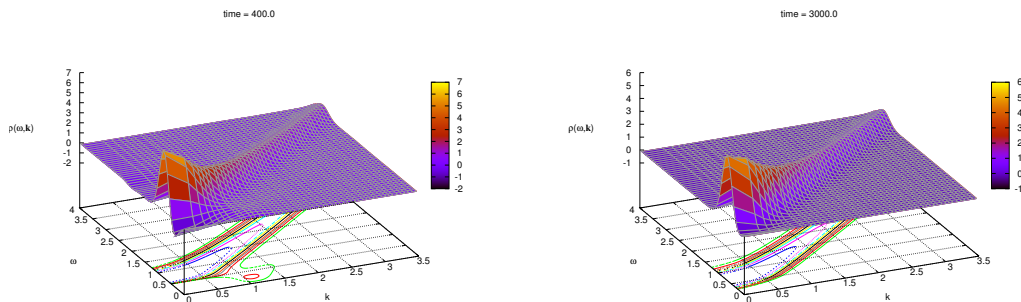
Figure 5.18: Spectral function $\rho(\omega, \boldsymbol{k}; y^0)$ at the times $y^0 = 400$ (left) and $y^0 = 3000$ (right). The numerical simulation corresponds to the same parameters as in the figure 5.17.

At a time $y^0 = 400$, the higher mass excitations have almost completely decayed, and nothing is left but the lower mass excitation at a time $y^0 = 3000$. This means that the system can be correctly described by a collection of quasi-particles of mass [10] m. The transient regime during which this quasi-particle description is not valid approximately corresponds to the regime before the formation of an EOS. The remaining question to be answered here is what is the quasi-particle mass, and more importantly, can we understand it theoretically? We have fitted at various times the peak of the main branch as $\omega = \sqrt{k^2 + m^2}$. The result that we got from here is the green curve of the following figure 5.19.
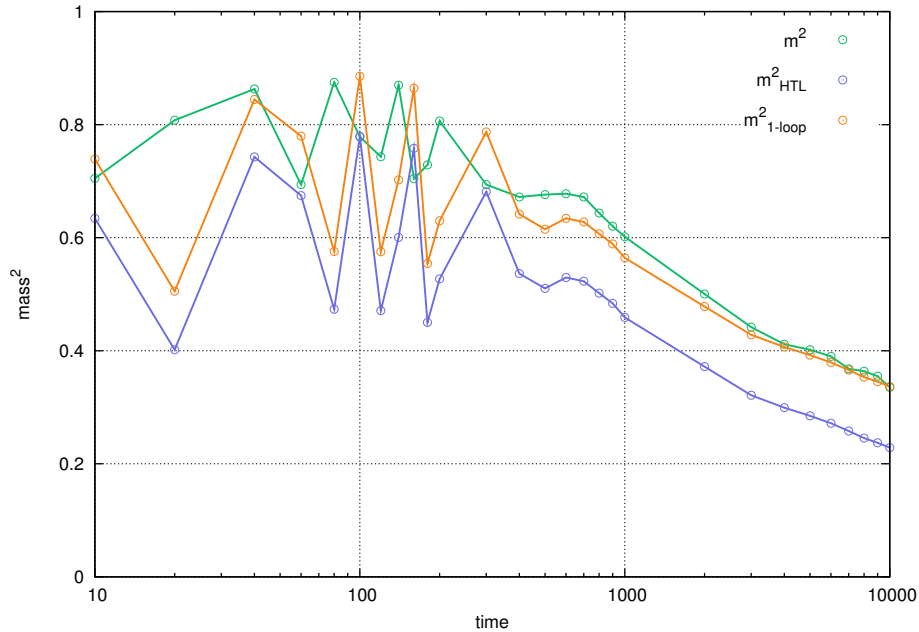
Figure 5.19: Mass of the quasi-particles. The green line was obtained by a fit of the main dispersion branch with a function of the form $\omega = \sqrt{k^2 + m^2}$. The blue line is the outcome of a 1-loop analytic calculation from the occupation number, while the orange one is the result of a 1-loop gap equation that resums recursively all the daisy diagrams.

As one can see, the result for this m is not stable until $y^0 \sim 100 - 400$, and evolves smoothly afterwards. In addition, one can see on this curve that after this time, the mass of the quasi-particles slowly decreases. One can relate this with a change in the occupation number. Indeed, a naive estimate for m can be made within the hard thermal loop (HTL) framework [149, 150]

$$m^2_{\text{HTL}} = \int \frac{\mathrm{d}^3 \boldsymbol{k}}{(2\pi)^3 2k} f_{\boldsymbol{k}} \ . \tag{5.97}$$

This m gives qualitatively the same behaviour as the one numerically extracted form the spectral function, but differs by an almost constant offset. Nevertheless, it allows us to interpret the global decrease of the mass as a transfer of energy from soft modes to hard modes – this interpretation is correct only if the number of quasi-particles $N \sim \int \mathrm{d}^3 \boldsymbol{k} \, f_{\boldsymbol{k}}$ is approximately conserved during the time evolution. This will be discussed in the next subsection, as well as the origin of the orange line that seems to agree much better.

5.4.2.2 Classical thermal equilibration with overpopulated initial conditions

We now turn our attention to the occupation number, defined in equation (5.90). A good numerical check can first be performed by taking $J = 0$, which leads to $\varphi = 0$. In this case, the

---

10. See the appendix 5.B for the effective Hamiltonian that would account for this hypothesis.

small fluctuations which were plane waves in the remote past stay plane waves during their whole evolution at negative times, where they follow the vacuum linearized equation

$$\Box a_k = 0 . \tag{5.98}$$

At $x^0 = 0$, the initial condition therefore reads

$$\phi(0, \boldsymbol{x}) = \int \frac{\mathrm{d}^3 \boldsymbol{k}}{(2\pi)^3 \sqrt{2|\boldsymbol{k}|}} \operatorname{Re}\left[c_{\boldsymbol{k}} \, e^{i k.x}\right] ,$$

$$\dot{\phi}(0, \boldsymbol{x}) = \int \frac{\sqrt{|\boldsymbol{k}|}\mathrm{d}^3 \boldsymbol{k}}{(2\pi)^3 \sqrt{2}} \operatorname{Re}\left[i \, c_{\boldsymbol{k}} \, e^{i k.x}\right] , \tag{5.99}$$

which means

$$\phi_{\boldsymbol{k}}(0) = \frac{c_{\boldsymbol{k}} + c_{\boldsymbol{k}}^*}{\sqrt{2|\boldsymbol{k}|}} \qquad\qquad \dot{\phi}_{\boldsymbol{k}}(0) = i|\boldsymbol{k}|\frac{c_{\boldsymbol{k}} - c_{\boldsymbol{k}}^*}{\sqrt{2|\boldsymbol{k}|}} . \tag{5.100}$$

Since in the discrete case

$$\langle c_{\boldsymbol{k}} c_{\boldsymbol{k}'}^* \rangle = V \delta_{\boldsymbol{k}\boldsymbol{k}'} , \tag{5.101}$$

by plugging (5.100) into (5.90) we obtain

$$f_{\boldsymbol{k}}^{\mathrm{resum}}(x^0) = \frac{1}{2|\boldsymbol{k}|V} \left\langle |\dot{\phi}_{\boldsymbol{k}}(x^0)|^2 + \omega_{\boldsymbol{k}}^2 |\phi_{\boldsymbol{k}}(x^0)|^2 \right\rangle - \frac{1}{2} = 0 . \tag{5.102}$$

Therefore, in the vacuum case the occupation number is zero. Note that this would not be the case if the $\frac{1}{2}$ term was not present (the latter coming from the non vanishing commutator between the creation $a_{\boldsymbol{k}}^\dagger$ and the annihilation $a_{\boldsymbol{k}}$ operators). We have performed a simulation with (5.100) as initial conditions and we have obtained $f_{\boldsymbol{k}} = 0$ up to statistical error (that scale as $\frac{1}{\sqrt{N_{\mathrm{conf}}}}$, with N_{conf} the number of initial configuration in the Monte-Carlo simulation) until very late times, even larger than those presented in the following [11]. Let us now see what we obtain for non-zero J, i.e. a non-zero φ. We first considered a spatially homogeneous J. In this case, φ_0 does not depend on position, and $\varphi_{\boldsymbol{k}}(0)$ is therefore localized at $k = 0$. Since the spectrum of fluctuations is just an order 1 correction compared to the background field $\varphi_0 \sim \frac{1}{g}$, the occupation number should be localized at $k = 0$ at the initial time [12]. This is indeed the case, as can be seen on the figure 5.20.

---

11. Let us note here that this may no longer be true in classical Yang-Mills simulations, where a phenomenon called vacuum thermalization takes place [151]. This phenomenon appears faster than in the scalar theory, especially if one increases the coupling.

12. Of course the hierarchy between the background field and the small fluctuations is less obvious for $g \sim 1$, but the prefactor $\frac{1}{4!}$ plays an important role in this case and $g \sim 1$ still corresponds to a weakly coupled scalar interaction. This hierarchy is therefore still respected at $g = 1$.
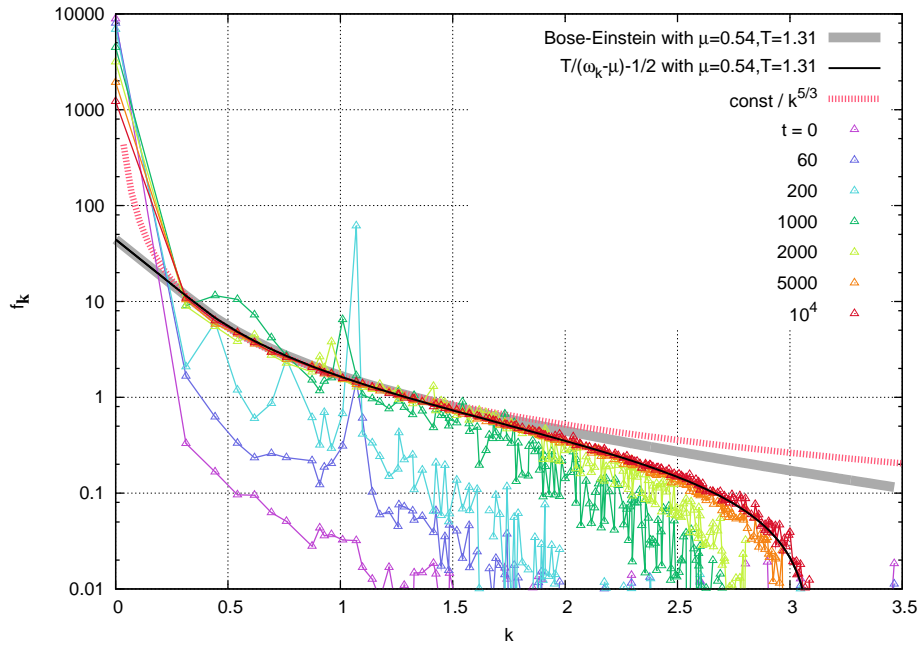
Figure 5.20: Time evolution of the occupation number f_k. The gray band represents a fit by a Bose-Einstein distribution. The dashed red band is a fit by a pure power law $k^{-5/3}$ (5.103). The thin black line is a fit by a distribution of the form given in eq. (5.108).

As expected, f_0 is five orders of magnitude above its value for $k \neq 0$ at the initial time. But as time increases, the picture for f_k is modified: is stops being localized at zero momentum and starts to expand towards higher momentum. This is in complete agreement with the decoherence explained in the section 5.3. The peak in the occupation number that appears in the previous plot at quite early times around $k = 1.1$ also has a well understood explanation: it corresponds to the resonance band given our set of parameters. At later times, the evolution of f_k is slower, and not much happens after a time $x^0 \sim 10^4$. An equilibrium distribution function seems to be reached. To find what it is, we have performed several fits, explained in the legend of the figure 5.20. The first idea is to fit f_k as

$$f_k = a\, k^b \,, \tag{5.103}$$

with a and b two free parameters. This scaling distribution function is inspired from the physics of turbulence [31, 37, 38, 152–156]. Indeed, our system shares some features with the Kolmogorov cascade process [157, 158], where energy is constantly injected into the soft modes and cascades towards higher momenta at a given rate k^b. In our simulation, we have found the best fit for $b \sim \frac{5}{3}$, and we have observed that while a band of soft modes are well-fitted, nor the zero-mode neither the hardest modes of the simulation are well described. In addition, this fit should not work at infinitely late times, since in our system the energy is injected once and for all at the start of the time evolution, and is then conserved. If a Kolmogorov cascade phenomenon was to happen in our system, it could therefore only be a transient process: it would cease after the energy of the soft modes is depleted. The second fit that we have tried was with a Bose-Einstein distribution function

$$f_k^{\text{BE}} = \frac{1}{e^{\frac{\omega_k - \mu}{T}} - 1} \,. \tag{5.104}$$

An interesting fact is that the best fit was achieved with a non-zero chemical potential. Even if the particle number is not exactly conserved, this seems to suggest that the particle number-changing processes are slow compared to the ones that conserve it. But this should not be a surprise in a weakly coupled scalar field theory. Indeed, since $\times \sim g^2$, the cross-section

of elastic collisions (that do conserve the particle number and that are 2 to 2 processes in the quartic scalar field theory) is of the order

$$\sigma_{\text{el}} \sim g^4 , \tag{5.105}$$

while the first particle changing process is $\times \sim g^4$, which gives a cross-section of the order of

$$\sigma_{\text{inel}} \sim g^8 . \tag{5.106}$$

The bottom line of this hand waving argument is that we can understand the presence of $\mu \neq 0$ since the number-changing inelastic processes are much slower than the elastic ones (but μ should decrease as time goes to infinity since the particle number is not conserved). The particle number should therefore only experience slow changes. This is confirmed in the figure 5.21
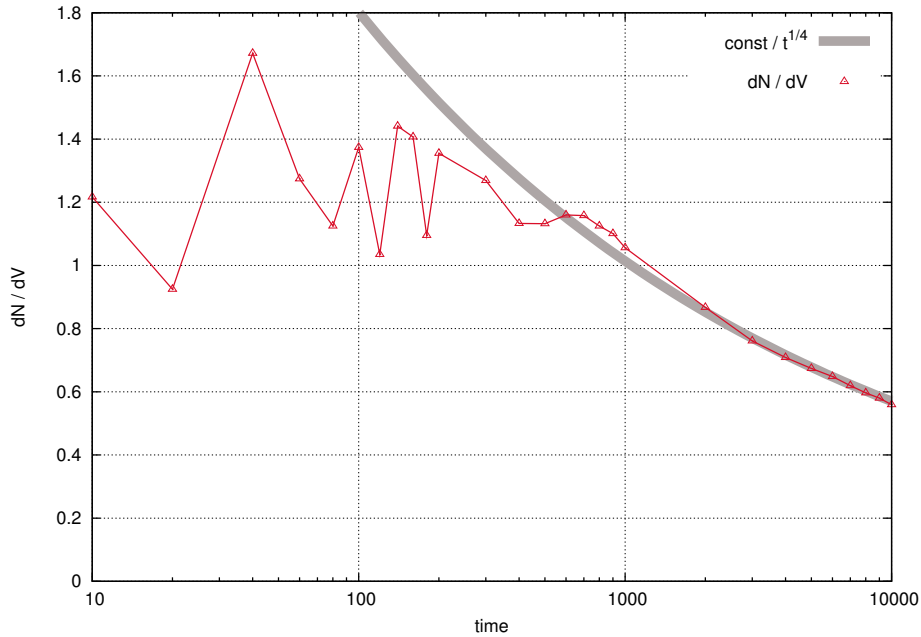
Figure 5.21: Time evolution of the quasi-particle density in the system. Gray band: fit of the tail with a power law $\left(x^0\right)^{-\frac{1}{4}}$.

where we have plotted

$$n = \int \frac{\mathrm{d}^3 k}{(2\pi)^3} f_k . \tag{5.107}$$

After a first stage where n is ill-defined (expected since the quasi-particles are not yet formed in the system), it starts to very slowly decay. Let us now discuss the sign of the chemical potential. We find it positive, meaning that there is an excess of particles in the system, that a Bose-Einstein distribution cannot accommodate. Let us conclude the analysis of this Bose-Einstein fit by saying that although it describes correctly a wider band of modes than the power law fit, it still fails to describe the zero-mode and the hard tail of the spectrum. The best fit that we have found is a classical fit, obtained by Taylor-expanding the Bose-Einstein distribution function and keeping only the first two terms

$$f_k^{\text{clas}} = \frac{T}{\omega_k - \mu} - \frac{1}{2} . \tag{5.108}$$

The $\frac{1}{2}$ is crucial in order to correctly reproduce the hard tail of the distribution function at late times. Since we are using the classical-statistical framework, where we know from section 4.3 that f_k should be much larger than 1, it should not really matter to keep it or not. But there are three reasons to do so. Firstly, since the CSA completely takes into account the LO and the NLO of the full theory, it makes sense to keep the first two terms (and not only the leading one) when Taylor-expanding f_k^{BE}. Secondly, in the derivation of f_k, one can track the origin of this $\frac{1}{2}$ and in formula (5.86) we see that it comes from the canonical commutation relation between creation and annihilation operators. Thirdly, one would not obtain a vanishing occupation for vacuum fluctuations if this $\frac{1}{2}$ is was neglected. We therefore keep it, even if in this hard mode region where $f_k \leq 1$ the result of the CSA should not be trusted. Indeed, in the the full theory f_k should converge towards f_k^{BE}, that differs from f_k^{clas} precisely in this region. With f_k^{clas}, all the modes except $k = 0$ are perfectly fitted at late time. In addition, it should be noted that the best fit is achieved for $\mu \approx m$. This is the maximal value that μ can take, otherwise the occupation number would be negative at soft momentum. When a chemical potential reaches its maximal value and one still observes a particle excess in the zero mode, this is a strong evidence of the formation of a Bose-Einstein condensate. Consider for a moment that both ϵ_0 and n_0 are conserved by the time evolution. If the classical equilibrium is reached at some point (assuming that $\mu = m$), then at this time one has

$$\epsilon = \int \frac{\mathrm{d}^3 k}{(2\pi)^3} \, \omega_k \left(\frac{T}{\omega_k - m} - \frac{1}{2} \right) = \epsilon_0 \, , \tag{5.109}$$

from which one deduces T. If

$$n_0 > n = \int \frac{\mathrm{d}^3 k}{(2\pi)^3} \left(\frac{T}{\omega_k - m} - \frac{1}{2} \right) \, , \tag{5.110}$$

then the system cannot accommodate all the particles that are present at the initial time. In order to still conserve the energy, the excess is stored in the zero-mode. This is Bose-Einstein condensation. In our case this should only be a transient state as n is not conserved: the Bose-Einstein condensate should decay at very late times. This will be confirmed in the figure 5.24. We have thus shown that the (transient in the sense just explained) equilibrium distribution function is not just f_k^{clas} but instead

$$f^{\mathrm{class}} = n_0 \, \delta(k) + \frac{T}{\omega_k - \mu} - \frac{1}{2} \, . \tag{5.111}$$

With this in mind, one can compute what fraction of energy is stored in which modes during the time evolution, and do the same for the fraction of particle number. The results are shown in the figure 5.22.
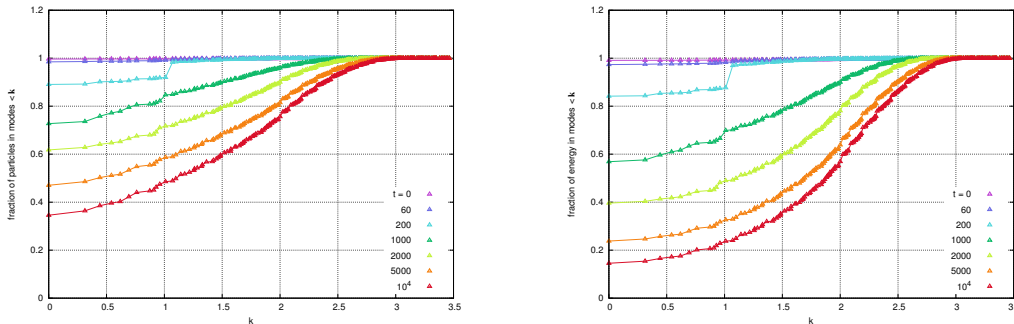

Figure 5.22: Left: fraction of particles contained in the modes $|l| \leq |k|$, at various stages of the time evolution. Right: fraction of energy contained in the modes $|l| \leq |k|$.

At early times (up to $x^0 \sim 100$), all the particles and all the energy are stored in the zero mode, as a consequence of our initial condition $\varphi_k \propto \delta(k)$. At subsequent times ($x^0 = 200$), a

large fraction of the energy is still in the zero mode, while the remainder is almost entirely in the resonance band. At the latest times represented in the previous figures ($x^0 = 10^4$ in lattice units), the zero mode still contains about 35% of the particles and 15% of the energy.

One objection could be made on the existence of the Bose-Einstein condensate: since we have initialized the system with $\varphi_k(0) = \varphi_0 \delta(k)$, one could be tempted to say that the excess in f_k that we observe at late times is just a remaining feature of our initial condition. The following figure 5.23 disproves this argument.
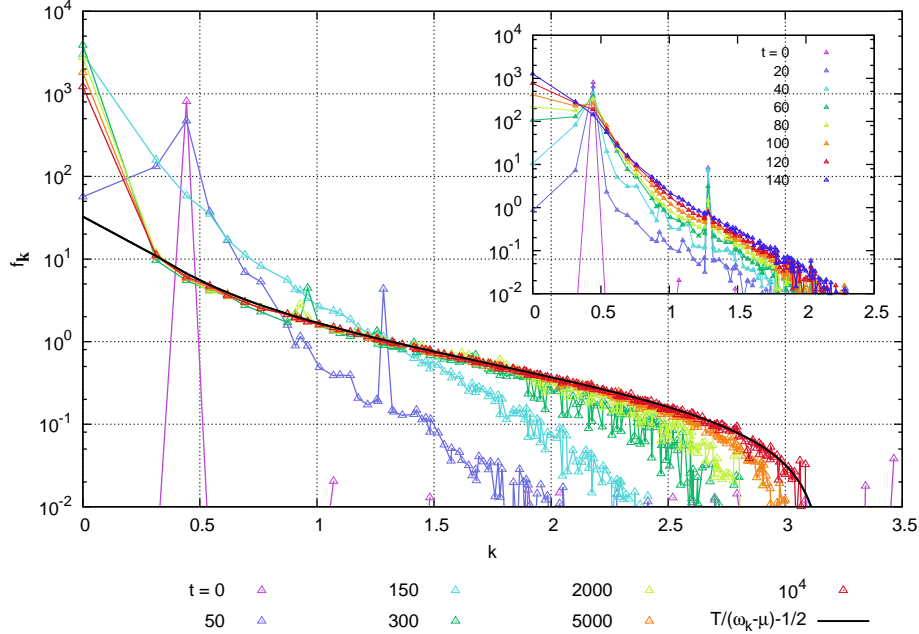
Figure 5.23: Time evolution of the occupation number f_k for a system initialized in the modes $(k_x, k_y, k_z) = (1, 1, 0)$ and $(-1, -1, 0)$. In the top right inset, the behavior at short times is shown.

In this simulation, J has been chosen so that

$$\varphi_k(0) = \cos(k_1.x) \tag{5.112}$$

with (recalling 5.61)

$$k_1^2 = k_{1,1,0}^2 = \frac{2}{a}\left[2 - 2\cos\left(\frac{2\pi}{L}\right)\right] . \tag{5.113}$$

Even if the occupation at $k = 0$ is 0 at the initial time, one sees in the inset of the figure 5.23 a rapid build up of f_0. At very late times, the behaviour of f_k is exactly the same as in the simulation of figure 5.20 where $\varphi_k(0)$ was spatially homogeneous. Namely, the best fit is still achieved by a classical distribution with a non-zero chemical potential μ. Last evidence in favor of the existence of a Bose-Einstein condensate: given equation (5.111), the ratio $\frac{f_0}{V}$ should not depend on the size of the lattice considered. We have performed three simulations with three different lattice sizes ($L = 20, 30, 40$), and the outcome is shown in the figure 5.24
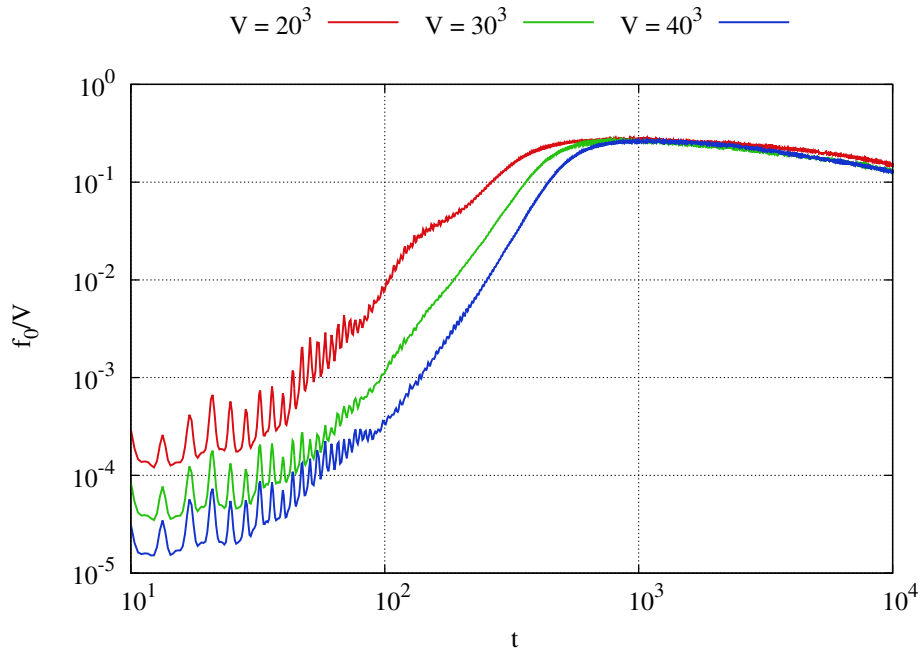
Figure 5.24: Time evolution of the ratio $\frac{f_0}{V}$ for three different lattice sizes.

Here, one can see that after a short transient regime, the three curves reach a plateau where they are all equal, confirming the volume scaling of a Bose-Einstein condensate. The slow decay of this plateau is due to the already explained fact that the particle number is not conserved exactly, and therefore the Bose-Einstein condensate should disappear at asymptotically large times.

5.4.3   Deeper analysis of the quasi-particle picture

The reader may refer to the appendix 5.B for more details on the quasi-particle description in term of an effective Hamiltonian. Now that we understand the origin and the importance of the $\frac{1}{2}$ term in our simulations, we can try to fit the mass of the quasi-particles by the following adaptation of the HTL formula

$$m^2_{1-\text{loop}} = \int \frac{\mathrm{d}^3 k}{(2\pi)^3 2\omega_k} \left(f_k + \frac{1}{2} \right) . \tag{5.114}$$

This gives a gap equation (that one cannot solve analytically, as the right hand side also depends on m through $\omega_k = \sqrt{k^2 + m^2}$), that we solve numerically in order to obtain the orange curve of the figure 5.19. As one can see, the agreement with the mass extracted from the spectral function is much better. Another test that can be performed on the quasi-particle picture is to compare the energy-density that it predicts

$$\epsilon_{\text{qp}} = \int \frac{\mathrm{d}^3 k}{(2\pi)^3} \omega_k f_k \tag{5.115}$$

with the true energy-density. This gives the figure 5.25.
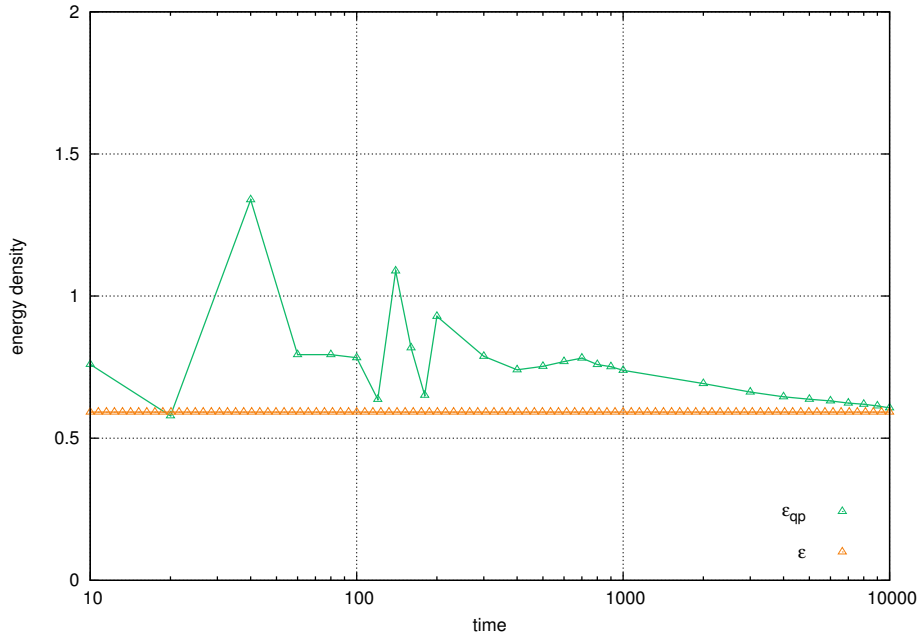
Figure 5.25: Time evolution of the quasi-particle energy-density (in green), compared to the true energy-density (in orange).

As one can see, the energy-density of the quasi particles is always above the true energy-density of the system. This means that the residual interaction (the $\mathcal{H}'_{\text{int}}$ of appendix 5.B) is attractive. This is a standard result in ϕ^4 theory [13]. In addition, the difference between ϵ and ϵ_{qp} decreases as time increases, and becomes almost negligible. This is another evidence in favor of the description by a collection of free quasi-particles. The last one comes from the computation of the entropy-density predicted by the quasi-particle description

$$s_{\text{qp}} = \int \frac{\mathrm{d}^3 \boldsymbol{k}}{(2\pi)^3} \left(1 + f_{\boldsymbol{k}}\right) \ln(1 + f_{\boldsymbol{k}}) - f_{\boldsymbol{k}} \ln f_{\boldsymbol{k}} \,, \tag{5.116}$$

that we can compare with the entropy of a free gas of massive bosons

$$s_{\text{BE}} = \int \frac{\mathrm{d}^3 \boldsymbol{k}}{(2\pi)^3} \left(1 + f_{\boldsymbol{k}}^{\text{BE}}(\mu = 0)\right) \ln(1 + f_{\boldsymbol{k}}^{\text{BE}}(\mu = 0)) - f_{\boldsymbol{k}}^{\text{BE}}(\mu = 0) \ln f_{\boldsymbol{k}}^{\text{BE}}(\mu = 0) \tag{5.117}$$

with the mass extracted from the fit of the spectral function and with the temperature extracted from the energy-density, knowing that for a free gas of bosons

$$\epsilon_{\text{BE}} = \int \frac{\boldsymbol{k}\mathrm{d}^3 \boldsymbol{k}}{(2\pi)^3} f_{\boldsymbol{k}}^{\text{BE}}(\mu = 0) = \frac{\pi^2 T^4}{30} \,. \tag{5.118}$$

The result is shown in the figure 5.26

---

13. See [159] for recent developments.
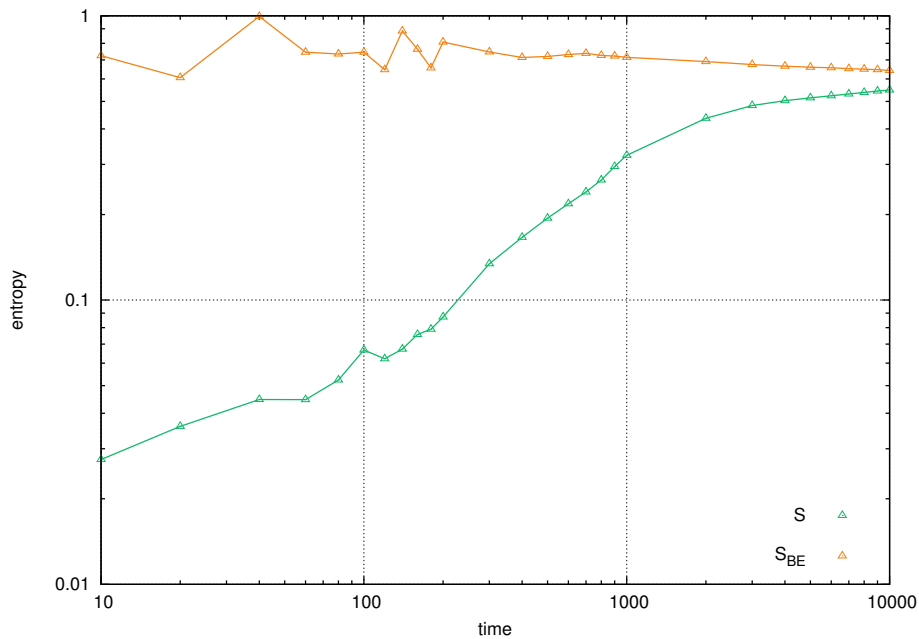
Figure 5.26: Time evolution of the quasi-particle entropy-density (in green), compared to the entropy-density of a free gas of massive bosons.

Two important observations can be made here. Firstly, the entropy computed thanks to (5.116) (green line) increases by approximately a factor 20. This goes along with the decoherence picture already advocated several times. Secondly, the quasi-particle entropy approaches the one of a free gas of bosons (orange line) at late times, confirming the validity of the quasi-particle approximation at late times.

5.5 Summary

> - The purely classical ϕ^4 scalar theory does not have an EOS.
> - A naive loop expansion leads to secular divergences.
> - Secular divergences can be cured by the use of the classical statistical approximation, which also correctly accounts for the instabilities.
> - The CSA leads to an EOS, and thermalization. In addition, a Bose-Einstein Condensate may be formed for certain initial conditions.
> - After a transient time corresponding to the formation of the EOS, the system can be correctly described by weakly interacting quasi-particles.

Appendix

5.A Instabilities in the fixed-volume case

5.A.1 Analytical study

In this appendix we determine the resonance band for the fixed volume scalar field theory. We start with a massive Lagrangean, as this does not forbid us to perform the analytical study all the way down to the resonance band. The Lagrangean therefore reads

$$\mathcal{L} = \frac{1}{2} \left(\partial_\mu \phi \right) \left(\partial^\mu \phi \right) - \frac{g^2}{4!} \phi^4 + \frac{m^2}{2} \phi^2 \tag{5.119}$$

Assuming as explained in section 5.2 that the background field is space independent, the EOM is therefore

$$\ddot{\varphi} + \frac{g^2}{6}\varphi^3 + m^2\varphi = 0 \,. \tag{5.120}$$

We now consider a small perturbation of momentum $\boldsymbol{k}$ propagating on top of this background field. The linearized EOM reads

$$\ddot{a}_{\boldsymbol{k}} + \left(\boldsymbol{k}^2 + \frac{g^2}{2}\varphi^2 + m^2\right) a_{\boldsymbol{k}} = 0 \,. \tag{5.121}$$

To go further, we first integrate (5.120), recalling that the initial condition at $x^0 = 0$ is $(\varphi, \dot{\varphi}) = (\varphi_0, 0)$:

$$\dot{\varphi} = \sqrt{\frac{g^2}{12}\left(\varphi_0^4 - \varphi^4\right) + m^2\left(\varphi_0^2 - \varphi^2\right)} \,, \tag{5.122}$$

and then perform the change of variable $\varphi = \varphi_0\sqrt{z}$, which gives

$$\dot{z} = \sqrt{z(1-z)}\sqrt{\frac{g^2\varphi_0^2}{3}(1+z) + 4m^2} \,. \tag{5.123}$$

We also need

$$\ddot{z}\dot{z} = \frac{1}{2}\left[4m^2(1-2z) + \frac{g^2\varphi_0^2}{3}(1-3z^2)\right] \,. \tag{5.124}$$

We now want to re-express the EOM for $a_{\boldsymbol{k}}(x^0)$ as an EOM for $a(z)$. Starting from (5.121), we obtain

$$z(1-z)\left(\frac{g^2\varphi_0^2}{3}(1+z) + 4m^2\right)a'' + \frac{1}{2}\left[4m^2(1-2z) + \frac{g^2\varphi_0^2}{3}(1-3z^2)\right]a'$$
$$+ \left(\frac{g^2\varphi_0^2}{2}z + m^2 + \boldsymbol{k}^2\right)a = 0 \,, \tag{5.125}$$

where the prime denotes a derivative with respect to z. Taking $m_0^2 = \frac{g^2\varphi_0^2}{2}$, $\xi = \frac{m}{m_0}$ and $\kappa = \frac{k}{m_0}$, this gives

$$z(1-z)\left(2(1+z) + 12\xi^2\right)a'' + \left[6\xi^2(1-2z) + (1-3z^2)\right]a' + 3\left(z + \xi^2 + \kappa^2\right)a = 0 \,. \tag{5.126}$$

Given two solutions a, b, and looking at $M = ab$, we have

$$M' = a'b + ab'$$
$$M'' = a''b + 2a'b' + ab''$$
$$M''' = a'''b + 3a''b' + 3a'b'' + ab''' \,. \tag{5.127}$$

Differentiating (5.126) with respect to z, we obtain

$$z(1-z)\left(2(1+z) + 12\xi^2\right)a''' + \left[3(1-3z^2) + 18\xi^2(1-2z)\right]a'' + 3\left(\kappa^2 - 3\xi^2 - z\right)a' + 3a = 0 \,. \tag{5.128}$$

We now multiply (5.128) by b, (5.126) by $3b'$, and add these quantities together with the same ones with $a \leftrightarrow b$ to obtain

$$\left(2z(1-z^2) + 12z(1-z)\xi^2\right)M''' + 3\left[(1-3z^2) + 6\xi^2(1-2z)\right]M'' + 6(z + 2\kappa^2)M' + 6M = 0 \,. \tag{5.129}$$

If we search a polynomial solution of degree n to this equation, then n satisfies

$$(n-2)(n+3)(2n+1) = 0 , \qquad (5.130)$$

which implies that $n = 2$. We are thus looking for a solution of the form

$$M = z^2 + \alpha z + \beta . \qquad (5.131)$$

Inserting this in (5.129) gives

$$M = z^2 - 2(\kappa^2 - 3\xi^2)z + 4k^4 - 1 - 6\xi^2(2k^2 + 1) . \qquad (5.132)$$

Now, looking at the Wronskian $W = a'b - ab'$, we see that

$$W' = a''b - ab'' = -\frac{6\xi^2(1 - 2z) + (1 - 3z^2)}{2z(1 - z^2) + 12z(1 - z)\xi^2} W , \qquad (5.133)$$

which can be integrated into

$$W = \frac{w_0}{\sqrt{z(1 - z)(6\xi^2 + 1 + z)}} . \qquad (5.134)$$

Since we are looking for an exponentially growing solution, and since $M = ab$ is a degree 2 polynomial, we must have $a \neq b$. Assuming that a is the growing solution, we have

$$W = a'b - ab' = \left(\frac{a'}{a} - \frac{b'}{b}\right) M = \frac{w_0}{\sqrt{z(1 - z)(6\xi^2 + 1 + z)}}$$

$$\frac{a}{b} = \exp\left(\int_z \frac{w_0 \, dx}{M(x)\sqrt{x(1 - x)(6\xi^2 + 1 + x)}}\right) . \qquad (5.135)$$

Finally, multiplying by M and taking the square root gives

$$a = \sqrt{M(z)} \exp\left(\frac{w_0}{2} \int_z \frac{dx}{M(x)\sqrt{x(1 - x)(6\xi^2 + 1 + x)}}\right)$$

$$b = \sqrt{M(z)} \exp\left(-\frac{w_0}{2} \int_z \frac{dx}{M(x)\sqrt{x(1 - x)(6\xi^2 + 1 + x)}}\right) . \qquad (5.136)$$

To find the value of ω_0, one has to insert these expressions into (5.126). To have an exponential behaviour for a, we should have

$$-\kappa^2 \left(1 + 2\kappa^2\right) \left[6\kappa^6 - 3(1 + 10\xi^2)\kappa^4 + 2(9\xi^4 - 3\xi^2 - 1)\kappa^2 + (1 + 3\xi^2)^2(1 + 6\xi^2)\right] > 0 . \quad (5.137)$$

so that

$$\sqrt{\frac{1 + 6\xi^2}{2}} < \kappa < \sqrt{\xi^2 + \sqrt{\frac{1 + 6\xi^2 + 12\xi^4}{3}}} . \qquad (5.138)$$

As ξ increases, this band shrinks very fast. Indeed, we have for $\xi \gg 1$

$$\sqrt{\xi^2 + \sqrt{\frac{1 + 6\xi^2 + 12\xi^4}{3}}} - \sqrt{\frac{1 + 6\xi^2}{2}} \approx \frac{\xi^{-3}}{96\sqrt{3}} + \mathcal{O}(\xi^{-4}) \qquad (5.139)$$

If we want the period of the oscillations of φ, using (5.120) we find

$$\dot{\phi} = \sqrt{\frac{g^2}{12} \left(\varphi_0^4 - \varphi^4\right) + m^2 \left(\varphi_0^2 - \varphi^2\right)}$$

$$\frac{T}{4} = \int_0^{\varphi_0} \frac{d\varphi}{\sqrt{\frac{g^2}{12} \left(\varphi_0^4 - \varphi^4\right) + m^2 \left(\varphi_0^2 - \varphi^2\right)}} = \frac{\sqrt{6}}{m_0\sqrt{1 + 6\xi^2}} K(-\frac{1}{1 + 6\xi^2}) , \qquad (5.140)$$

where

$$K(k) = \int_0^1 \frac{\mathrm{d}x}{\sqrt{(1-x^2)(1-kx^2)}} \, . \tag{5.141}$$

The conclusion of this analytical study is that the fixed volume scalar field theory is affected by instabilities. The nature of these instabilities is parametric resonance, and the resonance band shrinks as the mass increases. Going back to the massless case, the resonance band is

$$\sqrt{\frac{1}{2}} < \kappa < \sqrt{\sqrt{\frac{1}{3}}} \, . \tag{5.142}$$

5.A.2 Numerical confirmation: trace of the monodromy matrix

Given what we did in the previous section, we have for $\xi = 0$,

$$0.707107 < \kappa < 0.759836 \, , \tag{5.143}$$

There is a simple way to check this numerically. Take $a_1(t,k)$ and $a_2(t,k)$ two independent solutions of (5.121) and let $M_k \in M_2 \mathbb{R}$ being the so-called monodromy matrix, i.e. the matrix that relates $a_{1,2}$ from one time t to the time $t + T$.

$$\begin{pmatrix} a_1(T,k) & a_2(T,k) \\ \dot{a}_1(T,k) & \dot{a}_2(T,k) \end{pmatrix} = M_k \begin{pmatrix} a_1(0,k) & a_2(0,k) \\ \dot{a}_1(0,k) & \dot{a}_2(0,k) \end{pmatrix} \, . \tag{5.144}$$

Our aim is to study the stability of the pair (a_1, a_2) thanks to M_k. The conservation of the Wronskian implies that

$$\det(M_k) = \lambda_1 \lambda_2 = 1 \, , \tag{5.145}$$

where $\lambda_{1,2}$ are the two eigenvalues of M_k. These two eigenvalues are therefore the inverse of one another. One can thus write the trace of M_k as

$$\mathrm{tr}\,(M_k) = \lambda + \lambda^{-1} \, . \tag{5.146}$$

Since

$$\begin{pmatrix} a_1(nT,k) & a_2(nT,k) \\ \dot{a}_1(nT,k) & \dot{a}_2(nT,k) \end{pmatrix} = M_k^n \begin{pmatrix} a_1(0,k) & a_2(0,k) \\ \dot{a}_1(0,k) & \dot{a}_2(0,k) \end{pmatrix} \, , \tag{5.147}$$

there are three distinct cases for the stability of (a_1, a_2)

- $\lambda \in \mathbb{R}$ and $|\lambda| > 1$, i.e. $\mathrm{tr}\,(M) > 2$. In this case, one of the solutions is exponentially growing and one exponentially decreasing.
- $\lambda \in \mathbb{R}$ and $|\lambda| = 1$, i.e. $\mathrm{tr}\,(M) = 2$. In this case M_k can be written as

$$M_k = P^{-1} \begin{pmatrix} 1 & \alpha \\ 0 & 1 \end{pmatrix} P \, , \tag{5.148}$$

so that

$$M_k^n = P^{-1} \begin{pmatrix} 1 & n\alpha \\ 0 & 1 \end{pmatrix} P \, , \tag{5.149}$$

which implies that one of the solutions is stable while the other is linearly increasing.

- $\lambda \in \mathbb{C}/\mathbb{R}$. In this case since $M_k \in M_2(\mathbb{R})$ this implies that the two eigenvalues are on the unit circle and complex conjugates of one another, therefore $\mathrm{tr}\,(M_k) = 2\cos\theta < 2$. The two solutions are thus stable.

One can evaluate numerically what is $\mathrm{tr}\,(M_k)$. The result is shown on the figure (5.27)
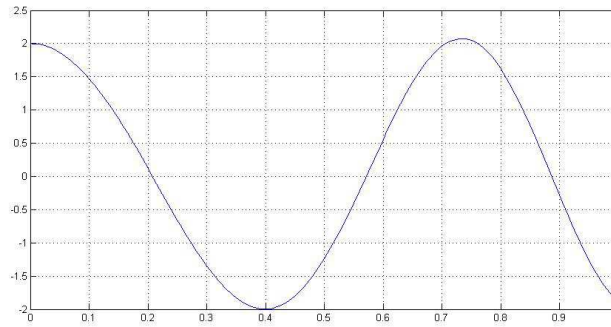
Figure 5.27:   The trace of the monodromy matrix computed numerically. The two solutions $a_{1,2}$ are initialized such that they are independents from one another: $a_1 = (1,0)$ and $a_2 = (0,1)$. This study has been performed with $m_0 = 1$.

As one can see, the resonance band (where $\mathrm{tr}\,(M_k) > 2$) is located where we expect it to be. From this study we also see that two modes are linearly growing (for $k = 0$ and $k = 0.4$), while all the other modes are stable.

One can also compare the value of the Lyapunov exponent μ given by the two approaches, μ being such that for the increasing solution $a_1(T, k) = e^{\mu(k, m_0)} a_1(0, k)$. For $\zeta = 0$ one finds the following analytical result for μ

$$\mu(k, m_0) = 2m_0 \sqrt{\kappa^2 \left(\frac{1}{3} - \kappa_4\right) \left(\kappa_4 - \frac{1}{4}\right)} \frac{\int_0^1 \frac{\mathrm{d}x}{(z^2 - 2\kappa^2 z + 4\kappa^4 - 1)\sqrt{z(1-z^2)}}}{\int_0^1 \frac{\mathrm{d}x}{\sqrt{1 - x^4}}} , \qquad (5.150)$$

and μ can also be extracted from the monodromy matrix in the following way

$$\mu(k, m_0) = \frac{1}{T} \ln\left(\max \lambda_{1,2}\right) . \qquad (5.151)$$

The comparison between (5.150) and (5.151) is shown in the figure 5.28.
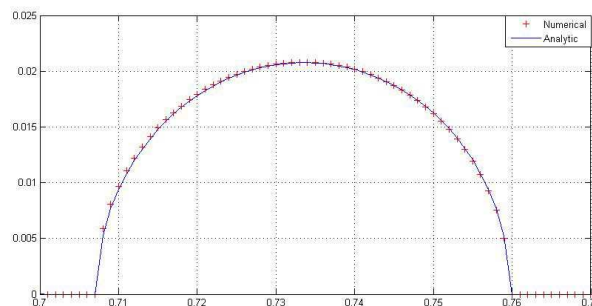
Figure 5.28:   The Lyapunov exponent computed numerically thanks to (5.151) and analytically thanks to formula (5.150).

Since $\mu = 0$ when $k \notin [\frac{1}{\sqrt{2}}, \frac{1}{3^{1/4}}]$, a_k cannot increase faster than linearly. On the following figures are represented some modes as a function of time, to give a final evidence of the correctness of out analytical computation. To observe a mode that experiences a linear growth one can refer to the following figure 5.29.
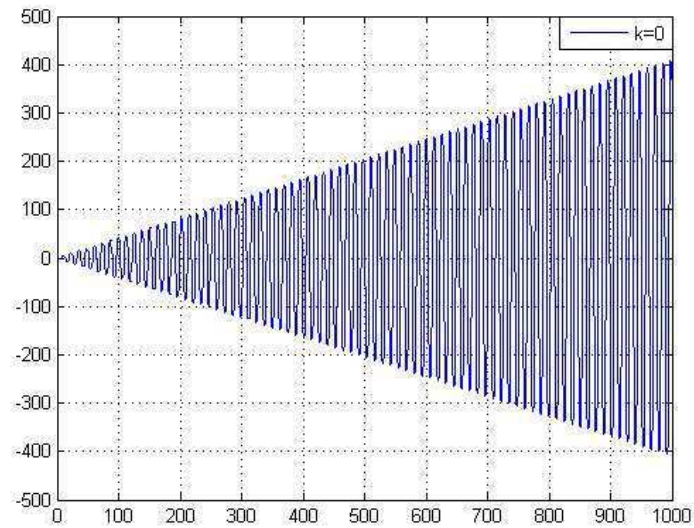
Figure 5.29: $k = 0$ mode, linear growth

One of the stable mode is shown on the figure 5.30.
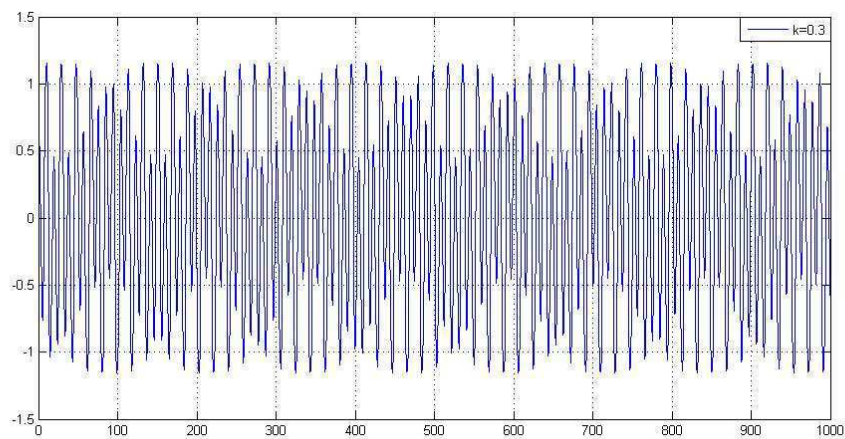
Figure 5.30: $k = 0.3$ mode, stability

Finally, one of the unstable mode is represented in the figure 5.31.
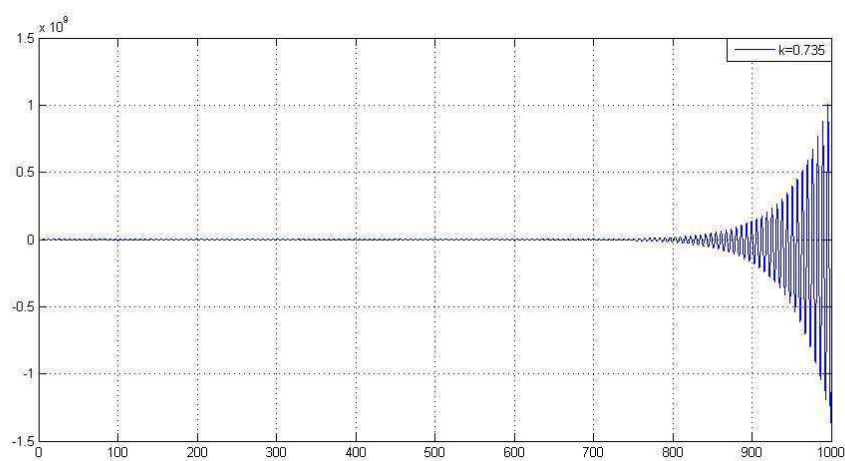
Figure 5.31: $k = 0.735$ mode, exponential growth

5.B   Appendix: Effective Hamiltonian

In this section we want to derive an effective Hamiltonean that describes the quasi-particle picture observed in section 5.4. To do so, we start with the usual Hamiltonian.

$$\mathcal{H} = \int \mathrm{d}^3x \, \frac{1}{2} \left(\dot{\varphi}^2 + (\nabla \varphi)^2 \right) + \frac{g^2}{4!} \varphi^4 \,. \tag{5.152}$$

Given what we saw in section 5.4, we know that after a finite time the system behaves as if it contains massive quasi-particles, their mass being m. One could therefore do the following operation on the Hamiltonian

$$\mathcal{H} = \int \mathrm{d}^3x \, \underbrace{\frac{1}{2} \left(\dot{\varphi}^2 + (\nabla \varphi)^2 + m^2 \varphi^2 \right)}_{\mathcal{H}_0} + \underbrace{\frac{g^2}{4!} \varphi^4 - \frac{1}{2} m^2 \varphi^2}_{\mathcal{H}'_{\mathrm{int}}} \,. \tag{5.153}$$

This operation is for the moment trivial: we have just added and subtracted a mass term by hand, and the parameter m^2 is still arbitrary. Things become interesting when one tries to reduce the residual interaction term $\mathcal{H}'_{\mathrm{int}}$. In order to do so, one can choose the mean field value for m^2,

$$m^2 = \frac{g^2}{2} \left\langle \varphi^2(x) \right\rangle \,, \tag{5.154}$$

where as usual the angle brackets denote an ensemble average [14]. By performing a Fourier transform of the fields in $\mathcal{H}_0$, one can rewrite it as a sum of independent harmonic oscillators [15]

$$\mathcal{H}_0 = \int \frac{\mathrm{d}^3k}{(2\pi)^3} \, \underbrace{\frac{1}{2} |\dot{\varphi}_k|^2 + \frac{1}{2} \omega_k^2 |\varphi_k|^2}_{h_k} \,, \tag{5.155}$$

where as defined in the core of the manuscript in section 5.4.2.1 $\omega_k \equiv (k^2 + m^2)^{1/2}$ and where φ_k is the spatial Fourier transform of φ. Assuming

$$\mathcal{H}'_{\mathrm{int}} \ll \mathcal{H}_0 \tag{5.156}$$

and one gets an effective Hamiltonian meant to describe a system formed by the collection of – almost free – massive particles.

---

14. One can check numerically that this mean field expression of the mass is in very good agreement with the measured mass of the quasi-particles through the spectral function (figure 5.19).

15. Even if the following momentum integral appears strongly ultraviolet divergent, it is naturally regularize on the lattice, where Λ plays the role of an upper bound on the integral over the k modulus.

Chapter 6

☸ Expanding system ☸

Contents

6.1   Expanding scalar theory

6.1.1   Generalities

iven the work performed in the previous chapter, we now know that the quartic scalar theory in a fixed volume and initial conditions mimicking those of a heavy-ion collision tends to thermalize. Before turning our attention to the realistic case of QCD, it is interesting to study another toy model, namely the same scalar field with one dimensional expansion. Indeed, a heavy-ion-collision is more properly described as a three dimensional system expanding in the direction of the collision axis (taken to be the z direction in the following), as described in the figure 6.1
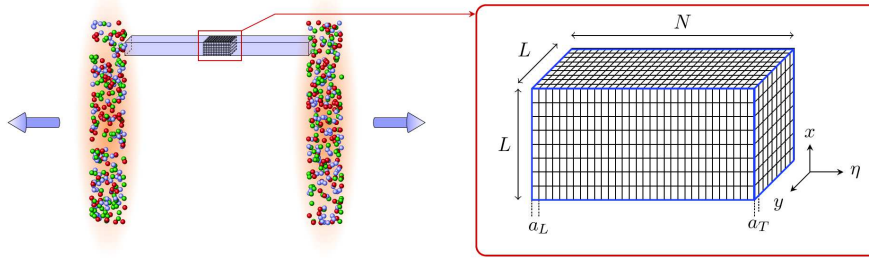
Figure 6.1: Left side: the two heavy-ions after they have collided. The system is expanding in the direction of the collision axis. Right side: asymmetric grid with a smaller lattice spacing in the longitudinal direction, to cope with the expansion.

The appropriate coordinate system to describe this expanding scalar theory is no longer the Cartesian one. Indeed, since the two nuclei are traveling at the speed of light, the system (at the classical level) is boost invariant (as was explained in the section 3.8 in the gauge case). This has a simple expression in the proper-time/rapidity coordinate system: the classical background field is rapidity independent (for reasons explained in **??**). The expression of the new coordinates $(\tau, x_\perp, \eta)$ in terms of the Cartesian (t, x, y, z) ones is

$$\tau = \sqrt{t^2 - z^2} \qquad\qquad \eta = \frac{1}{2}\ln\frac{t+z}{t-z} \ , \qquad\qquad (6.1)$$

$$t = \tau\cosh\eta \qquad\qquad z = \tau\sinh\eta \ . \qquad\qquad (6.2)$$

and the classical background field will therefore only depend on τ and $x_\perp$. The following figure 6.2 illustrates constant τ and η surfaces
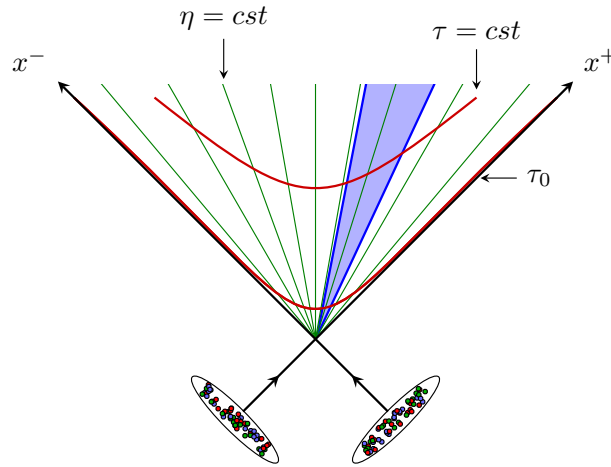
Figure 6.2: Constant τ and η surfaces in the (τ, η) coordinate system. The blue area is a fixed interval in η, corresponding to an expansion in the z direction.

As one can see, if one describes the scalar theory in a volume $(x_\perp, \eta)$ grid – such as the one depicted in the figure 6.1 – this corresponds to an expanding volume in (x, y, z) space – blue surface of the figure 6.2. In this new system of coordinates, the d'Alembertian reads

$$\Box = \frac{\partial^2}{\partial\tau^2} + \frac{1}{\tau}\frac{\partial}{\partial\tau} - \nabla_\perp^2 - \frac{1}{\tau^2}\frac{\partial^2}{\partial\eta^2} \ . \qquad\qquad (6.3)$$

The metric is

$$g_{\mu\nu} = \text{diag}(1, -1, -1, -\tau^2) \ . \qquad\qquad (6.4)$$

The Fourier conjugate variables to $(x_\perp, \eta)$ will be denoted $(k_\perp, \nu)$.

6.1.2 The spectrum of fluctuations

For this study we used a different way for computing the spectrum of small fluctuations. Indeed, since the proper-time rapidity coordinate system is only meant for describing the forward light cone (τ cannot be negative), it is not possible to perform the evolution in the other regions of the light cone in the same coordinate system. We will therefore directly start our numerical simulations at positive proper-times. How to find the spectrum of small fluctuations propagating on top of the classical background field then? We know the small fluctuations in the remote past ($x^0 \to -\infty$)

$$a_k(x) = e^{ikx} \,, \qquad\qquad \dot{a}_k(x) = ike^{ikx} \,, \qquad\qquad (6.5)$$

and the following scalar product is conserved during the time evolution [1]

$$(a_k|a_{k'}) = i \int \mathrm{d}^3 x \left(a_k(x)\dot{a}^*_{k'}(x) - \dot{a}_k(x)a^*_{k'}(x) \right) = (2\pi)^3 2|k|\delta(k - k') \,. \qquad (6.6)$$

It is trivial to obtain this scalar product in the proper-time/rapidity coordinate system

$$(a_{k_\perp,\nu}|a_{k'_\perp,\nu'}) = i\tau \int \mathrm{d}^2 x_\perp \, \mathrm{d}\eta \left(a^*_{k_\perp,\nu}(\tau, x_\perp, \eta)\dot{a}_{k'_\perp,\nu'}(\tau, x_\perp, \eta) - \dot{a}^*_{k_\perp,\nu}(\tau, x_\perp, \eta)a_{k'_\perp,\nu'}(\tau, x_\perp, \eta) \right) \,. \qquad (6.7)$$

We will therefore look for a set of mode functions $a_{k_\perp,\nu}(\tau, x_\perp, \eta)$ that obey the linearized equation of motion at $\tau = 0^+$, and normalized in such a way that they have the right scalar product. As we will see in the chapter 8, this procedure is at best approximate. It can be justified if the background field φ is turned on adiabatically, but not in the situation encountered in heavy-ion collisions. Given the expression of the D'Alembertian, we therefore need to solve

$$\left(\frac{\partial^2}{\partial\tau^2} + \frac{1}{\tau}\frac{\partial}{\partial\tau} - \nabla_\perp^2 - \frac{1}{\tau^2}\frac{\partial^2}{\partial\eta^2} + \frac{g^2}{2}\varphi^2(\tau, x_\perp) \right) a(\tau, x_\perp, \eta) = 0 \,. \qquad (6.8)$$

This equation is also subject to instabilities (see [160] for instance for an analytical analysis) and we therefore expect the same physical mechanisms than those that appeared in the section 5.2: exponential amplification of the NLO, decoherence... To solve (6.8), we first assume that the variations of φ are slow compared to those of a. As in section 5.2, we therefore define

$$\varphi_0(x_\perp) = \lim_{\tau \to 0} \varphi(\tau, x_\perp) \,. \qquad (6.9)$$

The fact that φ is well behaved in the vicinity of the origin can be explained in the following way: taking the classical Klein-Gordon equation

$$\left(\frac{\partial^2}{\partial\tau^2} + \frac{1}{\tau}\frac{\partial}{\partial\tau} - \nabla_\perp^2 \right) \varphi(\tau, x_\perp) + \frac{g^2}{6}\varphi^3(\tau, x_\perp) = 0 \qquad (6.10)$$

we see that the term $\frac{1}{\tau}\frac{\partial}{\partial\tau}$ (specific to the expanding problem) dominates the term $\frac{g^2}{6}\varphi^3(\tau, x_\perp)$. In other words, for τ sufficiently small, the expansion rate dominates the interaction rate. In this range of τ (taking $k_\perp = |k_\perp|$), we have

$$\left(\frac{\partial^2}{\partial\tau^2} + \frac{1}{\tau}\frac{\partial}{\partial\tau} + k_\perp^2 \right) \varphi(\tau, x_\perp) = 0 \,, \qquad (6.11)$$

which admits the solution $J_0(k_\perp\tau)$ and $Y_0(k_\perp\tau)$. Since only the further is well-defined as $\tau \to 0^+$, we can assume

$$\lim_{\tau \to 0} \varphi(\tau, x_\perp) \propto J_0(k_\perp\tau) \,, \qquad\qquad \lim_{\tau \to 0} \dot{\varphi}(\tau, x_\perp) = 0 \,. \qquad (6.12)$$

---

1. This is just a consequence of the fact that the derivative of the Wronskian is zero in the Minkowskian coordinate system.

So φ is indeed well-behaved in the vicinity of the origin. Performing the Fourier transform of the η variable (since φ does not depend on η), we write the small fluctuations as

$$a_\nu(\tau, \boldsymbol{x}_\perp, \eta) = e^{i\nu\eta} b_\nu(\tau, \boldsymbol{x}_\perp) , \tag{6.13}$$

and the function b_ν satisfies

$$\left(\frac{\partial^2}{\partial\tau^2} + \frac{1}{\tau}\frac{\partial}{\partial\tau} - \boldsymbol{\nabla}_\perp^2 + \frac{\nu^2}{\tau^2} + \frac{g^2}{2}\varphi_0^2(\boldsymbol{x}_\perp) \right) b_\nu(\tau, \boldsymbol{x}_\perp) = 0 . \tag{6.14}$$

The operator $-\boldsymbol{\nabla}_\perp^2 + \frac{g^2}{2}\varphi_0^2(\boldsymbol{x}_\perp)$ is real and symmetric, it can therefore be diagonalized over a basis of orthogonal eigenfunctions $\chi_{\boldsymbol{k}_\perp}(\boldsymbol{x}_\perp)$, with eigenvectors $\omega_{\boldsymbol{k}_\perp}$

$$\left(-\boldsymbol{\nabla}_\perp^2 + \frac{g^2}{2}\varphi_0^2(\boldsymbol{x}_\perp) \right) \chi_{\boldsymbol{k}_\perp}(\boldsymbol{x}_\perp) = \omega_{\boldsymbol{k}_\perp}^2 \chi_{\boldsymbol{k}_\perp}(\boldsymbol{x}_\perp) . \tag{6.15}$$

The fact that the solution are orthonormal means that

$$\int \mathrm{d}^2\boldsymbol{x}_\perp \, \chi_{\boldsymbol{k}_\perp}(\boldsymbol{x}_\perp)\chi_{\boldsymbol{p}_\perp}^*(\boldsymbol{x}_\perp) = \delta_{\boldsymbol{k}_\perp \boldsymbol{p}_\perp} , \tag{6.16}$$

where $\delta_{\boldsymbol{k}_\perp \boldsymbol{p}_\perp}$ is such that

$$\int \mathrm{d}\mu_{\boldsymbol{k}_\perp}\delta_{\boldsymbol{k}_\perp \boldsymbol{p}_\perp} = 1 . \tag{6.17}$$

$\mathrm{d}\mu_{\boldsymbol{k}_\perp}$ is the measure corresponding to the Fourier conjugates variables of $\boldsymbol{x}_\perp$. If we take $\mathrm{d}\mu_{\boldsymbol{k}_\perp} = \frac{\mathrm{d}^2\boldsymbol{k}_\perp}{(2\pi)^2}$, then $\delta_{\boldsymbol{k}_\perp \boldsymbol{p}_\perp}$ reads $(2\pi)^2\delta^2(\boldsymbol{k}_\perp - \boldsymbol{p}_\perp)$. Writing

$$b_{\nu\boldsymbol{k}_\perp}(\tau, \boldsymbol{x}_\perp) = \chi_{\boldsymbol{k}_\perp}(\boldsymbol{x}_\perp)\alpha_\nu(\tau) , \tag{6.18}$$

we should have

$$\left(\frac{\partial^2}{\partial\tau^2} + \frac{1}{\tau}\frac{\partial}{\partial\tau} + \frac{\nu^2}{\tau^2} + \omega_{\boldsymbol{k}_\perp}^2 \right) \alpha_\nu(\tau) = 0 . \tag{6.19}$$

This is a Bessel equation, whose solutions are linear combinations of Bessel functions $J_{i\nu}$ and $Y_{i\nu}$. But it turns out that the $J_{i\nu}$ and $Y_{i\nu}$ functions mix positive and negative frequency solutions. To avoid this, we take the Hankel basis, and only keep the positive frequency solutions[2] $H_{i\nu}^{(2)}(k_\perp\tau)$. We therefore have

$$a_{\nu\boldsymbol{k}_\perp}(\tau, \boldsymbol{x}_\perp, \eta) = \beta_{\nu\boldsymbol{k}_\perp} e^{i\nu\eta}\chi_{\boldsymbol{k}_\perp}(\boldsymbol{x}_\perp)H_{i\nu}^{(2)}(k_\perp\tau) , \tag{6.20}$$

$\beta_{\nu\boldsymbol{k}_\perp}$ being an overall normalization constant such that the scalar product is orthonormal. To find it, we inject back the expression of $a_{\nu\boldsymbol{k}_\perp}$ into (6.7)

$$(a_{\nu\boldsymbol{k}_\perp}|a_{\nu'\boldsymbol{k}'_\perp}) = i(2\pi)\delta_{\boldsymbol{k}_\perp \boldsymbol{k}'_\perp}\delta(\nu - \nu')|\beta_{\nu\boldsymbol{k}_\perp}|^2\tau \left(H_{i\nu}^{(2)*}(k_\perp\tau) \overleftrightarrow{\partial_\tau} H_{i\nu}^{(2)}(k_\perp\tau) \right) , \tag{6.21}$$

and using the fact that [147, 161]

$$H_{i\nu}^{(2)*}(\boldsymbol{k}_\perp\tau) \overleftrightarrow{\partial_\tau} H_{i\nu}^{(2)}(\boldsymbol{k}_\perp\tau) = \frac{-4ie^{-\nu\pi}}{\pi\tau} , \tag{6.22}$$

we obtain

$$(a_{\nu\boldsymbol{k}_\perp}|a_{\nu'\boldsymbol{k}'_\perp}) = (2\pi)\delta_{\boldsymbol{k}_\perp \boldsymbol{k}'_\perp}\delta(\nu - \nu')\frac{4e^{-\nu\pi}|\beta_{\nu\boldsymbol{k}_\perp}|^2}{\pi} . \tag{6.23}$$

---

2. This can be seen by looking at the asymptotic expression of the Hankel functions.

To get an orthonormal spectrum of fluctuations, we therefore need

$$\beta_{\nu k_\perp} = \frac{\sqrt{\pi} e^{\frac{\nu\pi}{2}}}{2} \, ,$$

(6.24)

which leads to

$$a_{\nu k_\perp}(\tau, \boldsymbol{x}_\perp, \eta) = \frac{\sqrt{\pi} e^{\frac{\nu\pi}{2}}}{2} \, e^{i\nu\eta} \chi_{k_\perp}(\boldsymbol{x}_\perp) H_{i\nu}^{(2)}(k_\perp \tau) \, .$$

(6.25)

Armed with this result, we can now turn our attention to the numerical implementation of the classical-statistical method to compute the energy-momentum tensor and the occupation number in this expanding scalar field theory.

6.2 Numerical implementation

Given (6.25), we get as an initial condition of the classical-statistical method for $\tau \to 0^+$

$$\phi(\tau, \boldsymbol{x}_\perp, \eta) = \varphi_0(\boldsymbol{x}_\perp) + \frac{\sqrt{\pi} e^{\frac{\nu\pi}{2}}}{2} \text{Re} \left(\int \frac{\mathrm{d}\nu}{2\pi} \, \mathrm{d}\mu_{k_\perp} \, e^{i\nu\eta} \, c_{\nu k_\perp} \, \chi_{k_\perp}(\boldsymbol{x}_\perp) H_{i\nu}^{(2)}(k_\perp \tau) \right) ,$$

(6.26)

with

$$\left\langle c_{\nu k_\perp} c_{\nu' k'_\perp}^* \right\rangle = (2\pi)\delta(\nu - \nu')\delta_{k_\perp k'_\perp} \, .$$

(6.27)

A quick look at (6.26) indicates that ϕ is not well behaved as $\tau \to 0^+$, as $H_{i\nu}^{(2)}(\boldsymbol{k}_\perp \tau)$ behaves as $\tau^{\pm i\nu}$ in this limit. This forces us to start our numerical simulations at some small but non-zero proper-time τ_0. But as we will show in section 6.3, the physical observables will not depend on this τ_0. One can see the τ_0 dependence of the spectrum (6.25) as in a renormalization group procedure: this τ_0 dependence of the $a_{k_\perp \nu}$ is such that the physical observables do not depend on τ_0. It is important to stress that this property would not hold had we chosen an arbitrary spectrum of fluctuations.

Numerically, we discretize space-time in the following way (see the figure 6.1 for the details):
— Time is kept as a continuous variable. Numerically this means that the time steps can be chosen as small as necessary, and can be dynamically changed in order to obtain the desired accuracy.
— The transverse coordinates $\boldsymbol{x}_\perp$ are encoded on a $L \times L$ lattice. The different lattice sites are characterized by a pair of integers ij (each one ranging from 0 to $(L-1)$). a_T is the transverse lattice spacing, and we use periodic boundary conditions. This can be justified if one recalls that the system that we are dealing with is meant to mimic a small part of the interaction region in a heavy-ion collision (as depicted in the figure 6.1).
— The rapidity η is discretized on a lattice of size N ($N > L$ to cope with the longitudinal expansion). The different lattice sites are characterized by an integer n (ranging from 0 to $(N-1)$). a_L is the longitudinal lattice spacing. The grid also has periodic boundary conditions.
— The transverse Laplacian and the second derivative in η become

$$\partial_\eta^2 \phi \to \frac{1}{a_L^2} \left(\phi_{n+1ij} + \phi_{n-1ij} - 2\phi_{nij} \right) ,$$

$$\nabla_\perp^2 \to \frac{1}{a_T^2} \left(\phi_{ni+1j} + \phi_{ni-1j} + \phi_{nij+1} + \phi_{nij-1} - 4\phi_{nij} \right) .$$

(6.28)

If we express all the quantities in units of the transverse lattice spacing, we can take $a_T = 1$. If we want the rapidity to be between 0 and 1, then we should take $a_L = \frac{1}{N}$.

The next step is to diagonalize $-\nabla_{\perp}^2 + V''(\varphi)$, whose action on a eigenvector is

$$(D\chi)_{ij} = 4\chi_{ij} - \chi_{i+1j} - \chi_{i-1j} - \chi_{ij+1} - \chi_{ij-1} + V''(\varphi_{ij})\chi_{ij} . \tag{6.29}$$

Thus we have to diagonalize a $L^2 \times L^2$ matrix that has the form

$$D_{ij,kl} = (4 + V''(\varphi_{ij}))\delta_{ik}\delta_{jl} - \delta_{jl}(\delta_{i+1k} + \delta_{i-1k}) - \delta_{ik}(\delta_{j+1l} + \delta_{j-1l}) . \tag{6.30}$$

This provides us a set of L^2 eigenvectors $\chi_{ij}^{(p)}$ such that

$$\sum_{kl} D_{ij,kl}\chi_{kl}^{(p)} = \omega_{(p)}^2 \chi_{ij}^{(p)} \qquad\qquad \sum_{ij} \left(\chi_{ij}^{(p)}\right)\left(\chi_{ij}^{(q)}\right)^* = L^2 \delta_{pq} . \tag{6.31}$$

We can finally write the discrete analogue of (6.26)

$$\phi_{nij}(\tau) = \varphi_{ij}(\tau) + \sqrt{\frac{\pi}{4hNL^2}} \sum_{u=0}^{N-1} e^{\frac{\pi \nu_{(u)}}{2}} \sum_{p=0}^{L^2-1} \mathrm{Re}\left(c_{up} e^{\frac{2i\pi u}{N}} \chi_{ij}^{(p)} H_{i\nu}^{(2)}(\omega_{(p)}\tau)\right) . \tag{6.32}$$

where $\nu_{(u)}$ is the modulus of the η Fourier conjugate variable

$$\nu_{(u)} = \frac{1}{a_L}\sqrt{2\left(1 - \cos\frac{2\pi u}{N}\right)} , \tag{6.33}$$

and c_{up} are random Gaussian numbers of variance one (given how the prefactor in (6.32) has been chosen)

$$\langle c_{up} c_{u'p'}\rangle = \delta_{uu'}\delta_{pp'} . \tag{6.34}$$

Before going any further, let us state the obvious fact that for the vacuum, $\varphi_{ij} = 0$, the transverse index p can be decomposed in two indices that range from 0 to $L - 1$: k and l. The eigenvectors and eigenvalues read

$$\chi_{ij}^{(kl)} = e^{i\frac{2\pi(ki+lj)}{L}} , \qquad\qquad \omega_{(kl)} = \sqrt{2\left(2 - \cos\frac{2\pi k}{L} - \cos\frac{2\pi l}{L}\right)} \tag{6.35}$$

If the background field in non-zero but homogeneous, then $\chi_{ij}^{(kl)}$ is unchanged and $\omega_{(kl)}^2$ is shifted by a constant mass term $m^2 = \frac{g^2\varphi_0}{2}$.

6.3   Independence with respect to the initial time

In the previous section we explained that we must start at a non-zero initial time τ_0, but argued that with the use of (6.32) physical observables would not depend on τ_0. In the figure 6.3, the time evolution of the transverse pressure and of the energy density (to be defined more precisely in the section 6.6) are shown for two different initial times $\tau_0 = 0.01$ and $\tau_0' = 0.1$.
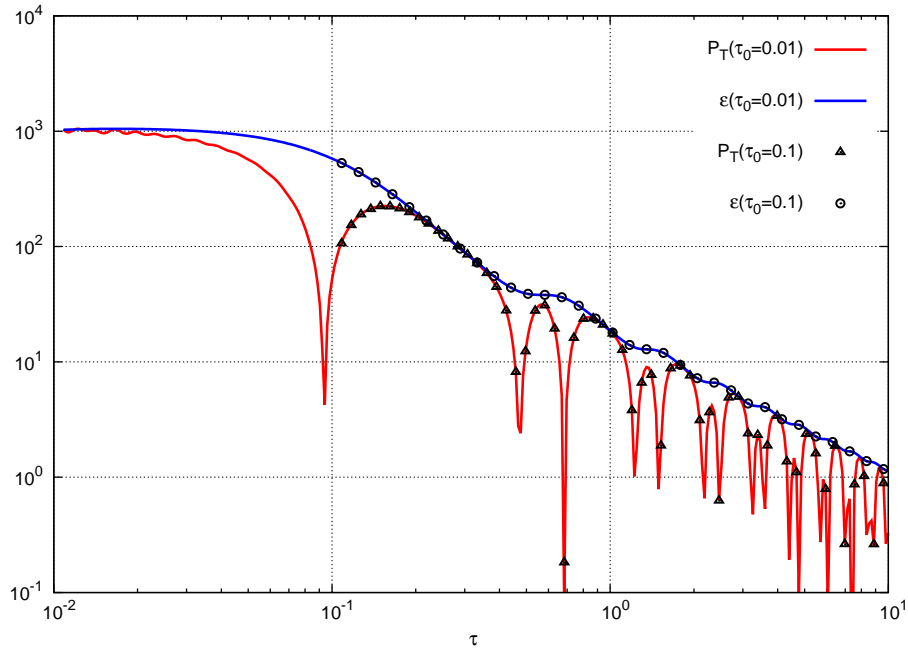
Figure 6.3: Transverse pressure and energy-density for two different initial times $\tau_0 = 0.01$ (solid lines) and $\tau_0' = 0.1$ (dots).

As one can see, the two simulations agree perfectly after $\tau_0 = 0.1$. Note that in order to obtain the two $\varphi(\tau_0, x_\perp)$, we took $\varphi(10^{-8}, x_\perp) = \varphi_0$ and $\dot{\varphi}(10^{-8}, x_\perp) = 0$, and then evolved it with the classical Klein-Gordon equation up to τ_0 and τ_0' respectively.

6.4 Resonance band

As we showed in the previous chapter, a mode k is resonant in the fixed volume scalar field theory if

$$\frac{1}{\sqrt{2}} \leq \kappa \leq \frac{1}{3^{\frac{1}{4}}} \ , \quad \frac{g^2 \varphi_0^2}{2} \kappa^2 = k^2 \tag{6.36}$$

In the present case, we will see that the resonance band is not fixed, and is in fact moving from low ν towards high ν as time increases. This statement can be checked as follows:

  i. Initializing each fluctuation mode as follows [3]

$$a_{\nu k}(\tau) = \frac{\sqrt{\pi}}{2} e^{\frac{\pi \nu}{2}} H_{i\nu}^{(2)} \left(\sqrt{\frac{g^2 \varphi_0^2}{2} + k_\perp^2} \, \tau \right) . \tag{6.37}$$

Here we have taken a homogeneous background field for simplicity.

  ii. Solve the non-linear EOM for φ and the linearized EOM for each $a_{\nu k_\perp, \nu}$. Because φ is homogeneous, this reduces to

$$\ddot{\varphi} + \frac{\dot{\varphi}}{\tau} + V'(\varphi) = 0 \ ,$$

$$\ddot{a}_{\nu k_\perp} + \frac{\dot{a}_{\nu k_\perp}}{\tau} + \left(\frac{\nu^2}{\tau^2} + k_\perp^2 + V''(\varphi) \right) a_{\nu k_\perp} = 0 \ . \tag{6.38}$$

---

3. These fluctuations are initialized in such a way that they are normalized to 1 at all times, with respect to the scalar product defined before, if there is no background field.

iii. Calculate the quantity

$$\tau \left| a_{\nu k} \right|^2 , \tag{6.39}$$

at each time of interest, for each mode. The prefactor τ is here because non-resonant modes are supposed to behave at late time as

$$a_{\nu k} \approx \frac{1}{\sqrt{\tau}} , \tag{6.40}$$

This is due to the asymptotic expression of the Hankel functions:

$$\lim_{\tau \to \infty} H_{i\nu}^{(2)}(\tau) \approx \sqrt{\frac{2}{\pi \tau}} e^{-i\left(\tau - i\frac{\pi\nu}{2} - \frac{\pi}{4}\right)} . \tag{6.41}$$

If the quantity calculated in (6.39) is greater than 1, then the mode has been amplified by instabilities between the initial time and the time of interest.

Our numerical results are summarized in the figure 6.4.
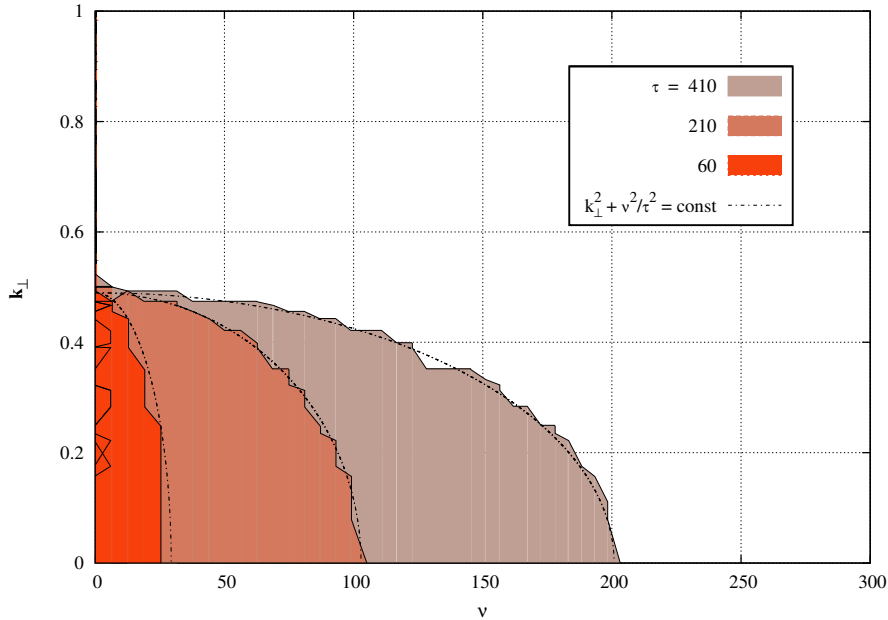
Figure 6.4: Resonance band during the time evolution of the system.

The colored areas indicate the modes that have been amplified by parametric resonance between the initial time and the time of interest. One way to qualitatively understand how the resonance behaves in this model is the following: in the fixed volume case, as recalled in (6.36), the resonance band is for modes that are between

$$R_- < k_\perp^2 + k_z^2 < R_+ , \tag{6.42}$$

where $R_{-,+} \propto \varphi_0^2$. Since $\eta \sim \frac{z}{\tau}$, we have that $\nu \sim k_z \tau$ and the previous condition becomes in term of the Fourier variables introduced in this section

$$R_- < k_\perp^2 + \frac{\nu^2}{\tau^2} < R_+ . \tag{6.43}$$

Therefore, the effect of the expansion is to shift the resonance band toward higher ν. The modes that are resonant at the time of interest are located on the front of the colored bands, which is indicated in the figure 6.4 by the dashed $k_\perp^2 + \frac{\nu^2}{\tau^2} = \text{const}$ line. As can be seen in this figure, this interpretation works quite well.

6.5 Occupation Number

6.5.1 Analytical expression

To compute the occupation number, one starts from the field operator $\hat{\phi}$ expressed in terms of the creation and annihilation operators, introduced in the section 4.1 and used in the section 5.4.1.2 to derive the occupation number of the fixed volume scalar field theory. But since the system of coordinates has changed, one should use the following decomposition for the field

$$\hat{\phi}(\tau, \boldsymbol{x}_\perp, \eta) = \frac{\sqrt{\pi}}{2} \int \frac{d^2 \boldsymbol{k}_\perp}{(2\pi)^2} \frac{d\nu}{2\pi} e^{\frac{\pi\nu}{2}} H_{i\nu}^{(2)}(k_\perp \tau) \hat{a}_{\boldsymbol{k}_\perp \nu} e^{i\nu\eta} e^{i\boldsymbol{k}_\perp . \boldsymbol{x}_\perp} + \text{h.c.} , \qquad (6.44)$$

where h.c. stands for Hermitian conjugate, and the choice that we did for the overall normalization factor will become clear in a moment. Given the work done in the section 6.1, it easy to see that $\hat{\phi}$ is a solution of the free equation of motion. We can invert this formula to obtain (equivalent to the formula 4.16 in the fixed volume case)

$$\hat{a}_{\boldsymbol{k}_\perp \nu} = i\tau \frac{\sqrt{\pi} e^{\frac{\pi\nu}{2}}}{2} \int d^2 \boldsymbol{x}_\perp d\eta\, e^{-i\nu\eta} e^{-i\boldsymbol{k}_\perp . \boldsymbol{x}_\perp} H_{i\nu}^{(2)*}(k_\perp \tau) \overleftrightarrow{\partial_\tau} \hat{\phi}(\tau, \boldsymbol{x}_\perp, \eta) , \qquad (6.45)$$

and thanks to the normalization factor, we have (in order to satisfy the canonical commutation relation between $\hat{\phi}$ and $\dot{\hat{\phi}}$)

$$\left[\hat{a}_{\boldsymbol{k}_\perp \nu}, \hat{a}_{\boldsymbol{k}'_\perp \nu'}^\dagger\right] = (2\pi)^3 \delta(\nu - \nu') \delta(\boldsymbol{k}_\perp - \boldsymbol{k}'_\perp) . \qquad (6.46)$$

Using (6.45) we get

$$\hat{a}_{\boldsymbol{k}_\perp \nu} \hat{a}_{\boldsymbol{k}_\perp \nu}^\dagger = \frac{\tau^2 \pi e^{\pi\nu}}{4} \left| \int d^2 \boldsymbol{x}_\perp d\eta\, e^{-i\nu\eta} e^{-i\boldsymbol{k}_\perp . \boldsymbol{x}_\perp} H_{i\nu}^{(2)*}(k_\perp \tau) \overleftrightarrow{\partial_\tau} \hat{\phi}(\tau, \boldsymbol{x}_\perp, \eta) \right|^2 \qquad (6.47)$$

and following the reasoning as in the section 5.4.1.2 we obtain the following resummed occupation number

$$f_{\boldsymbol{k}_\perp \nu} = -\frac{1}{2} + \frac{\tau^2 \pi e^{\pi\nu}}{4L^2 N} \left\langle \left| \int d^2 \boldsymbol{x}_\perp d\eta\, e^{-i\nu\eta} e^{-i\boldsymbol{k}_\perp . \boldsymbol{x}_\perp} H_{i\nu}^{(2)*}(k_\perp \tau) \overleftrightarrow{\partial_\tau} \phi(\tau, \boldsymbol{x}_\perp, \eta) \right|^2 \right\rangle . \qquad (6.48)$$

This is the quantity that we compute in the next section.

6.5.2 Numerical results

In all the following, the initial background field $\varphi_0(\boldsymbol{x}_\perp)$ is taken such that only one $\boldsymbol{k}_\perp^0$ mode is populated

$$\varphi_0(\boldsymbol{x}_\perp) = \varphi_0 \cos(\boldsymbol{k}_\perp^0 . \boldsymbol{x}_\perp) . \qquad (6.49)$$

In the simulations we took a $40 \times 40 \times 320$ grid with the arguably large $g = 4$ value, along with $k_\perp^0 = 0.77$ and $\varphi_0 = 15$. We started the simulation at $\tau_0 = 0.01$, but verified that the physical results do not depend on τ_0. The following four plots 6.5 show the occupation number in $\nu, k_\perp$ space at various times.
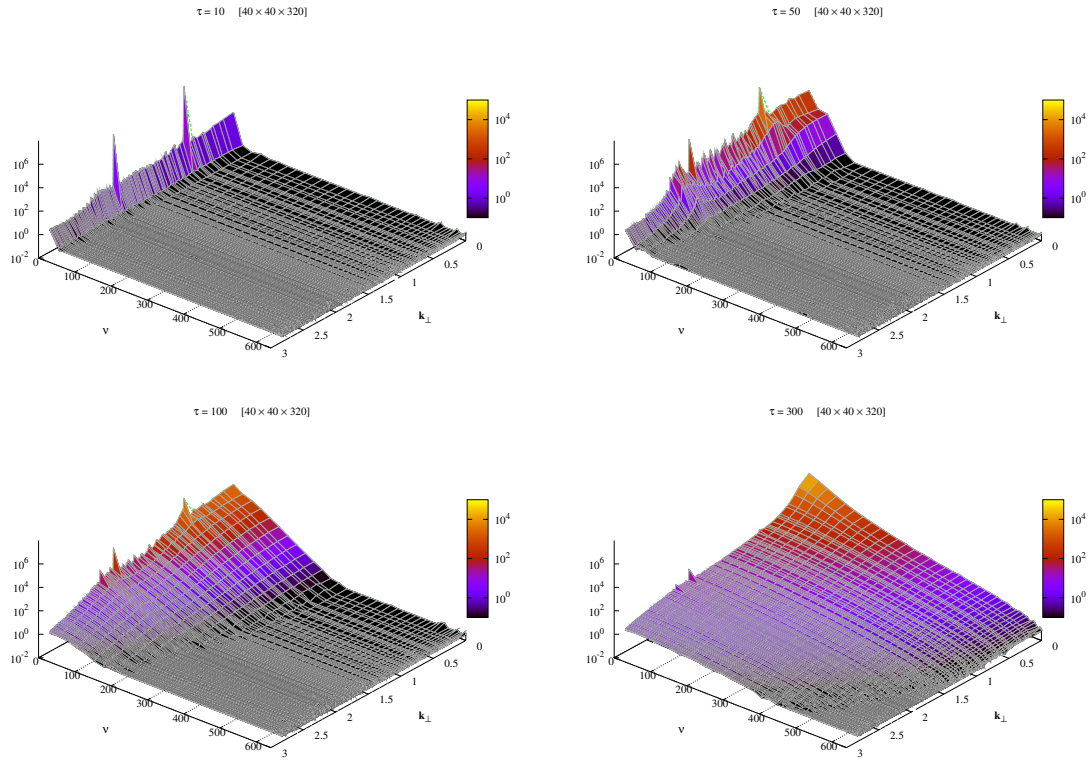
Figure 6.5: Occupation number computed from eq. (6.48) at various times.

As one can see, at time $\tau = 0.1$ a harmonic of the initial mode has already been populated (its frequency being a multiple of $k_\perp^0$). But the other modes, especially the $\nu \neq 0$ modes are still very small. Indeed, since the background field is rapidity independent, and the fluctuating term is small in comparison at the initial time, one expects this $\nu = 0$ localization at early times. As time increases, the occupation number expands towards higher ν values. At later times ($\tau \sim 300$ for the grid that we are using in this section), the occupation number reaches the UV cutoff in the longitudinal direction $\nu_{\max} = \frac{2}{N}$. This illustrates a serious limitation of the expanding simulations. Indeed, after $f_{\boldsymbol{k}_\perp \nu}$ has reached $\nu_{\max}$, the results are affected by lattice artifacts. The only way to circumvent this issue is to take rather large lattices in the longitudinal direction, in order to get results valid up to $\tau \sim 300$ (we did several tests with smaller lattices and the time at which $\nu_{\max}$ was reached was proportional to N). This behavior of $f_{\boldsymbol{k}_\perp \nu}$ is not surprising. Indeed, let us imagine for a moment that we are at thermal equilibrium. Then $\epsilon \sim \tau^{-\frac{4}{3}}$, and the temperature of the system evolves as $\tau^{-\frac{1}{3}}$. This is also the momentum scale, and

$$k_x \sim k_y \sim k_z \sim \tau^{-\frac{1}{3}} \ . \tag{6.50}$$

Now, since $\eta \sim \frac{z}{\tau}$, we have

$$\nu \sim \tau k_z \sim \tau^{\frac{2}{3}} \ . \tag{6.51}$$

Therefore if the system is thermal, this expansion of the distribution function towards higher ν is expected. Nevertheless, this prevents us from reaching a definitive conclusion on the late time behavior of the distribution function, as well as the formation of a Bose-Einstein condensate in the system [4].

---

4. Even if its presence seems plausible given the fast build-up of the zero mode as time increases in the figure 6.5.

6.6 Energy-momentum tensor

6.6.1 Definition, expectations

The usual definition of the canonical energy momentum tensor reads

$$
\begin{aligned}
T^{\tau\tau} &= \left\langle \frac{1}{2}(\partial_\tau\phi)^2 + \frac{1}{2}(\partial_x\phi)^2 + \frac{1}{2}(\partial_y\phi)^2 + \frac{1}{2\tau^2}(\partial_\eta\phi)^2 + \frac{g^2}{4!}\phi^4 \right\rangle \\
T^{xx} &= \left\langle \frac{1}{2}(\partial_\tau\phi)^2 + \frac{1}{2}(\partial_x\phi)^2 - \frac{1}{2}(\partial_y\phi)^2 - \frac{1}{2\tau^2}(\partial_\eta\phi)^2 - \frac{g^2}{4!}\phi^4 \right\rangle \\
T^{yy} &= \left\langle \frac{1}{2}(\partial_\tau\phi)^2 - \frac{1}{2}(\partial_x\phi)^2 + \frac{1}{2}(\partial_y\phi)^2 - \frac{1}{2\tau^2}(\partial_\eta\phi)^2 - \frac{g^2}{4!}\phi^4 \right\rangle \\
\tau^2 T^{\eta\eta} &= \left\langle \frac{1}{2}(\partial_\tau\phi)^2 - \frac{1}{2}(\partial_x\phi)^2 - \frac{1}{2}(\partial_y\phi)^2 + \frac{1}{2\tau^2}(\partial_\eta\phi)^2 - \frac{g^2}{4!}\phi^4 \right\rangle ,.
\end{aligned}
\tag{6.52}
$$

Since there is a one dimensional expansion, the space is not isotropic, but the transverse plane still is and we can therefore expect

$$
\left\langle (\partial_x\phi)^2 \right\rangle = \left\langle (\partial_y\phi)^2 \right\rangle .
\tag{6.53}
$$

What we will compute numerically will thus be the energy-density, the transverse and the longitudinal pressures, defined as

$$
\epsilon = T^{\tau\tau} , \qquad\qquad P_T = \frac{T^{xx} + T^{yy}}{2} , \qquad\qquad P_L = \tau^2 T^{\eta\eta} .
\tag{6.54}
$$

As we have already discussed when we proved that the classical field φ is well-behaved in the vicinity of the origin, the classical KG EOM in the proper-time rapidity system contains two terms that have opposite effects. The expansion term $E(\phi) = \frac{\phi}{\tau}$ tends to dilute the system in the longitudinal direction, which means that the expansion makes the system more anisotropic. In contrast, the interaction term $V(\phi) = \frac{g^2}{4!}\phi^4$ tends to redistribute the momentum in an isotropic way. How these two terms compete explain whether the system anisotropizes or isotropizes. This is summarized in the figure 6.6.
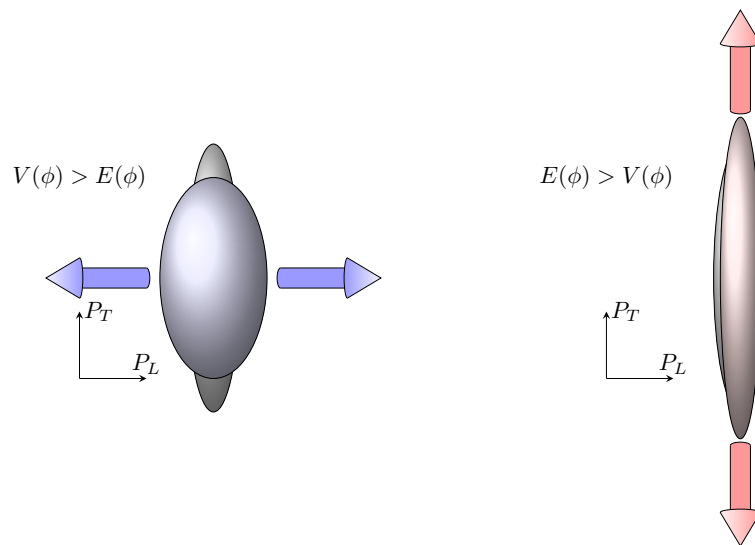
Figure 6.6: Effect of the expansion and interaction on the pressures. On both plots the ellipse at the second plan characterizes the initial anisotropic pressure profile. Left plot: as time evolves, the interaction term dominates over the expansion. Right plot: the opposite situation.

The key questions are therefore: what happens in the system under consideration? Is the answer time dependent? Answering these questions will be the aim of the following subsections.

6.6.2   The formation of an equation of state

The first study that we have performed on the energy-momentum tensor was to check whether or not an EOS forms, as it was the case in the fixed volume theory. Given the behavior of $f_{k_\perp \nu}$, one can expect that this is indeed the case. This is confirmed in the figure 6.7, that represents ϵ and the trace of the pressure tensor $2P_T + P_L$ in a log-log plot:
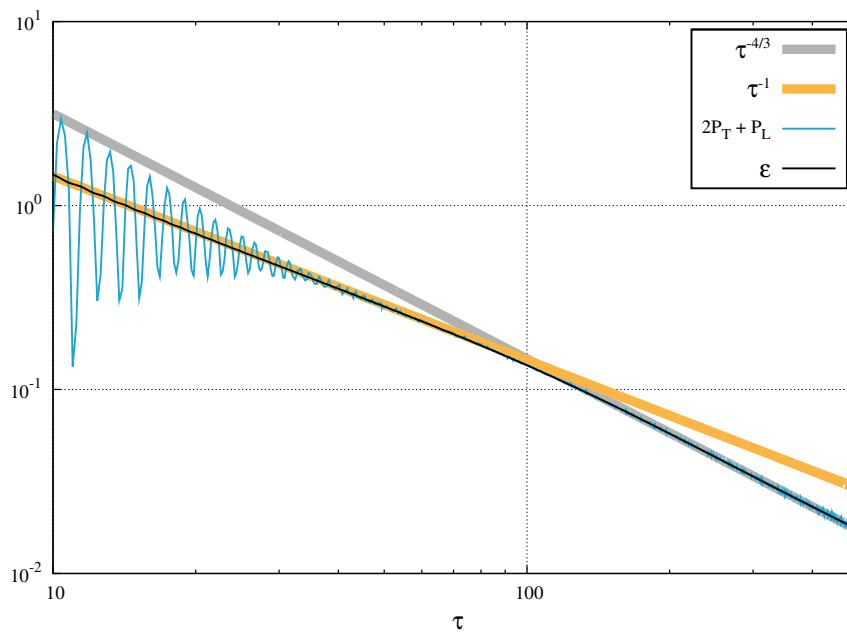
Figure 6.7: ϵ and $2P_T + P_L$ as a function of the proper time. Two fits are performed on the energy density: the gray band corresponds to a τ^{-1} behavior, while the orange one is $\tau^{-\frac{4}{3}}$.

Interestingly, one can observe three stages in the previous figure

— $\tau < 50$. The trace of the pressure tensor oscillates: the pressure is not related to ϵ by an EOS. In addition, the energy density is well fitted by τ^{-1}, a clear sign of free streaming if one recalls Bjorken's law (which has been checked numerically [5] in the figure 6.8).

$$\partial_\tau \epsilon + \frac{\epsilon + P_L}{\tau} = 0 \, , \tag{6.55}$$

provided that $P_L \ll \epsilon$.

---

5. This can be viewed as an accuracy check of our numerical computation since Bjorken's law is a consequence of energy-momentum conservation (recall 3.6), a property which must hold in the continuum case as well as on the lattice.
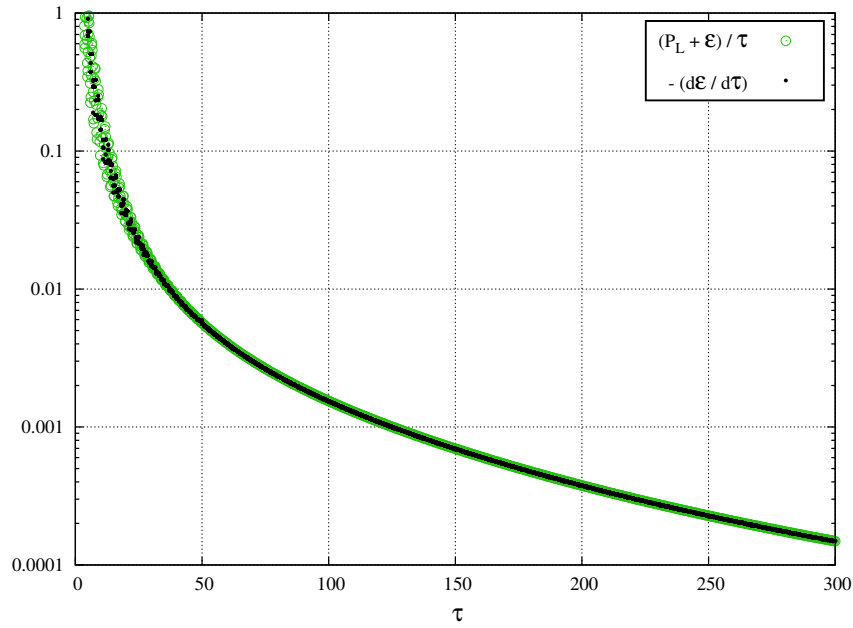
Figure 6.8: Numerical check of Bjorken's law.

— $50 < \tau < \sim 150$. The pressure tensor has stopped oscillating, and an equation of state has formed. But unlike in the fixed volume case, the system is still very anisotropic, since ϵ still behaves as τ^{-1}.

— $\tau \gtrsim 150$. Here, one observes a drastic change in the behavior of the energy-density, that starts scaling as $\tau^{-\frac{4}{3}}$, implying that $P_L \sim \frac{\epsilon}{3}$.

The physical process behind the formation of an equation of state is the same as the one described in the section 5.3.5: the presence of instabilities in the theory causes the trace of the pressure tensor to relax towards ϵ. But first the system is still very anisotropic. Then, at later times, it seems to isotropize.

6.6.3 Isotropization

In the next figure 6.9, the pressures P_L (red), P_T (green), the energy density ϵ (black) as well as trace $2P_T + P_L$ (blue) are represented.
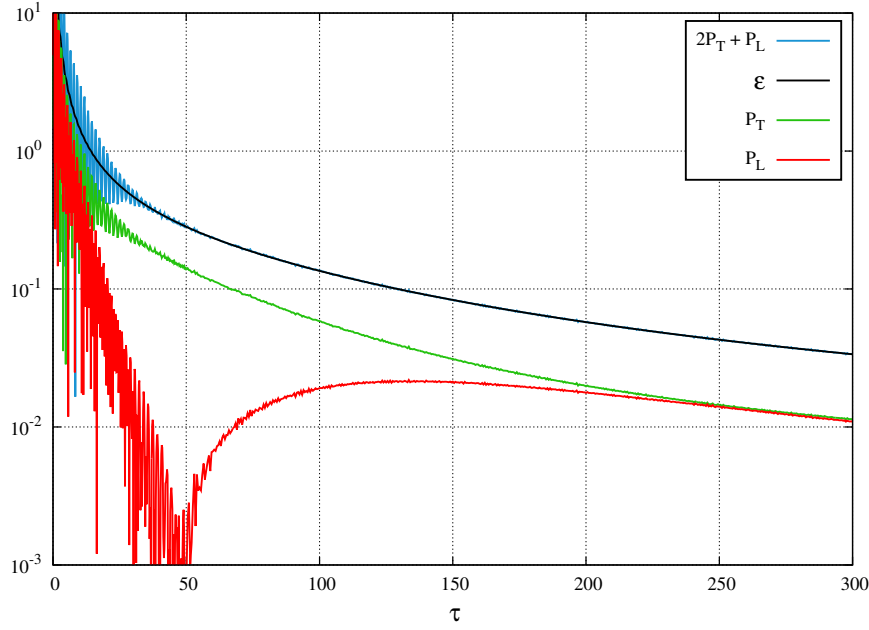
Figure 6.9: Components of the energy-momentum tensor. See the text for more details.

Here again we see the rather fast formation of an EOS at a time around $\tau \sim 50$. But at this time, the system is still far from being isotropic. Since we are considering a fixed slice in rapidity (recall the figure 6.2), and because the system is expanding, the particles are flying out of this slice and the system dilutes in the longitudinal direction. This explains the fast drop of P_L at early time. But then, the instabilities start to redistribute efficiently the momenta of the particles in all directions and this triggers in a second stage a raise in P_L, which becomes comparable to P_T at a time around $\tau \sim 200$. When this happens and because the EOS has already been formed, then $P_L \approx \frac{\epsilon}{3}$ and as explained in the previous section ϵ behaves as $\tau^{-\frac{4}{3}}$. This can also be understood from a kinetic description [162–164] of the pressures

$$P_T \sim \int d^2 k_\perp \frac{\mathrm{d}\nu}{\tau} \frac{k_\perp^2}{\sqrt{k_\perp^2 + \frac{\nu^2}{\tau^2}}} f_{k_\perp \nu} \qquad\qquad P_L \sim \int d^2 k_\perp \frac{\mathrm{d}\nu}{\tau} \frac{\nu^2}{\tau^2 \sqrt{k_\perp^2 + \frac{\nu^2}{\tau^2}}} f_{k_\perp \nu} . \qquad (6.56)$$

At early times, by looking at $f_{k_\perp \nu}$ one can see that the $\nu \sim 0$ modes dominate in the previous formula and therefore $P_L \ll P_T$. But as we approach equilibrium, $f_{k_\perp \nu}$ starts to expand in the ν direction at a $\tau^{\frac{2}{3}}$ pace while on dimensional ground $k_\perp$ is expected to shrink at a $\tau^{-\frac{1}{3}}$ one, and this leads to $P_L \sim P_T \sim \tau^{-\frac{4}{3}}$. The conclusion of this part is the following: the resummed pressures, computed in the classical-statistical approximation, evolve towards the formation of an EOS and later on isotropize. The resummed energy density exhibits a $\tau^{-\frac{4}{3}}$ behavior at late times. All of these features suggest that the postulates of hydrodynamics 3.2 are satisfied at late times.

6.7   Hydrodynamical behavior

6.7.1   Hydronamical model

To compare the outcome of the classical statistical simulations with viscous hydrodynamics, we use a very simple implementation of hydrodynamics. As briefly explained in the chapter 3 (and in more details in [108, 109]), the energy-momentum tensor of a viscous fluids reads

$$T_{\mathrm{visc}}^{\mu\nu} = T_{\mathrm{ideal}}^{\mu\nu} + \Pi^{\mu\nu} , \qquad (6.57)$$

where $\Pi^{\mu\nu}$ characterizes the deviation of the fluid from an ideal one. $T^{\mu\nu}_{\text{ideal}}$ reads

$$T^{\mu\nu}_{\text{ideal}} = (\epsilon_h + p_h)u^\mu u^\nu - p_h g^{\mu\nu} = \begin{pmatrix} \epsilon_h & 0 & 0 & 0 \\ 0 & \frac{\epsilon_h}{3} & 0 & 0 \\ 0 & 0 & \frac{\epsilon_h}{3} & 0 \\ 0 & 0 & 0 & \frac{\epsilon_h}{3} \end{pmatrix}, \tag{6.58}$$

where the h index stands for hydrodynamics. To make the comparison easier, we will choose a boost invariant hydrodynamical model where $u^\mu = (1,0,0,0)$ and

$$\Pi^{\mu\nu} = \eta \begin{pmatrix} 0 & 0 & 0 & 0 \\ 0 & \frac{2}{3\tau} & 0 & 0 \\ 0 & 0 & \frac{2}{3\tau} & 0 \\ 0 & 0 & 0 & -\frac{4}{3\tau} \end{pmatrix}. \tag{6.59}$$

In this model, one therefore has

$$P^h_T = \frac{\epsilon_h}{3} + \frac{2\eta}{\tau}, \qquad\qquad P^h_L = \frac{\epsilon_h}{3} - \frac{4\eta}{\tau}, \tag{6.60}$$

and there are two unknowns ϵ_h and η. We start from Bjorken's law, in which we replace the longitudinal pressure

$$\partial_\tau \epsilon_h + \frac{4}{3}\frac{\epsilon_h}{\tau} - \frac{4\eta}{3\tau^2} = 0. \tag{6.61}$$

To close the hydrodynamical model, one must make some assumptions on η. Firstly, we truncate the hydrodynamical expansion at first order, i.e. we assume that

$$\eta = \frac{\eta_0}{\tau}. \tag{6.62}$$

Then, we introduced the entropy by writing $\eta = \frac{\eta}{s}s$. To determine s, we assumed that the system is not far from local thermal equilibrium, where the occupation number follows Bose-Einstein statistics

$$n_B(\boldsymbol{k}) = \frac{1}{e^{\frac{k}{T}} - 1}. \tag{6.63}$$

Neglecting interactions, this leads to

$$\epsilon_e = \int \frac{d^3\boldsymbol{k}}{(2\pi)^3} k\, n_B(\boldsymbol{k}) = \frac{\Gamma(4)\zeta(4)}{2\pi^2} T^4 = \frac{\pi^2 T^4}{30}$$

$$s_e = \int \frac{d^3\boldsymbol{k}}{(2\pi)^3} \left([1 + n_B(\boldsymbol{k})]\ln[1 + n_B(\boldsymbol{k})] - n_B(\boldsymbol{k})\ln n_B(\boldsymbol{k})\right) = \frac{2\pi^2 T^3}{45}. \tag{6.64}$$

Therefore, at thermal equilibrium

$$s_e = \frac{4}{3}\left(\frac{\pi^2 \epsilon_e}{30}\right)^{\frac{3}{4}}. \tag{6.65}$$

We assume that this relation also holds in our case. Now, since ϵ behaves as $\tau^{-\frac{4}{3}}$, therefore $s \sim \tau^{-1}$ and this implies

$$\frac{\eta}{s} = \frac{\eta_0}{s_0} = \text{const}. \tag{6.66}$$

To summarize, our simplistic hydrodynamical model makes the following assumptions
    — The flow is boost invariant

— $T^{\mu\nu}$ is the ideal term plus a viscous term proportional to η described in the equation (6.59).

— The shear-viscosity behaves as τ^{-1}

— The system is not so far from thermal, and therefore $s \approx \frac{4}{3}\left(\frac{\pi^2 \epsilon_h}{30}\right)^{\frac{3}{4}}$.

— $\frac{\eta}{s}$ is a constant

and one is left with

$$\partial_\tau \epsilon_h + \frac{4}{3}\frac{\epsilon_h}{\tau} - \frac{\eta_0}{s_0}\frac{16}{9}\left(\frac{\pi^2}{30}\right)^{\frac{3}{4}}\frac{\epsilon_h^{\frac{3}{4}}}{\tau^2} = 0 \;. \tag{6.67}$$

We need to specify the initial values ϵ_h^0, $\frac{\eta_0}{s_0}$ at some initial time τ_0. Since our aim is to compare with the classical-statistical simulations, we initialize the hydrodynamical parameters so that P_L and P_T agree with the statistical simulation at τ_0

$$\eta(\tau_0) = \frac{\tau_0(P_T - P_L)_0}{2} \;. \tag{6.68}$$

6.7.2 Hydronamical evolution

6.7.2.1 Pressure

Since hydrodynamics needs an EOS, it only makes sense to do the comparison at $\tau_0 > 50$. We have done so for three different τ_0 as one can see in the next figure 6.10.
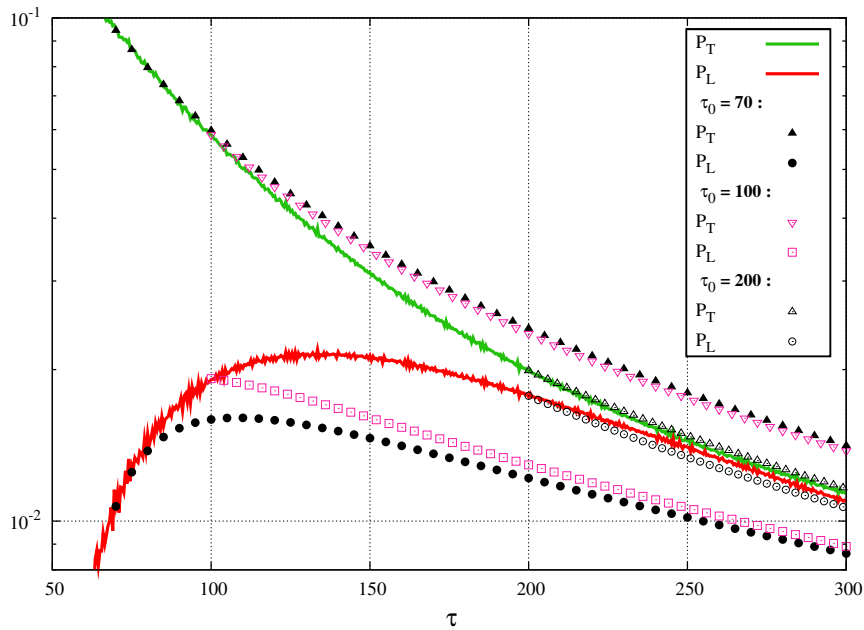
Figure 6.10: Comparison between a simplistic hydrodynamical model (6.67) and the the classical statistical simulations.

When the classical-statistical pressure tensor is still very anisotropic – $\tau_0 = 70$ (filled black dots for the hydrodynamical simulation) and $\tau_0 = 100$ (purple dots) – the hydrodynamical simulation leads to a slower isotropization. But once the classical statistical pressure tensor has almost isotropized – $\tau_0 = 200$ (black dots for the hydrodynamical simulation) – then the two models give very similar results. This would imply that isotropization is a prerequisite for hydrodynamics – a property that seems specific to a weakly coupled theory [6]

---

6. As recalled in the section 3.3 and as can be found in [29], Ads/Cft suggests that the opposite happens at strong coupling: namely hydrodynamical behavior starts before full isotropization.

6.7.2.2   Viscosity over entropy ratio

As we saw in the figure 6.10, the isotropization happens at different pace in classical-statistical simulations and in first order hydrodynamics. Indeed, for the latter one expects

$$\frac{P_T^h - P_L^h}{\epsilon_h} = \frac{2\eta}{\tau\epsilon_h} \sim \tau^{-\frac{2}{3}} \ . \tag{6.69}$$

In the figure 6.11, we have computed this ratio in the classical statistical framework .
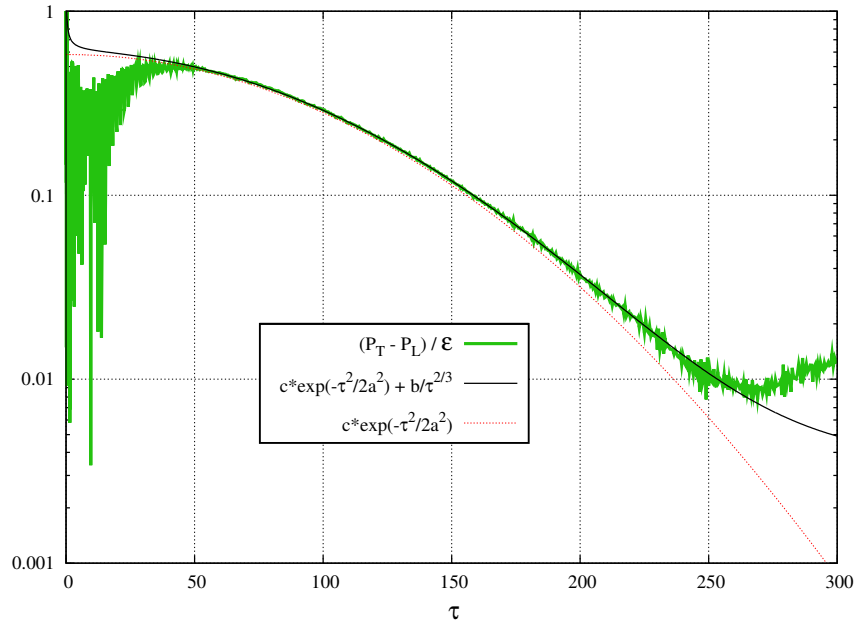
Figure 6.11: Approach to isotropization in classical statistical simulations.

As one can see, the approach to isotropization is much faster than a $\tau^{-\frac{4}{3}}$ power law, as one can fit the ratio (6.69) (green band) with a $e^{-\frac{\tau^2}{2a^2}}$ term (red line). But as the system approaches complete isotropization, the fit can be improved by adding an additional $\tau^{-\frac{2}{3}}$ to the red fit (black line). Presumably what it means is that the instabilities speed up the isotropization until a point where hydrodynamical behavior – the additional term in the fit – is observed. This term in $\tau^{-\frac{2}{3}}$ can give us some insight on the fixed $\frac{\eta}{s}$ value that is reached when the hydrodynamical behavior sets in

$$\frac{\eta}{s} \sim 0.26 \ , \tag{6.70}$$

i.e. a very small value of the viscosity over entropy ratio. To confirm this trend, on could also compute

$$\frac{\eta}{s} \sim \frac{\tau(P_T - P_L)}{2\epsilon^{\frac{3}{4}}} \ , \tag{6.71}$$

as a time dependent quantity. This is the black line in the following figure 6.12
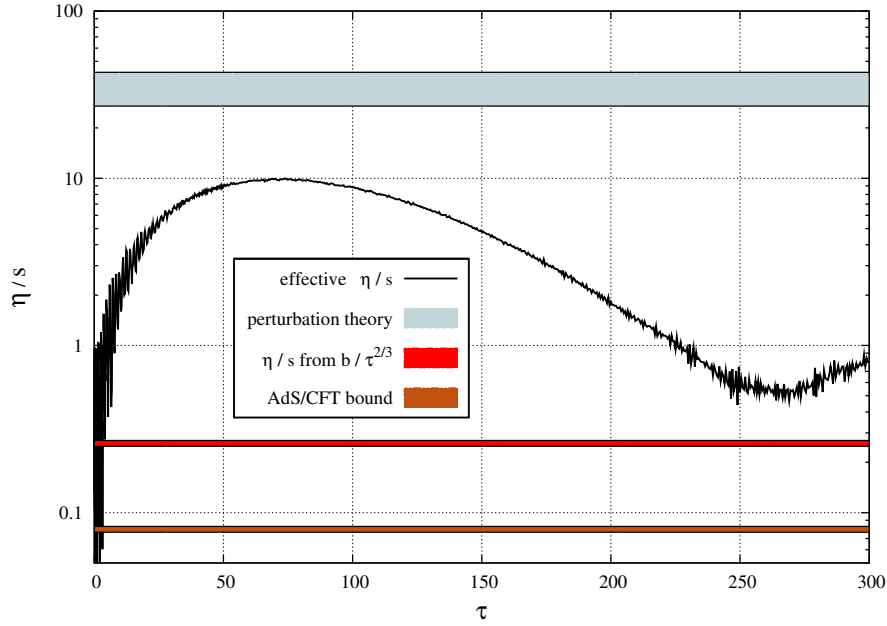
Figure 6.12: Different ways of extracting $\frac{\eta}{s}$ in the classical classical simulations, compared with the Leading order perturbative result (blue band, extracted from [102]) and the AdS/CFT conjectured lower bound (brown) $\frac{1}{4\pi}$ [115].

On this figure one should not take seriously what happens before $\tau \sim 50$ since there is no EOS yet, nor what happens after $\tau \sim 280$ when lattice artifacts start plaguing the simulation. In the range $50 \lesssim \tau \lesssim 280$, the ration $\frac{\eta}{s}$ decreases, and is always much smaller than the LO perturbative result. It is also rather close to the lower bound $\frac{1}{4\pi}$ conjectured from AdS/CFT calculations. This smaller than expected $\frac{\eta}{s}$ ratio has been called anomalous viscosity in the past, and have been predicted to happen in systems subject to unstable fields in [165, 166].

6.8   Summary

• For a ϕ^4 scalar field theory in an $3 + 1D$ space expanding in one spatial direction, the CSA also leads to an EOS.
• When the EOS is formed, the system is still very anisotropic due to the longitudinal expansion. But the instabilities are able to redistribute efficiently the momenta in all the spatial directions and one observes isotropization at later stages.
• One can compare the outcome of the CSA with a very simple first order hydrodynamical model. The two behave similarly as the system approaches full isotropization.
• The $\frac{\eta}{s}$ ratio crudely extracted from the CSA at the latest times considered when the system is almost isotropic is smaller (by orders of magnitude) than the LO perturbative calculation. It is close the conjectured lower bound $\frac{1}{4\pi}$

Appendix

6.A   Numerical considerations

6.A.1   Parallelization with OpenMP and MPI

As mentioned in the section 6.5.2, we had to use larger lattices in this chapter compared to the ones used in the fixed volume study, in order to cope with the longitudinal expansion of the system. Therefore, we were no longer able to run the program on a local computer, and we adapted our code to run on a cluster[7]. Running on a cluster saves a huge amount of time, as the Monte-Carlo method is trivially parallelizable. Let us recall here the structure of our algorithm, and see how we choose to implement it. There are three main steps in the numerical procedure:

- Diagonalization of the matrix of equation (6.30), which is a matrix of size $L^2 \times L^2$. Since we need the complete set of eigenvalues and eigenvectors, this is an operation that scales as L^6. This can be done with the LAPACK library. For larger transverse lattice sizes, we could have also used its parallelized version SCALAPACK. Even if these libraries cannot exploit the fact that we are diagonalizing a sparse matrix, they are sufficient for the values of L that we have considered.
- Generate the initial conditions thanks to equation (6.26). This step scales as $L^2 N \times L^2 N$, since for each spatial point we have to perform a loop over the momenta. In addition, we need to perform this step for each of the N_{conf} initial configurations of the Monte Carlo method. This step is easily parallelizable with MPI, as each node N_{node} can deal with its $\frac{N_{conf}}{N_{node}}$ initial conditions.
- Perform the time evolution. Numerically, we implement this step by splitting the Klein-Gordon (second order partial differential equation) into two first order equations

$$\phi_{ijk,n+1} = f(\dot{\phi}_{ijk,n}, \phi_{ijk,n}) , \qquad \dot{\phi}_{ijk,n+1} = g(\dot{\phi}_{ijk,n}, \phi_{ijk,n}) , \qquad (6.72)$$

where the details of f and g depend on the algorithm. Naively, this step scales as $2L^2 N$, but the actual cost is higher because of intermediate computations. It turns out that high degree precision algorithms (like Runge-Kutta methods of order 8: Dormand-Prince, Fehlberg, Cash-Karp) have the default of requiring many intermediate computations (time cost) and an important quantity of intermediate storage arrays. A good compromise is the recently developed low storage Runge-Kutta method described in [148]. While this is only an order 4 method, it has the advantage of only requiring one additional intermediate array. This is the method that we have implemented.

Our algorithm can be used in two different ways:

- The first version trivially parallelizes the Monte-Carlo method by dividing the N_{conf} configurations on the N_{node} nodes at our disposal on a cluster with MPI. Each subset of $\frac{N_{conf}}{N_{node}}$ configurations is then split with OpenMP on the N_{core} of each node. One just needs to use MPI_REDUCE at the end of the evolution to gather on the master node all the quantities of interest.
- The second version also trivially parallelizes the N_{conf} configurations on the N_{node} nodes with MPI. But then each of the $\frac{N_{conf}}{N_{node}}$ is assigned to a single node. A further parallelization is done with OpenMP by dividing the spatial domain in N_{core} slices. This allows one to use larger lattices without being limited by memory issues.

6.A.2   Performance tests

We have performed several tests of the two versions of our algorithm on a local computer and on the cluster TITANE. Our results are summarized in the figures 6.13 and 6.14.

---

7. We have submitted an application to GENCI (Grand Equipement National de Calcul Intensif) and obtained 100.000 hours on the TITANE cluster.
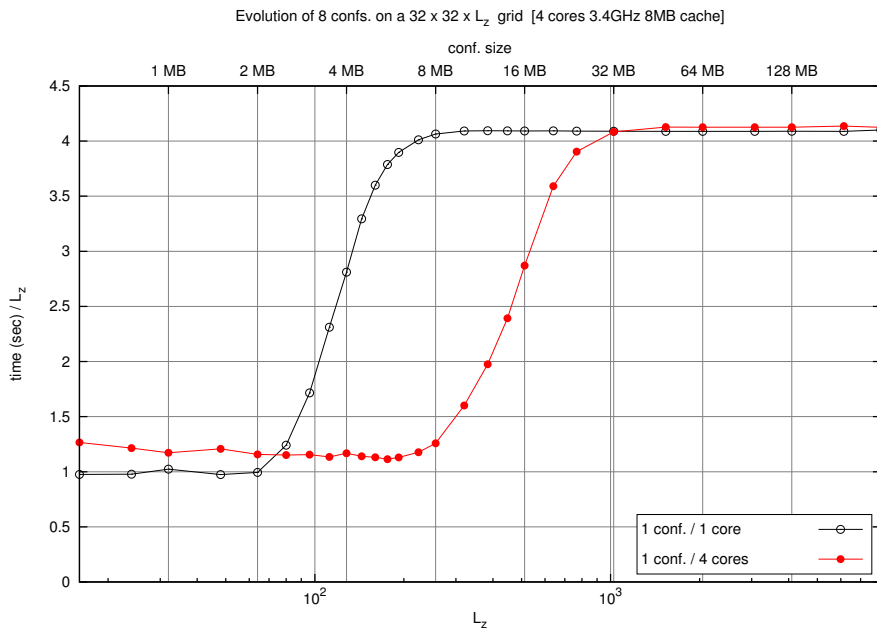
Figure 6.13:   Computation time as a function of the longitudinal lattice size. This study has been performed on a single i7 CPU (4 cores, 8 MB cache, 3.4 GHz), where 8 initial configurations have been evolved. The upper horizontal scale indicates the required memory for one configuration.
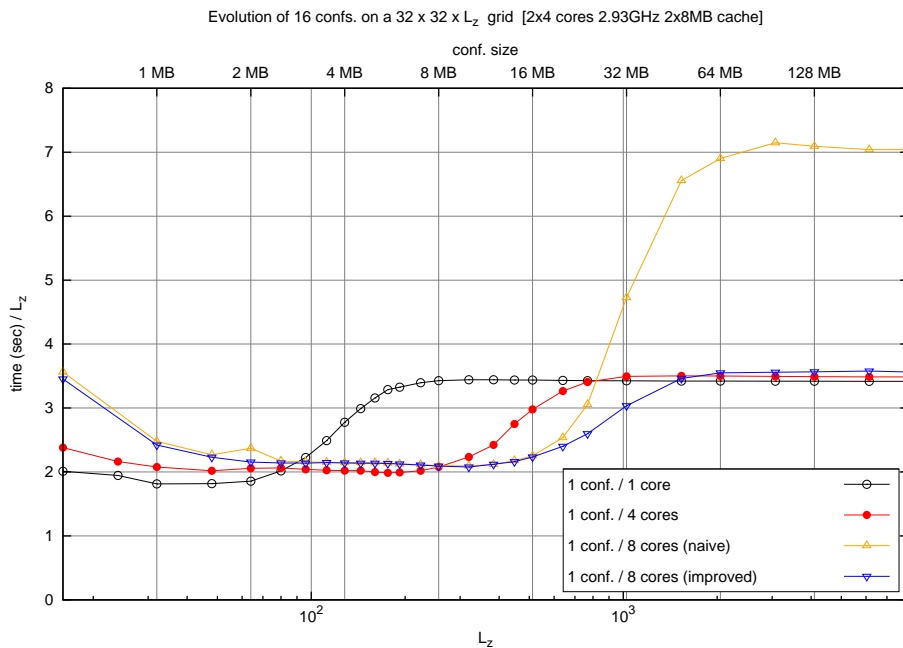
Figure 6.14:   Computation time as a function of the longitudinal lattice size. This study has been performed on one TITANE node (2×4 cores, 2×8 MB cache, 2.93 GHz), where 16 initial configurations have been evolved.

In the figure 6.13, 8 initial configurations have been evolved on a local computer with a single i7 CPU (4 cores). In the figure 6.13, 16 initial configurations (twice as many as in the previous test in order to have the same number of configurations per core) have been evolved on a TITANE node (8 cores). The execution time on the vertical axis has been divided by the longitudinal size of the lattice, a flat curve therefore corresponding to a linearly increasing

execution time. We have tested the following configurations:

- **One configuration per core**. This is the most naive and simple implementation. As one can see, the time execution increases linearly with the lattice size until the size of one configuration cannot be fit in cache memory anymore (2MB). Before this, the speed of the execution depends on the CPU frequency, and after that on the bandwidth memory [8]

- **Four configurations per core**. For small lattices sizes, there is a penalty of around 20%. This is presumably due to synchronization issues, as well as data exchange on the edges of the lattice slices (remember that OpenMP is used here to divide the spatial domain into several slices assigned to the available cores. The Laplacian operator involving nearest neighbors, the corresponding points can be on different cores for the edges of a slice). The advantage of this parallelization choice is that one is not limited by the bandwidth until 8 MB, which means that the cache of one node can fit a four times larger lattice size. In addition, larger lattice sizes (> 8 MB) only suffer from a few percent penalty compared with the one configuration per core implementation.

- **Eight configurations per core**. This test can obviously be performed only on the 8 core TITANE nodes. Here two implementations were considered. The first one naively increases the N_{core} value. If one does so, the performance is significantly worse than with four configurations per core. This is due to the fact that each node is made of two four-core CPUs, each with its own memory bank, and that nothing ensures that the data treated by a core located on the first CPU is stored in the memory bank handled by this CPU. One can force this by letting each core write on its assigned slice just after the memory has been allocated. To ensure that a given core will always deal with the same lattice slice, one should also set the following environment variables:
  ```
  OMP_PROC_BIND=true
  GOMP_CPU_AFFINITY="0-7"
  ```

With this implementation, one gets the desired scaling: a penalty for small lattice sizes, but a larger lattice size that can be fitted in the cache.

---

8. This is why the execution time is shorter on the *i*7 core (higher frequency and better set of vector instructions) for small lattice sizes. Nevertheless, the TITANE node is more efficient for large lattice sizes, since its memory bandwidth is larger.

Chapter 7

⊚Non Renormalizability of the Classical Statistical Approximation ⚛

Contents

I n the previous chapters we did not pay much attention to renormalization. Our aim was to study the appearance of the hydrodynamical behavior (formation of an EOS, isotropization). All the calculations were done on a lattice that provides an ultraviolet cutoff, and no attempt was made to take the continuum limit. This chapter aims at studying this issue.

7.1 Renormalization of Green's functions

In this chapter we consider for simplicity the fixed volume scalar field theory – this time with a mass, whose Lagrangean is

$$\mathcal{L} = \frac{1}{2} \left(\partial_\mu \phi \right) \left(\partial^\mu \phi \right) - \frac{m^2}{2} \phi^2 - \frac{g^2}{4!} \phi^4 + J\phi \,. \tag{7.1}$$

The usual renormalization procedure implies that $\mathcal{L}$ is unphysical, with m and g "bare" parameters. In other words, physical observables are not directly functions of these bare quantities, but rather functions of renormalized ones. Renormalizing $\mathcal{L}$ require that one introduces a finite number of counterterms in it: a mass counterterm δm, a coupling constant counterterm δg and a field amplitude counterterm δZ. After one has done so, all the Green's function become finite.

7.2   Renormalization of composite operators

The previous procedure is insufficient to renormalize local composite operators. For instance, even after doing the renormalization of the mass, coupling constant and field amplitude, there are still divergences in the energy-momentum tensor – a local composite operator of dimension 4

$$T_{\text{div}}^{\mu\nu} = d_0 \Lambda^4 + d_1(\phi)\Lambda^2 + d_2(\phi)\ln\Lambda \, , \tag{7.2}$$

where Λ is the UV cutoff. In the results of the sections 5.3.6.3 and 6.6.3, the Λ^4 has already been subtracted by performing two simulations: a first one with a non-zero background field φ and a second with $\varphi = 0$ (d_0 is the same in both simulations, and $d_1 = d_2 = 0$ in the vacuum simulations). These results were therefore (denoting Q the only dimensionful parameter of the theory)

$$T^{\mu\nu} - T_{\text{vac}}^{\mu\nu} \sim \frac{Q^4}{g^2} + d_1(\phi)\Lambda^2 + d_2(\phi)\ln\Lambda \, . \tag{7.3}$$

To completely renormalize $T^{\mu\nu}$, one should perform a special renormalization for composite operators (see for instance [167] for more details). A composite operator can mix with any operator of dimension $m \leq n$ provided they have the same quantum numbers. There are 6 rank 2 operators of dimension four or less

$$\mathcal{O}_1 = g^{\mu\nu}\phi^2 \, , \qquad \mathcal{O}_2 = g^{\mu\nu}\phi^4 \, , \qquad \mathcal{O}_3 = g^{\mu\nu}\phi\Box\phi \, ,$$
$$\mathcal{O}_4 = g^{\mu\nu}(\partial_\mu\phi)\partial^\mu\phi \, , \qquad \mathcal{O}_5 = (\partial^\mu\phi)(\partial^\nu\phi) \, , \qquad \mathcal{O}_4 = \phi\partial^\mu\partial^\nu\phi \, . \tag{7.4}$$

The composite operator renormalization procedure aims at computing the mixing matrix $\mathcal{Z}^{ij}$

$$\mathcal{O}_i^{\text{renor}} = \mathcal{Z}^{ij}\mathcal{O}_j^{\text{bare}} \, , \tag{7.5}$$

The method to compute $\mathcal{Z}^{ij}$ is explained in [167]. But all of this only applies to a renormalizable theory. What if the classical-statistical theory is not renormalizable? a key ingredient in the proof of the renormalizability of a theory is the Weinberg theorem [1]. The Weinberg theorem states that if all the subdivergences of a given diagram have been subtracted, then the remaining divergence is a polynomial of at most degree ω in the external momenta, where ω is the superficial degree of divergence of the diagram. From power counting, it is enough to investigate the two and four-point functions. To do so, we will reformulate the Lagrangean (7.1) in terms of the retarded-advanced basis.

7.3   The retarded-advanced basis

The key ingredient behind the CSA is the SCHWINGER-KELDYSH formalism, whose Lagrangean (7.1) is

$$\mathcal{L}[\phi^{(+)}, \phi^{(-)}] = \left[\frac{1}{2}\left(\partial_\mu\phi^{(+)}\right)\left(\partial^\mu\phi^{(+)}\right) - \frac{m^2}{2}\left(\phi^{(+)}\right)^2 - \frac{g^2}{4!}\left(\phi^{(+)}\right)^4 + J\phi^{(+)}\right]$$
$$- \left[\frac{1}{2}\left(\partial_\mu\phi^{(-)}\right)\left(\partial^\mu\phi^{(-)}\right) - \frac{m^2}{2}\left(\phi^{(-)}\right)^2 - \frac{g^2}{4!}\left(\phi^{(-)}\right)^4 + J\phi^{(-)}\right] \, . \tag{7.6}$$

---

1. First derived in [168]. The derivation was simplified in [169–172].

The associated free propagators (direct adaptation of those presented in formula (4.44-4.47))

$$G_{++} = \frac{i}{p^2 - m^2 + i\epsilon} \,, \qquad\qquad G_{--} = \frac{-i}{p^2 - m^2 - i\epsilon} \,,$$

$$G_{-+} = 2\pi\theta(p^0)\delta(p^2 - m^2) \,, \qquad\qquad G_{+-} = 2\pi\theta(-p^0)\delta(p^2 - m^2) \,. \qquad (7.7)$$

As explained in the section 4.1.3, we can perform a rotation of this basis to the more convenient retarded-advanced basis $G_{\alpha\beta}$ with $\alpha, \beta \in 1, 2$

$$G_{\alpha\beta} = \sum_{\epsilon,\epsilon'=\pm} \Omega_{\alpha\epsilon} G_{\epsilon\epsilon'} \Omega_{\epsilon'\beta}^\dagger \,, \qquad (7.8)$$

with the rotated matrix defined as

$$\Omega = \begin{pmatrix} 1 & -1 \\ \frac{1}{2} & \frac{1}{2} \end{pmatrix} \,. \qquad (7.9)$$

This lead to $G_{11} = 0$ and

$$G_{12} = G_A = \frac{i}{p^2 - m^2 - ip^0\epsilon} \,, \quad G_{21} = G_R = \frac{i}{p^2 - m^2 + ip^0\epsilon} \,, \quad G_{22} = G_S = \pi\delta(p^2 - m^2) \,. \qquad (7.10)$$

Following the section 4.3, we define[2] $\phi_2 = \frac{\phi^{(+)}+\phi^{(-)}}{2}$ and $\phi_1 = \phi^{(+)} - \phi^{(-)}$, and we get

$$\mathcal{L}[\phi_1, \phi_2] = (\partial_\mu \phi_1)(\partial^\mu \phi_2) - m^2 \phi_1 \phi_2 - \frac{g^2}{3!}\phi_1 \phi_2^3 - \frac{g^2}{4!}\phi_1^3 \phi_2 + J\phi_1 \,. \qquad (7.11)$$

Denoting $i\Gamma_{\alpha\beta\gamma\delta}$ the vertices, this implies that (not forgetting the 3! symmetry factor in Γ_{1222} and Γ_{1112})

$$\Gamma_{1111} = \Gamma_{1122} = \Gamma_{2222} = 0 \qquad \Gamma_{1222} = -ig^2 \,, \qquad \Gamma_{1112} = -i\frac{g^2}{4} \,. \qquad (7.12)$$

Finally, calling $J_{1,2}$ the sources that couple to ϕ_1, ϕ_2, we get

$$J_{\phi_2} = 0 \,, \qquad\qquad J_{\phi_1} = J \,. \qquad (7.13)$$

7.4 Eliminating the source term

As we have seen in the section 4.2.1, at leading order $\phi^{(-)} = \phi^{(-)} = \varphi$ which is just the solution of the classical Klein-Gordon equation

$$(\Box + m^2)\varphi + \frac{g^2}{6}\varphi^3 = J \,, \qquad (7.14)$$

with retarded initial conditions

$$\lim_{x^0 \to -\infty} \varphi, \dot{\varphi} = 0 \,. \qquad (7.15)$$

The Green's formula for φ reads

$$\varphi(x) = -i\left(\int_{y^0=0} d^3y \left(G_{21}(x,y) \overleftarrow{\partial_y^0} \varphi(y) \right) + \int_{y^0>0} d^4y \, G_{21}(x,y) V'(\varphi(y)) \right) \,, \qquad (7.16)$$

---

2. There we had used the notation $\phi_1 = \sigma$ and $\phi_2 = \varphi$.

and one can see that φ can only be attached to an index of type 2 in the Γ vertices. Therefore the J source can be eliminated by adding the following interacting terms to Lagrangean

$$\mathcal{L}_{\varphi \, \text{int}} = \frac{g^2}{2} \left[\varphi^2 \, \phi_1 \, \phi_2 + \frac{1}{2} \varphi \phi_1 \, \phi_2^2 + \frac{1}{3!} \varphi \, \phi_1^3 \right] \,, \tag{7.17}$$

and therefore
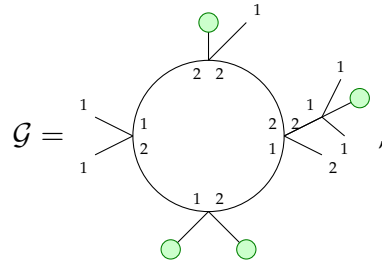
$$\mathcal{L} = \left(\partial_\mu \phi_1\right) \left(\partial^\mu \phi_2\right) - \frac{m^2}{2} \phi_1 \, \phi_2 - \frac{g^2}{3!} \phi_1 \, \phi_2^3 - \frac{g^2}{4!} \phi_1^3 \, \phi_2 - \frac{g^2}{2} \left[\varphi^2 \, \phi_1 \, \phi_2 + \frac{1}{2} \varphi \, \phi_1 \, \phi_2^2 + \frac{1}{3!} \varphi \, \phi_1^3 \right] \,. \tag{7.18}$$

Thanks to this Lagrangean, let us study the ultraviolet power counting of both the full theory and the CSA, whose Lagrangean is now

$$\mathcal{L} = \left(\partial_\mu \phi_1\right) \left(\partial^\mu \phi_2\right) - \frac{m^2}{2} \phi_1 \, \phi_2 - \frac{g^2}{3!} \phi_1 \, \phi_2^3 - \frac{g^2}{2} \left[\varphi^2 \, \phi_1 \, \phi_2 + \frac{1}{2} \varphi \, \phi_1 \, \phi_2^2 \right] \,. \tag{7.19}$$

7.5   Ultraviolet power counting in the full theory

In the full theory, the Lagrangean is (7.18). Considering generic connected graph

$$\mathcal{G} = \qquad , \tag{7.20}$$

We denote (see [173] for instance):
— E the number of external legs (6 in the previous diagram)
— I the number of internal lines (5 in the previous diagram)
— L the number of independent loops (1 in the previous diagram)
— V_{class} the number of $\frac{g^2}{3!} \phi_1 \, \phi_2^3$ vertices (one in the previous diagram)
— V_{quant} the number of $\frac{g^2}{4!} \phi_1^3 \, \phi_2$ vertices (one in the previous diagram)
— V_1 the number of $\frac{g^2}{2} \varphi^2 \, \phi_1 \, \phi_2$ vertices (one in the previous diagram)
— V_2 the number of $\frac{g^2}{4} \varphi \, \phi_1 \, \phi_2^2$ vertices (one in the previous diagram)
— V_3 the number of $\frac{g^2}{4!} \varphi \, \phi_1^3$ vertices (one in the previous diagram)
Our aim is to compute the superficial degree of divergence of this graph $\omega(\mathcal{G})$. To do so, two relations will prove helpful. Firstly, each of the four legs of every vertex must be attached to the endpoint of a propagator, which leads to

$$E + 2I = 4 \left(V_{\text{class}} + V_{\text{quant}}\right) + 3(V_2 + V_3) + 2V_1 \,, \tag{7.21}$$

and in our example one indeed has $6 + 5 \times 2 = 4 \times (1 + 1) + 3 \times (1 + 1) + 2 \times 1$. A second relation can be found by counting the number of independent momenta that can circulate into the loops of the diagram $\mathcal{G}$. It reads

$$L = I - \left(V_{\text{class}} + V_{\text{quant}} + V_1 + V_2 + V_3\right) + 1 \,, \tag{7.22}$$

and in our case indeed $1 = 5 - (1 + 1 + 1 + 1 + 1) + 1$. The superficial degree of divergence of the graph $\mathcal{G}$ is given by

$$\omega(\mathcal{G}) = 4L - 2I \,. \tag{7.23}$$

Indeed, each loop induces a $\int \mathrm{d}^4 p \sim p^4$ factor and each internal propagator[3] a factor p^{-2}. From the two equalities that we have just derived, we obtain

$$\omega(\mathcal{G}) = 4 - E - (V_2 + V_3) - 2V_1 = 4 - E - N_\varphi , \qquad (7.24)$$

with $N_\varphi = V_2 + V_3 + 2V_1$ corresponding to the numbers of external fields φ in $\mathcal{G}$ (in our previous example $N_\varphi = 4$). The $4 - E$ term is the usual result obtained in a four dimensional ϕ^4 scalar field theory without an external source. We now understand why we do not need to go beyond $4-$point functions in order to study the validity of the Weinberg theorem and the renormalizability of the theory. the N_φ can only decrease $\omega(\mathcal{G})$, therefore improving the convergence of Feynman graphs. This should have been expected since V_1, V_2 and V_3 are super-renormalizable interactions: all these vertices have a positive mass dimension.

7.6 Ultraviolet power counting in the CSA

An interesting fact that can be noticed in the formula (7.24) is that the superficial degree of divergence of a graph does not depend on the number of quantum vertices. As we know (section 4.3), the only difference between the CSA and the full theory is precisely that $V_{\mathrm{quant}} = 0$ in the CSA. Therefore the power counting is the same in the CSA and in the full theory. One could therefore expect that if the full theory is renormalizable – and it obviously is, as is well known [173] – then so is the CSA. But as we will see in the following, this is unfortunately not true, as a consequence of the fact that Weinberg's theorem is violated in the CSA. The latter being a necessary condition for renormalizability, this will prove the non-renormalizability of the CSA. To understand why Weinberg's theorem is satisfied in the full theory but not in the CSA, one must closely inspect the divergences that appear in the 2 and 4-point functions. We will restrict ourselves to one loop diagrams, as this is sufficient to disprove Weinberg's theorem.

7.7 Ultraviolet divergences in the CSA

In this section, we assume that $m = 0$ for simplicity.

7.7.1 Two-point functions

Let us start by the renormalization of the two-point functions at one loop. Only one topology contributes: the tadpole. We thus have (all the external legs are amputated)

$$-i\Sigma_{11} = \underset{\substack{1 \quad 1}}{\overset{\substack{1 \quad 2}}{\bigcirc}} = 0 , \qquad (7.25)$$

since a closed loop made of a retarded propagator is obviously 0. This diagram was not contributing to Σ_{11} in the CSA anyway, since it involves the quantum vertex. Next, we have

$$-i\Sigma_{22} = \underset{\substack{2 \quad 2}}{\overset{\substack{1 \quad 2}}{\bigcirc}} = 0 , \qquad (7.26)$$

for the same reason as before. Finally,

$$-i\Sigma_{12} = \underset{\substack{2 \quad 1}}{\overset{\substack{2 \quad 2}}{\bigcirc}} = -i\frac{g^2 \Lambda^2}{16\pi^2} , \qquad (7.27)$$

---

3. We will see later that this estimate is to naive in the classical approximation.

which is the usual tadpole divergence, that can be renormalized by adding a mass counterterm in the Lagrangean, whose only quadratic term is precisely of the form $\phi_1\phi_2$. There is therefore no issues in the renormalization procedure of the CSA for the two point functions at one loop, that amounts to adding a mass counterterm to the Lagrangean (7.19).

7.7.2 Four-point functions

7.7.2.1 Vanishing four-point functions

At one loop, some of the four-point functions are zero. This is the case of

$$-i\Gamma_{1111} = \quad \begin{array}{c} \text{(diagram)} \end{array} \quad = 0 \text{ (in the CSA and in the full theory)}, \qquad (7.28)$$

which: (i) does not exist in the CSA, (ii) is 0 in the full theory because it is formed by a closed loop made of two retarded propagators. One can therefore close the contour when doing the complex plane integration without encircling any poles. Other vanishing four point-functions in the CSA are

$$-i\Gamma_{1112} = \quad \begin{array}{c} \text{(diagram)} \end{array} \quad = 0 \text{ (in the CSA)}, \qquad (7.29)$$

this is a good thing, since as we have discarded the Γ_{1112} vertex in the CSA, we would not have been able to renormalize a divergence appearing in this function by adding a counterterm in the CSA Lagrangean (7.19). The calculation of Γ_{1112} in the full theory is done is the appendix 7.A. Finally, we have

$$-i\Gamma_{2222} = \quad \begin{array}{c} \text{(diagram)} \end{array} \quad = 0 \text{ (in the CSA and in the full theory)}, \qquad (7.30)$$

for the same reason that Γ_{1111} was zero.

7.7.2.2 Logarithmically divergent four-point function

Thing starts to be non-trivial for Γ_{2221} at one loop

$$-i\Gamma_{1222} = \quad \begin{array}{c} \text{(diagram)} \end{array} \quad . \qquad (7.31)$$

As one can see, this loop is the same as the one in Γ_{1112}. The complete calculation is performed in the appendix 7.A and one finds

$$-i\Gamma_{1222} \sim g^4 \ln \Lambda \text{ (in the CSA and in the full theory)}, \qquad (7.32)$$

which is the usual coupling constant renormalization. Since Γ_{1222} is present in the CSA Lagrangean (7.19), renormalizing it just implies to add the proper δg counterterm, proportional to the logarithmic divergence that we have just found. This term therefore does not forbid us to renormalize the theory.

7.7.2.3 Linear divergence in four-point functions: violation of Weinberg's theorem

What happens for Γ_{1122}? First, one can see that the following contribution to Γ_{1122} is zero

$$-i\Gamma_{1122} = \quad\underset{1}{\overset{1}{\times}}\!\!\!\!\bigcirc\!\!\!\!\underset{2}{\overset{2}{\times}}\quad = 0 \ (\text{in the CSA and in the full theory}) . \tag{7.33}$$

The non-zero diagrams therefore have $1 - 2$ legs on each side of the loop. To do the computation of Γ_{1122} properly, it is useful to label the external momenta $p_{1,2,3,4}$. We attach $p_{1,2}$ to 1 indices and $p_{3,4}$ to 2 indices. We also assume that all the momenta are incoming, which implies that

$$\sum_{i=1}^{4} p_i = 0 . \tag{7.34}$$

Γ_{1122} therefore reads

$$-i\Gamma_{1122} = \quad\text{(diagram)}\quad + \quad\text{(diagram)}\quad + \quad\text{(diagram)}$$
$$+ \quad\text{(diagram)}\quad + \quad\text{(diagram)}\quad + \quad\text{(diagram)} \ . \tag{7.35}$$

The diagrams of the first line are t-channel contributions, while the diagrams of the second line are u-channel contributions. The s-channel contribution is 0 as proved in (7.33). Let us first recall than since there is no Γ_{1122} vertex in the full Lagrangean (nor in the CSA), equation (7.35) should be finite in the full theory. But without performing the computation, one cannot know whether each individual diagram is finite or whether some cancellation occurs between diagrams present in the CSA and diagrams not included in the CSA. The diagrams present in the CSA read

$$-i\Gamma_{1122}^{\text{CSA}} = \quad\text{(diagram)}\quad + \quad\text{(diagram)}\quad . \tag{7.36}$$

The detailed calculation is done in the appendix 7.B. Denoting

$$t = (p_1 + p_3)^2 , \qquad\qquad u = (p_1 + p_4)^2 , \tag{7.37}$$

we obtain [4]

$$-i\Gamma_{1122}^{\text{CSA}} = -\frac{g^4}{64\pi}\left[\epsilon(t) + \epsilon(u) + 2\Lambda\left(\frac{\theta(-t)}{|\boldsymbol{p}_1 + \boldsymbol{p}_3|} + \frac{\theta(-u)}{|\boldsymbol{p}_1 + \boldsymbol{p}_4|}\right)\right] . \tag{7.39}$$

Despite the fact that $\omega(\Gamma_{1222}^{\text{CSA}}) = 0$, we have just found that $\Gamma_{1222}^{\text{CSA}}$ contains a linear divergence for space-like configurations. It turns that for loops formed by the product of two symmetric

---

4. ϵ is the sign function:

$$\epsilon(a) = \frac{a}{|a|} . \tag{7.38}$$

propagators, the superficial degree of divergence is misleading. Indeed, an individual $G_S(p)$ behaves at p^{-2}. But the contribution that comes from the product of two G_S in a closed loop of momentum K is of the form (here P^2 is either t or u)

$$G_S(P + K)G_S(K) = \pi^2 \delta((P + K)^2)\delta(K^2) , \qquad (7.40)$$

and by expanding the first δ function one finds

$$G_S(P + K)G_S(K) = \pi^2 \delta(P^2 + 2P.K)\delta(K^2) , \qquad (7.41)$$

and now the first δ function gives only a contribution that scales as K^{-1} instead of K^{-2}. This is the intuitive reason why **Weinberg's theorem is violated in the CSA**. At a deeper level, Weinberg's theorem requires to perform a Wick rotation of the loop momenta. For G_F propagators that have one pole on each side of the real axis in the complex plane, this Wick rotation can be performed without encountering the poles

$$(7.42)$$
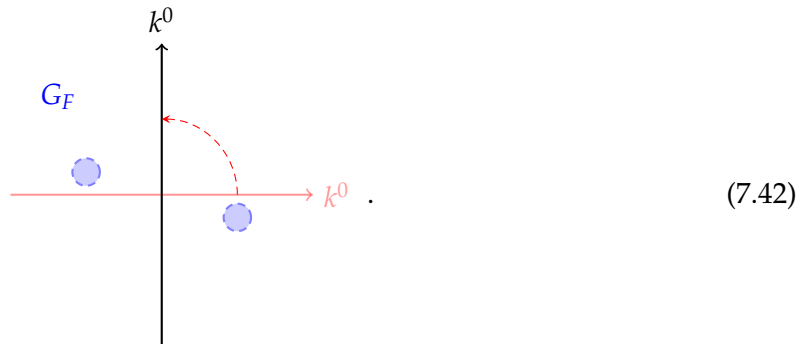
But one cannot perform this rotation when the integrand contains δ functions or retarded/advanced propagators that have all their poles on the same side of the real axis, since the poles cannot be avoided.

$$(7.43)$$
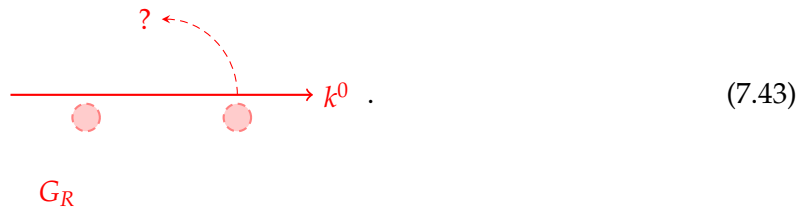
In the full theory, things are easier to understand in the $+-$ basis. The corresponding problematic four-point function is Γ_{--++} (Γ_{---+} and Γ_{-+++} are trivially zero given the vertices present in the Lagrangean: Γ_{++++} and Γ_{----}. The latter can be renormalized without any problem, like Γ_{1112}). Here, everything works as in the $1-2$ basis except that one has additional θ functions in front of the δ's in G_{-+} and G_{+-}. This constraints the energy k^0 to flow in one direction of the diagram, and it cannot grow up to the cutoff

Figure 7.1: Potentially problematic four-point function of the full theory (left side) and of the CSA (right side). In the former, the θ function prevents the modulus of the loop momentum from reaching the UV cutoff. In the latter, nothing prevents $|\mathbf{k}|$ from reaching Λ.

Therefore, in the full theory, the momentum of the internal leg is bounded. In the CSA, nothing prevents the momentum of one legs from reaching Λ. To see how the cancellations occur in the full theory in the 12 basis, we have also computed the remaining diagrams that contributed to the t and u channels (see the appendix 7.B) and found

$$-i\left(\Gamma_{1122} - \Gamma_{1222}^{\text{CSA}}\right) = -\frac{g^4}{32\pi}\left[1 - \Lambda\left(\frac{\theta(-t)}{|\boldsymbol{p}_1 + \boldsymbol{p}_3|} + \frac{\theta(-u)}{|\boldsymbol{p}_1 + \boldsymbol{p}_4|}\right)\right].\tag{7.44}$$
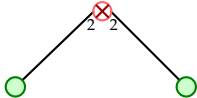
By adding (7.39) and (7.44) one sees that

$$-i\Gamma_{1122} = -\frac{g^4}{32\pi}\left(\theta(t) + \theta(u)\right),\tag{7.45}$$
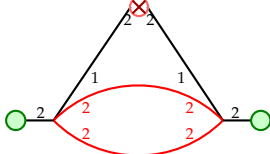
which is finite, in agreement with the renormalizability of the full theory. The conclusion of this calculation is therefore that **the classical-statistical approximation is not renormalizable**.

7.8 Impact of the non-renormalizability of the CSA on $T^{\mu\nu}$

The function Γ_{1122} appears as a subdiagram of NNLO contributions to $T_{\text{resum}}^{\mu\nu}$. Indeed, focusing on the quadratic part of $T^{\mu\nu}$, that only implies type 2 fields, one has (where the black lines now denote dressed propagators)

$$T_{\text{LO}}^{\mu\nu} = \qquad\qquad T_{\text{NLO}}^{\mu\nu} = \qquad,\tag{7.46}$$

with $T_{\text{LO}}^{\mu\nu} \sim \frac{Q^4}{g^2}$, $T_{\text{NLO}}^{\mu\nu} \sim Q^4$ and one of the contributing diagram to $T_{\text{NNLO}}^{\mu\nu} \sim Q^4 g^2$ is

$$T_{\text{NNLO}}^{\mu\nu} = \qquad\qquad,\tag{7.47}$$

The problematic $\Gamma_{1122}^{\text{CSA}}$ subdiagram is the one delimited by the four black legs. This diagram behaves as

$$T_{\text{NNLO}}^{\mu\nu} \sim \frac{Q^4}{g^2} \times g^4\frac{\Lambda}{Q} \sim g^2 Q^3 \Lambda,\tag{7.48}$$

to be compared with the leading contribution $\sim \frac{Q^4}{g^2}$. This means that as long as

$$\Lambda \ll \frac{Q}{g^4},\tag{7.49}$$

this diagram is a small correction (at a fixed time). If one wants to obtain at least NLO accuracy (as the CSA contains fully the next to leading order contribution), the problematic divergent term in the vertex Γ_{1122} should be small compared to the bare $4-$gluon vertex g^2. This gives

$$g^4\frac{\Lambda}{Q} \ll g^2 \;\rightarrow\; \Lambda \ll \frac{Q}{g^2}.\tag{7.50}$$

This inequality is satisfied for a broad range of Λ at weak coupling.

7.9 Cumulative effects of the non-renormalizability

At late times and moderate couplings, a kinetic description (see the section 3.1 for a brief introduction, and reference [174] for more details) may be used, since quasi-particles have been formed (see the chapter 5). The Boltzmann equation for a spatially homogeneous system reads

$$\partial_{x^0} f_k = C[f_k] \, . \tag{7.51}$$

The collision term can be deduced can be expressed in terms of the two loops self energies Σ_{11}, Σ_{21} and Σ_{12} in the retarded-advanced basis. More precisely [175]

$$\partial_{x^0} f_k = \frac{-i}{2|\boldsymbol{k}|} \left(\Sigma_{11}(k) - \left[\frac{1}{2} + f_k \right] [\Sigma_{21}(k) - \Sigma_{12}(k)] \right) \, . \tag{7.52}$$

One can show that, in the CSA, for massless particles ($P^2 = 0$ and $p^0 > 0$)

$$
-i\Sigma_{11}^{\text{CSA,2 loops}} = \quad = -\frac{g^4}{1024\pi^3} \left(\Lambda^2 - \frac{2}{3}|\boldsymbol{p}|^2 \right) \, ,
$$

$$
\text{Im } \Sigma_{12}^{\text{CSA,2 loops}} = \quad = -\frac{g^4}{1024\pi^3} \left(\Lambda^2 - \frac{2}{3}|\boldsymbol{p}|^2 \right) \, . \tag{7.53}
$$
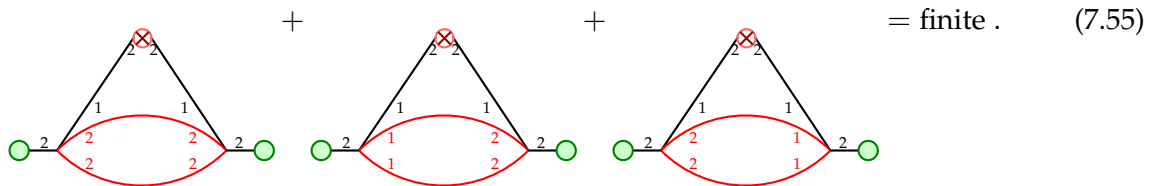
The origin of the divergence is the presence of a $\Gamma_{1122}^{\text{CSA}}$ sub-diagram [5]. One can see from these formulas that the collision term vanishes [6] in the vacuum, but diverge if $f_k \neq 0$. This spurious contribution to the collision term is of order $\frac{g^4}{2048\pi^3} \frac{\Lambda^2}{Q}$, where Q is some typical momentum scale in the problem. Therefore, after a time

$$x^0_{\text{renor}} \sim \frac{2048\pi^3}{g^4} \frac{Q}{\Lambda^2} \, , \tag{7.54}$$

these unphysical terms will have a sizable effect on the particle distribution. By comparing the solution of the Boltzmann equation with the full collision term, and the one with a classical approximation where one keeps only the leading terms in f_k, one can assess the time evolution of the artifacts generated by the CSA. This remains to be done and will be the subject of a future study.

7.10 Possible partial cure

A natural question after this somehow negative result obtained in the section 7.7 is whether the linear term in Λ that appears in NNLO contributions to physical observables can be removed. For instance, we saw in the section 7.8 that the problematic $4-$point function enters into $T_{\text{NNLO}}^{\mu\nu}$. This linear divergence is canceled in the full theory when one takes into account the other contributions that involve the quantum vertex

$$
+ \qquad + \qquad = \text{finite} \, . \tag{7.55}
$$

The question is therefore the following one: is there a way to reintroduce in the CSA the divergent part of the second and third diagram in order to eliminate the linear divergence

---

5. One can notice that this sub-diagram only enters once in Σ_{12} while entering 3 times in Σ_{11}. This will have some consequences on the outcome of section 7.11.

6. This is a consequence of the KMS relation, see [176, 177].

that appears in the CSA term (first diagram)? To understand what it would take to do so, it is convenient to look at the previous diagrams in space-time, starting from some initial time surface. For the CSA contribution, this gives

$$\text{,} \tag{7.56}$$
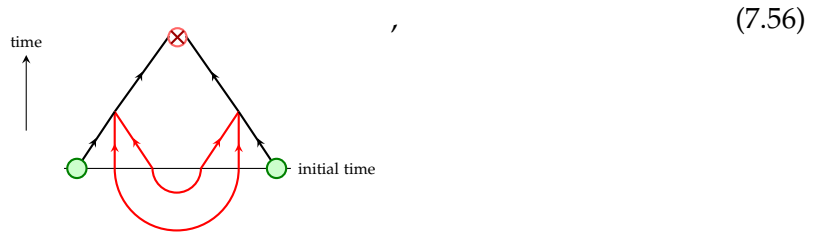
where the lines with an arrow retarded propagators. Here, all the vertices are classical ones, of type Γ_{1222}. In terms of this time oriented representation, we see that the loop correction is coming entirely from the initial condition, as it is expected to be the case in the CSA. For the other two diagrams, things are different. Indeed, in this representation, they look like

$$\text{.} \tag{7.57}$$
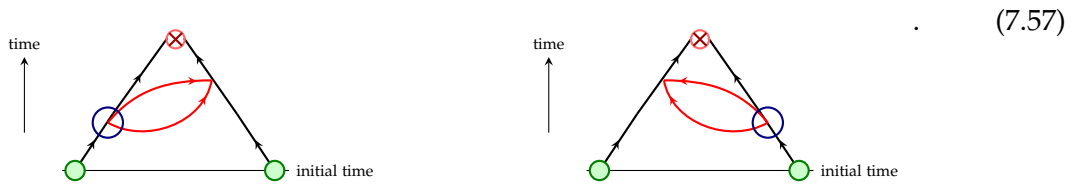
Here, some of the vertices (circled in blue) are quantum Γ_{1112} vertices. In terms of this time oriented representation, it means that the CSA neglects loop corrections arising after the initial time, as we are already aware of (see the section 4.3). The divergent part of these diagrams can be read from (7.44). In coordinate space, a straightforward calculation shows that it is proportional to

$$\frac{1}{|\boldsymbol{x} - \boldsymbol{y}|} \delta \left((x^0 - y^0)^2 - |\boldsymbol{x} - \boldsymbol{y}|^2 \right) \text{,} \tag{7.58}$$

where x and y are the space-time positions of the two vertices. Therefore, this divergent term, although non-local, has its support on the light-cone, as illustrated in the following cartoons

$$\text{.} \tag{7.59}$$
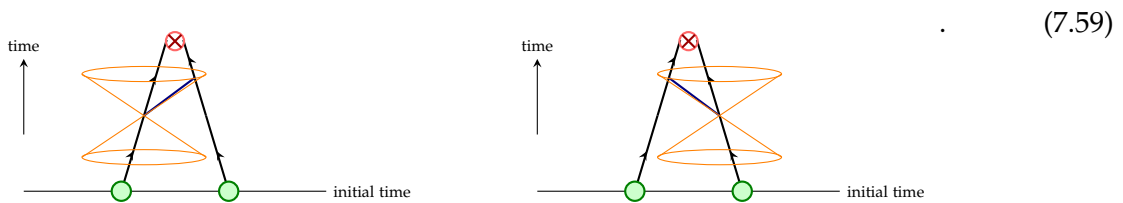
This somewhat simplifies the structure of those divergent terms. But multiple loops of that kind can appear in higher order diagrams, at every space-time position. For this reason, one cannot subtract them locally. If something may be done, it has to be at the Lagrangean level. Since the divergent part of all these diagrams always comes from the Γ_{1122} vertex, one could try to add to the Lagrangean a counterterm of the form $\phi_1^2 \phi_2^2$, which means

$$\Delta S = \frac{i}{2} \int \mathrm{d}^4 x \, \mathrm{d}^4 y \, [\phi_1(x)\phi_2(x)] \, v(x,y) \, [\phi_1(y)\phi_2(y)] \text{.} \tag{7.60}$$

The coefficient $v(x,y)$ should be tuned in order to cancel the linear divergence in Γ_{1122}. To do so, one should take

$$v(x,y) = \frac{g^4}{64\pi^3} \frac{\Lambda}{|\boldsymbol{x} - \boldsymbol{y}|} \delta \left((x^0 - y^0)^2 - |\boldsymbol{x} - \boldsymbol{y}|^2 \right) \text{.} \tag{7.61}$$

Using the Hubbard-Stratonovitch [178, 179] transformation, the functional equivalent of the simple identity

$$e^{-\frac{x^2}{2}} = \sqrt{2\pi} \int \mathrm{d}y \, e^{\frac{y^2}{2}} \, e^{iyx} \text{,} \tag{7.62}$$

one can re-express the additional term in the action as

$$e^{i\Delta S} = \int [D\xi] \, e^{\frac{1}{2}\int d^4x \, d^4y \, \zeta(x)v(x,y)\zeta(y)} \, e^{i\int d^4x \, \zeta(x)\phi_1(x)\phi_2(x)} \; . \tag{7.63}$$

This formulation allows one to perform the functional integration over ϕ_1 as was done in the CSA (see section 4.3) in order to recover a "classical" equation of motion for the field φ

$$\Box\varphi + \frac{g^2}{6}\varphi^3 + \zeta\varphi = j \; , \tag{7.64}$$

which is almost identical to the usual classical KG EOM, except for the additional $\zeta\varphi$ term. In order to get a positive definite variance for this random Gaussian noise, we redefine ζ as $\zeta = i\xi$. Therefore

$$\Box\varphi + \frac{g^2}{6}\varphi^3 + i\xi\varphi = j \; , \tag{7.65}$$

with

$$\langle \xi(x) \rangle = 0 \; , \qquad\qquad \langle \xi(x)\xi(y) \rangle = v(x,y) \; . \tag{7.66}$$

Thanks to the additional term in the action, for every Γ_{1122} subdiagram that appears in a physical observable, another diagram similar to those of (7.59) will also be present, and the combination of the two will be free of the linear Λ divergence.

7.11   Could the cure be implemented numerically?

In the previous section, we have presented a possible way to get rid of the linear Λ divergences that come from Γ_{1122} subdiagrams. But can this method be used in practice? It turns out that there are difficulties to do so

— Firstly, one needs to generate the noise term ξ. This is easy in momentum space, as it is diagonal there. But the problem is that the correlation between two ξ is non-local in time. One should therefore compute the noise configurations before starting to evolve the field φ, and store this noise for all space-time points.

— Secondly, and perhaps even worse than the previous point, the noise term is imaginary. Even if every Hermitian observable will remain real because ξ has a zero mean, this means that (7.65) is a complex Langevin equation. The latter has been studied on numerous occasions [180–183], and can suffer from a lack or convergence or even a convergence to the wrong solution. It is therefore unclear if the method proposed here offers any gain in comparison to considering the CSA as an effective field theory with the constraint (7.50).

As a final remark, let us notice that even if the subtraction procedure advocated in the previous subsection was to be applicable, this would not completely renormalized the theory (it would do so at NLO, but not at higher orders). One can see this by inspecting the symmetry factor of the Γ_{1122} sub-diagram that enters into Σ_{12} and Σ_{11} at two loops. Since it is not the same, one cannot renormalize both of those diagrams by the renormalization of Γ_{1122} at one loop.

7.12 Summary

> • Despite having the same degree of divergence than the full quantum scalar field theory, the CSA is non-renormalizable.
> • Some cancellations that happen in the full theory between diagrams with the same topology do not happen in the CSA because the quantum vertex $\phi_1^3 \phi_2$ has been discarded.
> • In practice, the cutoff should not be too large compared to the physical scales.
> • One may improve the range of validity of the CSA by promoting the classical Klein-Gordon EOM to a Langevin equation, but implementing the latter seems difficult in practice.

Appendix

7.A Calculation of Γ_{1112} and Γ_{1222}

We want to calculate (with only incoming momentum)

$$-i\Gamma_{1222} = \qquad . \tag{7.67}$$

Labeling as in section 7.7 the four momenta $p_{1,2,3,4}$ with p_1 always associated to the 1 leg, this amounts to compute three different diagrams

$$-i\Gamma_{1222} =$$

$$= -i \left(I(p_1 + p_2) + I(p_1 + p_3) + I(p_1 + p_4) \right) . \tag{7.68}$$

where (P standing either for $p_1 + p_2$, $p_1 + p_3$ or $p_1 + p_4$)

$$I(P) = -g^4 \int \frac{\mathrm{d}^4 k}{(2\pi)^4} G_R(k+P) G_S(k) \tag{7.69}$$

Similarly, one has for Γ_{1112}, with now p_1 attached to the unique leg of type 2

$$-i\Gamma_{1222} =$$

$$= -\frac{i}{4} \left(I(p_1 + p_2) + I(p_1 + p_3) + I(p_1 + p_4) \right) , \tag{7.70}$$

where the $\frac{1}{4}$ is coming from the quantum vertex. Γ_{1112} is therefore 0 in the CSA as it always involves a quantum vertex at one loop. Using [7]

$$\frac{i}{x+i\epsilon} = \pi \delta(x) + i\mathrm{pv}\left(\frac{1}{x}\right) , \tag{7.71}$$

---

7. pv standing for principal value.

a straightforward yet tedious calculation leads to ($\mathcal{P} = \sqrt{(p^0)^2 - |\boldsymbol{p}|^2}$)

$$I(P) = \frac{g^4}{32\pi^2} \left(i\pi \left[\epsilon(p^0)\theta(\mathcal{P}^2) - \theta(-\mathcal{P}^2)\frac{p^0}{|\boldsymbol{p}|} \right] + 4\ln \left| \frac{\mathcal{P}}{2\Lambda} \right| + \frac{p^0}{|\boldsymbol{p}|} \ln \left| \frac{p^0 + |\boldsymbol{p}|}{p^0 - |\boldsymbol{p}|} \right| \right) , \tag{7.72}$$

which is logarithmically divergent as announced in section 7.7.2.

7.B Calculation of Γ_{1122}

7.B.1 CSA contribution

Let us give a flavor of a detailed one-loop computation in the CSA. Here

$$-i\Gamma_{1122}^{\text{CSA}} = \quad$$

$$= i\frac{g^4}{2} \left(J(p_1 + p_3) + J(p_1 + p_4) \right) , \tag{7.73}$$

with (P standing either for $p_1 + p_3$ or $p_1 + p_4$)

$$J(P) = \int \frac{\mathrm{d}^4 k}{(2\pi)^4} G_S(P - k) G_S(k) . \tag{7.74}$$

Then one has

$$\begin{aligned}
J(P) &= \frac{\pi}{2} \int \mathrm{d}k^0 \int \frac{\mathrm{d}^3 \boldsymbol{k}}{2|\boldsymbol{k}|(2\pi)^3} \left(\delta(k^0 + |\boldsymbol{k}|) + \delta(k^0 - |\boldsymbol{k}|) \right) \delta(\mathcal{P}^2 - 2P.k) \\
&= \frac{1}{8\pi} \int_0^\pi \sin\theta \, \mathrm{d}\theta \int_0^\Lambda \frac{k\mathrm{d}k}{2} \left(\delta(\mathcal{P}^2 - 2kp^0 + 2k|\boldsymbol{p}|\cos\theta) + \delta(\mathcal{P}^2 + 2kp^0 + 2k|\boldsymbol{p}|\cos\theta) \right) \\
&= \frac{1}{8\pi} \int_{-1}^1 \mathrm{d}x \int_0^\Lambda \frac{\mathrm{d}k}{4|\boldsymbol{p}|} \left(\delta\left(\frac{\mathcal{P}^2}{2k|\boldsymbol{p}|} - \frac{p^0}{|\boldsymbol{p}|} + x \right) + \delta\left(\frac{\mathcal{P}^2}{2k|\boldsymbol{p}|} + \frac{p^0}{|\boldsymbol{p}|} + x \right) \right) \\
&= \frac{1}{32|\boldsymbol{p}|\pi} \int_0^\Lambda \mathrm{d}k \left(\theta\left(\frac{\mathcal{P}^2}{2k|\boldsymbol{p}|} - \frac{p^0}{|\boldsymbol{p}|} + 1 \right) \theta\left(1 - \frac{\mathcal{P}^2}{2k|\boldsymbol{p}|} + \frac{p^0}{|\boldsymbol{p}|} \right) \right. \\
&\quad \left. + \theta\left(\frac{\mathcal{P}^2}{2k|\boldsymbol{p}|} + \frac{p^0}{|\boldsymbol{p}|} + 1 \right) \theta\left(1 - \frac{\mathcal{P}^2}{2k|\boldsymbol{p}|} - \frac{p^0}{|\boldsymbol{p}|} \right) \right) .
\end{aligned} \tag{7.75}$$

This expression is symmetric in the change $p^0 \to -p^0$, we can therefore take $p^0 > 0$. Let us first assume that $\mathcal{P}^2 > 0$, which means $|p^0| > |\boldsymbol{p}|$. Therefore, the first two θ functions give $\frac{p^0 - |\boldsymbol{p}|}{2} < k < \frac{p^0 + |\boldsymbol{p}|}{2}$. The fourth one implies $0 > |\boldsymbol{p}| - p^0 > \frac{p^2}{2k} > 0$, and is therefore identically 0. The final result thus is

$$\frac{1}{32|\boldsymbol{p}|\pi} \int_{\frac{p^0 - |\boldsymbol{p}|}{2}}^{\frac{p^0 + |\boldsymbol{p}|}{2}} \mathrm{d}k = \frac{1}{32\pi} . \tag{7.76}$$

If we now assume $\mathcal{P}^2 < 0$, then the first two θ functions give $k > \frac{p^0 + |\boldsymbol{p}|}{2} > 0 > \frac{p^0 - |\boldsymbol{p}|}{2}$. The fourth one implies $|\boldsymbol{p}| - p^0 > 0 > \frac{\mathcal{P}^2}{2k}$ and is therefore always satisfied. One is thus left with the third θ which implies $k > \frac{|\boldsymbol{p}| - p^0}{2}$. The final result is therefore

$$\frac{1}{32|\boldsymbol{p}|\pi} \int_{\frac{p^0 + |\boldsymbol{p}|}{2}}^\Lambda \mathrm{d}k + \frac{1}{32|\boldsymbol{p}|\pi} \int_{\frac{|\boldsymbol{p}| - p^0}{2}}^\Lambda \mathrm{d}k = \frac{\Lambda}{16\pi} - \frac{1}{32\pi} . \tag{7.77}$$

The final answer is

$$J(P) = \frac{\epsilon(\mathcal{P}^2)}{32\pi} + \frac{\Lambda\theta(-\mathcal{P}^2)}{16|\boldsymbol{p}|\pi} . \tag{7.78}$$

7.B.2 Non-CSA contribution

as explained in the section 7.7.2.3, the diagrams not included in Γ^{CSA}_{1122} are

$$= -\frac{g^4}{8} \int \frac{d^4k}{(2\pi)^4} \left(G_R(k)G_R(p_1 + p_3 - k) + G_A(k)G_A(p_1 + p_3 - k) \right.$$
$$\left. + G_R(k)G_R(p_1 + p_4 - k) + G_A(k)G_A(p_1 + p_4 - k) \right) .. \tag{7.79}$$

One can observe that exchanging k for $-k$ in the terms containing G_A gives those that contain G_R provided that one also exchanges P to $-P$ (P standing for either $p_1 + p_3$ or $p_1 + p_4$). Calling

$$K(P) = \frac{1}{4} \int \frac{d^4k}{(2\pi)^4} G_R(k)G_R(P - k) , \tag{7.80}$$

we therefore only need to keep the odd P part of this quantity. First performing the k^0 integration in the complex plane, we get

$$K(P) = \frac{i}{32\pi^2} \int_{-1}^{1} dx \int_{0}^{\Lambda} k dk \left(\frac{1}{\mathcal{P}^2 - 2k(p^0 - |\boldsymbol{p}|x) + i(p^0 - k)\epsilon} \right.$$
$$\left. - \frac{1}{{}^2 + 2k(p^0 + |\boldsymbol{p}|x) + i(p^0 + k)\epsilon} \right) . \tag{7.81}$$

Using

$$\frac{i}{x + i\epsilon} = \pi\delta(x) + i\mathrm{pv}\left(\frac{1}{x}\right) , \tag{7.82}$$

we obtain for the real part

$$K_R(P) = \frac{1}{32\pi} \int_{-1}^{1} dx \int_{0}^{\Lambda} k dk \left(\epsilon(p^0 - k)\delta(\mathcal{P}^2 - 2k(p^0 - |\boldsymbol{p}|x)) - \epsilon(p^0 + k)\delta(\mathcal{P}^2 + 2k(p^0 + |\boldsymbol{p}|x)) \right)$$
$$= \frac{1}{64|\boldsymbol{p}|\pi} \int_{-1}^{1} dx \int_{0}^{\Lambda} dk \left(\epsilon(p^0 - k)\delta(\frac{\mathcal{P}^2}{2k|\boldsymbol{p}|} - \frac{p^0}{|\boldsymbol{p}|} + x)) - \epsilon(p^0 + k)\delta(\frac{\mathcal{P}^2}{2k|\boldsymbol{p}|} + \frac{p^0}{|\boldsymbol{p}|} + x)) \right)$$
$$= -\frac{1}{2}J(P) + \frac{1}{32|\boldsymbol{p}|\pi} \int_{-1}^{1} dx \left(\theta(p^0) \int_{0}^{p^0} dk \delta(\frac{\mathcal{P}^2}{2k|\boldsymbol{p}|} - \frac{p^0}{|\boldsymbol{p}|} + x)) \right.$$
$$\left. + \theta(-p^0) \int_{0}^{-p^0} dk \delta(\frac{\mathcal{P}^2}{2k|\boldsymbol{p}|} + \frac{p^0}{|\boldsymbol{p}|} + x) \right) . \tag{7.83}$$

Focusing on the sum pf the two integrals, we see that it is symmetric under the transformation $p^0 \to -p^0$, and we can therefore compute it by assuming that $p^0 > 0$.

$$\frac{1}{32|\boldsymbol{p}|\pi} \int_{0}^{p^0} dk \, \theta\left(\frac{\mathcal{P}^2}{2k|\boldsymbol{p}|} - \frac{p^0}{|\boldsymbol{p}|} + 1 \right) \theta\left(1 - \frac{\mathcal{P}^2}{2k|\boldsymbol{p}|} + \frac{p^0}{|\boldsymbol{p}|} \right) = \frac{\theta(\mathcal{P}^2)}{32|\boldsymbol{p}|\pi} . \tag{7.84}$$

The real part of K is then

$$\frac{1}{64\pi} - \frac{\Lambda\theta(-\mathcal{P}^2)}{32|\boldsymbol{p}|\pi} . \tag{7.85}$$

We are now left with the computation of the imaginary part of K

$$K_I(P) = \frac{i}{32\pi} \int_{-1}^{1} \mathrm{d}x \int_{0}^{\Lambda} k\mathrm{d}k \left(\mathrm{pv} \left(\frac{1}{\mathcal{P}^2 - 2k(p^0 - |\boldsymbol{p}|x)} \right) - \mathrm{pv} \left(\frac{1}{\mathcal{P}^2 + 2k(p^0 + |\boldsymbol{p}|x)} \right) \right).$$

(7.86)

which is antisymmetric in p^0. It therefore vanishes when one takes into account all the possible combinations for the incoming momentum. Putting this result in (7.79) gives what was announced in the section 7.7.2.3.

Part III

Yang-Mills theory

Chapter 8

⚛ Spectrum of fluctuations above the light cone ⚛

Contents

n this chapter, we will try to derive the spectrum of fluctuations in the forward light cone at $\tau = 0^+$, as this is a necessary step in order perform the realistic CSA simulations that will be the topic of next chapter 9. This spectrum have received some attentions in the past[1] [185–187], but has never been derived from first principles in a completely satisfactory manner.

8.1   Spectrum of fluctuations: a new derivation

Following the work of section 4.2, we write a formula analogous to 4.110 for the propagator $\mathcal{G}_{+-}^{\mu\nu ab}$ in the gauge theory[2]

$$\mathcal{G}_{+-}^{\mu\nu ab}(x,y) = \frac{1}{2}\sum_{\lambda,c}\int \frac{\mathrm{d}^3 k}{2|k|(2\pi)^3}\, a_{k\lambda c}^{\mu a}(x)a_{k\lambda c}^{\nu b*}(y). \tag{8.1}$$

---

1. See also [184] for the quark case.
2. Where the fact that $a_{-k\lambda c}^{\nu b} = a_{k\lambda c}^{\nu b*}$ was used.

As one recall, this formula entered into the resummation formula in a crucial way (through the Gaussian distribution function). We therefore see that in the gauge case, one also need to know the $a^{\mu a}_{k \lambda c}$. based on 4.2, we can state that those $a^{\mu a}_{k \lambda c}$ are the solution of the linear Yang-Mills equations with plane wave initial condition in the remote past (the analogous of 4.111). In this section, we will therefore use the linear equation of motion for the small fluctuations in order to derive the form of the initial condition just after the collision, which is function of these small fluctuations and the classical field $\mathcal{A}^{\mu a}$ presented in section 3.8. While an attempt was made in [187] to obtain those mode functions, we will start here by explaining why this derivation suffers from an important caveat. Indeed, the spectrum found in [187] was derived thanks to the conservation of the following scalar product

$$S_{k_\perp \nu \lambda c, k'_\perp \nu' \lambda' d} = -i \int d^2 x_\perp \, d\eta \, g_{\mu\nu} \left(a^{\mu a *}_{k_\perp \nu \lambda c} e^{\mu a}_{k'_\perp \nu' \lambda' d} - e^{\mu a *}_{k_\perp \nu \lambda c} a^{\mu a}_{k'_\perp \nu' \lambda' d} \right) . \tag{8.2}$$

Here $e^\mu(\tau, x_\perp, \eta) = -g^{\mu\nu} \tau \partial_\tau a_\nu(\tau, x_\perp, \eta)$ is the electric field. The (τ, η) coordinates are defined as usual (z being chosen to be the collision axis)

$$\tau = \sqrt{\tau^2 - z^2} \qquad\qquad \eta = \frac{1}{2} \ln \frac{t+z}{t-z} , \tag{8.3}$$

λ labels the polarization of the fluctuations, and $(k_\perp, \nu)$ are the conjugate momenta associated to $(x_\perp, \eta)$. The color indices will be denoted by latin letters $a, b, c...$ in all the following. The reasoning in [187] was that if one knows a set of orthonormal small fluctuations $(a^{\mu a}_{k \lambda c}, e^{\mu a}_{k \lambda c})$ at $\tau = 0^+$, then it can be related (up to a unitary transformation) to the one at $t = -\infty$, where the small fluctuations are known to be plane waves. We now shortly explain why this can be uncorrect in some cases[3]. The scalar product (8.2) is just a complex version of what is called a symplectic form. A symplectic form conserves the volume in phase-space. For example, given two pairs (a_1, e_1) and (a_2, e_2), their symplectic product is the shaded area of the left part of figure 8.1. Unfortunately, some set of solutions that are orthonormal with respect to (8.2) cannot be related to the correct set of fluctuations (that evolved from $-\infty$) by an orthogonal[4] transformation. This can be easily seen geometrically: an orthogonal transformation Ω is just a rotation in phase-space (middle part of figure 8.1).
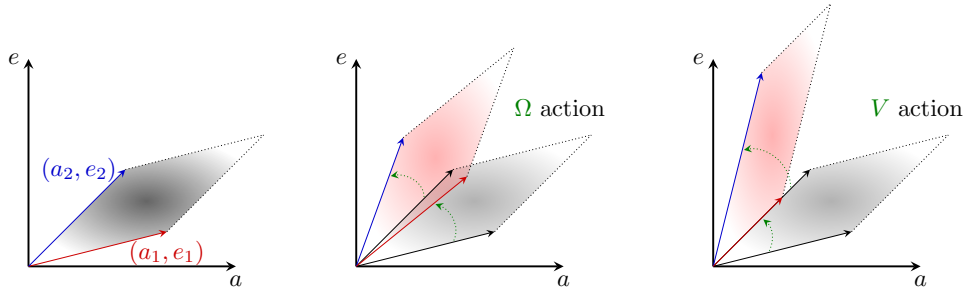
Figure 8.1: Left part: symplectic product of two pairs (a_1, e_1) and (a_2, e_2) Middle part: Orthogonal transformation of two pairs (a_1, e_1) and (a_2, e_2). Right part: symplectic transformation of two pairs (a_1, e_1) and (a_2, e_2)

But there are many more transformations V that conserve the volume in phase space[5]. For example, dividing by 2 the a and multiplying by 2 the e gives the figure of the right part of 8.1. Here the two colored domains have the same area, but the pair (Va, Ve) cannot be related anymore to the original (a, e). Therefore the correct way to construct the spectrum of

---

3. Let us note here that this method gives the correct result for the vacuum fluctuations, but not for the interacting spectrum.

4. Real version of a unitary transformation.

5. These are the symplectic transformations.

fluctuations in the forward light cone requires more than just imposing the orthonormality of the $(a_{k\lambda c}^{\mu a}, e_{k\lambda c}^{\mu a})$ with respect to (8.2). What we will do instead in this section is the complete evolution of the real solution from the remote past to the forward light cone, as this is the only method that unambiguously relates the spectrum of fluctuations just after the collision to the one at $-\infty$.

8.2 Known results for the background field

The way we derive the spectrum of small fluctuations in the forward light cone takes advantage of the gauge choice used in [50], that was used there to re-derive the formulas for the background field generated by two intense sources that are located into two infinitesimal strips along the $x^{\pm}$ axis (recall section 3.6)

$$J_1^{\mu a}(x^+, \boldsymbol{x}_\perp) = \delta^{\mu -} \rho_n^a(x^+, \boldsymbol{x}_\perp) , \qquad J_2^{\mu a}(x^-, \boldsymbol{x}_\perp) = \delta^{\mu +} \rho_n^a(x^-, \boldsymbol{x}_\perp) , \qquad (8.4)$$

The ρ are as usual in this context random color sources described by a probability distribution $W[\rho]$, that we have discussed in section 3.7. One usually takes the high energy limit, which implies (the index n labels the two nuclei) $\rho_n^a(x^{\pm}, \boldsymbol{x}_\perp) = \delta(x^{\pm})\rho_n^a(\boldsymbol{x}_\perp)$. Here we will only take this limit at the end of the calculation, and consider the support of the sources to have a small width of size ϵ in the variables $x^{\pm}$. The formulas for the background field induced by these sources, first obtained in [188], states that in (τ, η, x, y) coordinate system and in the so-called Fock-Schwinger gauge $\mathcal{A}^{\tau} = 0$, the background field on the $\tau = 0^+$ surface reads

$$\mathcal{A}^{ia}(\boldsymbol{x}_\perp) = \mathcal{A}_1^{ia}(\boldsymbol{x}_\perp) + \mathcal{A}_2^{ia}(\boldsymbol{x}_\perp) \qquad \mathcal{A}^{\eta a}(\boldsymbol{x}_\perp) = \frac{ig}{2} \mathcal{A}_1^{iab}(\boldsymbol{x}_\perp) \mathcal{A}_2^{ib}(\boldsymbol{x}_\perp) , \qquad (8.5)$$

where the fields $\mathcal{A}_n^a$ that a priori depend on $(x^{\pm}, \boldsymbol{x}_\perp)$ are pure gauges formed by the Wilson lines $\mathcal{U}_n$

$$\mathcal{A}_n^{ab}(x^{\pm}, \boldsymbol{x}_\perp) = \frac{i}{g} \mathcal{U}_n^{ac\dagger}(x^{\pm}, \boldsymbol{x}_\perp) \partial^i \mathcal{U}_n^{cb}(x^{\pm}, \boldsymbol{x}_\perp) \qquad \mathcal{U}_n(x^{\pm}, \boldsymbol{x}_\perp) = \mathcal{T}_{\pm} e^{ig \int_{-\infty}^{x^{\pm}} dz^{\pm} \mathcal{A}_n^{\mp}(z^{\pm}, \boldsymbol{x}_\perp)} , \qquad (8.6)$$

where $\mathcal{T}_{\pm}$ are the time ordering operators along $x^{\pm}$, and the fields $\mathcal{A}_n^{\pm a}$ are solutions of the 2-dimensional Poisson equation

$$-\boldsymbol{\nabla}_\perp^2 \mathcal{A}_n^{\pm a} = J_n^{\pm a} . \qquad (8.7)$$

The fields $\mathcal{A}_{1,2}^{\pm a}$ in equation (8.5) are obtained by taking the limit $x^{\pm} \to +\infty$ in the Wilson lines, reducing the spatial dependence of all the object considered to a transverse one. In order to apply the procedure developed in [50] to derive the spectrum of small fluctuations propagating on top of the background field $\mathcal{A}$, we briefly recall its key aspects here [6].

8.3 The axial gauge

The key idea introduced in [50] is to work in the same axial gauge for the whole system formed by the two nuclei. What was done before was to work in the covariant gauge $\partial_\mu \mathcal{A}_n^\mu = 0$, which implies that $\mathcal{A}_1^\mu \propto \delta^{\mu -}$ and $\mathcal{A}_2^\mu \propto \delta^{\mu +}$. Since we will consider the $\mathcal{A}^- = 0$ gauge in all this section, this implies that the nucleus 2 is so to say in the correct gauge, since it only has a non-zero $\mathcal{A}_2^+$ component, but not the nucleus 1, which only has a non-zero $\mathcal{A}_1^-$ component. To get rid of it, one has to perform a gauge transform $\Omega_1 = \mathcal{U}_1$. The gauge transform of the $\mathcal{A}_1$ field reads

$$\mathcal{A}_1^{\mu ab} \mapsto \Omega_1^{ac} \mathcal{A}_1^{\mu cd} \Omega_1^{\dagger db} + \frac{i}{g} \Omega_1^{ac} \partial^\mu \Omega_1^{cb\dagger} \qquad (8.8)$$

---

6. The technical details are relegated to the appendix 8.A and 8.B.

and the only non-zero components after this gauge transformation are the transverse ones, which are equal to a pure gauge. Figure (8.2) clarifies the different notations.
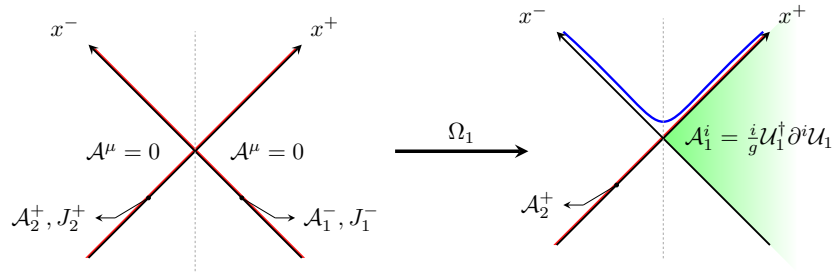

Figure 8.2: The gauge transformation that transforms $\mathcal{A}_1^-$ into a pure gauge $\mathcal{A}_1^i$. The second nucleus is unaffected by this transformation.

One could be tempted to choose the gauge in such a way that the two nuclei are represented by pure gauges, hence a symmetric treatment of the problem. The reason for not doing so is only technical: it turns out that the calculations are a lot simpler in this mixed gauge, and we will therefore stick with it. To determine the field just after the collision (blue line on the right side of figure (8.2)), one can independently study its left and right branches, for obvious causality reasons[7]. The result found is the same on the two branches and is[8], for x^+ or x^- equal to ϵ.

$$\partial^- \mathcal{A}^{+a}(\mathbf{x}_\perp) = \left(\partial^i \mathcal{U}_2^{ab}(\mathbf{x}_\perp)\right) \mathcal{A}_1^{ib}(\mathbf{x}_\perp) \quad \mathcal{A}^{ia}(\mathbf{x}_\perp) = \mathcal{U}_2^{ab}(\mathbf{x}_\perp)\mathcal{A}_1^{ib}(\mathbf{x}_\perp) \quad \mathcal{A}^{\pm a}(\mathbf{x}_\perp) = 0 \,. \quad (8.9)$$

which means that $\mathcal{A}$ only depends on $\mathbf{x}_\perp$ on the blue surface of figure (8.2). The $\epsilon \to 0$ limit is then taken.

8.4   Going to Fock-Schwinger gauge

Since it is more natural to use the τ, η coordinates to describe the evolution of the fields in the forward light cone, and since in this coordinate system the usual gauge choice is the temporal Fock-Schwinger gauge

$$\mathcal{A}^\tau = x^- \mathcal{A}^+ + x^+ \mathcal{A}^- = 0 \,, \quad (8.10)$$

one needs to perform a new gauge transform that leads to this condition. In this gauge, the field before the collision is made of two pure gauges, and the first step is then to perform a gauge transform $\Omega_2 = \mathcal{U}_2^\dagger$ to modify $\mathcal{A}_2^+ \mapsto \mathcal{A}_2^i$. After this gauge transform, (8.9) now reads

$$\partial^- \mathcal{A}^{+a}(\mathbf{x}_\perp) = -ig\mathcal{A}_2^{iab}(\mathbf{x}_\perp)\mathcal{A}_1^{ib}(\mathbf{x}_\perp) \quad \mathcal{A}^{ia}(\mathbf{x}_\perp) = \mathcal{A}_1^{ib}(\mathbf{x}_\perp) + \mathcal{A}_2^{ib}(\mathbf{x}_\perp) \quad \mathcal{A}^{\pm a}(\mathbf{x}_\perp) = 0 \,. \quad (8.11)$$

As explained in [50], the last step to go from the light-cone gauge $\mathcal{A}^- = 0$ to the Fock-Schwinger gauge is to perform a gauge transform Ω such that

$$\mathcal{A}_{LC}^{ab\mu} = \Omega^{ac} \mathcal{A}_{FS}^{cd\mu} \Omega^{db\dagger} + \frac{i}{g}\Omega^{ac}\partial^\mu\Omega^{cb\dagger} \,, \quad (8.12)$$

where $\mathcal{A}_{LC}^- = 0$. Using the definition $\mathcal{A}_{FS}^\pm = \pm x^\pm \mathcal{A}_{FS}^\eta$ and $\mathcal{A}_{LC}^+ = x^+ \mathcal{A}_{LC}^\eta$, one then finds $\Omega(\tau, \mathbf{x}_\perp) = e^{\frac{ig\tau^2}{2}\mathcal{A}^\eta(\mathbf{x}_\perp)}$ and one recovers the known result from [22, 47–49]

$$\mathcal{A}_{FS}^{\eta a} = \frac{1}{2}\partial^- \mathcal{A}_{LC}^{+a}(\mathbf{x}_\perp) = \frac{ig}{2}\mathcal{A}_2^{iab}(\mathbf{x}_\perp)\mathcal{A}_1^{ib}(\mathbf{x}_\perp) \qquad \mathcal{A}_{FS}^{ia}(\mathbf{x}_\perp) = \mathcal{A}_1^{ib}(\mathbf{x}_\perp) + \mathcal{A}_2^{ib}(\mathbf{x}_\perp) \,. \quad (8.13)$$

The final steps will be identical when we consider the small fluctuations.

---

7. The left (right) branch of the blue line is not causally related to the right (left) part of the light cone.
8. See [50].

8.5 Small fluctuations in the forward light cone

We now turn to the problem of computing analytically the small fluctuations a on top of the background field in the axial gauge $\mathcal{A}^- = 0$. The setup is described in the figure 8.3
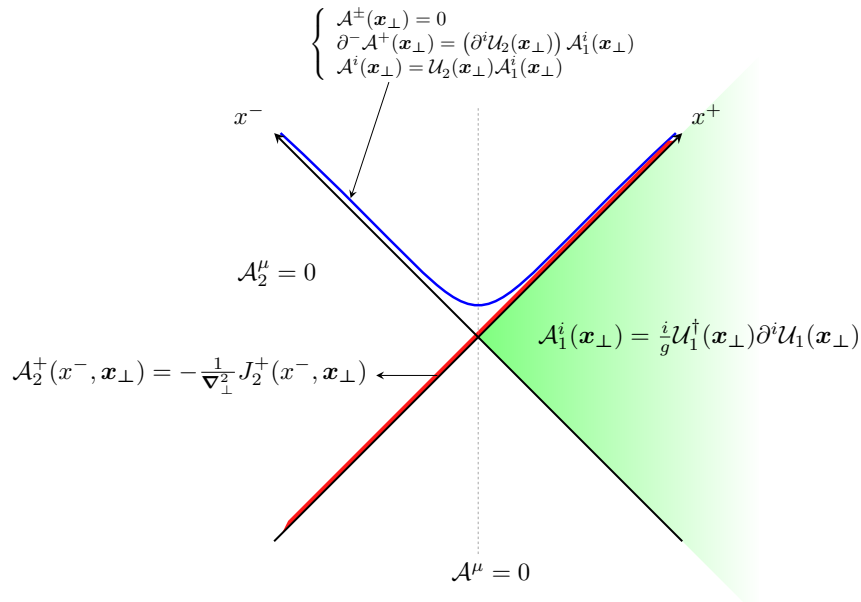
Figure 8.3: Structure of the background field in the light-cone gauge $\mathcal{A}^- = 0$.

This implies several steps that have to be performed in chronological order. They are summarized in the figure 8.4. As already mentioned, what happens on the left side of the light cone is independent from what happens on the right side (for the same causal argument that was presented for the background field). We will therefore treat the right part and deduce by symmetry the result for the left part.
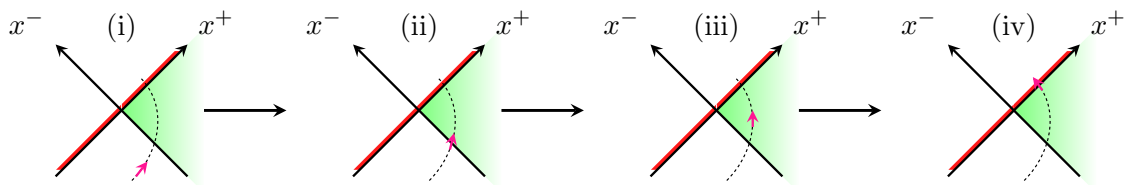
Figure 8.4: The four steps that one has to perform in order to derive the small fluctuations in the forward light cone. See in order sections 8.5.1, 8.5.2, 8.5.3 and 8.5.4

There are four steps to perform
— (i) evolve in the $x^\pm < 0$ region.
— (ii) cross the first nucleus.
— (iii) evolve on top of $\mathcal{A}_1$ ($x^+ > 0, x^- < 0$ region).
— (iv) cross the second nucleus.
We will start with a plane wave $a^{\mu a}_{k\lambda c}$ at $-\infty$, that have a color c, a polarization vector $\epsilon^\mu_{k\lambda}$, which satisfies $\epsilon^{k\lambda}_\mu \epsilon^\mu_{k\lambda'} = \delta^{\lambda\lambda'}$ as well as $k_\mu \epsilon^\mu_{k\lambda} = 0$ and a momentum $\boldsymbol{k} = (k^x, k^y, k^z)$

$$\lim_{t \to -\infty} a^{\mu a}_{k\lambda c}(x^+, x^-, \boldsymbol{x}_\perp) = \delta^a_c \epsilon^{k\lambda}_\mu e^{ikx} \ . \tag{8.14}$$

8.5.1   Step 1: evolution in the backward light cone

From now on we will work in light-cone coordinate system[9]. In $a^- = 0$ gauge, the physical solution in the region[10] $x^+, x^- < 0$ of the YM equation of motion, recalled here for the vacuum,

$$[g^{\mu\nu}\Box - \partial^\mu\partial^\nu]\, a^{\mu a}_{\mathbf{k}\lambda c}(x) = 0 \,, \tag{8.15}$$

can be written as

$$a^{ia}_{\mathbf{k}\lambda c} = \delta^c_a \epsilon^i_{\mathbf{k}\lambda} e^{ikx} \qquad\qquad a^{+a}_{\mathbf{k}\lambda c} = \delta^a_c \frac{k^i \epsilon^i_{\mathbf{k}\lambda}}{k^-} e^{ikx} \qquad\qquad a^{-a}_{\mathbf{k}\lambda c} = 0 \,, \tag{8.16}$$

the ϵ satisfying $\epsilon^i_{\mathbf{k}\lambda} \epsilon^i_{\mathbf{k}\lambda'} = \delta^{\lambda\lambda'}$. This means that the mode k at $-\infty$ with the c color and polarization ϵ^i keeps the same form until it crosses the first nucleus. Gauss's law, $\partial_\mu a^{\mu a} = 0$, is satisfied thanks to the fact that $k_\mu \epsilon^\mu_{\mathbf{k}\lambda} = 0$.

8.5.2   Step 2: crossing the first nucleus

We now want to determine what becomes the a for $x^+ > 0$ and $x^- < 0$ (still in $a^- = 0$ gauge). The useful quantities and notations are illustrated in figure 8.5. But before doing so, we also need to now what is the form of the classical YM equations and the current conservation equations in this region

$$\mathcal{D}^{ab}_{1\mu}\mathcal{F}^{\mu\nu b}_1 = J^\nu_1 \qquad\qquad\qquad \mathcal{D}^{ab}_{1\nu}J^{\nu b}_1 = 0 \,. \tag{8.17}$$

The solution to the second of these equations can be

$$J^{ia}_1 = J^{+a}_1 = 0 \qquad\qquad J^{-a}_1(x^+, \mathbf{x}_\perp) = \mathcal{U}^{\dagger ab}_1(x^+, \mathbf{x}_\perp)\rho^b(x^+, \mathbf{x}_\perp) \,. \tag{8.18}$$

Here, one could be tempted to use the result from [188], which gives the crossing formulas for a small fluctuation passing through a nucleus of infinitesimal width. However, two subtleties prevent us to do so. The first one is that the background field has only a finite step when we go from $x = 0^-$ to $x = 0^+$ while [188] studied the case of an infinite discontinuity (through a δ function). The second is that we are not in the same gauge as the $a^+ = 0$ used in [188], and things would be simpler in this gauge. Indeed in the $a^- = 0$ gauge there is a precession of a^+ on J^-, that will produce an induced current j^-. More precisely, because we still want

$$(\partial^+ \delta^{ab} - iga^{+ab})(J^{-b}_1 + j^{-b}_1) = 0 \,, \tag{8.19}$$

we must have (since J^-_1 does not depend on x^-)

$$j^{-a}_1 = -igJ^{-ab}_1(x^+, \mathbf{x}_\perp)\frac{1}{\partial^+}a^{+b}(x^+ = 0) \,. \tag{8.20}$$

Because of these complications, we have to re-derive the crossing formulas for the small fluctuations when they go through the first nucleus. For that purpose, we have to look at the linearized YM equations

$$\mathcal{D}^{ab}_\mu\left(\mathcal{D}^{\mu bc}a^{\nu c} - \mathcal{D}^{\nu bc}a^{\mu c}\right) - ig\mathcal{F}^{\nu\mu ab}a^b_\mu = j^{\nu a} \,, \tag{8.21}$$

---

9. We will go back in (τ, η) coordinate system only in section 8.5.6, after having studying the whole history of the small fluctuations.
10. Which means the two physical polarizations, as for massless gluons there is a pure gauge polarization.
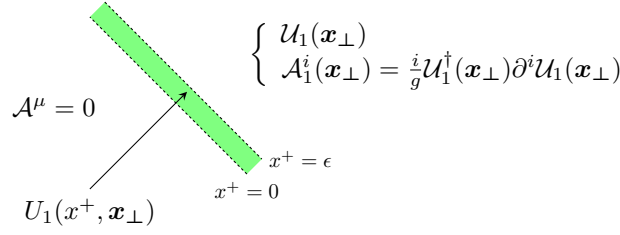
Figure 8.5: Crossing the first nucleus.

recalling that $\mathcal{F}^{\mu\nu} = 0$ for $x^+ > \epsilon$ and $\mathcal{F}^{\nu\mu a} = \delta^{j\mu}\delta^{ij}\delta^{-\nu}\partial^-\mathcal{A}_1^{ja}$. For $x^+ \in [0,\epsilon]$, this allows the following simplifications in the EOM

$$-\mathcal{D}_{1\mu}^{ab}(\partial^- a^{\mu b}) - ig(\partial^-\mathcal{A}_{1\mu}^{ab})a^{\mu b} = j_1^{-a}$$

$$\left(\delta^{ab}2\partial^-\partial^+ - \mathcal{D}_1^{iac}\mathcal{D}_1^{icb}\right)a^{+b} - \partial^+\left(\partial^- a^{+a} - \mathcal{D}_1^{iab}a^{ib}\right) = 0$$

$$\left(2\delta^{ab}\partial^-\partial^+ - \mathcal{D}_1^{iac}\mathcal{D}_1^{icb}\right)a^{jb} - \partial^-\mathcal{D}_1^{jab}a^{+b} + \mathcal{D}_1^{iac}\mathcal{D}_1^{jcb}a^{ib} + ig(\partial^-\mathcal{A}_1^{jab})a^{+b} = 0 \,. \qquad (8.22)$$

To further simplify these equations, we recall that there is a $\theta(x^+)$ term in $\mathcal{A}^i$ and therefore a singularity $\delta(x^+)$ in $\partial^-\mathcal{A}^i$. The first equation has no ∂^+ derivatives and can be seen as a constraint: it is nothing but Gauss's law for the small fluctuations in this gauge. It gives

$$\partial^-\left(\partial^- a^{+a} - \mathcal{D}_1^{iab}a^{ib}\right) = 2ig(\partial^-\mathcal{A}_1^{iab})a^{ib} - j_1^{-a} \,, \qquad (8.23)$$

which implies that $\partial^- a^{+a} - \mathcal{D}^{iab}a^{ib}$ has only a finite jump when going from $x^+ = 0$ to $x^+ = \epsilon$. Taking this fact into account in the second equation implies that a^{+a} varies continuously. Knowing that, we can simplify all the continuous terms into the third equation to get

$$\partial^-\partial^+ a^{ja} = -ig(\partial^-\mathcal{A}_1^{jab})a^{+b} \,, \qquad (8.24)$$

which can be integrated over x^+ from 0 to ϵ, and since a^+ is continuous it can be taken out of the integral. We are left with

$$a^{ja}(x^+ = \epsilon) = a_0^{ja} - ig\mathcal{A}_1^{jab}(\epsilon)\frac{1}{\partial^+}a_0^{+b} \,, \qquad (8.25)$$

where we have used again the fact that $\mathcal{A}^j$ does not depend on x^-, and noted the components of a at $x^+ = 0$ with the label a_0. All we have to do now is determine the jump of $\partial^- a^+$. For that, we use Gauss's law integrated over x^+ from 0 to ϵ

$$\left[\partial^- a^{+a}\right]_{x^+=0}^\epsilon = \int_0^\epsilon dx^+\left[\mathcal{D}_1^{iab}\partial^- a^{ib} + ig(\partial^-\mathcal{A}_1^{iab})a^{ib} - j_1^{-a}\right] \,. \qquad (8.26)$$

Using (8.25) the EOM for the background field $\mathcal{D}_1^{iab}\partial^-\mathcal{A}_1^{ib} = J_1^{-a}$, we obtain the following result

$$\left[\partial^- a^{+a}\right]_{x^+=0}^\epsilon = \int_0^\epsilon dx^+ ig(\partial^-\mathcal{A}_1^{iab}(x^+))\left(a_0^{ib} - \frac{\partial^i}{\partial^+}a_0^{+b}\right) = ig\mathcal{A}_1^{iab}(\epsilon)\left(a_0^{ib} - \frac{\partial^i}{\partial^+}a_0^{+b}\right) \,. \qquad (8.27)$$

Equations (8.25) and (8.27), together with the continuity of a^+ through the crossing are the central result of this part. We can check Gauss's law at this point, as this is a good way to test the validity of our results at the various intermediate steps

$$\partial^-\left(\partial^- a^{+a} - \mathcal{D}^{iab}a^{ib}\right)_{x^+=\epsilon} = \partial^-\left(ig\mathcal{D}_1^{iac}\mathcal{A}_1^{icb}\frac{1}{\partial^+}a_0^{+b} + ig\mathcal{A}_1^{iab}a_0^{ib}\right) = 0 \,. \qquad (8.28)$$

8.5.3   Step 3: propagation in the region $x^+ > \epsilon$, $x^- < 0$

In this section, we perform the evolution of the small fluctuation on top of the pure gauge $\mathcal{A}_1^i$. Since the calculation is quite tedious, we will perform several consistency checks in appendix 8.B. To perform the evolution on top of the pure gauge, one has to realize first that the linearized EOM (8.21) for the small fluctuations become [11]

$$\mathcal{U}_1^{\dagger ac}(\boldsymbol{x}_\perp) \left(g^{\mu\nu}\Box - \partial^\mu\partial^\nu\right)\mathcal{U}_1(\boldsymbol{x}_\perp)^{cb}(\boldsymbol{x}_\perp)a_\mu^b(x) = 0 \,, \tag{8.29}$$

which means that $\tilde{a}_\mu^a(x) = \mathcal{U}_1(\boldsymbol{x}_\perp)^{ab}(\boldsymbol{x}_\perp)a_\mu^b(x)$ propagates on top of the vacuum. One can therefore write the following Green's formula for it [12]

$$\tilde{a}^\rho(x) = i \int_{y^+=0^+} \mathrm{d}y^- \, \mathrm{d}^2\boldsymbol{y}_\perp \Big\{ -\left[\partial_\mu^y D_{0,R}^{\rho\mu}(x,y)\right] \tilde{a}^+(y) + D_{0,R}^{\rho+}(x,y)\left[\partial_y^\mu\tilde{a}_\mu(y)\right]$$

$$+ D_{0,R}^{\rho i}(x,y) \overset{\leftrightarrow}{\partial_y^+} \tilde{a}^i(y)\Big\} \,, \tag{8.30}$$

where $D_{0,R}^{\mu\nu}$ is the free retarded propagator in the a^- gauge

$$D_{0,R}^{\mu\nu} = -i\frac{1}{k^2+ik^0\epsilon}\left(g^{\mu\nu} - \frac{k^\mu n^\nu + k^\nu n^\mu}{n.k+i\epsilon}\right) \,, \tag{8.31}$$

with $n^+ = 1$, $n^- = n^i = 0$. The following formulas, derived in appendix 8.A, will prove useful

$$\partial_\mu^x D_{0,R}^{\mu\nu}(x,y) = -i\delta^{\nu+}\theta(x^+-y^+)\delta(x^--y^-)\delta(\boldsymbol{x}_\perp-\boldsymbol{y}_\perp)$$
$$\partial_\nu^y\partial_\mu^x D_{0,R}^{\mu\nu}(x,y) = i\delta(x^+-y^+)\delta(x^--y^-)\delta(\boldsymbol{x}_\perp-\boldsymbol{y}_\perp) \,. \tag{8.32}$$

The Green's formula (8.30) is valid everywhere in the region $x^+ > \epsilon$ and $x^- < 0$. In particular, it preserves Gauss's law. Indeed, since above the $x^+ = \epsilon$ line $\mathcal{U}_1$ does not depend on x^+ Gauss's law (8.23) becomes

$$\partial^-(\mathcal{D}_1^{\mu ab}a^{\mu b}) = \mathcal{U}_1^{\dagger ab}(\boldsymbol{x}_\perp)\partial^-\left(\partial^-\tilde{a}^{+a} - \partial^i\tilde{a}^{ia}\right) = 0 \,, \tag{8.33}$$

which implies that $\partial_\mu\tilde{a}^\mu$ is independent of x^+. This can be easily checked thanks to (8.30) and (8.32)

$$\partial_\rho^x\tilde{a}^\rho(x) = i \int_{y^+=0^+} \mathrm{d}y^- \, \mathrm{d}^2\boldsymbol{y}_\perp \Big\{ \left[-\partial_\mu^y\partial_\rho^x D_{0,R}^{\rho\mu}(x,y)\right] \tilde{a}^+(y) + \partial_\rho^x D_{0,R}^{\rho+}(x,y)\left[\partial_y^\mu\tilde{a}_\mu(y)\right]$$

$$+ \partial_\rho^x D_{0,R}^{\rho i}(x,y) \overset{\leftrightarrow}{\partial_y^+} \tilde{a}^i(y)\Big\}$$

$$= \delta(x^+-y^+)\tilde{a}^+(y) + \theta(x^+-y^+)\left[\partial_\mu^y\tilde{a}^\mu(y)\right] \,, \tag{8.34}$$

and using the fact that $x^+ > y^+$ we get what was announced. To calculate $\tilde{a}(x)$ for $x^+ > \epsilon$, we need the results of appendix 8.A. Defining $\tilde{\epsilon}_{\boldsymbol{k}\lambda}^j = \left(\delta^{jk} - \frac{2k^jk^k}{k^2}\right)\epsilon_{\boldsymbol{k}\lambda}^k$, we obtain [13]

$$\tilde{a}_{\boldsymbol{k}\lambda c}^{ia}(x) = e^{ik^+x^-} \int_{\boldsymbol{p}_\perp} e^{i\boldsymbol{p}_\perp\cdot\boldsymbol{x}_\perp} \left(e^{i\frac{p^2}{2k^+}x^+}\left(\delta^{ij} - \frac{2p^ip^j}{p^2}\right) + 2p^i\left(\frac{p^j}{p^2} + \frac{k^j}{k^2}\right)\right)\tilde{\mathcal{U}}_1^{ac}(\boldsymbol{p}_\perp+\boldsymbol{k}_\perp)\tilde{\epsilon}_{\boldsymbol{k}\lambda}^j$$

$$\tilde{a}_{\boldsymbol{k}\lambda c}^{+a}(x) = 2k^+e^{ik^+x^-} \int_{\boldsymbol{p}_\perp} e^{i\boldsymbol{p}_\perp\cdot\boldsymbol{x}_\perp} \left(e^{i\frac{p^2}{2k^+}x^+}\frac{p^i}{p^2} - \left(\frac{p^i}{p^2} + \frac{k^i}{k^2}\right)\right)\tilde{\mathcal{U}}_1^{ac}(\boldsymbol{p}_\perp+\boldsymbol{k}_\perp)\tilde{\epsilon}_{\boldsymbol{k}\lambda}^i \,. \tag{8.35}$$

---

11. Since now $\mathcal{U}_1\boldsymbol{x}_\perp)$ only depends on $\boldsymbol{x}_\perp$ and $\mathcal{A}_1$ is truly a pure gauge.

12. The derivation of this Green's formula can be found in [58].

13. Calling from now on $k = |\boldsymbol{k}_\perp|$, $\epsilon_{\boldsymbol{k}\lambda}^- = \frac{k^j\epsilon_{\boldsymbol{k}\lambda}^j}{k}$, $\int_{\boldsymbol{p}_\perp} = \int\frac{\mathrm{d}^2\boldsymbol{p}_\perp}{(2\pi)^2}$, using the fact that $\partial^i = -\partial_i$ and $2k^+k^- - k^2 = 0$.

Introducing the notation

$$\mathcal{V}^{ia}_{1k_\perp \lambda c}(x_\perp, p_\perp) = \mathcal{U}^{ab\dagger}_1(x_\perp)\tilde{\mathcal{U}}^{bc}_1(p_\perp + k_\perp)\tilde{\epsilon}^i_{k\lambda} \,, \tag{8.36}$$

with

$$\tilde{\mathcal{U}}^{bc}_1(k_\perp) = \int d^2 x_\perp \, e^{-ik_\perp \cdot x_\perp} \mathcal{U}^{bc}_1(x_\perp) \,, \tag{8.37}$$

we obtain for the a

$$a^{ia}_{k\lambda c}(x) = e^{ik^+ x^-}\int_{p_\perp} e^{ip_\perp \cdot x_\perp}\left(e^{i\frac{p^2}{2k^+}x^+}\left(\delta^{ij} - \frac{2p^i p^j}{p^2}\right) + 2p^i\left(\frac{p^j}{p^2} + \frac{k^j}{k^2}\right)\right)\mathcal{V}^{ja}_{1k_\perp \lambda c}(x_\perp, p_\perp) \,, \tag{8.38}$$

$$\tilde{a}^{+a}_{k\lambda c}(x) = 2k^+ e^{ik^+ x^-}\int_{p_\perp} e^{ip \cdot x_\perp}\left(e^{i\frac{p^2}{2k^+}x^+}\frac{p^i}{p^2} - \left(\frac{p^i}{p^2} + \frac{k^i}{k^2}\right)\right)\mathcal{V}^{ia}_{1k_\perp \lambda c}(x_\perp, p_\perp) \,. \tag{8.39}$$

At this point, several constraints can be checked in order to confirm that we have the correct result. These consistency checks are performed in appendix 8.B. The last thing to do before going further is to take the $\epsilon = 0$ limit for the first nucleus (and therefore recovering the δ functions for J_1, j_1).

8.5.4   Step 4: crossing the second nucleus

Performing the second crossing would be trivial thanks to [188] if $\mathcal{A}^i$ was 0. Here it is not the case, and we should thus re-derive the crossing formulas. The notations are recalled on figure (8.6)

$$\mathcal{A}^i_1(x_\perp) = \frac{i}{g}\mathcal{U}_2(x_\perp)\mathcal{U}^\dagger_1(x_\perp)\partial^i\mathcal{U}_1(x_\perp)$$

$$\mathcal{A}^i_1(x_\perp) = \frac{i}{g}\mathcal{U}^\dagger_1(x_\perp)\partial^i\mathcal{U}_1(x_\perp)$$

$$\begin{cases} \mathcal{A}^+_2(x^-, x_\perp) = -\frac{1}{\nabla^2_\perp}J^+_2(x^-, x_\perp) \\ \mathcal{A}^i_1(x^-, x_\perp) = \frac{i}{g}\mathcal{U}_2(x^-, x_\perp)\mathcal{U}^\dagger_1(x_\perp)\partial^i\mathcal{U}_1(x_\perp) \end{cases}$$

Figure 8.6: Crossing the second nucleus.

Here by opposition to the first crossing we are in the gauge where there is no precession of J^μ due to a^μ. The linearized YM equations therefore take the form

$$\mathcal{D}^{ab}_\mu\left(\mathcal{D}^{\mu bc}a^{\nu c} - \mathcal{D}^{\nu bc}a^{\mu c}\right) - ig\mathcal{F}^{\nu\mu ab}a^b_\mu = 0 \,, \tag{8.40}$$

which gives Gauss's law for $\nu = -$ (since $\mathcal{A}_1$ does not depend on x^+)

$$\partial^-\left(\partial^- a^{+a} - \mathcal{D}^{iab}_1 a^{ib}\right) = 0 \,. \tag{8.41}$$

For $\nu = j$, neglecting all the non-dominant terms reduces to $\partial^-\mathcal{D}^{+ab}_2 a^{jb} = 0$. The solution is therefore

$$a^{ia}_{k\lambda c}(x^- = \epsilon) = \mathcal{U}^{ab}_2(x^-, x_\perp)a^{ib}_{k\lambda c}(x^- = 0^-) \,, \tag{8.42}$$

and finally, for $\nu = +$

$$0 = \left(2\partial^-\mathcal{D}^{+ab}_2 - \mathcal{D}^{iac}_1\mathcal{D}^{icb}_1\right)a^{+b} - \left(\partial^-\mathcal{D}^{+ab}_2 a^{+b} - \mathcal{D}^{iac}_1\mathcal{D}^{+cb}_2 a^{ib}\right)$$
$$+ gf^{abc}(\partial^+\mathcal{A}^{ic}_1 - ig\mathcal{A}^{+cd}_2\mathcal{A}^{id}_1 - \partial^i\mathcal{A}^{+c}_2)a^{ib} \,. \tag{8.43}$$

Since $\partial^+ \mathcal{A}_1^{ic} = ig\mathcal{A}_2^{+cd}\mathcal{A}_1^{id}$ in the $0 < x^- < \epsilon$ region, the previous equation can be simplified into

$$\mathcal{D}_2^{+ab}a^{+b} = ig(\partial^i \mathcal{A}_2^{+ab})\frac{1}{\partial^-}a^{ib} , \tag{8.44}$$

from which the solution is known (see [188] again). The final form of a therefore is (at $x^- = \epsilon$)

$$a_{\boldsymbol{k}\lambda c}^{+a}(x^- = \epsilon) = \mathcal{U}_2^{ab}(\boldsymbol{x}_\perp)a_{\boldsymbol{k}\lambda c}^{+b}(x^- = 0^-) + (\partial^i\mathcal{U}_2^{ab}(\boldsymbol{x}_\perp)\frac{1}{\partial^-}a_{\boldsymbol{k}\lambda c}^{ib}(x^- = 0^-) \tag{8.45}$$

$$a_{\boldsymbol{k}\lambda c}^{ib}(x^- = \epsilon) = \mathcal{U}_2^{ab}(\boldsymbol{x}_\perp)a_{\boldsymbol{k}\lambda c}^{ib}(x^- = 0^-) . \tag{8.46}$$

The crossing formula of [188] are therefore not affected by the presence of a non-vanishing $\mathcal{A}_1^i$. One can check that Gauss's law is still satisfied. We can now take the $\epsilon = 0$ limit for the second nucleus.

8.5.5   Going to Fock-Schwinger gauge

We should first go to the $\mathcal{A}^- = 0$ gauge with two pure gauges on both sides of the light cone. To do so, we first have to perform a gauge transform $\Omega_2 = \mathcal{U}_2^\dagger$ which trivially affects the small fluctuations: $a \to \mathcal{U}_2 a \mathcal{U}_2^\dagger$. After this gauge transform we therefore have

$$a_{\boldsymbol{k}\lambda c}^{+a}(x^- = \epsilon) = a_{\boldsymbol{k}\lambda c}^{+b}(x^- = 0^-) - ig\mathcal{A}_2^{iab}(\boldsymbol{x}_\perp)\frac{1}{\partial^-}a_{\boldsymbol{k}\lambda c}^{ib}(x^- = 0^-)$$

$$a_{\boldsymbol{k}\lambda c}^{ia}(x^- = \epsilon) = a_{\boldsymbol{k}\lambda c}^{ib}(x^- = 0^-)$$

$$\mathcal{A}_{LC}^{\pm a}(\boldsymbol{x}_\perp) = 0$$

$$\partial^- \mathcal{A}_{LC}^{+a}(\boldsymbol{x}_\perp) = ig\mathcal{A}_1^{iab}(\boldsymbol{x}_\perp)\mathcal{A}_2^{ib}(\boldsymbol{x}_\perp)$$

$$\mathcal{A}_{LC}^{ia}(\boldsymbol{x}_\perp) = \mathcal{A}_1^{ia}(\boldsymbol{x}_\perp) + \mathcal{A}_2^{ia}(\boldsymbol{x}_\perp) . \tag{8.47}$$

Let's also notice that the covariant derivative $\mathcal{D}^i$ is now $\partial^i - ig\mathcal{A}^i = \partial^i - ig(\mathcal{A}_1^i + \mathcal{A}_2^i)$. To go to Fock-Schwinger gauge, we finally have to perform a gauge transform W in analogy with what was done in section 8.4. Nevertheless $W \neq \Omega$ since now the a depends on the rapidity η. We will assume that $W = \Omega + ig\omega$, which means that the action of this gauge transformation on the background field and on the small fluctuations can be split. Ω is already known, and has no effect on the a (since its limit is $\mathbb{I}$ when $\tau \mapsto 0$). We then just need to determine ω such that

$$\begin{cases} a_{LC}^{ai} = a_{FS}^{ai} + \mathcal{D}_{FS}^{abi}\omega^b \\ a_{LC}^{a-} = a_{FS}^{a-} + \mathcal{D}_{FS}^{ab-}\omega^b = 0 \\ a_{LC}^{a+} = a_{FS}^{a+} + \mathcal{D}_{FS}^{ab+}\omega^b \end{cases} .$$

Taking the same ansatz as for the background field we assume in addition that the small fluctuations in the two different gauges are related through $a_{FS}^\pm = \pm x^\pm a_{FS}^\eta$ and $a_{LC}^+ = x^+ b_{LC} = x^+ a_{LC}^\eta$. From the second equation we get $x^- a_{FS}^{a\eta} = \partial^-\omega^a - ig\mathcal{A}_{FS}^{ab-}\omega^b$, and in terms of τ, η, we obtain

$$\tau a_{FS}^{a\eta} = \partial_\tau\omega^a + \frac{1}{\tau}\partial_\eta\omega^a + ig\tau\mathcal{A}_{FS}^{ab\eta}\omega^b . \tag{8.48}$$

Injecting this back into the third equation gives

$$\omega^a(\tau, \eta, \boldsymbol{x}_\perp) = \int_0^\tau d\tau' \frac{\tau'}{2}a_{LC}^{a\eta}(\tau', \eta, \boldsymbol{x}_\perp) . \tag{8.49}$$

So the final formula for the infinitesimal gauge transform are (replacing the background field in the LC gauge thanks to the result of section 8.4)

$$a_{FS}^{ai} = a_{LC}^{ai} - \mathcal{D}_{LC}^{abi}\omega^b \qquad\qquad a_{FS}^{a\eta} = \frac{1}{2}a_{LC}^{a\eta} + \frac{ig}{2}\mathcal{A}_{LC}^{ab\eta}\omega^b + \frac{1}{\tau^2}\partial_\eta\omega^a . \tag{8.50}$$

It turns out that the $\mathcal{D}_{LC}^{abi}\omega^b$ and $\frac{ig}{2}\mathcal{A}_{LC}^{ab\eta}\omega^b$ do not contribute at lowest non-zero order in τ.

8.5.6 Transformation $k_z \mapsto \nu$

The last thing that we need to do is to go to the τ, η coordinate system, with the (k_x, k_y, ν) momenta, where ν is the Fourier conjugate of the rapidity η. For that, one has to calculate ω. First, choosing the integration constant for the $\frac{1}{\partial^-}a^i$ to be such that it gives 0 in $x^+ = 0$ gives (denoting with a 0 index the small fluctuations given by formula (8.38-8.39))

$$\frac{1}{2x^+ \partial^-} a_{0,LC}^{ai} = -i \frac{k e^{y-\eta}}{\tau} \int_{\boldsymbol{p}} e^{i \boldsymbol{p}_\perp \cdot \boldsymbol{x}_\perp} \mathcal{V}_{1 k_\perp \lambda c}^{ia}(\boldsymbol{x}_\perp, \boldsymbol{p}_\perp) \left(e^{i \frac{\tau p^2 e^{\eta - y}}{2k}} - 1 \right) \left(\delta^{ij} - \frac{2 p^i p^j}{p^2} \right) \frac{1}{p^2}$$

$$+ \int_{\boldsymbol{p}_\perp} e^{i \boldsymbol{p}_\perp \cdot \boldsymbol{x}_\perp} p^i \left(\frac{p^j}{p^2} + \frac{k^j}{k^2} \right) \mathcal{V}_{1 k_\perp \lambda c}^{ja}(\boldsymbol{x}_\perp, \boldsymbol{p}_\perp) . \tag{8.51}$$

We will also need

$$\frac{a_{0,LC}^{a+}}{2x^+} = \frac{k e^{y-\eta}}{\tau} \int_{\boldsymbol{p}} e^{i \boldsymbol{p} . \boldsymbol{x}_\perp} \mathcal{V}_{1 k_\perp \lambda c}^{ia}(\boldsymbol{x}_\perp, \boldsymbol{p}) \left(e^{i \frac{\tau p^2 e^{\eta - y}}{2k}} \frac{p^i}{p^2} - \left(\frac{p^i}{p^2} + \frac{k^i}{k^2} \right) \right)$$

$$a_{0,LC}^{ai} = \int_{\boldsymbol{p}} e^{i \boldsymbol{p} . \boldsymbol{x}_\perp} \mathcal{V}_{1 k_\perp \lambda c}^{ia}(\boldsymbol{x}_\perp, \boldsymbol{p}) \left(e^{i \frac{\tau p^2 e^{\eta - y}}{2k}} \left(\delta^{ij} - \frac{2 p^i p^j}{p^2} \right) + 2 p^i \left(\frac{p^j}{p^2} + \frac{k^j}{k^2} \right) \right) ,$$

$$\omega^a = \int_0^\tau \mathrm{d}\tau' \frac{\tau'}{2x^+} \left(a_{0,LC}^{+a} - i g \mathcal{A}_2^{iab}(\boldsymbol{x}_\perp) \frac{1}{\partial^-} a_{0,LC}^{ib} \right) . \tag{8.52}$$

The last thing we need to know is how to transform

$$I_R = \int \mathrm{d}y \, e^{i\nu y} e^{y-\eta} e^{i \frac{\tau p}{2} \frac{p}{k} e^{\eta - y}} , \tag{8.53}$$

and this can be done if we perform the change of variable $y \mapsto y = y' + \delta + \eta$ with $\delta = \ln\left(\frac{k}{p}\right)$, which gives

$$I_R = e^{i\nu\eta} \left(\frac{p}{k}\right)^{i\nu+1} \int \mathrm{d}y \, e^{(i\nu+1)y} e^{i \frac{\tau p}{2} e^{-y}} = -i e^{i\nu\eta} \left(\frac{p}{k}\right)^{i\nu+1} \Gamma(-1 - i\nu) e^{\frac{\nu\pi}{2}} \left(\frac{\tau p}{2}\right)^{1+i\nu} , \tag{8.54}$$

The rest is just a tedious calculation, that leads to the following result on the right branch

$$a_\eta^{R,FS}(\tau, \eta, \boldsymbol{x}_\perp) = -\frac{\tau^2}{2 + i\nu} \mathcal{D}^{iab} F_{k_\perp \nu \lambda c}^{R,ia}(\tau, \eta, \boldsymbol{x}_\perp) , \quad a_i^{R,FS}(\tau, \eta, \boldsymbol{x}_\perp) = -F_{k_\perp \nu \lambda c}^{R,ia}(\tau, \eta, \boldsymbol{x}_\perp) ,$$

$$e_{R,FS}^\eta(\tau, \eta, \boldsymbol{x}_\perp) = -\mathcal{D}^{iab} F_{k_\perp \nu \lambda c}^{R,ia}(\tau, \eta, \boldsymbol{x}_\perp) , \qquad e_{R,FS}^i(\tau, \eta, \boldsymbol{x}_\perp) = -i\nu F_{k_\perp \nu \lambda c}^{R,ia}(\tau, \eta, \boldsymbol{x}_\perp) , \tag{8.55}$$

were

$$F_{k_\perp \nu \lambda c}^{R,ia}(\tau, \eta, \boldsymbol{x}_\perp) = e^{i\nu\eta} \Gamma(-i\nu) e^{\frac{\nu\pi}{2}} \int_{\boldsymbol{p}_\perp} e^{i \boldsymbol{p}_\perp \cdot \boldsymbol{x}_\perp} \left(\frac{p^2 \tau}{2k}\right)^{i\nu} \left(\delta^{ij} - \frac{2 p^i p^j}{p^2} \right) \mathcal{V}_{1 k_\perp \lambda c}^{ja}(\boldsymbol{x}_\perp, \boldsymbol{p}_\perp) . \tag{8.56}$$

Formulas (8.55) are the central result of this section. They give analytically the spectrum of fluctuations on top a non-zero background field in the forward light cone, in a convenient gauge choice (Fock-Schwinger), in the more adapted coordinate system to describe a heavy ion collision (proper time-pseudo rapidity) and in terms of the momenta (k_x, k_y, ν). One should add now that (8.55) has been derived by evolving the small fluctuations in the right side of the light cone (crossing first the nucleus 1, then evolving on top of $\mathcal{A}_1$ and finally crossing the nucleus 2). We are therefore missing at time τ the contribution that evolved in the other part of the light cone (crossing first the nucleus 2, then evolving on top of $\mathcal{A}_2$ and finally crossing the nucleus 1). To get it, one has to be careful with some small changes. First, the convenient axial gauge for negative times is now the $a^+ = 0$ gauge. This changes the definition of $\mathcal{A}^\eta$: one has to exchange the $1 \leftrightarrow 2$ indices. Nevertheless, this does not affect the final result. What does is the change in the gauge transform $LC \to FS$. (8.50) is still valid but the definition of

a^η_{LC} (and therefore the value of ω) is affected: it is now $a^\eta_{LC} = -\frac{a^-_{LC}}{2x}$. The other thing that changes is the form of the integrals that appear

$$I_L = \int \mathrm{d}y\, e^{i\nu y} e^{\eta-y} e^{i\frac{\tau p}{2}\frac{p}{k} e^{y-\eta}} \,, \tag{8.57}$$

and performing the change of variable $y \mapsto y = y' + \delta + \eta$ with now $\delta = \ln\left(\frac{p}{k}\right)$, gives

$$I_L = e^{i\nu\eta}\left(\frac{k}{p}\right)^{i\nu+1} \int \mathrm{d}y\, e^{(i\nu-1)y} e^{i\frac{\tau p}{2} e^y} = ie^{i\nu\eta}\left(\frac{k}{p}\right)^{i\nu+1} \Gamma(-1+i\nu) e^{-\frac{\nu\pi}{2}}\left(\frac{\tau p}{2}\right)^{1-i\nu} \,. \tag{8.58}$$

We finally obtain

$$a^{L,FS}_\eta(\tau,\eta,\boldsymbol{x}_\perp) = \frac{\tau^2}{2-i\nu} \mathcal{D}^{iab} F^{L,ia}_{\boldsymbol{k}_\perp\nu\lambda c}(\tau,\eta,\boldsymbol{x}_\perp)\,, \quad a^{L,FS}_i(\tau,\eta,\boldsymbol{x}_\perp) = -F^{L,ia}_{\boldsymbol{k}_\perp\nu\lambda c}(\tau,\eta,\boldsymbol{x}_\perp)$$

$$e^\eta_{L,FS}(\tau,\eta,\boldsymbol{x}_\perp) = \mathcal{D}^{iab} F^{L,ia}_{\boldsymbol{k}_\perp\nu\lambda c}(\tau,\eta,\boldsymbol{x}_\perp)\,, \qquad\qquad e^i_{L,FS}(\tau,\eta,\boldsymbol{x}_\perp) = i\nu F^{L,ia}_{\boldsymbol{k}_\perp\nu\lambda c}(\tau,\eta,\boldsymbol{x}_\perp)\,, \tag{8.59}$$

where

$$F^{L,ia}_{\boldsymbol{k}_\perp\nu\lambda c}(\tau,\eta,\boldsymbol{x}_\perp) = e^{i\nu\eta}\Gamma(i\nu)e^{\frac{-\nu\pi}{2}} \int_{\boldsymbol{p}_\perp} e^{i\boldsymbol{p}_\perp\cdot\boldsymbol{x}_\perp}\left(\frac{p^2\tau}{2k}\right)^{-i\nu}\left(\delta^{ij} - \frac{2p^i p^j}{p^2}\right) \mathcal{V}^{ja}_{2\boldsymbol{k}_\perp\lambda c}(\boldsymbol{x}_\perp,\boldsymbol{p}_\perp)\,. \tag{8.60}$$

8.5.7 Final checks on (8.55) and (8.59)

A convincing check that we can perform on our solution is to check Gauss's law. We indeed find

$$\partial_\eta e^\eta_{FS} - \mathcal{D}^i_{FS} e^i_{FS} = 0\,. \tag{8.61}$$

In fact, both $F^{L,R}$ parts of the solution satisfy independently Gauss's law, as they should since both evolved independently. Another check passed independently by those two parts is that they satisfy the EOM at lowest order

$$\frac{1}{\tau}\partial_\tau\left(\frac{1}{\tau}\partial_\tau\right)a^a_\eta + \frac{i\nu}{\tau^2}\mathcal{D}^{ab}_i a^b_i = 0\,, \qquad\qquad \left[\frac{1}{\tau}\partial_\tau(\tau\partial_\tau) + \frac{\nu^2}{\tau^2}\right]a^a_j = 0\,. \tag{8.62}$$

Finally, one can again compute the scalar product for the sum of (8.55)-(8.59). One finds that the $a^*_\eta e^\eta - e^{\eta*}a_\eta$ term does not contribute at lowest order in τ, and therefore it reads

$$S_{\boldsymbol{k}_\perp\nu\lambda c,\boldsymbol{k}'_\perp\nu'\lambda'd} = -i\int \mathrm{d}^2\boldsymbol{x}_\perp \int \mathrm{d}\eta\left(a^{\boldsymbol{k}_\perp\nu\lambda c}_{ia*} e^{ia}_{\boldsymbol{k}'_\perp\nu'\lambda'd} - e^{ia*}_{\boldsymbol{k}_\perp\nu\lambda c} a^{\boldsymbol{k}'_\perp\nu'\lambda'd}_{ia}\right)\,, \tag{8.63}$$

and using the fact that $\nu|\Gamma(i\nu)|^2(e^{\pi\nu} - e^{-\pi\nu}) = 2\pi$, we find

$$PS = 4\pi\delta(\nu - \nu')\delta^{(2)}(\boldsymbol{k}_\perp - \boldsymbol{k}'_\perp)\delta_{\lambda\lambda'}\delta^{cd}\,. \tag{8.64}$$

To convince ourselves that this is the correct answer, we can compare with what we obtain for this scalar product in light cone coordinates (8.77). Using

$$2k^0(2\pi)^3\delta^2(\boldsymbol{k}_\perp - \boldsymbol{k}'_\perp)\delta(k^z - k'^z) = 2(2\pi)^3\delta^2(\boldsymbol{k}_\perp - \boldsymbol{k}'_\perp)\delta(y - y')\,, \tag{8.65}$$

and the fact that the transformation $k_z \mapsto \nu$ that we performed was normalized without a factor $\frac{1}{2\pi}$, we find that (8.77) and (8.64) are equivalent [14].

---

14. The limit $\epsilon \to 0$ has now been taken, and therefore the $j^\pm$ do not contribute anymore.

8.6 Summary

To conclude this section, let us state the final result for the spectrum of fluctuations at $\tau = 0^+$

$$a_\eta^{FS} = \tau^2 \mathcal{D}^{iab} \left(\frac{F^{L,ia}_{\mathbf{k}_\perp \nu \lambda c}(\tau,\eta,\mathbf{x}_\perp)}{2-i\nu} - \frac{F^{R,ia}_{\mathbf{k}_\perp \nu \lambda c}(\tau,\eta,\mathbf{x}_\perp)}{2+i\nu} \right), \qquad a_i^{FS} = - \left(F^{L,ia}_{\mathbf{k}_\perp \nu \lambda c}(\tau,\eta,\mathbf{x}_\perp) + F^{R,ia}_{\mathbf{k}_\perp \nu \lambda c}(\tau,\eta,\mathbf{x}_\perp) \right),$$

$$e_{FS}^\eta = \mathcal{D}^{iab} \left(F^{L,ia}_{\mathbf{k}_\perp \nu \lambda c}(\tau,\eta,\mathbf{x}_\perp) - F^{R,ia}_{\mathbf{k}_\perp \nu \lambda c}(\tau,\eta,\mathbf{x}_\perp) \right) \qquad e_{FS}^i = i\nu \left(F^{L,ia}_{\mathbf{k}_\perp \nu \lambda c}(\tau,\eta,\mathbf{x}_\perp) - F^{R,ia}_{\mathbf{k}_\perp \nu \lambda c}(\tau,\eta,\mathbf{x}_\perp) \right)$$

$$(8.66)$$

where

$$F^{RL,ia}_{\mathbf{k}_\perp \nu \lambda c}(\tau,\eta,\mathbf{x}_\perp) = e^{i\nu\eta} \Gamma(\mp i\nu) e^{\pm \frac{\nu\pi}{2}} \int \frac{\mathrm{d}^2 \mathbf{p}_\perp}{(2\pi)^2} e^{i\mathbf{p}_\perp \cdot \mathbf{x}_\perp} \left(\frac{p^2 \tau}{2k} \right)^{\pm i\nu} \left(\delta^{ij} - \frac{2p^i p^j}{p^2} \right) \mathcal{V}^{ja}_{1,2\mathbf{k}_\perp \lambda c}(\mathbf{x}_\perp, \mathbf{p}_\perp),$$

$$(8.67)$$

and

$$\mathcal{V}^{ja}_{1,2\mathbf{k}_\perp \lambda c}(\mathbf{x}_\perp, \mathbf{p}_\perp) = \mathcal{U}^{ab\dagger}_{1,2}(\mathbf{x}_\perp) \int \mathrm{d}^2 \mathbf{y}_\perp \, e^{-i(\mathbf{p}_\perp + \mathbf{k}_\perp) \cdot \mathbf{y}_\perp} \mathcal{U}^{bc}_{1,2}(\mathbf{y}_\perp) \left(\delta^{ij} - \frac{2k^i k^j}{k^2} \right) \epsilon^i_{\mathbf{k}\lambda}. \qquad (8.68)$$

Formula (8.66) will be one of the key ingredients of the initial conditions of our numerical simulations, the results of which are described in the next chapter.

Appendix

8.A Useful formulas to derive (8.35)

This section is devoted to a quick explanation of the intermediate results (8.35). First, we need all the combinations that enter in (8.30). They are deduced from formula (8.25)-(8.27)

$$\tilde{a}^{ia}_{\mathbf{k}\lambda c}(x^+ = \epsilon) = \left[\mathcal{U}^{ac}_1(\mathbf{x}_\perp) \epsilon^i_{\mathbf{k}\lambda} - 2i(\partial^i \mathcal{U}^{ac}_1(\mathbf{x}_\perp)) \frac{\epsilon^-_{\mathbf{k}\lambda}}{k} \right] e^{ikx}$$

$$\tilde{a}^{+a}_{\mathbf{k}\lambda c}(x^+ = \epsilon) = \mathcal{U}^{ac}_1(\mathbf{x}_\perp) \frac{k^i \epsilon^i_{\mathbf{k}\lambda}}{k^-} e^{ikx}$$

$$\partial^- \tilde{a}^{+a}_{\mathbf{k}\lambda c}(x^+ = \epsilon) = \left[i\mathcal{U}^{ac}_1(\mathbf{x}_\perp) k^i \epsilon^i_{\mathbf{k}\lambda} - (\partial^i \mathcal{U}^{ax}_1(\mathbf{x}_\perp)) \left(\epsilon^i_{\mathbf{k}\lambda} - \frac{2k^i k^j}{k^2} \epsilon^j_{\mathbf{k}\lambda} \right) \right] e^{ikx}$$

$$\partial^i \tilde{a}^{ia}_{\mathbf{k}\lambda c}(x^+ = \epsilon) = \left[i\mathcal{U}^{ac}_1(\mathbf{x}_\perp) k^j + (\partial^i \mathcal{U}^{ac}_1(\mathbf{x}_\perp)) \left(\delta^{ij} + 2\frac{k^i k^j}{k^2} \right) - 2i(\partial^i \partial^i \mathcal{U}^{ac}_1(\mathbf{x}_\perp)) \frac{k^j}{k} \right] \epsilon^j_{\mathbf{k}\lambda} e^{ikx}$$

$$\partial_\mu \tilde{a}^{\mu a}_{\mathbf{k}\lambda c}(x^+ = \epsilon) = 2 \left[i(\partial^i \partial^i \mathcal{U}^{ac}_1(\mathbf{x}_\perp)) \frac{\epsilon^-_{\mathbf{k}\lambda}}{k} - (\partial^i \mathcal{U}^{ac}_1(\mathbf{x}_\perp)) \epsilon^i_{\mathbf{k}\lambda} \right] e^{ikx}. \qquad (8.69)$$

We also need the following integrals [15]

$$i \int_{y^+=0^+} dy^- \, d^2\boldsymbol{y}_\perp \, D_{0,R}^{ji}(x,y) \, \overset{\leftrightarrow}{\partial_y^+} \, e^{iky} \alpha(\boldsymbol{y}_\perp) = \delta^{ij} e^{ik^+x^-} \int_{\boldsymbol{p}_\perp} \tilde{\alpha}(\boldsymbol{p}_\perp + \boldsymbol{k}_\perp) e^{i\boldsymbol{p}_\perp \cdot \boldsymbol{x}_\perp} e^{i\frac{p^2}{2k^+}x^+} \, ,$$

$$i \int_{y^+=0^+} dy^- \, d^2\boldsymbol{y}_\perp \, D_{0,R}^{i+}(x,y) e^{iky} \alpha(\boldsymbol{y}_\perp) = -i e^{ik^+x^-} \int_{\boldsymbol{p}_\perp} \tilde{\alpha}(\boldsymbol{p}_\perp + \boldsymbol{k}_\perp) e^{i\boldsymbol{p}_\perp \cdot \boldsymbol{x}_\perp} \frac{p^i}{p^2} \left(1 - e^{i\frac{p^2}{2k^+}x^+} \right) \, ,$$

$$i \int_{y^+=0^+} dy^- \, d^2\boldsymbol{y}_\perp \, D_{0,R}^{+i}(x,y) \, \overset{\leftrightarrow}{\partial_y^+} \, e^{iky} \alpha(\boldsymbol{y}_\perp) = 2k^+ e^{ik^+x^-} \int_{\boldsymbol{p}_\perp} \tilde{\alpha}(\boldsymbol{p}_\perp + \boldsymbol{k}_\perp) e^{i\boldsymbol{p}_\perp \cdot \boldsymbol{x}_\perp} \frac{p^i}{p^2} \left(1 - e^{i\frac{p^2}{2k^+}x^+} \right) \, ,$$

$$-i \int_{y^+=0^+} dy^- \, d^2\boldsymbol{y}_\perp \, \left[\partial_\mu^y D_{0,R}^{+\mu}(x,y) \right] \tilde{a}^+(y) = \tilde{a}^+(x^+ = 0^+)$$

$$i \int_{y^+=0^+} dy^- \, d^2\boldsymbol{y}_\perp \, D_{0,R}^{++}(x,y) e^{iky} \alpha(\boldsymbol{y}_\perp) = i e^{ik^+x^-} \int_{\boldsymbol{p}_\perp} \tilde{\alpha}(\boldsymbol{p}_\perp + \boldsymbol{k}_\perp) e^{i\boldsymbol{p}_\perp \cdot \boldsymbol{x}_\perp} \frac{2k^+}{p^2} \left(1 - e^{i\frac{p^2}{2k^+}x^+} \right) \, .$$

$$(8.70)$$

Putting everything together gives the desired result.

8.B   Several checks on the step 3

The first check is Gauss's law (8.28). As one can clearly see from (8.38)-(8.39)

$$\partial_\mu \tilde{a}_{\boldsymbol{k}\lambda c}^{\mu a}(x) = 2 e^{ik^+x^-} e^{-i\boldsymbol{k}_\perp \cdot \boldsymbol{x}_\perp} \left(i \frac{\partial^i \partial^i k^j \epsilon_{\boldsymbol{k}\lambda}^j}{k^2} - \partial^i \epsilon_{\boldsymbol{k}\lambda}^i \right) \mathcal{U}_1^{ac}(\boldsymbol{x}_\perp) \, . \tag{8.71}$$

and using (8.33), we find (8.28) again [16]. Another convincing test passed by our solution is that we recover the vacuum limit when we turn off the background field. If $\mathcal{U}_1^{ab\dagger}(\boldsymbol{x}_\perp) = \delta^{ab}$, then $\tilde{\mathcal{U}}_1^{bc}(\boldsymbol{p}_\perp + \boldsymbol{k}_\perp) = (2\pi)^2 \delta(\boldsymbol{p}_\perp + \boldsymbol{k}_\perp) \delta^{bc}$, and therefore $a_{\boldsymbol{k}\lambda c}^{\mu a} = a_{0\boldsymbol{k}\lambda c}^{\mu a}$. We can also check that when x^+ goes to 0^+, we indeed recover $a^+ = a_0^+$ (continuity of a^+ through the first crossing) and $a^i = a_0^i - ig\mathcal{A}_1^i \frac{1}{\partial^+} a_0^+$ (formula (8.25)). Finally, we can check the scalar product on the $x^- = 0^-$ surface

$$S_{\boldsymbol{k}\lambda c, \boldsymbol{k}'\lambda' d} = -i \int_{x^-=0} d^2\boldsymbol{x}_\perp \int_{-\infty}^{+\infty} dx^+ \, a_{\boldsymbol{k}\lambda c}^{ia*} \, \overset{\longleftrightarrow}{\partial^-} \, a_{\boldsymbol{k}'\lambda' d}^{ia} \, . \tag{8.73}$$

That is calculated by cutting the integral on x^+ in three parts: $\epsilon < x^+ < +\infty, -\infty < x^+ < 0$ and [17] $0 < x^+ < \epsilon$. This calculation is tedious but straightforward. The following properties are used in the process

$$\frac{i}{x + i\epsilon} = \pi \delta(x) + iP\left(\frac{1}{x}\right) \, , \tag{8.74}$$

$$\int_{\boldsymbol{p}_\perp} \tilde{\mathcal{U}}_1^{cb\dagger}(\boldsymbol{p}_\perp + \boldsymbol{k}_\perp) \tilde{\mathcal{U}}_1^{bd}(\boldsymbol{p}_\perp + \boldsymbol{k}'_\perp) = \delta^{cd} (2\pi)^2 \delta^2(\boldsymbol{k}_\perp - \boldsymbol{k}'_\perp) \, , \tag{8.75}$$

---

15. Derived thanks to the residue theorem.
16. A property that will turn useful is the fact that $\mathcal{D}_1^{iac}(\boldsymbol{x}_\perp) \mathcal{U}_1^{cb\dagger}(\boldsymbol{x}_\perp) = 0$, and therefore

$$\mathcal{D}_1^{iac}(\boldsymbol{x}_\perp) \mathcal{A}_1^{icb}(\boldsymbol{x}_\perp) = \frac{i}{g} \mathcal{U}_1^{act}(\boldsymbol{x}_\perp) \partial^i \partial^i \mathcal{U}_1^{cb}(\boldsymbol{x}_\perp) \, . \tag{8.72}$$

This also implies that $\mathcal{D}_1^{\mu ac}(\boldsymbol{x}_\perp) a^{\mu c} = \partial_\mu \tilde{a}^{\mu a}$.
17. Which gives a contribution despite its infinitesimal size because $\partial^- \mathcal{A}_1^i$ has a $\delta(x^+)$.

and also, since $k^2 = k'^2$, $k^0 = \sqrt{k^2 + (k^z)^2}$, $k^+ = \frac{k^0 + k^z}{\sqrt{2}}$

$$k^+ \delta(k^+ - k'^+) = k^- \delta(k^- - k'^-) = k^0 \delta(k^z - k^{z'}) . \tag{8.76}$$

The final answer is

$$S_{k\lambda c, k'\lambda' d} = \delta^{\lambda\lambda'} \delta^{cd} (2\pi)^3 2k^0 \delta^3(k - k)$$

$$+ 4g \frac{\epsilon_{k\lambda} \epsilon_{k'\lambda'}}{kk'} \int\limits_0^\epsilon dx^+ \int d^2 x_\perp e^{i(k_\perp - k'_\perp) \cdot x_\perp} J_1^{-cd}(x^+, x_\perp) . \tag{8.77}$$

The origin of the second term, proportional to J_1^-, should be clarified. In order to do so, one should go back the derivation of the scalar product, from the EOM for the small fluctuations (8.21), recalling that an induced current j^- has been created by the precession of a^+. Following [187], we find

$$(a_{k\lambda c} | a_{k'\lambda' d}) = -i \int_{x^-=0} d^2 x_\perp \int\limits_0^\epsilon dx^+ \, a_{k\lambda c}^{ia*} \overleftrightarrow{\partial^-} a_{k'\lambda' d}^{ia}$$

$$+ i \int_\Omega d^4 x \left[a_{k\lambda c}^{+a*}(x) j^{-a}{}_{k'\lambda' d}(x) - j_{k\lambda c}^{-a*}(x) b_{k'\lambda' d}^{+a}(x) \right] , \tag{8.78}$$

and the second term is exactly the additional term of (8.77).

Chapter 9

⚛ Numerical results ⚛

Contents

9.1 Numerical implementation of the Yang-Mills Equations

n this chapter, we will present the first numerical computation performed in the Yang-Mills case with a realistic set of initial conditions based on the quantum corrections described in the sections 4.2 and 4.3. But before doing so, let us introduce the discretized formulation of the YM EOM (in the forward light cone)

$$D_\mu^{ab} F^{\mu\nu b} = 0 \,, \tag{9.1}$$

that is used in practice. The Yang-Mills equations are usually not implemented in the form of equation 9.1. A more practical formulation is the Hamiltonian one, where the dynamical variables are the gauge potentials and the conjugate electric fields.

9.1.1 Hamiltonian formulation of the Yang-Mills Equations: continuous case

To find HAMILTON's formulation of the Yang-Mills equations, we start from the Yang-Mills action (derived from 3.10, with $\mathrm{Tr}\,[AB] = A^a A^b \mathrm{Tr}\,[t^a t^b]$)

$$S = -\frac{1}{2} \int \mathrm{d}^4 x \, \mathrm{Tr}\,[\mathcal{F}_{\mu\nu}\mathcal{F}^{\mu\nu}] = \int \mathrm{d}^4 x \, \mathcal{L} \,. \tag{9.2}$$

In the proper time-rapidity/coordinate system, we have

$$S = -\frac{1}{2} \int \tau \mathrm{d}\tau \, \mathrm{d}\eta \, \mathrm{d}\boldsymbol{x}_\perp \, \mathrm{Tr} \left[\mathcal{F}_{\mu\nu} g^{\alpha\mu} g^{\beta\nu} \mathcal{F}_{\alpha\beta} \right] \, , \tag{9.3}$$

which means that the Lagrangean density is

$$\mathcal{L} = -\frac{\tau}{2} \mathrm{Tr} \left[\mathcal{F}_{\mu\nu} g^{\alpha\mu} g^{\beta\nu} \mathcal{F}_{\alpha\beta} \right] = \tau \, \mathrm{Tr} \left(\frac{\mathcal{F}_{\tau\eta}^2}{\tau^2} + \mathcal{F}_{\tau i}^2 - \frac{\mathcal{F}_{\eta i}^2}{\tau^2} - \mathcal{F}_{xy}^2 \right) \, . \tag{9.4}$$

In the Fock-Schwinger $\mathcal{A}_\tau = 0$ gauge, we get

$$\mathcal{L} = \tau \, \mathrm{Tr} \left(\frac{(\partial_\tau \mathcal{A}_\eta)^2}{\tau^2} + (\partial_\tau \mathcal{A}_i)^2 - \frac{\mathcal{F}_{\eta i}^2}{\tau^2} - \mathcal{F}_{xy}^2 \right) \, . \tag{9.5}$$

Finally, since in the fundamental representation of $SU(N)$ we have

$$\mathrm{Tr} \left(t^a t^b \right) = \frac{\delta^{ab}}{2} \, , \tag{9.6}$$

we can write

$$\mathcal{L} = \frac{\tau}{2} \left(\frac{\left(\partial_\tau \mathcal{A}_\eta^a \right)^2}{\tau^2} + \left(\partial_\tau \mathcal{A}_i^a \right)^2 - \frac{\left(\mathcal{F}_{\eta i}^a \right)^2}{\tau^2} - \left(\mathcal{F}_{xy}^a \right)^2 \right) \, . \tag{9.7}$$

In order to derive HAMILTON's equations, we first need the Hamiltonian. Its derivation starts with the computation the conjugate momenta of the gauge fields: the electric fields,

$$\mathcal{E}^{ia} = \frac{\partial \mathcal{L}}{\partial \left(\partial_\tau \mathcal{A}_i^a \right)} = \tau \, \partial_\tau \mathcal{A}_i^a \, , \qquad\qquad \mathcal{E}^{\eta a} = \frac{\partial \mathcal{L}}{\partial \left(\partial_\tau \mathcal{A}_\eta^a \right)} = \frac{\partial_\tau \mathcal{A}_\eta^a}{\tau} \, . \tag{9.8}$$

We thus find

$$\mathcal{H} = \mathcal{E}^{\mu a} \left(\partial_\tau \mathcal{A}_\mu^a \right) - \mathcal{L} = \frac{1}{2} \left(\tau \left(\mathcal{E}^{\eta a} \right)^2 + \frac{\left(\mathcal{E}^{ia} \right)^2}{\tau} + \frac{\left(\mathcal{F}_{\eta i}^a \right)^2}{\tau} + \tau \left(\mathcal{F}_{xy}^a \right)^2 \right) \, , \tag{9.9}$$

and HAMILTON's equations read

$$\frac{\partial \mathcal{H}}{\partial \mathcal{E}^{\mu a}} = \partial_\tau \mathcal{A}_\mu^a \, , \qquad\qquad \frac{\partial \mathcal{H}}{\partial \mathcal{A}_\mu^a} = -\partial_\tau \mathcal{E}^{\mu a} \, . \tag{9.10}$$

The first equation just gives (9.8), and the second equation leads to

$$-\partial_\tau \mathcal{E}^{\eta a} = \frac{\mathcal{D}_i^{ab} \mathcal{F}_{\eta i}^b}{\tau} \, , \qquad\qquad -\partial_\tau \mathcal{E}^{ia} = \frac{\mathcal{D}_\eta^{ab} \mathcal{F}_{i\eta}^b}{\tau} + \tau \, \mathcal{D}_j^{ab} \mathcal{F}_{ij}^b \, . \tag{9.11}$$

Finally, we observe that we did not use the Yang-Mills equation for $\nu = \tau$

$$\mathcal{D}_\mu^{ab} \mathcal{F}^{\mu\tau b} = 0 \, , \tag{9.12}$$

which gives GAUSS's law

$$\mathcal{D}_i^{ab} \mathcal{E}^{ib} + \mathcal{D}_\eta^{ab} \mathcal{E}^{\eta b} = 0 \, . \tag{9.13}$$

9.1.2 Hamiltonian formulation of Yang-Mills Equations: discretized case

Numerically, we represent space by
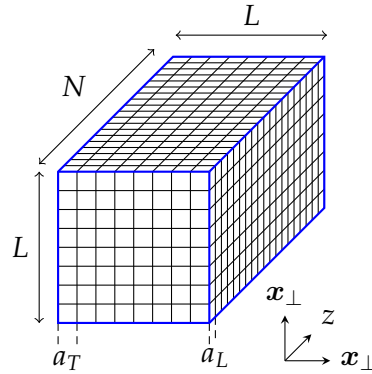
Figure 9.1: The asymmetric lattice used for numerical simulations.

Here a_T is the lattice spacing in the transverse directions and a_L the spacing in the rapidity η direction. In the following we will take $a_T = 1$, which means that dimensionful quantities are expressed in units of a_T. This grid is asymmetric in order to cope with the longitudinal expansion of the system: it is better to have a finer discretization in the longitudinal direction. In order to preserve gauge invariance despite the discretization, it is necessary to introduce link variables, defined as the exponential of a gauge field $\mathcal{A}$ on the link that connects two neighboring sites

$$\mathcal{U}_\mu(x) = e^{-iga\mathcal{A}_\mu(x)} = e^{-iga\mathcal{A}_\mu^a(x)t^a} = \quad x \longrightarrow x + a\hat{\mu} \;\cdot \tag{9.14}$$

In terms of these link variables and the electric fields, the Hamiltonian as well as all the physical observables are invariant under gauge transformations $\Omega(x)$ that has the following action

$$\mathcal{U}_\mu(x) \to \Omega(x)\mathcal{U}_\mu(x)\Omega^\dagger(x + a\hat{\mu}) \;, \qquad\qquad \mathcal{E}^\mu(x) \to \Omega(x)\mathcal{E}^\mu(x) \;. \tag{9.15}$$

The differential equations satisfied by the U_μ are deduced from (9.11). From

$$\partial_\tau \mathcal{U}_\mu(x) = \left(\partial_\tau \mathcal{A}_\mu(x)\right) \frac{\partial \mathcal{U}_\mu(x)}{\partial \mathcal{A}_\mu(x)} \;, \tag{9.16}$$

we obtain

$$\partial_\tau \mathcal{U}_i = -\frac{i\,g\,a_T}{\tau}\mathcal{E}^i(x)\mathcal{U}_i(x) \;, \qquad\qquad \partial_\tau \mathcal{U}_\eta = -i\,g\,a_L\,\tau\,\mathcal{E}^\eta(x)\mathcal{U}_\eta(x) \;. \tag{9.17}$$

Note that (9.17) is a differential equation on 2×2 matrices [1]. We will be more explicit about this representation when we present the leap-frog algorithm in the section 9.3. To derive the discretized equations of motion for $\mathcal{E}^\mu$ we will first derive the discretized Hamiltonian and then use the discretized HAMILTON's equations. To do so, we need the expression of $\mathcal{F}_{\mu\nu}$ in terms of the gauge links. It turns out that [2]

$$\mathcal{U}_{\mu\nu}(x) = e^{-iga^2\mathcal{F}_{\mu\nu}(x)} + O\left(a^4\right) \;, \tag{9.18}$$

---

1. In this chapter, the computations are performed for a gauge group $SU(2)$.
2. To prove this, one needs to apply the BAKER-CAMPBELL-HAUSDORFF formula.

where $U_{\mu\nu}$ is called a plaquette variable, defined as

$$\mathcal{U}_{\mu\nu}(x) = \mathcal{U}_\mu(x)U_\nu(x+\hat{\mu})U_\mu^\dagger(x+\hat{\nu})U_\nu^\dagger(x) = \qquad\qquad . \qquad (9.19)$$

Using $\mathcal{F}_{\mu\nu} = \mathcal{F}_{\mu\nu}^a t^a$ and the fact that for $SU(2)$

$$e^{ian^a t^a} = \cos\left(\frac{a\sqrt{n^a n^a}}{2}\right)\mathbb{I} + \frac{2i}{\sqrt{n^a n^a}}\sin\left(\frac{a\sqrt{n^a n^a}}{2}\right)n^a t^a\,, \qquad (9.20)$$

we find (with $|\mathcal{F}_{\mu\nu}| = \sqrt{\mathcal{F}_{\mu\nu}^a \mathcal{F}_{\mu\nu}^a}$)

$$2\,\mathrm{Tr}\left[\mathrm{Re}\,\mathcal{U}_{\mu\nu}(x)\right] = \mathrm{Tr}\left[\mathcal{U}_{\mu\nu}(x) + \mathcal{U}_{\mu\nu}^\dagger(x)\right] = 4\cos\left(\frac{ga^2}{2}|\mathcal{F}_{\mu\nu}|\right) = 4\left(1 - \frac{g^2 a^4}{8}\left(\mathcal{F}_{\mu\nu}^a\right)^2\right) + O\left(a^4\right)\,, \qquad (9.21)$$

which means that the discrete Hamiltonian is

$$\mathcal{H} = \sum_{x,y,\eta \in \text{lattice}} \frac{1}{2}\left(\tau\,(\mathcal{E}^{\eta a})^2 + \frac{(\mathcal{E}^{ia})^2}{\tau} + \frac{4}{g^2 a_L^2 \tau}\sum_i (2 - \mathrm{Tr}\,\mathcal{U}_{\eta i}) + \frac{4\tau}{g^2}(2 - \mathrm{Tr}\,\mathcal{U}_{xy})\right)\,. \qquad (9.22)$$

We can now derive the equation of motion of $\mathcal{E}^\mu$. For that, we just apply HAMILTON's equations, which implies to calculate terms like $\frac{\partial \mathcal{U}_{\mu\nu}}{\partial \mathcal{A}_\rho}$. To see how this works, consider a 2D slice of the grid, assuming that we want to calculate $\frac{\partial \mathcal{U}_{\eta i}}{\partial \mathcal{A}_\eta}(x)$

$$(9.23)$$

therefore, eight plaquettes contribute to $\frac{\partial \mathcal{U}_{\eta i}(x)}{\partial \mathcal{A}_\eta(x)}$:

$$\mathcal{U}_{\eta x},\ \mathcal{U}_{\eta x}^\dagger,\ \mathcal{U}_{\eta-x},\ \mathcal{U}_{\eta-x}^\dagger,\ \mathcal{U}_{\eta y},\ \mathcal{U}_{\eta y}^\dagger,\ \mathcal{U}_{\eta-y},\ \mathcal{U}_{\eta-y}^\dagger\,, \qquad (9.24)$$

and taking the derivative with respect to $\mathcal{A}_\eta(x)$ will introduce a $\pm ia_L$ in front of all those terms. Keeping track of all the signs[3], we get

$$\partial_\tau \mathcal{E}^\eta = -\frac{i}{2ga_L\tau}\sum_i\left[\left(\mathcal{U}_{\eta i}(x) + \mathcal{U}_{\eta-i}(x) - \mathcal{U}_{\eta i}^\dagger(x) - \mathcal{U}_{\eta-i}^\dagger(x)\right)\right]\,. \qquad (9.25)$$

Similarly

$$\partial_\tau \mathcal{E}^i = -\frac{i}{ga_L^2\tau}\left[\mathcal{U}_{i\eta} - \mathcal{U}_{i\eta}^\dagger + \mathcal{U}_{i-\eta} - \mathcal{U}_{i-\eta}^\dagger\right] - i\frac{\tau}{2}g\sum_{i\neq j}\left[\mathcal{U}_{ij} - \mathcal{U}_{ij}^\dagger + \mathcal{U}_{i-j} - \mathcal{U}_{i-j}^\dagger\right]\,. \qquad (9.26)$$

---

3. With the notation $\mathcal{U}_{-\mu}(x) = \mathcal{U}_\mu^\dagger(x - \hat{\mu})$.

Equations (9.25-9.26) are also two differential equations on 2×2 matrices. Finally, we need the discretized Gauss's law. One has the freedom to take either forward or backward covariant derivatives

$$\mathcal{D}_{\mu,B}(x)A(x) = \frac{A(x) - \mathcal{U}_\mu^\dagger(x - \hat{\mu})A(x - \hat{\mu})\mathcal{U}_\mu(x - \hat{\mu})}{a_\mu} \ ,$$

$$\mathcal{D}_{\mu,F}(x)A(x) = \frac{\mathcal{U}_\mu(x)A(x + \hat{\mu})\mathcal{U}_\mu^\dagger(x) - A(x)}{a_\mu} \ , \tag{9.27}$$

for the one that enters in (9.13). But once this choice is made, all the derivatives that appear in other places are constrained to be either forward or backward[4]. In the rest of this manuscript we implement Gauss's law with a backward derivative

$$\frac{\mathcal{E}^\mu(x) - \mathcal{U}_\mu^\dagger(x - \hat{\mu})\mathcal{E}^\mu(x - \hat{\mu})\mathcal{U}_\mu(x - \hat{\mu})}{a_\mu} = 0 \ . \tag{9.28}$$

9.2 Matrix multiplication on the lattice

Given (9.20), 3 real numbers are sufficient to characterize $\mathcal{U}_\mu$: these are the different color components of the gauge fields $\mathcal{A}_\mu^a$. But this choice implies the numerical evaluation of many trigonometric functions. Since this is very costly, we will prefer to encode $\mathcal{U}_\mu$ with 4 real numbers (u_μ^0, u_μ^a):

$$\mathcal{U}_\mu = u_\mu^0 \mathbb{I} + i u_\mu^a t^a \ . \tag{9.29}$$

In the section 9.1.2, a frequent operation is the multiplication of two matrices $\mathcal{U}$. With the representation for the gauge links, the result of this multiplication is

$$\mathcal{U}\mathcal{V} = \left(u^0 v^0 - \frac{u^a v^a}{4}\right)\mathbb{I} + i\left(u^0 v^a + u^a v^0 - \frac{1}{2}\epsilon^{abc}u^b v^c\right)t^a \ . \tag{9.30}$$

In the following, we will write[5]

$$\mathcal{U} = u^0 \mathbb{I} + i u^a t^a = \begin{pmatrix} u^0 \\ u^a \end{pmatrix} \ , \qquad \mathcal{U}^\dagger = u^0 \mathbb{I} - i u^a t^a = \begin{pmatrix} u^0 \\ -u^a \end{pmatrix} \ , \qquad \mathcal{E} = \mathcal{E}^a t^a \ , \tag{9.31}$$

and the matrix product becomes

$$\mathcal{U} \otimes \mathcal{V} = \begin{pmatrix} u^0 v^0 - \frac{u^a v^a}{4} \\ u^0 v^a + u^a v^0 - \frac{1}{2}\epsilon^{abc}u^b v^c \end{pmatrix} \ , \qquad \mathcal{E} \otimes \mathcal{U} = i\begin{pmatrix} \frac{1}{4}\mathcal{E}^a u^a \\ \frac{1}{2}\epsilon^{abc}\mathcal{E}^b u^c - \mathcal{E}^a u^0 \end{pmatrix} \ . \tag{9.32}$$

Gauss's law can therefore be written as

$$\mathcal{D}_{\mu,B}\mathcal{E}^\mu(x) = \frac{\mathcal{E}^\mu(x) - U_\mu^\dagger(x - \hat{\mu}) \otimes \mathcal{E}^\mu(x - \hat{\mu}) \otimes U_\mu(x - \hat{\mu})}{a} = 0 \ . \tag{9.33}$$

Since one needs to know $U_{x,y,\eta}$ and $\mathcal{E}^{x,y\eta}$ at each point of the lattice, and given our choice for encoding the $\mathcal{U}$, all the information is therefore encoded in 21 real numbers at each point of the lattice.

---

4. See for instance the covariant derivative that enters into the formulas for the spectrum of fluctuations (8.66). If one takes the derivative in Gauss's law to be backward, then the one for a_η must be backward. This will play a role in the section 9.7.

5. Notice that we have not included the factor i in the components $a = 1, 2, 3$ in this notation.

9.3   Leap-frog algorithm

We use the Leap-frog algorithm to perform numerically the time evolution of the discretized Hamilton equations. In its most basic implementation, which is the one used here, the error made at each step $\Delta\tau$ is of order $\Delta\tau^2$. It is therefore less precise that the Runge-Kutta method used in chapters 5 and 6 for the scalar theory, which was of order 4. It is nevertheless advantageous to use it, since it is a symplectic solver. This implies that quantities like the phase space volume, Gauss's law... are exactly conserved. In addition, it is faster that the Runge-Kutta method, which is a good thing since one would naively expect the gauge simulations to be at least 10 time slower than the scalar ones [6]. In our case, the EOM become

$$\mathcal{E}^i\left(\tau+\frac{\Delta\tau}{2}\right)=\mathcal{E}^i\left(\tau-\frac{\Delta\tau}{2}\right)-\frac{i\,\Delta\tau}{2g}\mathcal{U}_i\left(\tau,x\right)\otimes\left[\frac{1}{a_L^2\tau}V_{i\eta}\left(\tau,x\right)+\tau\sum_{j\neq i}\mathcal{V}_{ij}\left(\tau,x\right)\right]\,,\tag{9.34}$$

$$\mathcal{E}^\eta\left(\tau+\frac{\Delta\tau}{2}\right)=\mathcal{E}^\eta\left(\tau-\frac{\Delta\tau}{2}\right)-\frac{i\,\Delta\tau}{2ga_L\tau}\mathcal{U}_\eta\left(\tau,x\right)\otimes\sum_i\mathcal{V}_{\eta i}\left(\tau,x\right)\,,\tag{9.35}$$

$$U_i\left(\tau+\Delta\tau,x\right)=\,\exp\left[-\frac{ig\Delta\tau}{\tau+\frac{\Delta\tau}{2}}\mathcal{E}^i\left(\tau+\frac{\Delta\tau}{2},x\right)\right]\otimes U_i\left(\tau,x\right)\,,\tag{9.36}$$

$$U_\eta\left(\tau+\Delta\tau,x\right)=\,\exp\left[-ig\Delta\tau\,a_L\left(\tau+\frac{\Delta\tau}{2}\right)\mathcal{E}^\eta\left(\tau+\frac{\Delta\tau}{2},x\right)\right]\otimes U_\eta\left(\tau,x\right)\,.\tag{9.37}$$

where (9.36)-(9.37) have been modified in order to preserve unitarity. Here several notations have to be clarified

$$\mathcal{V}_{\mu\nu}\left(\tau,x\right)=\mathcal{S}_{\mu\nu}\left(\tau,x\right)-\mathcal{S}_{\mu\nu}^\dagger\left(\tau,x\right)+\mathcal{S}_{\mu-\nu}\left(\tau,x\right)-\mathcal{S}_{\mu-\nu}^\dagger\left(\tau,x\right)$$

$$\mathcal{S}_{\mu\nu}\left(\tau,x\right)=\mathcal{U}_\nu\left(\tau,x+\hat{\mu}\right)\otimes\mathcal{U}_\mu^\dagger\left(\tau,x+\hat{\nu}\right)\otimes\mathcal{U}_\nu^\dagger\left(\tau,x\right)\,.\tag{9.38}$$

9.4   Initial conditions for the background field

Following [24], we generate the initial conditions for the background field in the following way: first we generate random color sources $\rho_n(\boldsymbol{x}_\perp)$ (where $n=1,2$ labels the two nuclei) Gaussian distributed

$$\langle\rho_n(\boldsymbol{x}_\perp)\rho_{n'}(\boldsymbol{y}_\perp)\rangle=\frac{Q_s^2}{g^2}\,\delta_{nn'}\delta^{(2)}(\boldsymbol{x}_\perp-\boldsymbol{y}_\perp)\,,\tag{9.39}$$

where the saturation scale Q_s is the only dimensionful parameter of the problem (as we know from 3.5.1). Then we define $U_i^n(\boldsymbol{x}_\perp)$ to be the classical field in the MV model for a single color source.

$$U_i^n(\boldsymbol{x}_\perp)=V_n(\boldsymbol{x}_\perp)\otimes V_{n\dagger}(\boldsymbol{x}_\perp+\hat{i})\,,\tag{9.40}$$

with

$$V_n(\boldsymbol{x}_\perp)=e^{-i\Lambda_n(\boldsymbol{x}_\perp)}\,,\tag{9.41}$$

and $\Lambda_n(\boldsymbol{x}_\perp)$ the solution of the 2D Poisson equation

$$\boldsymbol{\nabla}_\perp\Lambda_n(\boldsymbol{x}_\perp)=-\rho_n(\boldsymbol{x}_\perp)\,.\tag{9.42}$$

At $\tau=0^+$, two initial conditions are trivial (see [49])

$$\mathcal{E}^i(\boldsymbol{x}_\perp,\eta)=0\qquad\qquad\mathcal{U}_\eta(\boldsymbol{x}_\perp,\eta)=\mathbb{I}\,.\tag{9.43}$$

---

6. This estimate is just based on the amount of data that needs to be manipulated. In the scalar case, one needs to know the field and its derivative at each point of the lattice.

The transverse links are

$$\mathcal{U}_i(\boldsymbol{x}_\perp, \eta) = \left(U_i^1(\boldsymbol{x}_\perp) + U_i^2(\boldsymbol{x}_\perp) \right) \otimes \left(U_i^{1\dagger}(\boldsymbol{x}_\perp) + U_i^{2\dagger}(\boldsymbol{x}_\perp) \right)^{-1} , \tag{9.44}$$

and the longitudinal chromo-electric field is

$$\begin{aligned}
\mathcal{E}^\eta(\boldsymbol{x}_\perp, \eta) = \frac{-i}{4g} \sum_i \Big[& (U_i(\boldsymbol{x}_\perp) - \mathbb{I}) \otimes \left(U_i^{1\dagger}(\boldsymbol{x}_\perp) - U_i^{2\dagger}(\boldsymbol{x}_\perp) \right) \\
& + \left(U_i^\dagger(\boldsymbol{x}_\perp - \hat{\imath}) - \mathbb{I} \right) \otimes \left(U_i^1(\boldsymbol{x}_\perp - \hat{\imath}) - U_i^2(\boldsymbol{x}_\perp - \hat{\imath}) \right) \\
& - \left(U_i^1(\boldsymbol{x}_\perp) - U_i^2(\boldsymbol{x}_\perp) \right) \otimes \left(U_i^\dagger(\boldsymbol{x}_\perp) - \mathbb{I} \right) \\
& - \left(U_i^{1\dagger}(\boldsymbol{x}_\perp - \hat{\imath}) - U_i^{2\dagger}(\boldsymbol{x}_\perp - \hat{\imath}) \right) \otimes (U_i(\boldsymbol{x}_\perp - \hat{\imath}) - \mathbb{I}) \Big] .
\end{aligned} \tag{9.45}$$

9.5 Discretized form of the energy-momentum tensor

Given our discrete Hamiltonian, we define the transverse and longitudinal chromo-electric and chromo-magnetic fields as follow:

$$E_L^2 = \left(\mathcal{E}_a^\eta \right)^2 \qquad\qquad E_T^2 = \frac{\left(\mathcal{E}_a^x \right)^2 + \left(\mathcal{E}_a^y \right)^2}{\tau^2} , \tag{9.46}$$

$$B_L^2 = \frac{4}{g^2} \left(2 - \operatorname{Tr} U_{xy} \right) \qquad\qquad B_T^2 = \frac{4}{g^2 a_L^2 \tau^2} \sum_i \left(2 - \operatorname{Tr} U_{\eta i} \right) , \tag{9.47}$$

Which gives the following expressions for the $T^{\mu\nu}$ components

$$\epsilon = \frac{E_L^2 + E_T^2 + B_T^2 + B_L^2}{2} , \tag{9.48}$$

$$P_T = \frac{E_L^2 + B_L^2}{2} , \tag{9.49}$$

$$P_L = \frac{E_T^2 + B_T^2 - E_L^2 - B_L^2}{2} . \tag{9.50}$$

9.6 Numerical checks

Several checks can be performed on our algorithm. First, we can check that it conserves the unitarity of the link variables and Gauss's law. With the initial conditions of the previous section, this is the case up to machine precision[7]. Another test passed by our code is that ϵ and P_L averaged over the lattice volume obey Bjorken's law (recall section 3.A and 6.6.2). Indeed, because of the conservation of energy and momentum, we expect

$$\frac{\mathrm{d}\epsilon}{\mathrm{d}\tau} + \frac{\epsilon + P_L}{\tau} = 0 . \tag{9.51}$$

This is exactly what we obtain numerically

---

7. This is not the most general initial condition. Indeed, since the classical initial condition is rapidity independent, the longitudinal degrees of freedom are not checked with this initial condition. For the full initial condition (sum of the background field and the rapidity dependent fluctuations), Gauss's law and unitarity are nevertheless also preserved with very good accuracy in all our simulations.
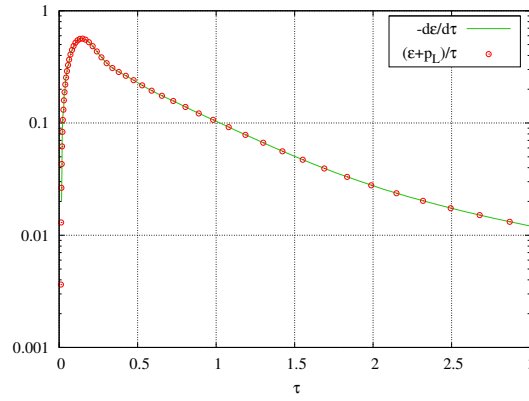
Figure 9.2: BJORKEN's law is satisfied in our computation.

A final test is to compute a gauge invariant quantity in two different gauges, and check that the result is the same in both gauges. We performed two simulations: in one we do not fix the residual gauge freedom of the initial condition and in the other we constrain it with Coulomb gauge condition[8]. At later times, the discrepancy in the energy density is always

$$\frac{\Delta \epsilon}{\epsilon} < 10^{-10} \, , \tag{9.52}$$

at all times in our simulations

9.7   Initial conditions for the small fluctuations

9.7.1   Discretized version for each mode of equation (8.66)

In this section, we want to find the discretized version of equation (8.66). We first need the discrete momenta. Calling them (k_x, k_y, k_z), the norms of the transverse and longitudinal momentum[9] read

$$\nu(k_z) = \frac{1}{a_L}\sqrt{2\left[1 - \cos\left(\frac{2\pi k_z}{N}\right)\right]} \quad k(k_x, k_y) = \sqrt{2\left[2 - \cos\left(\frac{2\pi k_x}{L}\right) - \cos\left(\frac{2\pi k_y}{L}\right)\right]} \, , \tag{9.53}$$

that we will simply denote ν and k from now on. We also need the definition of the backward and forward momenta k_B^i, k_F^i and ν_B, ν_F. They can be obtained by applying backward or forward derivatives on a discrete plane wave

$$\partial_{B,F}^x e^{i\frac{2\pi k i}{L}} = \mp\left(e^{\mp i\frac{2\pi k}{L}} - 1\right)e^{i\frac{2\pi k i}{L}} \tag{9.54}$$

which implies

$$k_B^i = -i\left(1 - e^{-\frac{2\pi i}{L}k_i}\right) \, , \qquad\qquad k_F^i = i\left(1 - e^{\frac{2\pi i}{L}k_i}\right) \, ,$$

$$\nu_B = -\frac{i}{a_L}\left(1 - e^{-\frac{2\pi i}{N}n}\right) \, , \qquad\qquad \nu_F = \frac{i}{a_L}\left(1 - e^{\frac{2\pi i}{N}n}\right) \, . \tag{9.55}$$

Note that $k_F^i k_B^i = k^2$ and $\nu_F \nu_B = \nu^2$. Given our choice of a backward covariant derivative in Gauss's law, we have, denoting

$$\tilde{F}(\nu) = \mathrm{FT}\left[F\right](\nu) = \sum_k e^{-\frac{2\pi i}{N}kk_z}F(\eta) \, , \quad \tilde{F}(\boldsymbol{k}_\perp) = \mathrm{FT}\left[F\right](\boldsymbol{k}_\perp) = \sum_{i,j} e^{-\frac{2\pi i}{L}\left(ik_x + jk_y\right)}F(\boldsymbol{x}_\perp) \, ,$$

$$F(\eta) = \tilde{\mathrm{F}}\mathrm{T}\left[\tilde{F}\right](\eta) = \sum_{k_z} e^{\frac{2\pi i}{N}kk_z}\tilde{F}(\nu) \, , \quad F(\boldsymbol{x}_\perp) = \tilde{\mathrm{F}}\mathrm{T}\left[\tilde{F}\right](\boldsymbol{x}_\perp) = \sum_{k_x,k_y} e^{\frac{2\pi i}{N}\left(ik_x + jk_y\right)}\tilde{F}(\boldsymbol{k}_\perp) \, , \tag{9.56}$$

---

8. Fixed thanks to the algorithm presented in [189, 190].
9. Discretized equivalents of ν and k of the section 8.5.6.

we have [10]

$$F_{k_\perp \nu \lambda c}^{RL,ia}(\tau, \boldsymbol{x}_\perp) = \Gamma(\mp i\nu) e^{\pm \frac{\nu \pi}{2}} \mathcal{U}_{1,2}^{ab\dagger}(\boldsymbol{x}_\perp) \tilde{\mathrm{FT}} \left[\left(\frac{p^2 \tau}{2k} \right)^{\pm i\nu} \left(\delta^{ij} - \frac{2 p_F^i p_B^j}{p^2} \right) \mathcal{V}_{1,2k_\perp \lambda c}^{ja}(\boldsymbol{p}_\perp) \right] (\boldsymbol{x}_\perp) ,$$

(9.57)

and

$$\mathcal{V}_{1,2k_\perp \lambda c}^{ja}(\boldsymbol{p}_\perp) = \left(\delta^{ij} - \frac{2 k_F^i k_B^j}{k^2} \right) \epsilon_{k\lambda}^i \mathrm{FT} \left[\mathcal{U}_1^{bc}(\boldsymbol{y}_\perp) \right] (\boldsymbol{k}_\perp + \boldsymbol{p}_\perp) .$$

(9.58)

Finally,

$$
\begin{aligned}
a_\eta^{\nu k_\perp \lambda c} &= \frac{\nu_F \tau^2}{\nu} \mathcal{D}_B^{iab}(\boldsymbol{x}_\perp) \left(\frac{F_{k_\perp \nu \lambda c}^{L,ia}(\tau, \boldsymbol{x}_\perp)}{2 - i\nu} - \frac{F_{k_\perp \nu \lambda c}^{R,ia}(\tau, \boldsymbol{x}_\perp)}{2 + i\nu} \right) , \\
a_i^{\nu k_\perp \lambda c} &= - \left(F_{k_\perp \nu \lambda c}^{L,ia}(\tau, \boldsymbol{x}_\perp) + F_{k_\perp \nu \lambda c}^{R,ia}(\tau, \boldsymbol{x}_\perp) \right) , \\
e_{\nu k_\perp \lambda c}^\eta &= \frac{\nu_F}{\nu} \mathcal{D}_B^{iab}(\boldsymbol{x}_\perp) \left(F_{k_\perp \nu \lambda c}^{L,ia}(\tau, \boldsymbol{x}_\perp) - F_{k_\perp \nu \lambda c}^{R,ia}(\tau, \boldsymbol{x}_\perp) \right) \\
e_{\nu k_\perp \lambda c}^i &= i\nu \left(F_{k_\perp \nu \lambda c}^{L,ia}(\tau, \boldsymbol{x}_\perp) - F_{k_\perp \nu \lambda c}^{R,ia}(\tau, \boldsymbol{x}_\perp) \right) .
\end{aligned}
$$

(9.59)

The linearized Gauss's law

$$\mathcal{D}_{i,B}^{ab}(\boldsymbol{x}_\perp) e^{ib}(\tau, \boldsymbol{x}_\perp) + i\nu_B e^{\eta b}(\tau, \boldsymbol{x}_\perp) = 0 ,$$

(9.60)

has been checked numerically up to machine precision for each mode at each point of the lattice and for each color. The final change with the continuum version of the system has to do with the sign of ν. Indeed, because ν varies between $-\infty$ and $+\infty$ in the continuum case, this means that either the nucleus 1 or 2 dominates depending on the sign of ν, because of the factor $\Gamma(\mp i\nu) e^{\pm \frac{\pi \nu}{2}}$. This property should be reproduced for the discretized modes, but $\nu = \frac{1}{a_L} \sqrt{2 \left(1 - \cos \frac{2 k_z \pi}{N} \right)}$ is always positive. To circumvent this problem, because $|\nu(k_z)| = |\nu(N - k_z)|$ and ν could be either $\pm \sqrt{\nu_B \nu_F}$, one can take positive values of ν for $k_z < \frac{N}{2}$ and negative ones for $k_z > \frac{N}{2}$.

9.7.2 Numerical implementation of (9.59)

To obtain the spectrum of fluctuation that enters in the initial condition of the classical-statistical method, we need to generate complex random Gaussian numbers $c_{c\nu k\lambda}$ of variance 1

$$\left\langle c_{c\nu k\lambda} c_{d\nu' k' \lambda'}^* \right\rangle = \delta_{\nu \nu'} \delta_{kk'} \delta_{\lambda \lambda'} \delta_{cd} ,$$

(9.61)

if one chooses the overall normalization factor in front of the spectrum of fluctuations in the following way (calling $V = a_L N L^2$ the volume of the box)

$$A_{\mu a}(\tau, \eta, \boldsymbol{x}_\perp) = \mathcal{A}_{\mu a}(\boldsymbol{x}_\perp) + \sqrt{\frac{1}{4\pi V}} \mathrm{Re} \sum_{\lambda k_\perp \nu c} e^{i\nu \eta} c_{c\nu k_\perp \lambda} a_{\mu a}^{c\nu k_\perp \lambda}(\tau, \boldsymbol{x}_\perp)$$

$$E^{\mu a}(\tau, \boldsymbol{x}_\perp) = \mathcal{E}^{\mu a}(\boldsymbol{x}_\perp) + \sqrt{\frac{1}{4\pi V}} \mathrm{Re} \sum_{\lambda k_\perp \nu c} e^{i\nu \eta} c_{c\nu k_\perp \lambda} e_{c\nu k_\perp \lambda}^{\mu a}(\tau, \boldsymbol{x}_\perp) .$$

(9.62)

---

10. Note that the $e^{i\nu \eta}$ factor has been removed from the definition of the F. The reason why we did so will be clearer in the next section.

With a naive implementation,, there are 10 entangled loops in the code in order to compute

$$a_{\mu a}(\tau, \eta, \boldsymbol{x}) = \sqrt{\frac{1}{4\pi V}} \text{Re} \sum_{\lambda \boldsymbol{k}_\perp \nu c} c_{c\nu \boldsymbol{k}_\perp \lambda} \, a_{\mu a}^{c\nu \boldsymbol{k}_\perp \lambda}(\tau, \eta, \boldsymbol{x}_\perp) \, , \tag{9.63}$$

for a total dimension [11] of $6N_c^2 \times (L^2 \times N)^2$. But since the longitudinal part of the fluctuation is trivial – it is just the plane wave $e^{i\nu\eta}$ – one can reduce the numbers of loops to 9, getting rid of a factor N by performing the sum over ν by the Fast Fourier Transform algorithm. Let us mention here a problem specific to the discretized case. On a lattice, one should exclude all the modes that have $k = 0$ or $\nu = 0$ in order to avoid a division by 0 (see formula 9.59). This implies that relations like

$$\int \frac{\mathrm{d}^2 \boldsymbol{p}_\perp}{(2\pi)^2} \tilde{\mathcal{U}}_1^{cb\dagger}(\boldsymbol{p}_\perp + \boldsymbol{k}_\perp) \tilde{\mathcal{U}}_1^{bd}(\boldsymbol{p}_\perp + \boldsymbol{k}'_\perp) = \delta^{cd}(2\pi)^2 \delta^2(\boldsymbol{k}_\perp - \boldsymbol{k}'_\perp) \, , \tag{9.64}$$

are not exactly satisfied on the lattice. Two trivial solutions appear in order to solve this issue. One could add a mass term to replace p by $\sqrt{p^2 + m^2}$, but this would break the gauge invariance. We therefore simply ignore this small violation of orthonormality on a lattice. After all, one only neglects $N + L^2$ out of $L^2 \times N$ modes. We can see this when we check the orthonormality of the small fluctuations by computing the scalar product

$$S_{\nu \boldsymbol{k}_\perp \lambda c, \nu' \boldsymbol{k}'_\perp \lambda' d} = -i \sum_{\eta, \boldsymbol{x}_\perp, a} \left(a_{ia}^{*\nu \boldsymbol{k}_\perp \lambda c}(\tau, \boldsymbol{x}_\perp, \eta) e_{\nu' \boldsymbol{k}'_\perp \lambda' d}^{ia}(\tau, \boldsymbol{x}_\perp, \eta) - e_{*\nu \boldsymbol{k}_\perp \lambda c}^{ia}(\tau, \boldsymbol{x}_\perp, \eta) a_{ia}^{\nu' \boldsymbol{k}'_\perp \lambda' d}(\tau, \boldsymbol{x}_\perp, \eta) \right)$$

$$= 4\pi \delta^{\lambda\lambda'} \delta^{cd} V \delta(\boldsymbol{k}_\perp - \boldsymbol{k}'_\perp) \delta_{\nu\nu'} \, . \tag{9.65}$$

Numerically, we obtain the $\delta^{\lambda\lambda'}$ and the $\delta(\nu - \nu')$ up to machine precision, but there are small violations [12] of the $4\pi \delta^{cd} \delta(\boldsymbol{k}_\perp - \boldsymbol{k}'_\perp)$ for the reason just explained.

9.8   Monte-Carlo: speed versus storage

To perform the Monte-Carlo sampling implied by the CSA, one needs repeat the time evolution (i.e. solving the classical YM equations) with different initial conditions. These initial conditions differ only by the Gaussian random numbers $c_{c\nu \boldsymbol{k}_\perp \lambda}$, that we will label from now on $c_{c\nu \boldsymbol{k}_\perp \lambda (l)}$, the index l labeling the $l_{\max}$ different initial conditions ($1 < l < l_{\max}$). Instead of recalculating the complicated objects $b_{\mu a}^{\nu \boldsymbol{k}_\perp \lambda c}(\tau, \boldsymbol{x}_\perp)$ for each $c_{c\nu \boldsymbol{k}_\perp \lambda (l)}$, we will compute instead

$$b_{\mu a}^{\nu (l)}(\tau, \boldsymbol{x}_\perp) = \sum_{\lambda \boldsymbol{k}_\perp c} a_{\mu a}^{\nu \boldsymbol{k}_\perp \lambda c}(\tau, \boldsymbol{x}_\perp) c_{\nu \boldsymbol{k}_\perp \lambda (l)}^c \, , \tag{9.66}$$

and then perform for each l the 1 dimensional inverse fft as before

$$a_{\mu a}^{(l)}(\tau, \eta, \boldsymbol{x}_\perp) = \sqrt{\frac{1}{4\pi V}} \text{Re} \sum_\nu e^{i\nu\eta} \, b_{\mu a}^{\nu (l)}(\tau, \boldsymbol{x}_\perp) \, . \tag{9.67}$$

Then we add the MV background field, to get

$$A_{\mu a}^{(l)}(\tau, \eta, \boldsymbol{x}_\perp) = \mathcal{A}_{\mu a}(\boldsymbol{x}_\perp) + a_{\mu a}^{(l)}(\tau, \eta, \boldsymbol{x}_\perp) \, , \quad E_{(l)}^{\mu a}(\tau, \eta, \boldsymbol{x}_\perp) = \mathcal{E}^{\mu a}(\boldsymbol{x}_\perp) + e_{(l)}^{\mu a}(\tau, \eta, \boldsymbol{x}_\perp) \, . \tag{9.68}$$

By doing this, one avoids to replicate the lengthy computation of $a_{\mu a}^{\nu \boldsymbol{k}_\perp \lambda c}(\tau, \boldsymbol{x}_\perp)$, which in effect reduces significantly the execution time. The only issue with this procedure is the storage of $b_{\mu a}^{\nu (l)}(\tau, \boldsymbol{x})$, which is [13] a $12 \, N_c \times L^2 \times N \times l_{\max}$ array of real number . For the $64^2 \times 128$ grid that we have used, this means $\sim 150 MB$ for each initial configuration stored in double precision.

---

11. The initial state is characterized by $2N_c \times L^2 \times N$ indices that correspond to $L^2 \times N$ modes (k_x, k_y, k_z), 2 polarizations and N_c initial color. To this we should add the spatial dependence of dimension $L^2 \times N$, 3 Lorentz indices and N_c colors.

12. Of the order of 0.1% for the lattice size we have used.

13. $12 = 3 \times 2 \times 2$ (3 Lorentz indices, 2 for complex numbers and 2 for the a and the e).

9.9 Enforcing the non-linear Gauss's law

In order to initialize our classical-statistical simulations, we start with (9.68) for the electric fields. But for the gauge fields, one needs to use gauge links in order to have exact gauge invariance on the lattice. We define the complete gauge link as

$$U_\mu = e^{-ig a_\mu^{(l)}(\tau,\eta,x_\perp)} e^{-ig \mathcal{A}_{\mu a}(x_\perp) t^a} . \tag{9.69}$$

But this way of introducing the a into the $\mathcal{U}$ leads to a g^2 violation of Gauss's law. Therefore we must restore Gauss's law. This is done with the relaxation algorithm described in [191]. The main idea is to update the electric fields as follows

$$E^{Ia}(x) \to E^{Ia}(x) + \gamma \left(U(x) C(x + \hat{I}) U^\dagger(x) - C(x) \right) , \tag{9.70}$$

where we denote

$$C(x) = D_I^B E^I . \tag{9.71}$$

The parameter γ can be adjusted to speed up the convergence, while preserving stability.

9.10 Renormalization

As explained in the section 7.2, the energy-momentum tensor contains up to quartic terms in the ultraviolet cutoff. Since we are on an asymmetric lattice, there are two cutoffs, that can be deduced from (9.53)

$$k_{\max} = \frac{\sqrt{8}}{a_T} , \qquad\qquad k_{\max}^z \sim \frac{\nu_{\max}}{\tau} = \frac{2}{a_L \tau} , \tag{9.72}$$

respectively the transverse and the longitudinal cutoffs. The τ factor in the second longitudinal cutoff can be understood on dimensional grounds, since $\tau k_z \sim \nu$. The divergent part of $T^{\mu\nu}$ can be written as

$$T_{\mathrm{div}}^{\mu\nu} = c_0^{\mu\nu} \sum_{m=0}^{4} k_{\max}^{4-m} \left(\frac{\nu_{\max}}{\tau} \right)^m + c_2^{\mu\nu}(Q_s) \sum_{m=0}^{2} k_{\max}^{2-m} \left(\frac{\nu_{\max}}{\tau} \right)^m + \log . \tag{9.73}$$

As we have seen in the chapter 7, the CSA is non-renormalizable due to spurious terms that are linear in the cutoff. Therefore, there is no point in trying to remove the log terms of (9.73). Nevertheless, we should still be able to subtract the $c_{0,2}$ terms. The first one is easy, since $c_0^{\mu\nu}$ cannot depend on Q_s (the dimension 4 of $T^{\mu\nu}$ is completely given by the cutoffs). As explained in the section 7.2, we should perform two CSA simulations: one with the background field (9.43)-(9.45) that gives a non-zero Q_s and one for the vacuum. Subtracting the result of the second simulation from the first one the $c_0^{\mu\nu}$ term and nothing else since $c_2^{\mu\nu}$ vanishes if $Q_s = 0$. The second term $c_2^{\mu\nu}$ is quadratic in the cutoff as one can read from (9.73). It should not be there in the continuum limit since there are no local operators of dimension two that are gauge invariants. However, since $\mathcal{F}^{\mu\nu}$ is slightly non-local on the lattice (through the plaquette variables), such terms can exist in the discretized theory, provided that they vanish in the continuum limit.

So far we have not been able to derive analytically the precise form of the $c_2^{\mu\nu}$ coefficient, but general arguments can constrain its form. Firstly, simple kinetic arguments similar to those presented in the section 6.6.3 lead to

$$c_2^{\perp\perp} \sim k_{\max}^2 \sim \tau^0 \qquad\qquad c_2^{\eta\eta} \sim c_2^{\tau\tau} \sim \frac{\nu_{\max}^2}{\tau^2} \sim \tau^{-2} . \tag{9.74}$$

Therefore, new divergences proportional to τ^{-2} can arise in ϵ and P_L but not in P_T. This is confirmed numerically in figure 9.3.
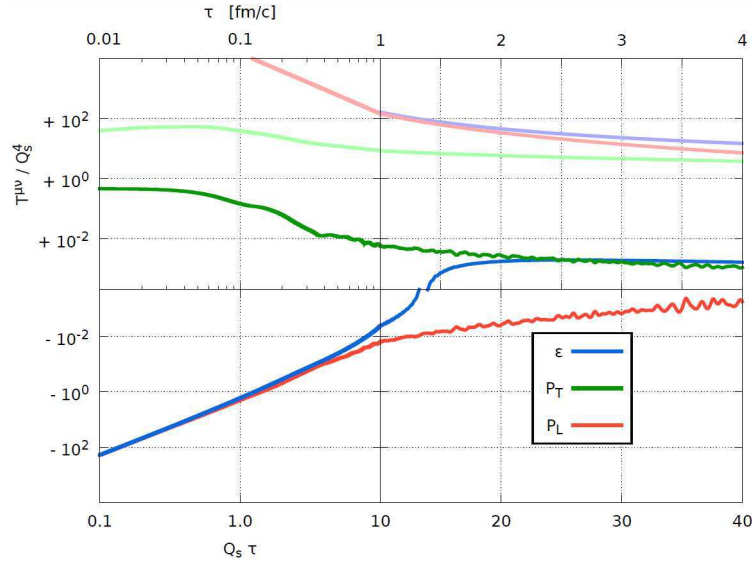
Figure 9.3: Divergences in ϵ, P_L and P_T. The three lines on top are before the vacuum subtraction. The three lines on the bottom are after the vacuum subtraction and before subtracting the additional $c_2^{\eta\eta}$ term in P_L and ϵ. As one can see, P_T is finite when $\tau \to 0$, but P_L and ϵ behave as τ^{-2}.

Since we must have $\epsilon = 2P_T + P_L$ in Yang-Mills theory at this order, we have

$$c_2^{\eta\eta} = c_2^{\tau\tau} .\tag{9.75}$$

In addition, since this divergent term should also satisfy Bjorken's law $\partial_\tau \epsilon + \frac{\epsilon + P_L}{\tau} = 0$, its time dependence can only be τ^{-2}. As already stated we are at the moment unable to analytically compute the coefficient $c_2^{\tau\tau}$, and we have fitted it in order to obtain finite ϵ, P_L when $\tau \to 0^+$. This can be seen in the figures 9.5 and 9.6. Further justification for this subtraction is the fact that the leading order result is recovered when $\tau \to 0^+$, as it should be since it takes time for the instabilities to deviate the system from its LO behavior.

9.11   Numerical results: isotropization, anomalous viscosity

The ingredients of our numerical simulation are summarized in the next plot 9.4.
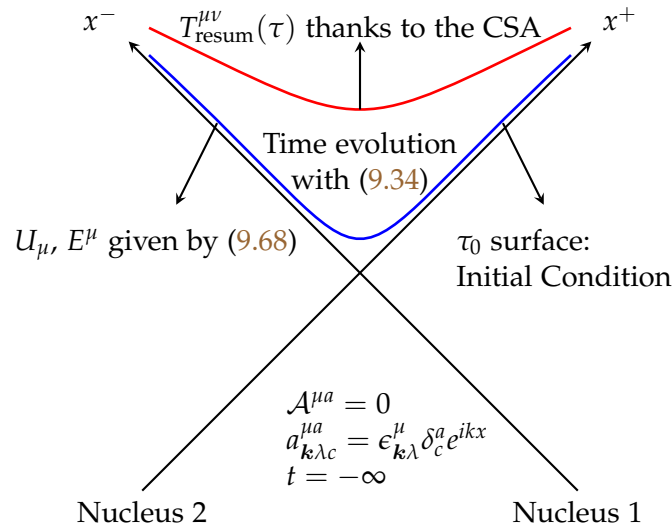
Figure 9.4: Schematic picture of what is done in the gauge case.

We have used this procedure on a $64 \times 64 \times 128$ lattice [14]. This is arguably a small lattice size [15], but this is because the initial condition algorithm depicted in sections 9.7-9.8 scales poorly with the transverse lattice size (like L^4). But as explained in the chapter 7, since the CSA is non-renormalizable, we do expect the CSA results to depend on the cutoff anyway after some time. Ensuring that the cutoff is in the range advocated in (7.50) should be enough [16]. The result for $g = 0.1$ is presented in the figure 9.5.
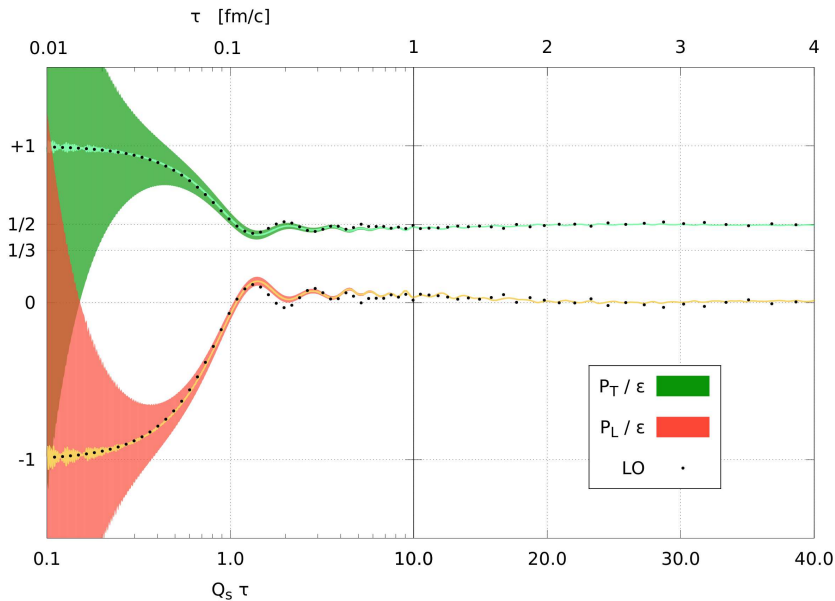
Figure 9.5: Pressure to energy density ratios for $g = 0.1$. 200 initial conditions were used in the Monte-Carlo average.

On this plot the ratios $\frac{P_T}{\epsilon}$ (in green) and $\frac{P_L}{\epsilon}$ (in red) are shown, as well as for the pure LO result with initial condition of equations given by (9.43)-(9.45) (black dots). Several important

---

14. Recall the figure 9.1. N has been chosen larger than L to cope with the longitudinal expansion of the system, as explained in the section 6.1.

15. To be compared for instance with the sizes of [37, 38]

16. In the gauge theory the prefactor is not known. The largest coupling constant we have used is $g = 0.5$.

conclusions can be drawn from the figure 9.5. Firstly, the purely classical result and the resummed one are almost the same for $g = 0.1$, meaning that at the latest stages considered here the pressure anisotropy in the system is still large since $P_L \sim 0$. One can fit ϵ by a power of τ and the free streaming behavior τ^{-1} is found to work quite well. Presumably, the Weibel instabilities mentioned in the section 3.9 did not develop on the time scales studied here for such a tiny value of the coupling constant [17]. Concerning the time scale, the bottom one is expressed in units of Q_s^{-1}, while the upper one is a more physical time scale corresponding to a value of $Q_s = 2GeV$, the one that is presumably reached at the LHC. To conclude on this plot, let us discuss the statistical error, shown as a red band for $\frac{P_L}{\epsilon}$ and a green one for $\frac{P_T}{\epsilon}$. As one can see, it is quite big at early time. One can understand this as follows: the physical contribution behaves as $\frac{Q_s^4}{g^2}$ while as explained in the previous section we have to subtract terms that behave as $\left(\frac{\nu_{max}}{\tau}\right)^2$. Therefore we are subtracting two large numbers when $\tau \rightarrow 0^+$, compared to the physical result $\sim \frac{Q_s^4}{g^2}$. We therefore need many initial conditions in the Monte-Carlo in order to reduce the statistical error. The next plot 9.6 was obtained for a larger coupling $g = 0.5$, , however still to small in comparison with the realistic value $g = 2$ reached at the LHC.
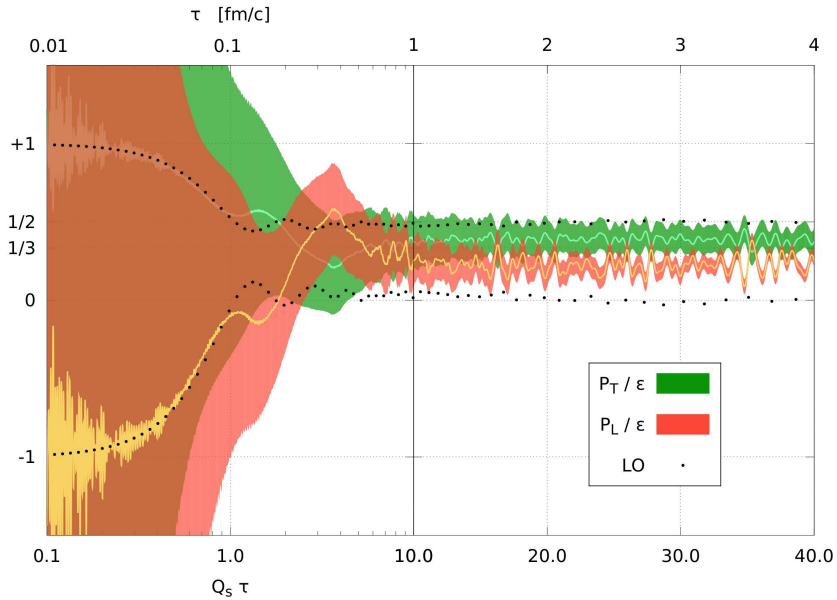
Figure 9.6: Pressure to energy density ratios for $g = 0.5$. 2000 initial conditions were used in the Monte-Carlo average.

Here, one observes drastic qualitative change when compared to the figure 9.5. After a transient regime of the order of $0.1 fm/c$ where the resummed $T^{\mu\nu}$ follows the LO one (black dots), it starts to significantly deviate. At around $1 fm/c$, the pressure anisotropy seems to reach a constant value, but this time $P_L \neq 0$ anymore. One can measure a fixed $1 - \frac{P_L}{P_T} \sim 30 - 40\%$ anisotropy in the system after $\sim 1 fm/c$. While this is still a significant anisotropy, it is much easier to accommodate within hydrodynamics than $P_L \approx 0$. In addition, one may conjecture that increasing the coupling would speed up the Weibel instabilities and increase their effect, leading to a smaller anisotropy.

As a further evidence that our system starts to behave as a fluid, we can compute the dimensionless viscosity over entropy ratio for the $g = 0.5$ simulation with the method advocated

---

17. Indeed, since $\alpha_s = \frac{g^2}{4\pi}$ it corresponds to $\alpha_s \sim 8.10^{-4}$, to be compared with the ~ 0.3 value reached at the LHC.

in the section 6.7.2.2. After $\tau \sim 1 fm/c$ we find that

$$\left. \frac{\eta}{s} \right|_{\text{CSA}} \lesssim 1 \, . \tag{9.76}$$

For $g = 0.5$, this can be compared to the LO perturbative result of [103]

$$\left. \frac{\eta}{s} \right|_{\text{LO,pert}} \sim 300 \, . \tag{9.77}$$

Therefore, it seems that instabilities, properly resummed by including quantum fluctuations, may be an alternative to the strong coupling scenarios that also lead to a small $\frac{\eta}{s}$.

To conclude this section, we also observe that the statistical error is much larger for $g = 0.5$ simulation at short times when compared to the $g = 0.1$. This is one of the reason that prevents us from taking $g = 2$, as the statistical error would be to important even with 2000 initial configurations. The other reason has to do with a phenomenon called thermalization of the vacuum fluctuations [151], that induces an unphysical feedback of the hard modes on the soft modes, that one wants to resolve properly since there are the modes subject to the Weibel instabilities [32, 51–54]. Thermalization of the vacuum fluctuations happens too fast for $g = 2$, voiding too rapidly the validity of the CSA.

9.12 Summary

- As for the scalar models, the CSA applied in the CGC framework shows hints of hydrodynamization.
- For already small values of the coupling ($\alpha_s = 0.02$), the Weibel instabilities can counterbalance the dilution of the system in the longitudinal direction, leading to a fixed anisotropy $\frac{P_L}{P_T} \approx 0.6$. This isotropization happens on time scales $\lesssim 1 \, fm/c$, compatible with the early onset of hydrodynamics.
- For $\alpha_s = 0.02$, the system has an anomalously small $\frac{\eta}{s} \lesssim 1$ ratio compared to the LO perturbative result (see [103] that gives $\frac{\eta}{s} \sim 300$).

Chapter 10

⚛ Conclusion ⚛

n this thesis, we have studied the approach to equilibrium in both scalar and gauge theories thanks to the the classical statistical method (CSA), that amounts to classically evolve a system whose initial condition is a coherent state centered around a classical value (the variance being given by a one loop calculation).

In the chapters 5 and 6, we focused our attention on scalar models. In the chapter 5, we considered a system with a fixed volume, and we showed good evidence for the onset of a hydrodynamical behavior in the system: the formation of an Equation of State (EOS) as well as a (classical) thermal equilibration of the occupation number. This can be understood as the decoherence of the initial coherent state when evolved with the classical yet fully non linear Klein-Gordon equation. In the chapter 6, we studied a one-dimensional expanding geometry, that mimics more realistically the expansion of the Quark Gluon Plasma along the collision axis. Here also we saw signs of a hydrodynamical behavior : the formation of an EOS and the isotropization of the pressure tensor (this expanding system is anisotropic at the beginning).

The chapter 7 was devoted to a discussion of the non-renormalizability of the CSA, due to the violation of the Weinberg's theorem. Even if the power counting is the same in the CSA and in the full quantum theory, the quantum vertex that has been discarded in the CSA appears to be essential for the cancellations of some ultraviolet divergences. This put some constraints on how the ultraviolet cutoff should be chosen in the CSA.

The chapters 8 and 9 finally tackled with the problem of the approach to equilibrium of the QGP, by applying the CSA in the Color Glass Condensate framework. After having derived the spectrum of fluctuations that enters in the initial condition of the CSA, we have performed the first realistic numerical simulations that go beyond the Leading Order CGC computations. There again we found evidences for an early onset of hydrodynamical behavior, even at relatively weak coupling ($\alpha_s = 2\,10^{-2}$): rapid isotropization of the pressure tensor, that leads to a fixed anisotropy, in addition to a very small viscosity over entropy ratio $\frac{\eta}{s} \lesssim 1$.

A lot remains to be done until a final proof for the complete thermalization of the QGP can be given. Firstly, it would be interesting to study how the momentum distribution equilibrates. This is however rendered difficult by the fact that there is no gauge invariant definition of the occupation number in QCD. Secondly, since the validity of the CSA stops when quantum corrections coming from the time evolution qualitatively alter the physics, it would be important to be able to include them in order to obtain full quantum thermalization – in contrast to the classical thermalization obtained in the chapter 5. Finally, the inclusion of the quarks may be important in order to give more quantitative statements. Indeed, even if the occupation number of the quarks never reaches non perturbatively large values due to the Pauli exclusion principle, they may affect the thermalization time scale [40].

Bibliography

[1] **J. Adams et al.** « Experimental and theoretical challenges in the search for the quark gluon plasma: The STAR Collaboration's critical assessment of the evidence from RHIC collisions ». In: *Nucl.Phys.* A757 (2005), pp. 102–183. DOI: 10.1016/j.nuclphysa.2005.03.085. arXiv:nucl-ex/0501009 [nucl-ex].

[2] **K. Adcox et al.** « Formation of dense partonic matter in relativistic nucleus-nucleus collisions at RHIC: Experimental evaluation by the PHENIX collaboration ». In: *Nucl.Phys.* A757 (2005), pp. 184–283. DOI: 10.1016/j.nuclphysa.2005.03.086. arXiv:nucl-ex/0410003 [nucl-ex].

[3] **I. Arsene et al.** « Quark gluon plasma and color glass condensate at RHIC? The Perspective from the BRAHMS experiment ». In: *Nucl.Phys.* A757 (2005), pp. 1–27. DOI: 10.1016/j.nuclphysa.2005.02.130. arXiv:nucl-ex/0410020 [nucl-ex].

[4] **B.B. Back et al.** « The PHOBOS perspective on discoveries at RHIC ». In: *Nucl.Phys.* A757 (2005), pp. 28–101. DOI: 10.1016/j.nuclphysa.2005.03.084. arXiv:nucl-ex/0410022 [nucl-ex].

[5] **K. Aamodt et al.** « The ALICE experiment at the CERN LHC ». In: *JINST* 3 (2008), S08002. DOI: 10.1088/1748-0221/3/08/S08002.

[6] **K. Aamodt et al.** « Elliptic flow of charged particles in Pb-Pb collisions at 2.76 TeV ». In: *Phys.Rev.Lett.* 105 (2010), p. 252302. DOI: 10.1103/PhysRevLett.105.252302. arXiv:1011.3914 [nucl-ex].

[7] **K. Aamodt et al.** « Suppression of Charged Particle Production at Large Transverse Momentum in Central Pb–Pb Collisions at $\sqrt{s_{NN}}$ = 2.76 TeV ». In: *Phys.Lett.* B696 (2011), pp. 30–39. DOI: 10.1016/j.physletb.2010.12.020. arXiv:1012.1004 [nucl-ex].

[8] **G. Aad et al.** « Observation of a Centrality-Dependent Dijet Asymmetry in Lead-Lead Collisions at $\sqrt{s_{NN}}$ = 2.77 TeV with the ATLAS Detector at the LHC ». In: *Phys.Rev.Lett.* 105 (2010), p. 252303. DOI: 10.1103/PhysRevLett.105.252303. arXiv:1011.6182 [hep-ex].

[9] **V. Khachatryan et al.** « Observation of Long-Range Near-Side Angular Correlations in Proton-Proton Collisions at the LHC ». In: *JHEP* 1009 (2010), p. 091. DOI: 10.1007/JHEP09(2010)091. arXiv:1009.4122 [hep-ex].

[10] **S. Chatrchyan et al.** « Observation and studies of jet quenching in PbPb collisions at nucleon-nucleon center-of-mass energy = 2.76 TeV ». In: *Phys.Rev.* C84 (2011), p. 024906. DOI: 10.1103/PhysRevC.84.024906. arXiv:1102.1957 [nucl-ex].

[11] **G. Aad et al.** « Jet energy measurement with the ATLAS detector in proton-proton collisions at $\sqrt{s}$ = 7 TeV ». In: *Eur.Phys.J.* C73 (2013), p. 2304. DOI: 10.1140/epjc/s10052-013-2304-2. arXiv:1112.6426 [hep-ex].

[12] **P. Romatschke and U. Romatschke**. « Viscosity Information from Relativistic Nuclear Collisions: How Perfect is the Fluid Observed at RHIC? » In: *Phys.Rev.Lett.* 99 (2007), p. 172301. DOI: 10.1103/PhysRevLett.99.172301. arXiv:0706.1522 [nucl-th].

[13] **M. Luzum and P. Romatschke**. « Conformal Relativistic Viscous Hydrodynamics: Applications to RHIC results at s(NN)**(1/2) = 200-GeV ». In: *Phys.Rev.* C78 (2008), p. 034915. DOI: 10.1103/PhysRevC.78.034915,10.1103/PhysRevC.79.039903. arXiv:0804.4015 [nucl-th].

[14] **H. Song and U.W. Heinz**. « Viscous hydrodynamics with bulk viscosity: Uncertainties from relaxation time and initial conditions ». In: *Nucl.Phys.* A830 (2009), pp. 467C–470C. DOI: 10.1016/j.nuclphysa.2009.10.041. arXiv:0907.2262 [nucl-th].

[15] **K. Dusling, G.D. Moore, and D. Teaney**. « Radiative energy loss and v(2) spectra for viscous hydrodynamics ». In: *Phys.Rev.* C81 (2010), p. 034907. DOI: 10.1103/PhysRevC.81.034907. arXiv:0909.0754 [nucl-th].

[16] **F.G. Gardim et al.** « Mapping the hydrodynamic response to the initial geometry in heavy-ion collisions ». In: *Phys.Rev.* C85 (2012), p. 024908. DOI: 10.1103/PhysRevC.85.024908. arXiv:1111.6538 [nucl-th].

[17] **E. Retinskaya, M. Luzum, and J.Y. Ollitrault**. « Directed flow at midrapidity in $\sqrt{s_{NN}} = 2.76$ TeV Pb+Pb collisions ». In: *Phys.Rev.Lett.* 108 (2012), p. 252302. DOI: 10.1103/PhysRevLett.108.252302. arXiv:1203.0931 [nucl-th].

[18] **H. Niemi et al.** « Event-by-event distributions of azimuthal asymmetries in ultrarelativistic heavy-ion collisions ». In: *Phys.Rev.* C87 (2013), p. 054901. DOI: 10.1103/PhysRevC.87.054901. arXiv:1212.1008 [nucl-th].

[19] **B. Schenke, P. Tribedy, and R. Venugopalan**. « Fluctuating Glasma initial conditions and flow in heavy ion collisions ». In: *Phys.Rev.Lett.* 108 (2012), p. 252301. DOI: 10.1103/PhysRevLett.108.252301. arXiv:1202.6646 [nucl-th].

[20] **B. Schenke, P. Tribedy, and R. Venugopalan**. « Event-by-event gluon multiplicity, energy density, and eccentricities in ultrarelativistic heavy-ion collisions ». In: *Phys.Rev.* C86 (2012), p. 034908. DOI: 10.1103/PhysRevC.86.034908. arXiv:1206.6805 [hep-ph].

[21] **C. Gale et al.** « Event-by-event anisotropic flow in heavy-ion collisions from combined Yang-Mills and viscous fluid dynamics ». In: *Phys.Rev.Lett.* 110 (2013), p. 012302. DOI: 10.1103/PhysRevLett.110.012302. arXiv:1209.6330 [nucl-th].

[22] **A. Krasnitz and R. Venugopalan**. « Nonperturbative computation of gluon minijet production in nuclear collisions at very high-energies ». In: *Nucl.Phys.* B557 (1999), p. 237. DOI: 10.1016/S0550-3213(99)00366-1. arXiv:hep-ph/9809433 [hep-ph].

[23] **T. Lappi and L.D. McLerran**. « Some features of the glasma ». In: *Nucl.Phys.* A772 (2006), pp. 200–212. DOI: 10.1016/j.nuclphysa.2006.04.001. arXiv:hep-ph/0602189 [hep-ph].

[24] **K. Fukushima and F. Gelis**. « The evolving Glasma ». In: *Nucl.Phys.* A874 (2012), pp. 108–129. DOI: 10.1016/j.nuclphysa.2011.11.003. arXiv:1106.1396 [hep-ph].

[25] **A. Rebhan, M. Strickland, and M. Attem**. « Instabilities of an anisotropically expanding non-Abelian plasma: 1D+3V discretized hard-loop simulations ». In: *Phys.Rev.* D78 (2008), p. 045023. DOI: 10.1103/PhysRevD.78.045023. arXiv:0802.1714 [hep-ph].

[26] **J.P. Blaizot et al.** « Bose–Einstein Condensation and Thermalization of the Quark Gluon Plasma ». In: *Nucl.Phys.* A873 (2012), pp. 68–80. DOI: 10.1016/j.nuclphysa.2011.10.005. arXiv:1107.5296 [hep-ph].

[27] **A. Kurkela and G.D. Moore**. « Thermalization in Weakly Coupled Nonabelian Plasmas ». In: *JHEP* 1112 (2011), p. 044. DOI: 10.1007/JHEP12(2011)044. arXiv:1107.5050 [hep-ph].

[28] **A. Kurkela and G.D. Moore**. « Bjorken Flow, Plasma Instabilities, and Thermalization ». In: *JHEP* 1111 (2011), p. 120. DOI: 10.1007/JHEP11(2011)120. arXiv:1108.4684 [hep-ph].

[29] **M.P. Heller, R.A. Janik, and P. Witaszczyk**. « The characteristics of thermalization of boost-invariant plasma from holography ». In: *Phys.Rev.Lett.* 108 (2012), p. 201602. DOI: 10.1103/PhysRevLett.108.201602. arXiv:1103.3452 [hep-th].

[30] **A. Kurkela and G.D. Moore**. « UV Cascade in Classical Yang-Mills Theory ». In: *Phys.Rev.* D86 (2012), p. 056008. DOI: 10.1103/PhysRevD.86.056008. arXiv:1207.1663 [hep-ph].

[31] **J. Berges and S. Schlichting**. « The non-linear Glasma ». In: *Phys.Rev.* D87 (2013), p. 014026. DOI: 10.1103/PhysRevD.87.014026. arXiv:1209.0817 [hep-ph].

[32] **M. Attems, A. Rebhan, and M. Strickland**. « Instabilities of an anisotropically expanding non-Abelian plasma: 3D+3V discretized hard-loop simulations ». In: (2012). DOI: 10.1103/PhysRevD.87.025010. arXiv:1207.5795 [hep-ph].

[33] **J.P Blaizot, J. Liao, and L.D. McLerran**. « Gluon Transport Equation in the Small Angle Approximation and the Onset of Bose-Einstein Condensation ». In: *Nucl.Phys.* A920 (2013), pp. 58–77. DOI: 10.1016/j.nuclphysa.2013.10.010. arXiv:1305.2119 [hep-ph].

[34] **J. Casalderrey-Solana et al.** « From full stopping to transparency in a holographic model of heavy ion collisions ». In: *Phys. Rev. Lett. 111*, 181601 (2013), p. 181601. DOI: 10.1103/PhysRevLett.111.181601. arXiv:1305.4919 [hep-th].

[35] **K. Fukushima**. « Turbulent pattern formation and diffusion in the early-time dynamics in the relativistic heavy-ion collision ». In: *Phys.Rev.* C89 (2014), p. 024907. DOI: 10.1103/PhysRevC.89.024907. arXiv:1307.1046 [hep-ph].

[36] **S. Floerchinger and C. Wetterich**. « Isotropization from Color Field Condensate in heavy ion collisions ». In: *JHEP* 1403 (2014), p. 121. DOI: 10.1007/JHEP03(2014)121. arXiv:1311.5389 [hep-ph].

[37] **J. Berges et al.** « Turbulent thermalization process in heavy-ion collisions at ultrarelativistic energies ». In: (2013). arXiv:1303.5650 [hep-ph].

[38] **J. Berges et al.** « Universal attractor in a highly occupied non-Abelian plasma ». In: (2013). arXiv:1311.3005 [hep-ph].

[39] **R. Ryblewski and W. Florkowski**. « Equilibration of anisotropic quark-gluon plasma produced by decays of color flux tubes ». In: *Phys.Rev.* D88 (2013), p. 034028. DOI: 10.1103/PhysRevD.88.034028. arXiv:1307.0356 [hep-ph].

[40] **J.P. Blaizot, B. Wu, and L. Yan**. « Quark production, Bose-Einstein condensates and thermalization of the quark-gluon plasma ». In: (2014). arXiv:1402.5049 [hep-ph].

[41] **M.C. Abraao York et al.** « UV Cascade in Classical Yang-Mills via Kinetic Theory ». In: (2014). arXiv:1401.3751 [hep-ph].

[42] **R. Baier et al.** « 'Bottom up' thermalization in heavy ion collisions ». In: *Phys.Lett.* B502 (2001), pp. 51–58. DOI: 10.1016/S0370-2693(01)00191-5. arXiv:hep-ph/0009237 [hep-ph].

[43] **L.D. McLerran and R. Venugopalan**. « Gluon distribution functions for very large nuclei at small transverse momentum ». In: *Phys.Rev.* D49 (1994), pp. 3352–3355. DOI: 10.1103/PhysRevD.49.3352. arXiv:hep-ph/9311205 [hep-ph].

[44] **L.D. McLerran and R. Venugopalan**. « Computing quark and gluon distribution functions for very large nuclei ». In: *Phys.Rev.* D49 (1994), pp. 2233–2241. DOI: 10.1103/PhysRevD.49.2233. arXiv:hep-ph/9309289 [hep-ph].

[45] **L.V. Gribov, E.M. Levin, and M.G. Ryskin**. « Semihard Processes in QCD ». In: *Phys.Rept.* 100 (1983), pp. 1–150. DOI: 10.1016/0370-1573(83)90022-4.

[46] **A.H. Mueller and J. Qiu**. « Gluon Recombination and Shadowing at Small Values of x ». In: *Nucl.Phys.* B268 (1986), p. 427. DOI: 10.1016/0550-3213(86)90164-1.

[47] **A. Kovner, L.D. McLerran, and H. Weigert**. « Gluon production from nonAbelian Weizsacker-Williams fields in nucleus-nucleus collisions ». In: *Phys.Rev.* D52 (1995), pp. 6231–6237. DOI: 10.1103/PhysRevD.52.6231. arXiv:hep-ph/9502289 [hep-ph].

[48] **A. Kovner, L.D. McLerran, and H. Weigert**. « Gluon production at high transverse momentum in the McLerran-Venugopalan model of nuclear structure functions ». In: *Phys.Rev.* D52 (1995), pp. 3809–3814. DOI: 10.1103/PhysRevD.52.3809. arXiv:hep-ph/9505320 [hep-ph].

[49] **A. Krasnitz and R. Venugopalan**. « The Initial energy density of gluons produced in very high-energy nuclear collisions ». In: *Phys.Rev.Lett.* 84 (2000), pp. 4309–4312. DOI: 10.1103/PhysRevLett.84.4309. arXiv:hep-ph/9909203 [hep-ph].

[50] **J.P. Blaizot and Y. Mehtar-Tani**. « The Classical field created in early stages of high energy nucleus-nucleus collisions ». In: *Nucl.Phys.* A818 (2009), pp. 97–119. DOI: 10.1016/j.nuclphysa.2008.11.010. arXiv:0806.1422 [hep-ph].

[51] **S. Mrowczynski**. « Stream Instabilities of the Quark - Gluon Plasma ». In: *Phys.Lett.* B214 (1988), p. 587. DOI: 10.1016/0370-2693(88)90124-4, 10.1016/j.physletb.2007.09.039.

[52] **S. Mrowczynski**. « Plasma instability at the initial stage of ultrarelativistic heavy ion collisions ». In: *Phys.Lett.* B314 (1993), pp. 118–121. DOI: 10.1016/0370-2693(93)91330-P.

[53] **S. Mrowczynski**. « Color collective effects at the early stage of ultrarelativistic heavy ion collisions ». In: (1993).

[54] **P. Arnold, J. Lenaghan, and G.D. Moore**. « QCD plasma instabilities and bottom up thermalization ». In: *JHEP* 0308 (2003), p. 002. DOI: 10.1088/1126-6708/2003/08/002. arXiv:hep-ph/0307325 [hep-ph].

[55] **P. Romatschke and R. Venugopalan**. « A Weibel instability in the melting color glass condensate ». In: *Eur.Phys.J.* A29 (2006), pp. 71–75. DOI: 10.1140/epja/i2005-10304-y. arXiv:hep-ph/0510292 [hep-ph].

[56] **P. Romatschke and R. Venugopalan**. « Collective non-Abelian instabilities in a melting color glass condensate ». In: *Phys.Rev.Lett.* 96 (2006), p. 062302. DOI: 10.1103/PhysRevLett.96.062302. arXiv:hep-ph/0510121 [hep-ph].

[57] **P. Romatschke and R. Venugopalan**. « The Unstable Glasma ». In: *Phys.Rev.* D74 (2006), p. 045011. DOI: 10.1103/PhysRevD.74.045011. arXiv:hep-ph/0605045 [hep-ph].

[58] **F. Gelis, T. Lappi, and R. Venugopalan**. « High energy factorization in nucleus-nucleus collisions ». In: *Phys.Rev.* D78 (2008), p. 054019. DOI: 10.1103/PhysRevD.78.054019. arXiv:0804.2630 [hep-ph].

[59] **G. Aarts and J. Smit**. « Finiteness of hot classical scalar field theory and the plasmon damping rate ». In: *Phys.Lett.* B393 (1997), pp. 395–402. DOI: 10.1016/S0370-2693(96)01624-3. arXiv:hep-ph/9610415 [hep-ph].

[60] **W. Buchmuller and A. Jakovac**. « Classical statistical mechanics and Landau damping ». In: *Phys.Lett.* B407 (1997), pp. 39–44. DOI: 10.1016/S0370-2693(97)00746-6. arXiv:hep-ph/9705452 [hep-ph].

[61] **G.F. Bonini and C. Wetterich**. « Time evolution of correlation functions and thermalization ». In: *Phys.Rev.* D60 (1999), p. 105026. DOI: 10.1103/PhysRevD.60.105026. arXiv:hep-ph/9907533 [hep-ph].

[62] **G. Aarts, Bonini, and Wetterich**. « On Thermalization in classical scalar field theory ». In: *Nucl.Phys.* B587 (2000), pp. 403–418. DOI: 10.1016/S0550-3213(00)00447-8. arXiv:hep-ph/0003262 [hep-ph].

[63] **G. Aarts, G.F. Bonini, and C. Wetterich**. « Exact and truncated dynamics in nonequilibrium field theory ». In: *Phys.Rev.* D63 (2001), p. 025012. DOI: 10.1103/PhysRevD.63.025012. arXiv:hep-ph/0007357 [hep-ph].

[64] **F. Cooper, A. Khare, and H. Rose**. « Classical limit of time dependent quantum field theory: A Schwinger-Dyson approach ». In: *Phys.Lett.* B515 (2001), pp. 463–469. DOI: 10.1016/S0370-2693(01)00872-3. arXiv:hep-ph/0106113 [hep-ph].

[65] **J. Berges**. « Introduction to nonequilibrium quantum field theory ». In: *AIP Conf.Proc.* 739 (2005), pp. 3–62. DOI: 10.1063/1.1843591. arXiv:hep-ph/0409233 [hep-ph].

[66] **K. Dusling et al.** « Role of quantum fluctuations in a system with strong fields: Onset of hydrodynamical flow ». In: *Nucl.Phys.* A850 (2011), pp. 69–109. DOI: 10.1016/j.nuclphysa.2010.11.009. arXiv:1009.4363 [hep-ph].

[67] **T. Epelbaum and F. Gelis**. « Role of quantum fluctuations in a system with strong fields: Spectral properties and Thermalization ». In: *Nucl.Phys.* A872 (2011), pp. 210–244. DOI: 10.1016/j.nuclphysa.2011.09.019. arXiv:1107.0668 [hep-ph].

[68] **K. Dusling et al.** « Instability induced pressure isotropization in a longitudinally expanding system ». In: *Phys.Rev.* D86 (2012), p. 085040. DOI: 10.1103/PhysRevD.86.085040. arXiv:1206.3336 [hep-ph].

[69] **T. Epelbaum, F. Gelis, and B. Wu**. « Non-renormalizability of the classical statistical approximation ». In: (2014). arXiv:1402.0115 [hep-ph].

[70] **T. Epelbaum and F. Gelis**. « Fluctuations of the initial color fields in high energy heavy ion collisions ». In: *Phys.Rev.* D88 (2013), p. 085015. DOI: 10.1103/PhysRevD.88.085015. arXiv:1307.1765.

[71] **T. Epelbaum and F. Gelis**. « Pressure isotropization in high energy heavy ion collisions ». In: *Phys.Rev.Lett.* 111 (2013), p. 232301. DOI: 10.1103/PhysRevLett.111.232301. arXiv:1307.2214 [hep-ph].

[72] **K.G. Wilson**. « Confinement of Quarks ». In: *Phys.Rev.* D10 (1974), pp. 2445–2459. DOI: 10.1103/PhysRevD.10.2445.

[73] **D.J. Gross and F. Wilczek**. « Ultraviolet Behavior of Nonabelian Gauge Theories ». In: *Phys.Rev.Lett.* 30 (1973), pp. 1343–1346. DOI: 10.1103/PhysRevLett.30.1343.

[74] **D.J. Gross and F. Wilczek**. « Asymptotically Free Gauge Theories. 1. » In: *Phys.Rev.* D8 (1973), pp. 3633–3652. DOI: 10.1103/PhysRevD.8.3633.

[75] **D.J. Gross and F. Wilczek**. « Asymptotically Free Gauge Theories. 2. » In: *Phys.Rev.* D9 (1974), pp. 980–993. DOI: 10.1103/PhysRevD.9.980.

[76] **H.D. Politzer**. « Asymptotic Freedom: An Approach to Strong Interactions ». In: *Phys.Rept.* 14 (1974), pp. 129–180. DOI: 10.1016/0370-1573(74)90014-3.

[77] **S. Bethke**. « Experimental tests of asymptotic freedom ». In: *Prog.Part.Nucl.Phys.* 58 (2007), pp. 351–386. DOI: 10.1016/j.ppnp.2006.06.001. arXiv:hep-ex/0606035 [hep-ex].

[78] **G. Aad et al.** « Observation of a new particle in the search for the Standard Model Higgs boson with the ATLAS detector at the LHC ». In: *Phys.Lett.* B716 (2012), pp. 1–29. DOI: 10.1016/j.physletb.2012.08.020. arXiv:1207.7214 [hep-ex].

[79] **S. Chatrchyan et al.** « Observation of a new boson at a mass of 125 GeV with the CMS experiment at the LHC ». In: *Phys.Lett.* B716 (2012), pp. 30–61. DOI: 10.1016/j.physletb.2012.08.021. arXiv:1207.7235 [hep-ex].

[80] **F. Englert and R. Brout**. « Broken Symmetry and the Mass of Gauge Vector Mesons ». In: *Phys.Rev.Lett.* 13 (1964), pp. 321–323. DOI: 10.1103/PhysRevLett.13.321.

[81] **P. Higgs**. « Broken Symmetries and the Masses of Gauge Bosons ». In: *Phys.Rev.Lett.* 13 (1964), pp. 508–509. DOI: 10.1103/PhysRevLett.13.508.

[82] **F.D. Aaron et al.** « Combined Measurement and QCD Analysis of the Inclusive e+- p Scattering Cross Sections at HERA ». In: *JHEP* 1001 (2010), p. 109. DOI: 10.1007/JHEP01(2010)109. arXiv:0911.0884 [hep-ex].

[83] **V.N. Gribov and L.N. Lipatov**. « Deep inelastic electron scattering in perturbation theory ». In: *Phys.Lett.* B37 (1971), pp. 78–80. DOI: 10.1016/0370-2693(71)90576-4.

[84] **V.N. Gribov and L.N. Lipatov**. « Deep inelastic e p scattering in perturbation theory ». In: *Sov.J.Nucl.Phys.* 15 (1972), pp. 438–450.

[85] **V.N. Gribov and L.N. Lipatov**. « e+ e- pair annihilation and deep inelastic e p scattering in perturbation theory ». In: *Sov.J.Nucl.Phys.* 15 (1972), pp. 675–684.

[86] **G. Altarelli, G. Parisi, and R. Petronzio**. « Transverse Momentum in Drell-Yan Processes ». In: *Phys.Lett.* B76 (1978), p. 351. DOI: 10.1016/0370-2693(78)90805-5.

[87] **J.D. Bjorken**. « Rapidity gaps and jets as a new physics signature in very high-energy hadron hadron collisions ». In: *Phys.Rev.* D47 (1993), pp. 101–113. DOI: 10.1103/PhysRevD.47.101.

[88] **R. Baier et al.** « Radiative energy loss of high-energy quarks and gluons in a finite volume quark - gluon plasma ». In: *Nucl.Phys.* B483 (1997), pp. 291–320. DOI: 10.1016/S0550-3213(96)00553-6. arXiv:hep-ph/9607355 [hep-ph].

[89] **R. Baier et al.** « Radiative energy loss and p(T) broadening of high-energy partons in nuclei ». In: *Nucl.Phys.* B484 (1997), pp. 265–282. DOI: 10.1016/S0550-3213(96)00581-0. arXiv:hep-ph/9608322 [hep-ph].

[90] **J. Casalderrey-Solana and C.A. Salgado**. « Introductory lectures on jet quenching in heavy ion collisions ». In: *Acta Phys.Polon.* B38 (2007), pp. 3731–3794. arXiv:0712.3443 [hep-ph].

[91] **Y. Mehtar-Tani, C.A. Salgado, and K. Tywoniuk**. « Anti-angular ordering of gluon radiation in QCD media ». In: *Phys.Rev.Lett.* 106 (2011), p. 122002. DOI: 10.1103/PhysRevLett.106.122002. arXiv:1009.2965 [hep-ph].

[92] **Y. Mehtar-Tani, C.A. Salgado, and K. Tywoniuk**. « Jets in QCD Media: From Color Coherence to Decoherence ». In: *Phys.Lett.* B707 (2012), pp. 156–159. DOI: 10.1016/j.physletb.2011.12.042. arXiv:1102.4317 [hep-ph].

[93] **J.P. Blaizot et al.** « Medium-induced gluon branching ». In: *JHEP* 1301 (2013), p. 143. DOI: 10.1007/JHEP01(2013)143. arXiv:1209.4585 [hep-ph].

[94] **J.P. Blaizot, E. Iancu, and Y. Mehtar-Tani**. « Medium-induced QCD cascade: democratic branching and wave turbulence ». In: *Phys.Rev.Lett.* 111 (2013). DOI: 10.1103/PhysRevLett.111.052001. arXiv:1301.6102 [hep-ph].

[95] **J.P. Blaizot et al.** « Probabilistic picture for medium-induced jet evolution ». In: (2013). arXiv:1311.5823 [hep-ph].

[96] **J.P. Blaizot and Y. Mehtar-Tani**. « Renormalization of the jet-quenching parameter ». In: (2014). arXiv:1403.2323 [hep-ph].

[97] **A.H. Guth**. « The Inflationary Universe: A Possible Solution to the Horizon and Flatness Problems ». In: *Phys.Rev.* D23 (1981), pp. 347–356. DOI: 10.1103/PhysRevD.23.347.

[98] **X.G. Huang and J. Liao**. « Glasma Evolution and Bose-Einstein Condensation with Elastic and Inelastic Collisions ». In: (2013). arXiv:1303.7214 [nucl-th].

[99] **A. Rebhan, P. Romatschke, and M. Strickland**. « Hard-loop dynamics of non-Abelian plasma instabilities ». In: *Phys.Rev.Lett.* 94 (2005), p. 102303. DOI: 10.1103/PhysRevLett.94.102303. arXiv:hep-ph/0412016 [hep-ph].

[100] **A. Rebhan, P. Romatschke, and M. Strickland**. « Dynamics of quark-gluon-plasma instabilities in discretized hard-loop approximation ». In: *JHEP* 0509 (2005), p. 041. DOI: 10.1088/1126-6708/2005/09/041. arXiv:hep-ph/0505261 [hep-ph].

[101] **J.P. Blaizot and E. Iancu**. « The Quark gluon plasma: Collective dynamics and hard thermal loops ». In: *Phys.Rept.* 359 (2002), pp. 355–528. DOI: 10.1016/S0370-1573(01)00061-8. arXiv:hep-ph/0101103 [hep-ph].

[102] **S. Jeon**. « Hydrodynamic transport coefficients in relativistic scalar field theory ». In: *Phys.Rev.* D52 (1995), pp. 3591–3642. DOI: 10.1103/PhysRevD.52.3591. arXiv:hep-ph/9409250 [hep-ph].

[103] **P.B. Arnold, G.D. Moore, and L.G. Yaffe**. « Transport coefficients in high temperature gauge theories. 1. Leading log results ». In: *JHEP* 0011 (2000), p. 001. DOI: 10.1088/1126-6708/2000/11/001. arXiv:hep-ph/0010177 [hep-ph].

[104] **P.B. Arnold, G.D. Moore, and L.G. Yaffe**. « Effective kinetic theory for high temperature gauge theories ». In: *JHEP* 0301 (2003), p. 030. DOI: 10.1088/1126-6708/2003/01/030. arXiv:hep-ph/0209353 [hep-ph].

[105] **P.B. Arnold, G.D. Moore, and L.G. Yaffe**. « Transport coefficients in high temperature gauge theories. 2. Beyond leading log ». In: *JHEP* 0305 (2003), p. 051. DOI: 10.1088/1126-6708/2003/05/051. arXiv:hep-ph/0302165 [hep-ph].

[106] **D. Teaney**. « Lecture notes on shear viscosity in heavy ion collisions ». In: *Prog.Part.Nucl.Phys.* 62 (2009), pp. 451–461. DOI: 10.1016/j.ppnp.2008.12.025.

[107] **J.Y. Ollitrault**. « Relativistic hydrodynamics for heavy-ion collisions ». In: *Eur.J.Phys.* 29 (2008), pp. 275–302. DOI: 10.1088/0143-0807/29/2/010. arXiv:0708.2433 [nucl-th].

[108] **P. Romatschke**. « New Developments in Relativistic Viscous Hydrodynamics ». In: *Int.J.Mod.Phys.* E19 (2010), pp. 1–53. DOI: 10.1142/S0218301310014613. arXiv:0902.3663 [hep-ph].

[109] **D. Teaney**. « Viscous Hydrodynamics and the Quark Gluon Plasma ». In: (2009). arXiv:0905.2433 [nucl-th].

[110] **W. Israel and J.M. Stewart**. « Transient relativistic thermodynamics and kinetic theory ». In: *Annals Phys.* 118 (1979), pp. 341–372. DOI: 10.1016/0003-4916(79)90130-1.

[111] **G.S. Denicol, T. Koide, and D.H. Rischke**. « Dissipative relativistic fluid dynamics: a new way to derive the equations of motion from kinetic theory ». In: *Phys.Rev.Lett.* 105 (2010), p. 162501. DOI: 10.1103/PhysRevLett.105.162501. arXiv:1004.5013 [nucl-th].

[112] **M. Luzum and H. Petersen**. « Initial State Fluctuations and Final State Correlations in Relativistic Heavy-Ion Collisions ». In: (2013). arXiv:1312.5503 [nucl-th].

[113] **J.Y. Ollitrault**. « Anisotropy as a signature of transverse collective flow ». In: *Phys.Rev.* D46 (1992), pp. 229–245. DOI: 10.1103/PhysRevD.46.229.

[114] **J.Y. Ollitrault**. « Phenomenology of the little bang ». In: *J.Phys.Conf.Ser.* 312 (2011), p. 012002. DOI: 10.1088/1742-6596/312/1/012002. arXiv:1008.3323 [nucl-th].

[115] **G. Policastro, D.T. Son, and A.O. Starinets**. « From AdS / CFT correspondence to hydrodynamics ». In: *JHEP* 0209 (2002), p. 043. arXiv:hep-th/0205052 [hep-th].

[116] **J.M. Maldacena**. « The Large N limit of superconformal field theories and supergravity ». In: *Adv.Theor.Math.Phys.* 2 (1998), pp. 231–252. arXiv:hep-th/9711200 [hep-th].

[117] **M. Martinez and M. Strickland**. « Dissipative Dynamics of Highly Anisotropic Systems ». In: *Nucl.Phys.* A848 (2010), pp. 183–197. DOI: 10.1016/j.nuclphysa.2010.08.011. arXiv:1007.0889 [nucl-th].

[118] **M. Martinez and M. Strickland**. « Non-boost-invariant anisotropic dynamics ». In: *Nucl.Phys.* A856 (2011), pp. 68–87. DOI: 10.1016/j.nuclphysa.2011.02.003. arXiv:1011.3056 [nucl-th].

[119] **M. Martinez, R. Ryblewski, and M. Strickland**. « Boost-Invariant (2+1)-dimensional Anisotropic Hydrodynamics ». In: *Phys.Rev.* C85 (2012), p. 064913. DOI: 10.1103/PhysRevC.85.064913. arXiv:1204.1473 [nucl-th].

[120] **M.P. Heller, R.A. Janik, and P. Witaszczyk**. « Hydrodynamic Gradient Expansion in Gauge Theory Plasmas ». In: *Phys.Rev.Lett.* 110.21 (2013), p. 211602. DOI: 10.1103/PhysRevLett.110.211602. arXiv:1302.0697 [hep-th].

[121] **J. Berges et al.** « Simulating plasma instabilities in SU(3) gauge theory ». In: *Phys.Lett.* B677 (2009), pp. 210–213. DOI: 10.1016/j.physletb.2009.05.008. arXiv:0812.3859 [hep-ph].

[122] **E. Iancu, A. Leonidov, and L.D. McLerran**. « The Color glass condensate: An Introduction ». In: (2002), pp. 73–145. arXiv:hep-ph/0202270 [hep-ph].

[123] **F. Gelis et al.** « The Color Glass Condensate ». In: *Ann.Rev.Nucl.Part.Sci.* 60 (2010), pp. 463–489. DOI: 10.1146/annurev.nucl.010909.083629. arXiv:1002.0333 [hep-ph].

[124] **F. Gelis**. « Color Glass Condensate and Glasma ». In: (2012). arXiv:1211.3327 [hep-ph].

[125] **J. Jalilian-Marian et al.** « The Intrinsic glue distribution at very small x ». In: *Phys.Rev.* D55 (1997), pp. 5414–5428. DOI: 10.1103/PhysRevD.55.5414. arXiv:hep-ph/9606337 [hep-ph].

[126] **J. Jalilian-Marian et al.** « The BFKL equation from the Wilson renormalization group ». In: *Nucl.Phys.* B504 (1997), pp. 415–431. DOI: 10.1016/S0550-3213(97)00440-9. arXiv:hep-ph/9701284 [hep-ph].

[127] **J. Jalilian-Marian et al.** « The Wilson renormalization group for low x physics: Towards the high density regime ». In: *Phys.Rev.* D59 (1998), p. 014014. DOI: 10.1103/PhysRevD.59.014014. arXiv:hep-ph/9706377 [hep-ph].

[128] **J. Jalilian-Marian et al.** « Unitarization of gluon distribution in the doubly logarithmic regime at high density ». In: *Phys.Rev.* D59 (1999), p. 034007. DOI: 10.1103/PhysRevD.59.034007,10.1103/PhysRevD.59.099903. arXiv:hep-ph/9807462 [hep-ph].

[129] **E. Iancu, A. Leonidov, and L.D. McLerran**. « Nonlinear gluon evolution in the color glass condensate. 1. » In: *Nucl.Phys.* A692 (2001), pp. 583–645. DOI: 10.1016/S0375-9474(01)00642-X. arXiv:hep-ph/0011241 [hep-ph].

[130] **E. Iancu, A. Leonidov, and L.D. McLerran**. « The Renormalization group equation for the color glass condensate ». In: *Phys.Lett.* B510 (2001), pp. 133–144. DOI: 10.1016/S0370-2693(01)00524-X. arXiv:hep-ph/0102009 [hep-ph].

[131] **E. Ferreiro et al.** « Nonlinear gluon evolution in the color glass condensate. 2. » In: *Nucl.Phys.* A703 (2002), pp. 489–538. DOI: 10.1016/S0375-9474(01)01329-X. arXiv:hep-ph/0109115 [hep-ph].

[132] **E.S. Weibel**. « Spontaneously Growing Transverse Waves in a Plasma Due to an Anisotropic Veloc ity Distribution ». In: *Phys.Rev.Lett.* 2 (1959), pp. 83–84. DOI: 10.1103/PhysRevLett.2.83.

[133] **T.N. Tudron**. « Instability of Constant Yang-Mills Fields Generated by Constant Gauge Potentials ». In: *Phys.Rev.* D22 (1980), p. 2566. DOI: 10.1103/PhysRevD.22.2566.

[134] **A. Iwazaki**. « Decay of Color Gauge Fields in Heavy Ion Collisions and Nielsen-Olesen Instability ». In: *Prog.Theor.Phys.* 121 (2009), pp. 809–822. DOI: 10.1143/PTP.121.809. arXiv:0803.0188 [hep-ph].

[135] **H. Fujii and K. Itakura**. « Expanding color flux tubes and instabilities ». In: *Nucl.Phys.* A809 (2008), pp. 88–109. DOI: 10.1016/j.nuclphysa.2008.05.016. arXiv:0803.0410 [hep-ph].

[136] **H. Fujii, K. Itakura, and A. Iwazaki**. « Instabilities in non-expanding glasma ». In: *Nucl.Phys.* A828 (2009), pp. 178–190. DOI: 10.1016/j.nuclphysa.2009.06.020. arXiv:0903.2930 [hep-ph].

[137] **J.D. Bjorken**. « Highly Relativistic Nucleus-Nucleus Collisions: The Central Rapidity Region ». In: *Phys.Rev.* D27 (1983), pp. 140–151. DOI: 10.1103/PhysRevD.27.140.

[138] **J.S. Schwinger**. « Brownian motion of a quantum oscillator ». In: *J.Math.Phys.* 2 (1961), pp. 407–432. DOI: 10.1063/1.1703727.

[139] **L.V. Keldysh**. « Diagram technique for nonequilibrium processes ». In: *Zh.Eksp.Teor.Fiz.* 47 (1964), pp. 1515–1527.

[140] **C. Itzykson and J.B. Zuber**. « Quantum Field Theory ». In: (1980).

[141] **F. Gelis and R. Venugopalan**. « Particle production in field theories coupled to strong external sources ». In: *Nucl.Phys.* A776 (2006), pp. 135–171. DOI: 10.1016/j.nuclphysa.2006.07.020. arXiv:hep-ph/0601209 [hep-ph].

[142] **F. Gelis and R. Venugopalan**. « Particle production in field theories coupled to strong external sources. II. Generating functions ». In: *Nucl.Phys.* A779 (2006), pp. 177–196. DOI: 10.1016/j.nuclphysa.2006.08.015. arXiv:hep-ph/0605246 [hep-ph].

[143] **G. Aarts and J. Smit**. « Particle production and effective thermalization in inhomogeneous mean field theory ». In: *Phys.Rev.* D61 (2000), p. 025002. DOI: 10.1103/PhysRevD.61.025002. arXiv:hep-ph/9906538 [hep-ph].

[144] **M. Salle, J. Smit, and J.C. Vink**. « Staying thermal with Hartree ensemble approximations ». In: *Nucl.Phys.* B625 (2002), pp. 495–511. DOI: 10.1016/S0550-3213(01)00659-9. arXiv:hep-ph/0012362 [hep-ph].

[145] **F. Cooper et al.** « Nonequilibrium dynamics of symmetry breaking in lambda Phi**4 field theory ». In: *Phys.Rev.* D55 (1997), pp. 6471–6503. DOI: 10.1103/PhysRevD.55.6471. arXiv:hep-ph/9610345 [hep-ph].

[146] **J. Berges**. « N-particle irreducible effective action techniques for gauge theories ». In: *Phys.Rev.* D70 (2004), p. 105010. DOI: 10.1103/PhysRevD.70.105010. arXiv:hep-ph/0401172 [hep-ph].

[147] **M. Abramowitz and I.A. Stegun**. *Handbook of Mathematical Functions*. Fifth. New York: Dover, 1964.

[148] **D.I. Ketcheson**. « Highly efficient strong stability preserving Runge-Kutta methods with low-storage implementations ». In: *SIAM Journal on Scientific Computing* 30(4) (2008), pp. 2113–2136.

[149] **R.D. Pisarski**. « Scattering Amplitudes in Hot Gauge Theories ». In: *Phys.Rev.Lett.* 63 (1989), p. 1129. DOI: 10.1103/PhysRevLett.63.1129.

[150] **E. Braaten and R.D. Pisarski**. « Soft Amplitudes in Hot Gauge Theories: A General Analysis ». In: *Nucl.Phys.* B337 (1990), p. 569. DOI: 10.1016/0550-3213(90)90508-B.

[151] **G.D. Moore**. « Problems with lattice methods for electroweak preheating ». In: *JHEP* 0111 (2001), p. 021. DOI: 10.1088/1126-6708/2001/11/021. arXiv:hep-ph/0109206 [hep-ph].

[152] **J. Berges, S. Scheffler, and Sexty**. « Turbulence in nonabelian gauge theory ». In: *Phys.Lett.* B681 (2009), pp. 362–366. DOI: 10.1016/j.physletb.2009.10.032. arXiv:0811.4293 [hep-ph].

[153] **S. Schlichting**. « Turbulent thermalization of weakly coupled non-abelian plasmas ». In: *Phys.Rev.* D86 (2012), p. 065008. DOI: 10.1103/PhysRevD.86.065008. arXiv:1207.1450 [hep-ph].

[154] **J. Berges and D. Sexty**. « Bose condensation far from equilibrium ». In: *Phys.Rev.Lett.* 108 (2012), p. 161601. DOI: 10.1103/PhysRevLett.108.161601. arXiv:1201.0687 [hep-ph].

[155] **J. Berges, S. Schlichting, and D. Sexty**. « Over-populated gauge fields on the lattice ». In: *Phys.Rev.* D86 (2012), p. 074006. DOI: 10.1103/PhysRevD.86.074006. arXiv:1203.4646 [hep-ph].

[156] **J. Berges et al.** « Basin of attraction for turbulent thermalization and the range of validity of classical-statistical simulations ». In: (2013). arXiv:1312.5216 [hep-ph].

[157] **A.N. Kolmogorov**. « The Local Structure of Turbulence in Incompressible Viscous Fluid for Very Large Reynolds Numbers ». In: *Proceedings of the USSR Academy of Sciences* 30 (1941), 299–303. DOI: 10.1098/rspa.1991.0075.

[158] **A.N. Kolmogorov**. « Dissipation of Energy in the Locally Isotropic Turbulence ». In: *Proceedings of the USSR Academy of Sciences* 32 (1941), 16–18. DOI: 10.1098/rspa.1991.0076.

[159] **A. Gynther et al.** « Four-loop pressure of massless O(N) scalar field theory ». In: *JHEP* 0704 (2007), p. 094. DOI: 10.1088/1126-6708/2007/04/094. arXiv:hep-ph/0703307 [HEP-PH].

[160] **J. Berges, K. Boguslavski, and S. Schlichting**. « Nonlinear amplification of instabilities with longitudinal expansion ». In: *Phys.Rev.* D85 (2012), p. 076005. DOI: 10.1103/PhysRevD.85.076005. arXiv:1201.3582 [hep-ph].

[161] **I.S. Gradshteyn and I.M. Ryzhik**. *Table of integrals, series, and products*. Elsevier/Academic Press, Amsterdam, 2007, pp. xlviii+1171. ISBN: 978-0-12-373637-6; 0-12-373637-4.

[162] **U.W. Heinz**. « Kinetic Theory for Nonabelian Plasmas ». In: *Phys.Rev.Lett.* 51 (1983), p. 351. DOI: 10.1103/PhysRevLett.51.351.

[163] **P.F. Kelly et al.** « Classical transport theory and hard thermal loops in the quark - gluon plasma ». In: *Phys.Rev.* D50 (1994), pp. 4209–4218. DOI: 10.1103/PhysRevD.50.4209. arXiv:hep-ph/9406285 [hep-ph].

[164] **J.P. Blaizot and E. Iancu**. « A Boltzmann equation for the QCD plasma ». In: *Nucl.Phys.* B557 (1999), pp. 183–236. DOI: 10.1016/S0550-3213(99)00341-7. arXiv:hep-ph/9903389 [hep-ph].

[165] **M. Asakawa, S.A. Bass, and B. Muller**. « Anomalous Transport Processes in Turbulent non-Abelian Plasmas ». In: *Nucl.Phys.* A854 (2011), pp. 76–80. DOI: 10.1016/j.nuclphysa.2010.07.013. arXiv:1008.3496 [nucl-th].

[166] **M. Asakawa, S.A. Bass, and B. Muller**. « Anomalous transport processes in anisotropically expanding quark-gluon plasmas ». In: *Prog.Theor.Phys.* 116 (2007), pp. 725–755. DOI: 10.1143/PTP.116.725. arXiv:hep-ph/0608270 [hep-ph].

[167] **J.C. Collins**. « Renormalization. An introduction to renormalization, the renormalization group, and the operator product expansion ». In: (1984).

[168] **S. Weinberg**. In: *Phys.Rev.* 111 (1960), p. 838.

[169] **W. Zimmermann**. « The power counting theorem for minkowski metric ». In: *Commun.Math.Phys.* 11 (1968), pp. 1–8. DOI: 10.1007/BF01654298.

[170] **Y. Hahn and W. Zimmerman**. « An elementary proof of Dyson's power counting theorem ». In: *Communications in Mathematical Physics* 10.4 (1968), pp. 330–342. URL: http://projecteuclid.org/euclid.cmp/1103841121.

[171] **W.E. Caswell and A.D. Kennedy**. « A Simple Approach To Renormalization Theory ». In: *Phys.Rev.* D25 (1982), p. 392. DOI: 10.1103/PhysRevD.25.392.

[172] **W.E. Caswell and A.D. Kennedy**. « The Asymptotic Behavior of Feynman Integrals ». In: *Phys.Rev.* D28 (1983), p. 3073. DOI: 10.1103/PhysRevD.28.3073.

[173] **M.E. Peskin and D.V. Schroeder**. « An Introduction to quantum field theory ». In: (1995).

[174] **E.M. Lifsic and L.P. Pitaevskij**. *Physical kinetics*. English. Oxford [u.a.]: Pergamon, 1995. ISBN: 0750626356 9780750626354.

[175] **A.H. Mueller and D.T. Son**. « On the equivalence between the Boltzmann equation and classical field theory at large occupation numbers ». In: *Physical Letter B* 582 (2004), p. 279.

[176] **R. Kubo**. « Statistical mechanical theory of irreversible processes. 1. General theory and simple applications in magnetic and conduction problems ». In: *J.Phys.Soc.Jap.* 12 (1957), pp. 570–586. DOI: 10.1143/JPSJ.12.570.

[177] **P.C. Martin and J.S. Schwinger**. « Theory of many particle systems. 1. » In: *Phys.Rev.* 115 (1959), pp. 1342–1373. DOI: 10.1103/PhysRev.115.1342.

[178] **R.L. Stratonovich**. In: *Sov. Phys. Dok.* 2 (1957), p. 416.

[179] **J. Hubbard**. « Calculation of partition functions ». In: *Phys.Rev.Lett.* 3 (1959), pp. 77–80. DOI: 10.1103/PhysRevLett.3.77.

[180] **J. Berges and D. Sexty**. « Real-time gauge theory simulations from stochastic quantization with optimized updating ». In: *Nucl.Phys.* B799 (2008), pp. 306–329. DOI: 10.1016/j.nuclphysb.2008.01.018. arXiv:0708.0779 [hep-lat].

[181] **G. Aarts et al.** « Stability of complex Langevin dynamics in effective models ». In: *JHEP* 1303 (2013), p. 073. DOI: 10.1007/JHEP03(2013)073. arXiv:1212.5231 [hep-lat].

[182] **G. Aarts et al.** « Controlling complex Langevin dynamics at finite density ». In: *Eur.Phys.J.* A49 (2013), p. 89. DOI: 10.1140/epja/i2013-13089-4. arXiv:1303.6425 [hep-lat].

[183] **K. Fukushima and T. Hayata**. « Schwinger Mechanism with Stochastic Quantization ». In: (2014). arXiv:1403.4177 [hep-th].

[184] **G. Gelis, K. Kajantie, and T. Lappi**. « Quark-antiquark production from classical fields in heavy ion collisions: 1+1 dimensions ». In: *Phys.Rev.* C71 (2005), p. 024904. DOI: 10.1103/PhysRevC.71.024904. arXiv:hep-ph/0409058 [hep-ph].

[185] **A.J. Baltz and L.D. McLerran**. « Two center light cone calculation of pair production induced by ultrarelativistic heavy ions ». In: *Phys.Rev.* C58 (1998), pp. 1679–1688. DOI: 10.1103/PhysRevC.58.1679. arXiv:nucl-th/9804042 [nucl-th].

[186] **K. Fukushima, F. Gelis, and L.D. McLerran**. « Initial Singularity of the Little Bang ». In: *Nucl.Phys.* A786 (2007), pp. 107–130. DOI: 10.1016/j.nuclphysa.2007.01.086. arXiv:hep-ph/0610416 [hep-ph].

[187] **K. Dusling, F. Gelis, and R. Venugopalan**. « The initial spectrum of fluctuations in the little bang ». In: *Nucl.Phys.* A872 (2011), pp. 161–195. DOI: 10.1016/j.nuclphysa.2011.09.012. arXiv:1106.3927 [nucl-th].

[188] **F. Gelis and Y. Mehtar-Tani**. « Gluon propagation inside a high-energy nucleus ». In: *Phys.Rev.* D73 (2006), p. 034019. DOI: 10.1103/PhysRevD.73.034019. arXiv:hep-ph/0512079 [hep-ph].

[189] **A. Cucchieri and T. Mendes**. « Critical slowing down in SU(2) Landau gauge fixing algorithms ». In: *Nucl.Phys.* B471 (1996), pp. 263–292. DOI: 10.1016/0550-3213(96)00177-0. arXiv:hep-lat/9511020 [hep-lat].

[190] **A. Cucchieri and T. Mendes**. « Study of critical slowing down in SU(2) Landau gauge fixing ». In: *Nucl.Phys.Proc.Suppl.* 53 (1997), pp. 811–814. DOI: 10.1016/S0920-5632(96)00789-X. arXiv:hep-lat/9608051 [hep-lat].

[191] **G.D. Moore**. « Motion of Chern-Simons number at high temperatures under a chemical potential ». In: *Nucl.Phys.* B480 (1996), pp. 657–688. DOI: 10.1016/S0550-3213(96)00445-2. arXiv:hep-ph/9603384 [hep-ph].